

UC San Diego

UC San Diego Electronic Theses and Dissertations

Title

Parametric band translation using highly-nonlinear and photonic crystal fibers

Permalink

<https://escholarship.org/uc/item/5fj6h26v>

Author

Jiang, Rui

Publication Date

2008

Peer reviewed|Thesis/dissertation

UNIVERSITY OF CALIFORNIA, SAN DIEGO

Parametric Band Translation using Highly-Nonlinear and Photonic
Crystal Fibers

A dissertation submitted in partial satisfaction of the requirements
for the degree Doctor of Philosophy

in

Electrical Engineering

by

Rui Jiang

Committee in charge:

Professor Stojan Radic, Chair
Professor Yeshaiyahu Fainman
Professor George Papen
Professor Lu Sham
Professor Amin Vahdat

2008

Copyright
Rui Jiang, 2008
All rights reserved

The dissertation of Rui Jiang is approved, and it is acceptable in quality and form for publication on microfilm and electronically:

Chair

University of California, San Diego

2008

TABLE OF CONTENTS

Signature Page	iii
Table of Contents	iv
List of Figures.	viii
List of Tables	xxiii
Acknowledgement.	xxiv
Vita and Publications.	xxvi
Fields of Study.	xxix
Abstract of the Dissertation.	xxx
Chapter 1 Introduction.	1
1.1 Underwater Communication Challenge.	1
1.2 Frequency Mixer as an enabling technology.	3
1.2.1 Electronic mixer.	3
1.2.2 Optical mixer.	5
1.3 Physics of Mixer Devices.	8
1.4 Optical mixing mechanism.	11
1.4.1 Nonlinear medium comparison.	11
1.4.2 Parametric process in fiber.	13
1.4.3 High-confinement fibers.	16
1.5 Summary.	21
Chapter 2 Parametric Process in Highly Nonlinear Fibers.	23
2.1 Introduction.	23
2.2 One-pump parametric process.	24

2.2.1 Phase matching condition.....	24
2.2.2 High-order dispersion contribution.....	30
2.2.3 Parametric gain discussion in a one-pump structure.....	34
2.3 Two-pump parametric structure.....	35
2.3.1 Four-sideband couple-mode equations.....	35
2.3.2 Two-sideband analysis.....	36
2.3.3 Four-sideband analysis.....	39
2.4 Optimizing the bandwidth of two-pump amplifier.....	45
2.5 Impact of dispersion fluctuation on parametric systems.....	51
2.5.1 Phase matching under dispersion fluctuation.....	51
2.5.2 Dispersion fluctuation in one- and two-pump parametric structure.....	56
2.5.3 Mathematical description of dispersion fluctuation in fiber.....	59
2.5.4 Stochastic Four-sideband Model.....	61
2.5.5 Numerical simulations.....	66
2.6 Practical implementation of two-pump interaction:40Gb/s switching.....	75
Chapter 3 Photonic Crystal as Parametric Platform.....	86
3.1 Introduction.....	86
3.2 Effective Index Model.....	92
3.3 2-D Fourier Analysis.....	98
3.4 Beam Propagation Method.....	103
3.5 The relationship between transverse structure and dispersion profile.....	106
3.6 Polarization maintaining (PM) PCF.....	109
3.7 Conclusion.....	110

Chapter 4 NIR-to-Visible Translation in Silica Photonic Crystal Fiber.....	112
4.1 Coupling optics.....	113
4.1.2 Free-Space coupling.....	114
4.2 Phase matching in PCF.....	120
4.3 Parametric generation in PCF.....	124
4.4 Amplitude modulation translation from telecom to visible band.....	131
4.5 Phase modulation translation from NIR to visible band.....	149
4.6 Characterization of Parametric Translation in PCF.....	157
4.6.1 SBS in PCF.....	157
4.6.2 Polarization decoupling.....	163
4.6.3 Multimode guiding.....	170
4.6.4 Dispersion fluctuation.....	177
4.6.4.1 Experiments.....	178
4.6.4.2 Theoretical analysis and simulations.....	183
4.7 Temperature dependence of the parametric translation process.....	189
4.8 Reverse translation: Visible to NIR Conversion.....	192
4.9 Conclusion.....	195
Chapter 5 Silica PCF design.....	196
5.1 Introduction.....	196
5.2 PCF design for telecom-to-visible translation.....	199
5.3 Discussion of structure variation.....	203
5.4 Experimental results on new fiber.....	208
5.5 Conclusion.....	207

Chapter 6 Chalcogenide PCF design.....	210
6.1 Introduction.....	211
6.2 Chalcogenide glass.....	212
6.3 Chalcogenide PCF.....	219
6.4 Theoretical results on telecom-to-MWIR translation.....	223
6.5 Conclusion.....	225
Chapter 7 Conclusion.....	226
7.1 Review of the work.....	226
7.2 Future direction.....	229
Appendix: Free-space-to-PCF Coupling Protocol.....	231
Reference.....	234

List of Figures

Figure 1 Schematic of the application of a mixer in an RF communication system.....	4
Figure 2 Distinctive optical bands serve different yet important applications.....	5
Figure 3 Optical system architecture that is enabled by optical mixer.....	7
Figure 4 I-V characteristics of a Schottky diode, showing a nonlinear behavior.....	8
Figure 5 A cavity structure is generally used in crystal based nonlinear optics.....	12
Figure 6 Illustration of parametric process in fiber.....	13
Figure 7 Two pump parametric interactions, in which three processes, namely, modulation instability, phase conjugation and bragg scattering, are coupled with each other and generate four sidebands with certain phase relations.....	15
Figure 8 Two typical HNLF transverse structures with 1) raised inner cladding and 2) depressed inner cladding.....	17
Figure 9 Transverse structure of a PCF consisting of a hexagonal silica core surrounded by a cladding with a honeycomb arrangement of circular air holes.....	18
Figure 10 Comparison of the dispersion profile of silica HNLF and PCF.....	19
Figure 11 a) wavenumber mismatch parameter and b) experimentally measured power spectrum for one-pump parametric scheme.....	29
Figure 12 One-pump parametric gain versus the pump wavelength.....	30
Figure 13 Parametric phase shift and corresponding gain shown in the same plot for $\beta_2 < 0$ and $\beta_4 < 0$. Fourth order dispersion change does not change the profile of parametric phase.....	31

Figure 14 Parametric phase shift and corresponding gain shown in the same plot for $\beta_2 < 0$ and $\beta_4 > 0$. Fourth order dispersion introduces additional phase matching region.....	33
Figure 15. Parametric phase shift and corresponding gain shown in the same plot for $\beta_2 > 0$ and $\beta_4 < 0$. Fourth order dispersion creates phase matching region for normal-positioned pump.....	34
Figure 16 Parametric phase shift of a PC process.....	37
Figure 17 Phase conjugation gain for a two-pump parametric system with the operation condition illustrated in the text.....	38
Figure 18 Four-sideband gain when a) signal injected at outer band and b) signal injected at inner band. Pumps are centered at ZDWL.....	40
Figure 19 Four-sideband gain when a) signal injected at outer band and b) signal injected at inner band. Pumps are centered at normal dispersion regime.....	41
Figure 20 Four-sideband gain when a) signal injected at outer band and b) signal injected at inner band. Pumps are centered at anomalous dispersion regime.....	42
Figure 21 Four-sideband gain when a) signal injected at outer band and b) signal injected at inner band. Pumps are centered at ZDWL.....	43
Figure 22 Four-sideband gain when a) signal injected at outer band and b) signal injected at inner band. Pumps are centered at normal dispersion regime.....	44
Figure 23 Four-sideband gain when a) signal injected at outer band and b) signal injected at inner band. Pumps are centered at ZDWL.....	45
Figure 24 Experimental setup of two pump parametric amplifier. λ_1 : C-band pump at 1539.5nm; λ_2 : L-band pump at 1614nm. λ_s : tunable signal; DET could be either a power meter or an OSA.....	47

Figure 25 a) ASE spectrum of the two-pump parametric amplifier; the measured 3dB bandwidth is 50.68nm b) Typical amplified signal and four-sideband spectrum. 40dB of gain is observed.....48

Figure 26 Measured gain spectra at different pump power levels. 50.28nm bandwidth with 41.5dB average gain is obtained. The pumps are at 1539.5nm and 1614nm, respectively. The resolution bandwidth is 2nm for all cases.....50

Figure 27 Predicted gain profile with the pumps placed at 1510nm and 1647.5 nm, respectively, with 1W incident power for both pumps.....51

Figure 28 A schematic illustration of parametric phase mismatch number κ along fiber length. κ jumps from 0 to κ_0 during the region $[z_0, z_0+1]$ due to dispersion fluctuation..54

Figure 29 Illustration of a random pattern of dispersion fluctuation along the fiber. Dispersion fluctuation induced negative parametric phase shift in region $[z_0+11, z_0+12]$ was partially compensated by the positive phase shift introduced in region $[z_0, z_0+11]$56

Figure 30 Parametric phase shift versus frequency shift in the MI process (one-pump structure) in a) an ideal condition and b) with longitudinal dispersion fluctuation.....57

Figure 31 Parametric phase shift versus frequency shift in the PC process in a) an ideal condition and b) with longitudinal dispersion fluctuation.....59

Figure 32 Illustration of β_2 as a function of both λ and z . Dispersion fluctuation offsets the ZDWL and changes the dispersion slope.....60

Figure 33 Comparison of the four-band and two-band model results on the impact of the dispersion fluctuation on two-pump gain profile. Pumps changed from 1575.12/

1525.12nm (solid curve) to 1602.6/1500.6nm (dashed curve). λ_d refers to the two-pump separation and l_c is the correlation length.....66

Figure 34 (a) Schematic of fiber sections for numerical simulations. L: fiber length; l_c : correlation length; Δz : section length within which dispersion is constant. (b) ZDWL offset at $z+\Delta z$ section determined by both the influence from the pervious section (D) and the local fluctuations (S). D: deterministic part; S: stochastic part.....68

Figure 35 Comparison of the numerical simulations and analytical results for different correlation lengths with two pumps at 1575.12nm and 1525.12nm respectively. l_c denotes correlation length. Other fiber parameters: $\gamma=10/\text{km}/\text{W}$, $\langle\lambda_0\rangle=1550\text{nm}$, $\beta_3=0.12\text{ps}^3/\text{km}$, $\beta_4=10^{-4}\text{ps}^4/\text{km}$, $L=500\text{ m}$, $P_1=P_2=0.5\text{W}$69

Figure 36 Calculations of gain profiles for different pump separations without (top plot) and with (bottom plot) dispersion fluctuations using four-band model. Reducing pump separations mitigates the impact of dispersion fluctuation in the inner band region. Calculations were performed assuming the following parameters: $\lambda_d=1\text{ nm}$, $l_c=5\text{ m}$, $L=500\text{ m}$, $\beta_3=0.1\text{ ps}^3/\text{km}$, $\beta_4=10^{-4}\text{ ps}^4/\text{km}$; $\gamma=10/\text{ km}/\text{W}$, and $P_1=P_2=0.5\text{ W}$71

Figure 37 Experimental results of the gain profile of two pump parametric process with different pump separations. Signal and idlers are shown to illustrate four-sideband nature of the two-pump interactions. It is demonstrated that reducing pump separations does flatten out the gain spectrum in the inner band region. Experimental condition: C band pump: $\lambda_C=1569\text{nm}$, $P_1=0.5\text{W}$, L band pump: $\lambda_L=1597\text{nm}$, $P_2=0.5\text{W}$; Fiber length $L=500\text{m}$; average ZDWL $\lambda_0=1583\text{nm}$; average dispersion slope $S=0.02\text{ps}/\text{nm}^2/\text{km}$73

Figure 38. Experimentally measured gain profiles of the two-pump parametric process with the equal pump positions and input power. Results are shown for 3 different HNL fiber coils drawn from the same process. B is the result for a 500m coil, whereas plots C and D correspond to coils A and B in the text, both with length of 1000m. The 500m coil is the best in terms of dispersion fluctuation.....74

Figure 39 Optical switching of the two-pump parametric gain by switching the L-band pump on and off.....76

Figure 40 Experimental setup. TF: tunable filter. PM: phase modulator. AM: amplitude modulator. PC: polarization controller. ODL: optical delay line. OSA: optical spectrum analyzer. OSC: oscilloscope. BS: band splitter. C1: 10/90 coupler. C2: 1/99 coupler. C: circulator. DET: detector; it can be either an OSA, an OSC, or a power meter used for characterizing the input signal, C- or L-band pump. OSA2 is used for monitoring Brillouin scattering of the pumps.....78

Figure 41 Optical spectrum measured at the output of HNLF, recorded with 0.2-nm resolution when a 1559-nm signal is launched. Other details are given in the text.....79

Figure 42 Temporal waveforms showing packet switching. A fixed input level was used in the oscilloscope for all signal/idlers waves. (a) Input 1559.0-nm signal; (b) L-band pump; (c) amplified signal; (d) switched 1578.1-nm idler; (e) switched 1588.1-nm idler; (f) switched 1608.0-nm idler.....82

Figure 43 Amplified 1-ns packet of the 1559.0-nm signal when the L-band pump is temporally shifted in such a way that its leading edge coincides with the signal bit marked by arrow 1 in Figure 42.....83

Figure 44 Temporal waveforms showing bit-level switching. (a) Input 1559.0-nm signal; (b) L-band pump; (c) amplified signal bit when the pump bit is located at Position 2. The inset shows the signal waveform when the pump bit is located at Position 1. (d) Switched bit for the outer-band idler at 1608.0 nm.....	84
Figure 45 Fundamental space filling mode of a PCF cladding structure.....	88
Figure 46 Illustration of typical PCF parameters. Λ , being the distance between the air holes is usually called period or pitch, and d is the diameter of the air holes.....	91
Figure 47 SEM scanning picture of a PCF structure with period $\Lambda=1.2\mu\text{m}$ and $d/\Lambda=0.6$	92
Figure 48 Two steps for modeling a PCF with EIM: a) Acquiring the effective cladding index n_{eff} by solving the FSM of the periodic cladding structure; b) The PCF is simplified to an equivalent step-index whose cladding index equals n_{eff} . n_{eff} is a function of λ	93
Figure 49 Equivalent circular unit cell of a hexagonal one for a PCF.....	93
Figure 50 Guiding properties of several PCF structures. V_{eff} curve versus the normalized frequency were calculated.....	96
Figure 51 Comparison of EIM results against the MPB method. EIM results closely resembles the MPB results provided proper effective fiber parameters are chosen. In all calculations, $d/\Lambda=0.55$ while period varies from 1.1mm to 1.3mm.....	97
Figure 52 Comparison of Sellmeier's model with the 6 order polynomial model accounting for the silica material dispersion.....	98

Figure 53 Calculated and measured field diameter for three waves. MFD: mode field diameter.....	102
Figure 54 Both scalar and full-vectorial iterative BPM are computed against the MPB results. In the plot, we also show the smoothed full-vector results. Calculation shows that full-vectorial method must be used (due to high index contrasts).....	105
Figure 55 Comparison of RSoft BPM implementations and MPB results – good agreement achieved.....	106
Figure 56 Dispersion profiles with fixed air-filling factor but various period values.....	108
Figure 57 Simulated dispersion profile with fixed period value but various air-filling factors.....	109
Figure 58 Cross section of a PM PCF in which two opposite holes in the innermost ring layer are deliberately made larger than other air holes, introducing birefringence and changing dispersion profile.....	110
Figure 59 Illustration of the impact of PM-hole size onto dispersion profile.....	111
Figure 60 Schematics of the experimental setup.....	113
Figure 61 A lens focusing optics. D is the incident beam size and d is the focusing spot size.....	114
Figure 62 System for simultaneously coupling 780 nm and 1550 nm waves. Telescope system in 780 nm is regular configuration while the telescope in 1550 nm arm is made into a focusing structure so that the focal spot of both 780nm and 1550nm are at position H. The dimension parameters are defined as the following: d_1, d_2, d_5, d_7 are the 780nm wave's beam diameter at position A, B, G, H; d_3, d_4, d_6, d_8 are the 1550 nm wave's	

beam diameter at position C, D, G, H; the optical path from position D to G is L, assuming all the optics components are thin elements.....	116
Figure 63 Schematics of optical path of 1550nm wave.....	118
Figure 64 Dispersion profile of a typical PCF. The PCF parameters are shown in the figure. Calculation shows that 6th order dispersion is important for an experimental operation with $\lambda_p=780\text{nm}$ and $D_w \sim 1000\text{THz}$	121
Figure 65 Phase matching contour corresponding the dispersion profile in Figure 64.....	123
Figure 66 Experimental setup. W: half-waveplate; T: telescope; MO1-MO2: microscopic objective; F: filter; S: spectrometer. The 90/10 tap is used for pump power and back-reflecting spectrum monitoring.....	124
Figure 67 Measured and calculated Phase-matching contours of the parametric generation at a) visible range (measured) and b) near-infrared range (calculated). The two contours circled together represent two polarization states, with the filled marker corresponding to slow axis and open marker fast axis.....	127
Figure 68 Measured phase matching contour for the two principle axes of the PCF. The asymmetric PCF transverse structure results in the phase matching condition difference for the two polarizations.....	129
Figure 69 Two PCF with their dispersion profile shown in a) and phase matching contour shown in b). We observe that the measured results agrees well with the calculations.....	130
Figure 70 Scanning electron microscope image of the commercial photonic crystal fiber used in this work.....	132

Figure 71 a) dispersion curve of the PCF with two zero dispersion wavelength at 750nm and 1260nm respectively, b) Phase matching contour of the PCF shown on the right.....	133
Figure 72 Experimental Setup; symbols as defined in text. Inset indicates typical visible (converted) single-channel spectrum. PC-Polarization Controller; MZ- Mach-Zehnder Amplitude modulator; PG- pattern generator; D- fiber decorrelator; S- Scope; A- Amplifier; F- filter; V- Variable Optical Attenuator; P1- Polarizer; W1-W2: $\lambda/2$ waveplate; T: Telescope; M1-metallic mirror; M2- Dichroic mirror; MO1-MO2: Microscopic Objective; GF-Grating Filter.....	135
Figure 73 Pump (800nm), signal (1550nm) and idler (539nm) evolution in case of lossless (dashed curve) and lossy PCF. Corresponding losses for signal/pump/idler bands in dB/km: 50/50/50 (heavy curve), 600/175/200 (medium curve) and 1200/350/400 (thin curve).....	137
Figure 74 Typical idler spectrum tuned across the visible band and measured by the visible spectrum analyzer.....	139
Figure 76 a) 200MHz harmonically modulated 1542nm signal (upper trace, 1550nm PIN receiver) and its translated waveform, corresponding to 3dB frequency rollover point of the visible receiver; b) 50MHz harmonically modulated 1541nm signal (upper trace) and its translated (531nm) waveform (lower trace).....	140
Figure 77 a) 50Mbps b) 155.52Mbps and c) 400Mbps modulated PRBS word received at 531nm.....	141
Figure 78 531nm eye pattern with 155.52Mbps NRZ modulation. The eye penalty is dominated by the operation of the visible receiver beyond 3dB rollover point.....	142

Figure 79 a) Four WDM channels at 1541nm, 1549nm, 1555nm and 1560nm are translated to visible spectral domain. Parametric pump is tuned to b) 791nm; c) 800nm and d) 802nm. Upper trace indicates visible (translated) and lower traces indicate 1550nm (signal) WDM band in all cases.....	144
Figure 80 Channels demultiplexed after visible translation: 574nm (upper trace) and 576nm (lower trace).....	144
Figure 81 Measured waveform at a) 1Gbps and b) 1.5Gbps and corresponding eye diagrams. Each division corresponds to 2ns for upper figures and 200ps for lower figures.....	146
Figure 82 Measured BER curve for idlers at 516.2nm and 514.4nm, respectively.....	147
Figure 83 Contour plot indicating the detection margin. The measured error-free detection threshold margin is one fourth of the eye opening and the error-free detection time margin is one half of the bit period.....	148
Figure 84 Experimental setup. λ_p : pump transmitter; λ_s : signal transmitter; PM – phase modulator; PG – pattern generator; C: collimator; P1 – polarizer; T1-T2: telescope system; M1 – M6: mirrors; W1-W2: half-waveplates; FM – flip mirror; BS1: 90/10 beam splitter; MO1-MO2 – microscopic objectives; D1-D2 – detectors; R1-R2: receivers; F: filter; S: oscilloscope; OSA: optical spectrum analyzer.....	150
Figure 85 Transverse structure of the PCF used in the experiment. The core, formed by missing one air hole in the center, is about 1.8 μ m diameter.....	152
Figure 86 Received visible channel at 518 nm with 1575 nm signal phase coded by data pattern a) 1000 b) 1000 0000 c) 1100. Time scale: 2 ns/div.....	154

Figure 87 a) Measured eye diagram for the translated 1Gbps phase coded signal. Time scale: 200 ps/div; b) measured BER curve c) BER contour plot of the eye diagram.....	155
Figure 88. a) Power transmission curve for the cases when the pump input polarization is aligned with the principle axes (open markers) and rotated at 45° to the principle axes (solid markers); Incident pump power refers to the power that is coupled into the PCF input end; b) Measured reflected and transmitted power when the pump is aligned on the principle axes; c) Back-reflecting spectrum of 780.2nm pump at 50mW input power level (black curve) and at 200mW input power level (gray curve) and input polarization aligned to the principle axes.....	160
Figure 89 a) Translated 1Gbps amplitude shift keying signal with SBS onset b) the identical waveform recorded by time-averaging. Time scale: 2ns/div.....	161
Figure 90 Measured (520nm) idler power with varying pump input. The signal power is fixed at 240mW. An exponential tendency was measured.....	162
Figure 91 Illustration of a) MFD and b) polarization evolution of pump, signal and idler waves in PCF. Different MFD results in diverse polarization evolution of the three waves.....	164
Figure 92 Setup for the fixed analyzer PMD measurement.....	165
Figure 93 PMD measurement response for a) 780nm and b) 1550nm.....	166
Figure 94 PER measurements for a) pump and b) signal, respectively. The results show that PER at signal wavelength is larger than that at pump wavelength, agreeing with the PMD measurements.....	167
Figure 95. a) Measured degree of linear polarization at the output of the PCF for both the 780 nm and 1550 nm waves. b) Measured idler power (518 nm) when the signal (1575nm)	

input polarization is aligned to the P1 axis, and tuning the pump (780nm) input polarization; c) Measured idler power (518 nm) when the pump input polarization is aligned to the P1 axis, while the signal input polarization is varied.....	169
Figure 96 Guiding metrics of PCF.....	171
Figure 97 Near-field image reveals that PCF with $L=1.2\text{mm}$ and $d/L=0.6$ can guide 780nm pump at second order transverse mode.....	173
Figure 98 Near-field image of the transverse mode at 500 nm with the same fiber in figure 33.....	173
Figure 99 Grating schematics.....	174
Figure 100 A grating helps separate high-order mode from fundamental mode. FM: fundamental mode; HOM: high order mode.....	175
Figure 101 Two sets of calculations show that by property set the incidental condition and the grating, separation of fundamental mode and high-order mode could be achieved.....	176
Figure 102 Impact of multi-mode guiding on the idler generation at various coupling lengths.....	177
Figure 103 SEM image of the three PCF coils: a) PCF A b) PCF B c) PCF C tested in the experiments.....	179
Figure 104 Cutback measurement results.....	181
Figure 105 Cutback measurements of the last 10-meter section.....	181
Figure 106 Power spectrum measurements for two-sections of a same PCF coil.....	182
Figure 107 Prediction of power evolution of pump, signal and idler in 40-meter PCF.....	186

Figure 108 Idler power spectrum assuming a random longitudinal variation with $d_a = 1\%$ and correlation length 2cm.....	187
Figure 109 Measured phase matching contours of a 5-meter, a 10-meter and a 20-meter section of the same PCF coil B. The phase matching contours overlap with each other, indicating the dispersion fluctuation period is much less than meter scale, agreeing with the cm-scale prediction.....	188
Figure 110 Dependence of the average thermal coefficient of refractive index of fused silica dn/dT on wavelength λ	190
Figure 111 Experimental setup. P1-P2: polarizer; W1-W2: half-waveplate; T1-T2: telescope system; M1-M2: mirrors; MO1-MO2: microscopic objectives; F: filter; OSA: optical spectrum analyzer.....	193
Figure 112. Signal spectrum with 3 peaks at 531.9nm, 532.08nm and 532.26nm.....	194
Figure 113 Translated telecom -band idler at various pump wavelengths.....	194
Figure 114 Flow chart illustrating the search procedure to find a proper PCF structure with targeted phase matching contour, air-filling factor and birefringence.....	198
Figure 115 Dispersion profiles of PCF with $d/\Lambda=0.5$ and various period values.....	200
Figure 116 Dispersion profiles of PCF with $d/\Lambda=0.5$, period = 1.4 μ m and various PM-hole sizes.....	201
Figure 117 a) optimum dispersion profile for telecom-to-visible band translation and b) the corresponding phase-matching contour.....	202
Figure 118 Phase matching contour with fixed period = 1.4 μ m and air-filling factor at 0.5 and various PM hole size.....	204

Figure 119 Phase matching contour with fixed air-filling factor at 0.5, PM hole size $d_2=1.55d$ and various period values.....	206
Figure 120 Phase matching contour with $L=1.4\text{mm}$, PM hole size $d_2=1.55d$ and altering air-filling factor.....	207
Figure 121 Typical structure of the newly-drawn fibers.....	209
Figure 122 Band translator that translates telecom band pump to MWIR idler. Modulation and processing is conducted on the tunable telecom pump. 980 nm is seeded as signal.....	212
Figure 123 Attenuation curve of chalcogenide glass, which shows a broad band transmission from 2-12 μm	213
Figure 124 nonlinear refractive index of chalcogenide and silica glass. Chalcogenide glass shows an n_2 that is 1000 times higher than that of silica glass.....	214
Figure 125 Measured chalcogenide PCF material refractive index overlapped with the fitted curve using Sellmeyer equation.....	217
Figure 126 Material dispersion profile of the chalcogenide PCF used in the experiment.....	218
Figure 127 a) preform and cross section of a typical chalcogenide PCF.....	219
Figure 128 Material dispersion, waveguide dispersion and total dispersion overlapped in one plot for the Chalcogenide PCF with $L=2.2\text{mm}$ and $d/L=0.5$	221
Figure 129 V_{eff} vs. Normalized frequency curve for various air-filling factors. The period is fixed at 2.2mm. When $d<1.1\text{mm}$, the Chalcogenide PCF becomes single-mode guiding at all three interacting waves. Normalized frequency = L/λ	221

Figure 130 a) dispersion profiles of various Chalcogenide PCF structure and b) their corresponding phase matching contour.....222

Figure 131 Power evolution in Chalcogenide PCF for a) $g = 500 \tilde{W} \cdot 1 \text{km}^{-1}$ b) $g = 5000 \tilde{W} \cdot 1 \text{km}^{-1}$. High conversion efficiency was achieved in both cases. Calculations show that fibers from tens of centimeters to several meters could be used.....224

List of Tables

Table 1.....	20
Table 2 PCF structure.....	125
Table 3 Loss information of three tested PCF coils.....	180
Table 4 Fiber parameters of the new-drawn fiber.....	209
Table 5 Approximate transmission windows of some chalcogenide glasses.....	213
Table 6 Fitting terms of the Sellmier equation for As ₂ S ₃ glass.....	215
Table 7 Fitting coefficients the Herzberger polynomial equation for Ge ₇ Sb ₃ Se ₁₅ glass.....	216
Table 8 Fitting coefficients the Sellmier equation for the experimental chalcogenide PCF.....	218

ACKNOWLEDGEMENT

With the completion of this thesis, I want to pay my cordial thanks to my advisor, Professor Stojan Radic. I am thankful to him for giving me persistent, professional and personal help, advice and guidance during my PhD study. I am also grateful to him for being considerate when I was at difficult times. Moreover, I appreciate his generous financial support so that I can finish my graduate study.

I want to thank my group colleagues: Dr. Nikola Alic, Slaven Moro, Evgeny Myslivets, Dr. Jose M. Chavez Boggio, Joshua Windmiller, Dr. Camille-Sophie Brès and James B Coles, for always being good help and nice friends. Meanwhile, I want to thank all my collaborators: Professor Yashiaiahu Fainman, Professor Joe Ford, Dr. Colin J. McKinstrie, Dr. Robert M. Jopson, Professor Govind P. Agrawal, Dr. Robert Sapperstein, Dr. Qiang Lin, and Trevor Chan, for their help and trust.

I am particularly indebted to my parents for their unfailing love and teaching. Last but not least, I want to say thank you to my wife. Her love inspired and encouraged me in all difficulties. She took good care of the family and our son so that I can focus on work and pursue my goal without hindrances and worries.

Chapter 2 contains the material from the following publications: R. Jiang, N. Alic, C.J. McKinstrie and S. Radic, “Two_Pump Parametric Amplifier with 40dB of Equalized Continuous Gain Over 50nm”, *Optical Fiber Communication Conference (2007)*, paper OWB2, Anaheim; R. Jiang, N. Alic, C.J. McKinstrie and S. Radic, “Four-sideband Analysis of Dispersion Fluctuations in Two Pump Fiber Parametric Devices”, *Conference for Laser and Electro-optics Society (2006)*, paper CMW1, Long Beach; Q. Lin, R. Jiang, C. F. Marki, C. J. McKinstrie, R. Jopson, G. P. Agrawal, S. Radic, “40-

gb/s optical switching and wavelength multicasting in a two-pump parametric device”, *IEEE Photonic Technology Letters*, Vol. 17, pp.2376-2378, 2005.

Chapter 4 contains the material from the following publication: R. Jiang, C.S. Bres, N. Alic, E. Myslivets and S. Radic, “Translation of Gbps Phase Modulated Optical Signal from Near-Infrared to Visible Band, *IEEE Journal of Lightwave Technology* Vol. 26, pp.131-137, 2008; R. Jiang, R. Saperstein, N. Alic, M. Nezhad, C. J. McKinstrie, J. Ford, Y. Fainman and S. Radic, “Continuous-Wave Band Translation between the Near-Infrared and Visible Spectral Ranges”, *IEEE Journal of Lightwave Technology*, Vol. 25, pp.58-66, 2007; R. Jiang, R. Saperstein, N. Alic, M. Nezhad, C. J. McKinstrie, J. Ford, Y. Fainman and S. Radic, “Parametric Wavelength Conversion from Conventional Near-Infrared to Visible Band”, *IEEE Photonic Technology Letters*, Vol. 18, pp.2445-2447, 2006; R. Jiang, N. Alic, C.B Sophie, S. Moro, and S. Radic. “Continuous-Wave Parametric Generation at Visible band in Photonic Crystal Fibers.” *20th Annual meeting of the IEEE Lasers and Electro-optics Society (2007)*, paper WQ5, Orlando

All material has been reproduced with the consent of all other authors.

–Rui Jiang

VITA

2000 Bachelor of Science, Department of Engineering Physics, Tsinghua University, Beijing, China

2003 Master of Science, Department of Mechanical Engineering, University of Rochester

2008 Doctor of Philosophy, University of California, San Diego

PUBLICATIONS

Journal publications:

1. R. Jiang, C.S. Bres, N. Alic, E. Myslivets and S. Radic, "Translation of Gbps Phase Modulated Optical Signal from Near-Infrared to Visible Band, *IEEE Journal of Lightwave Technology* Vol. 26, pp.131-137, 2008.
2. R. Jiang, R. Saperstein, N. Alic, M. Nezhad, C. J. McKinstrie, J. Ford, Y. Fainman and S. Radic, "Continuous-Wave Band Translation between the Near-Infrared and Visible Spectral Ranges", *IEEE Journal of Lightwave Technology*, Vol. 25, pp.58-66, 2007.
3. R. Jiang, R. Saperstein, N. Alic, M. Nezhad, C. J. McKinstrie, J. Ford, Y. Fainman and S. Radic, "Parametric Wavelength Conversion from Conventional Near-Infrared to Visible Band", *IEEE Photonic Technology Letters*, Vol. 18, pp.2445-2447, 2006.
4. J.M.C Boggio, R. Jiang, B. Stossel and S. Radic, "730-nm Optical Parametric Conversion from Near- to Short-Wave Infrared Band", submitted to *Optics Letters*

5. Q. Lin, R. Jiang, C. F. Marki, C. J. McKinstrie, R. Jopson, G. P. Agrawal, S. Radic, “40-gb/s optical switching and wavelength multicasting in a two-pump parametric device”, *IEEE Photononic Technology Letters*, Vol. 17, pp.2376-2378, 2005
6. T. K. Chan, J. Karp, R. Jiang, N. Alic, S. Radic, C. F. Marki and J. E. Ford, “1092 channel 2-D array demultiplexer for ultralarge data bandwidth”, *IEEE Journal of Lightwave Technology*, Vol. 25, pp.719-726, 2007.
7. C. J. McKinstrie, R. O. Moore, S. Radic and R. Jiang, “Phase-sensitive amplification of chirped optical pulses in fibers”, *Optics Express*, Vol. 15, pp.3737-3759, 2007
8. N. Alic, R.M Jopson, J. Ren, E. Myslivets; R. Jiang, A.H Gnauck, and S. Radic, “Impairments in deeply-saturated optical parametric amplifiers for amplitude- and phase-modulated signals”, *Optics Express*, Vol. 15, pp.8997-9008, 2007

Conference publications:

1. R. Jiang, N. Alic, C.B Sophie, S. Moro, and S. Radic. “Continuous-Wave Parametric Generation at Visible band in Photonic Crystal Fibers.” *20th Annual meeting of the IEEE Lasers and Electro-optics Society (2007), paper WQ5, Orlando.*
2. R. Jiang, N. Alic, R. Saperstein, E. Myslivets, C. J. McKinstrie+ and S. Radic, “Parametric Translation of a Phase-Coded Signal Over a Record Spectral Range”, *Optical Fiber Communication Conference (2007), postdeadline paper PDP37, Anaheim, Anaheim.*
3. R. Jiang, N. Alic, C.J. McKinstrie and S. Radic, “Two_Pump Parametric Amplifier with 40dB of Equalized Continuous Gain Over 50nm”, *Optical Fiber Communication Conference (2007), paper OWB2, Anaheim.*

4. R. Jiang, Nikola Alic, Joseph E. Ford, Colin J. McKinstrie, Stojan Radic, “Gbps-Rate Channel Translation from Near-Infrared to Visible Band”, *Optical Fiber Communication Conference (2007)*, paper OWQ4, Anaheim.
5. R. Jiang, R. Saperstein, N. Alic, M. Nezhad, C. McKinstrie, J. Ford, Y. Fainman and S. Radic, “375 THz Parametric Translation of Modulated Signal from 1550nm to Visible Band”, *Optical Fiber Communication Conference (2006)*, *postdeadline paper PDP16*, Anaheim
6. R. Jiang, N. Alic, C.J. McKinstrie and S. Radic, “Four-sideband Analysis of Dispersion Fluctuations in Two Pump Fiber Parametric Devices”, *Conference for Laser and Electro-optics Society (2006)*, paper CMW1, Long Beach
7. T.K. Chan, R. Jiang, N. Alic, S. Radic and J.E. Ford, “Data transmission through a 1014-channel two-dimensional array wavelength demultiplexer”, *Optical Fiber Communication Conference (2006)*, paper OTuF4, Anaheim.
8. N. Alic, G.C. Papen, R.E. Saperstein, R. Jiang, C. Marki, Y. Fainman, S. Radic, P.A. Andrekson, “Experimental demonstration of 10 Gb/s NRZ extended dispersion-limited reach over 600 km-SMF link without optical dispersion compensation”, *Optical Fiber Communication Conference (2006)*, paper OWB7, Anaheim.
9. N. Alic, E. Myslivets, J. Coles, P. Firth, C. Clarke, R. Saperstein, R. Jiang, J. Windmiller and S. Radic, “Equalized 42.8 Gb/s Transmission Based on a 10Gb/s EML Transmitter”, *European Conference on Optical Communications (2007)*, Berlin, Germany

FIELDS OF STUDY

Major Field: Electrical Engineering

Studies in nonlinear optics, optical communication and fiber optics

Professor Stojan Radic

ABSTRACT OF THE DISSERTATION

Parametric Band Translation using Highly-Nonlinear and Photonic Crystal

Fibers

by

Rui Jiang

Doctor of Philosophy in Electrical Engineering

University of California, San Diego, 2008

Professor Stojan Radic, Chair

The motivation of this thesis originated from the challenge of building high-speed underwater optical communication links. Since current optical communication technologies cannot be directly applied to the sea water transmission window (480-560nm) due to the significant loss, a solution was pursued by building an optical mixer that can translate the modulation from conventional optical communication window (1550nm) to the visible spectral window, using parametric conversion based on photonic crystal fiber (PCF) platform. The thesis therefore mainly focuses on the investigation of the near-infrared band to visible band parametric translation process, both experimentally and theoretically. We, for the first time, to the best of our knowledge, successfully demonstrated Gb/s both amplitude and phase modulation translation across the record 400THz optical spectrum with error-free performance. At the same time, we achieved the record conversion efficiency for such distant band translation in the PCF. We also, for the first time, identified and characterized the impairment mechanisms of the parametric conversion process in the PCF. The mathematical methods and fiber design process are

developed for PCF calculation and PCF fiber design. Proper fiber structure was designed for optimizing parametric phase matching and addressing the impairment mechanisms.

The idea of optical mixer is not confined to the NIR-to-visible translation application and can be extended to other applications such that the complex transmission, processing, amplification and reception technologies are accessible to arbitrary spectral bands as well, by translating the telecom-band signal to arbitrary optical bands, which is particularly useful and has found important applications in the fields of sensing, spectroscopy, atmospheric communication and so on, detailed in the thesis.

The thesis is divided into seven chapters. Chapter 1 serves as the introduction of the thesis, discussing in detail the motivation and the background knowledge including the current relevant technologies and the rationality of our technologies. The content and structure of the thesis are also briefed in Chapter 1. In Chapter 2, we study the parametric conversion within the telecom band using step-index highly nonlinear fibers (HNLF). One-pump and two-pump structures are compared and the differences between the two structures are quantified. In Chapter 3, we discuss the PCF, focusing on its guiding property and dispersion engineering feature. We also develop mathematical tools for PCF transverse structure calculation in this chapter. In Chapter 4, we characterize the parametric translation process from the telecom band to the visible band in PCF. For the first time, to the best of our knowledge, we have demonstrated Gb/s amplitude and phase translation from the telecom band to the visible band with error-free performance. The impairment mechanisms are identified, quantified and simulated. In Chapter 5, we perform the PCF structure design that aims for optimized phase matching condition and at the same time, address or mitigate the impairment mechanisms discussed in chapter 4.

In Chapter 6, parametric translation from the telecom band to the middle-wavelength infrared band was studied, using Chalcogenide glass fibers. We summarize the work in Chapter 7 and discuss the potential future directions.

Chapter 1 Introduction

1.1 Underwater Communication Challenge

The motivation for this thesis originated from the challenge of building high-speed underwater communication and sensing links. Traditional underwater communication uses ultrasound technology, which inherently limits the communication speeds to several kb/s^{1, 2}. On the other hand, optical technology could potentially provides communication bandwidth which are six orders of magnitude larger than ultrasound^{3, 4}. However, conventional optical communication works at near infrared (NIR) range, which possesses high absorption in the water. Sea water is in particular transparent in the 460-560 nm band^{5, 6}, commonly referred to as the blue-green band. Although there are optical sources operating at this window, their performance characteristics generally fall short of those required for reasonable optical communication which normally requires attributes such as high wavelength stability, high side-mode suppression ratio, narrow linewidth and spectral tunability⁷. Moreover, there are no fast modulation and amplification techniques at blue-green window; a fast receiver is not feasible either. It would be very costly and impractical to develop a complete set of new technologies for transmission, modulation, amplification and reception at this blue-green range as the future complement of technologies do not exist. One solution is seen in building an optical band translator to convert power from the conventional telecom band to the visible band at the transmitter side while the translation process is reversed at the receiver end, so that all the complex optical modulation, amplification, processing and

detection are performed at the telecom band to take advantage of the existing and well-developed optical communication technologies⁸. Moreover, since visible light generally has sufficient energy to excite electronic states, which for molecules larger than triatoms are typically weakly fluorescent⁹, the ability of fast encoding and decoding visible light provides new excitation and detection techniques in spectroscopy.

Distant-band communication challenges also exist in the $\sim 2\mu\text{m}$ Short-wavelength Infrared (SWIR) and 3-6 μm Mid-Wavelength Infrared (MWIR) windows, where enormous applications are abundant while suitable technologies have not been developed. For example, SWIR sensing and detection is critical for homeland security applications since 1.9 μm wave corresponds to a prominent TNT spectral feature¹⁰. MWIR can be efficiently transmitted through a set of low-absorption atmospheric windows¹¹. Remote sensing or general spectroscopy in the MWIR window is particularly important, because the vibrational transitions of most molecules of interest occupy this band¹². However, the same problems arise in this case that no suitable optical sources exist within this band; neither the complex optical processing nor sensitive detection technique are available.

These distinct problems point to a single common issue in current optical technology, that is, current optical technologies are very band specific - the optical spectrum is artificially divided into discrete bands such as visible, NIR, SWIR and MWIR band with technologies within different band being very different. This situation brings the fact that it is difficult to move optical bands freely, unlike in electronics where mixer is available to translate nearly arbitrary RF or microwave frequencies. Mixer operation leads to the implementation that complicated signal processing techniques can be developed at low frequencies and subsequently translated to an arbitrary RF band. In

optics, similar solutions have to be replicated in each optical band, which greatly limits the application of optical technologies. In this sense, an optical mixer that aims to convert arbitrary optical bands is highly desirable.

The goal of this thesis is to investigate solutions for the above-mentioned challenges. In particular, the discussion will be extended to the opportunities of building a wide-band operational optical mixer. We will first briefly examine the electronic mixer and then in the following sections, the concept, requirement and methods of the optical mixer will be discussed in detail.

1.2 Frequency Mixer as an enabling technology

1.2.1 Electronic mixer

A radio frequency (RF) mixer plays numerous roles in the electronics industry and has found important applications in very large scale circuit (VLSI) technology and wireless communication and so on^{13, 14}. A mixer converts RF power at one frequency (usually a high frequency carrier) into power at another frequency (usually an intermediate frequency) to make signal processing easier and to provide for more robust transmission of information¹⁵. For example, a receiver may require as much as over one-hundred decibels of gain. It might not be possible to put more than 40dB of gain into the subsequent RF section without risking instability and potential oscillations¹⁶. This situation is particularly severe at high frequency RF bands. Likewise, the gain of the audio section might be limited to 60dB because of parasitic feedback paths¹⁷. The additional gain needed for a sensitive receiver is normally achieved in an intermediate frequency (IF) section of the receiver. Furthermore, in communication systems RF is

used as the carrier; however, signal processing and filtering are generally performed at IF to allow improved selectivity and an easier implementation of low noise and high gain amplification.



Figure 1 Schematic of the application of a mixer in an RF communication system

Taking the wireless communication industry as an example, each service provider was assigned to a specific operational RF spectrum^{18, 19}. If mixers did not exist, each service provider would have to develop a complete list of technologies, including transmission, amplification, modulation and reception for that specific band, which would be very costly and impractical. The mixer makes the general structure illustrated in Figure 1 possible. All the processing techniques can now be developed in the low frequency IF band, while a mixer converts the IF signal to the target, or the assigned spectrum. The reverse process takes place at the receiving end: the RF signal is down-converted to the baseband (IF), processed and received. While there are many criteria and parameters that characterize an RF mixer such as conversion loss, noise figure, dynamic range and so on¹⁶, which are not going to be elaborated in this thesis, there are three basic characteristics that are worth noting. An RF mixer has to, firstly, be accurate, meaning that the IF signal has to be translated to a specific RF band precisely, which is extremely important as the RF spectrum becomes more and more populated. Second, a mixer has to be able to translate information (amplitude or phase) with high fidelity. In other words, a mixer cannot distort the original information significantly. Finally, an RF mixer has to be

efficient. There will be no practical use if a mixer consumes a lot of power to generate workable RF band signals.

1.2.2 Optical mixer – a missing link

The idea of RF mixer is very simple and can be in principle applied in the optical range. An optical mixer would, ideally, work the same way as an RF mixer does: it would serve to convert one optical band to another in an arbitrary manner. Illustrated in Figure 2, a few distinctive optical bands relate to practical applications.

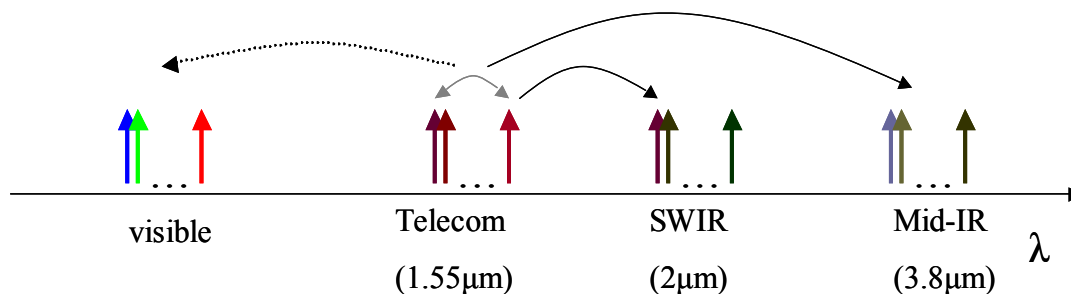


Figure 2 Distinctive optical bands serve different yet important applications.

Unfortunately, as explained earlier, optical technologies are band specific. There are no effective ways connecting various optical band, owing to the enormous bandwidth of the optical spectrum. First of all, present optical sources are not continuous over the optical spectrum. Lasers and transmitters are developed at various bands and are based on different materials, mechanisms and technologies²⁰. For example, depending on the output wavelength lasers are classified into UV-, visible-, NIR-, SWIR- and MWIR- lasers. Depending on the gain medium, we categorize these lasers as gas lasers, solid-state lasers, semiconductor lasers and so on. Lasers are also further differentiated by different pumping schemes, cavity structures or pulsing schemes. The different types of

laser technologies have enriched the laser and optical science and have found important applications in communications, biotechnology, and energy science, to name a few. However, this diversity also has complicated technology integration and thereby rendered enormous difficulties in developing a universal optical system architectures across the optical spectrum. An optical mixer would enable similar optical system to what is shown in Figure 1: in a transmitter operation, an optical mixer would translate an optical IF signal to an arbitrary optical band with high fidelity and high efficiency; it should be able to convert an arbitrary optical band to the IF window for easy processing and receiving in the receiver structure as well. A general optical mixer can be termed a “Universal Band Translator”, a term we adopted in previous works²¹.

A subsequent question is, then, what is the optical intermediate frequency? The comparison with electronics system implies that an optical IF should be the optical band that is suited for optical signal processing, modulation, amplification, reception and so on. Positioned between the visible and SWIR bands, near-infrared light (1550-nm) is capable of nearly-lossless propagation in silica fibers, which forms the backbone of the modern telecommunication infrastructure^{3, 22}, where mature transmission, modulation, amplification and receiving technologies are available. Indeed, no equivalents of erbium doped fiber amplifiers (EDFAs), fast modulators or receivers exist outside the near-infrared window. The overwhelming superiority of near-infrared technology is the result of three decades of communications research, which is unlikely to be replicated in any other spectral range in the near future⁸. Another optical window that could be potentially served as the optical IF is the so-called silicon detection peak²³ at around 800-nm range,

where the single-photon detector is available²⁴. However, the modulation technique at this band is inferior to those in the conventional telecom band.



Figure 3 Optical system architecture that is enabled by optical mixer

Figure 3 summarizes the optical system that could be enabled by the optical mixer: modulation is encoded on a telecom frequency and the optical mixer translates the telecom band (IF) signal to the target optical band, which is then transmitted. Reverse translation back to the 1550-nm band for reception and decoding is conducted at the receiving end in the communication link. Similarly, a general sensing architecture would also translate light from arbitrary optical windows to take advantage of low-noise 1550-nm amplifiers and detectors.

Indeed, a general optical mixer has the potential to bring fundamental changes to many optical technologies. Not only would it provide non-conventional communication functionality, such as submarine communications and transmission through the atmosphere, but it also would enable new spectroscopy tools and innovative sensing structures in a cost-effective manner by leveraging the mature telecom band technologies across the optical spectrum.

1.3 Physics of Mixer Devices

A mixer is generally a nonlinear device, which allows generation of new frequencies. Taking a simple example, Figure 4 shows the typical I-V characteristics of a Schottky diode, which can be described by the following equation²⁵:

$$I = a_1V + a_2V^2 + a_3V^3 + a_4V^4 + \dots \quad (1)$$

Assuming that the diode is excited by two sinusoidal voltages $\cos(\omega_1t)$ and $\cos(\omega_2t)$, then the current flow through the diode is

$$I = a_1(\cos \omega_1t + \cos \omega_2t) + a_2(\cos \omega_1t + \cos \omega_2t)^2 + \dots \quad (2)$$

When expanded, this relation contains the term $a_2 \cos(\omega_1t) \cos(\omega_2t)$ which produces the sum and difference frequencies. When a_2 becomes large, the sum and difference terms become prominent and result in significant mixing output growth.

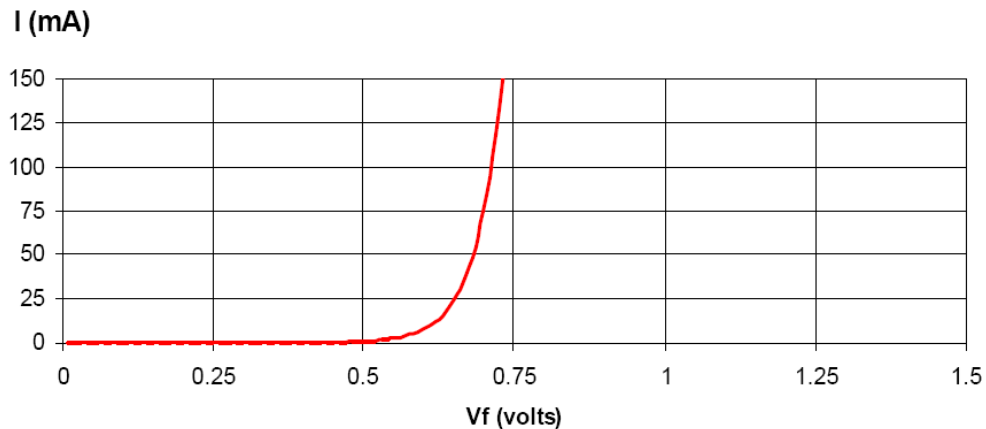


Figure 4 I-V characteristics of a Schottky diode, showing a nonlinear behavior

In the classical atomic model, the nonlinear behavior of a medium originates from the anharmonic motion of bounded electrons under the influence of an applied field. In brief, the total polarization \mathbf{P} induced by the electric dipoles is not linear with the electric field \mathbf{E} , and satisfies the following general relation for the atomic polarizability²⁶:

$$\mathbf{P} = \varepsilon_0(\chi^{(1)} \cdot \mathbf{E} + \chi^{(2)} : \mathbf{E}\mathbf{E} + \chi^{(3)} : \mathbf{E}\mathbf{E}\mathbf{E} + \dots) \quad (3)$$

where ε_0 is the vacuum permittivity and $\chi^{(j)}$ is the j th order susceptibility and, in general, a tensor of rank $j+1$. It is obvious that the first term is the linear dipole response of the medium, and the following terms represent the nonlinear terms of the second order, third order and so on.

Without losing generality, consider the simplest case of second order nonlinear behavior, enabling sum or difference frequency generation. Assuming that the nonlinear medium is homogenous and instantaneous so that $\chi^{(2)}$ becomes a constant and that the two fields incident in the medium are denoted as \mathbf{E}_1 and \mathbf{E}_2 and may be represented as the following

$$\begin{aligned} \mathbf{E}_1 &= \text{Re}\{\tilde{E}_1(r, t) \exp(-i\omega_1 t)\} \\ \mathbf{E}_2 &= \text{Re}\{\tilde{E}_2(r, t) \exp(-i\omega_2 t)\} \end{aligned} \quad (4)$$

where $\text{Re}\{\}$ represents the real part of the complex field. According to equation (3), the nonlinear polarization corresponding to the second order nonlinearity should be

$$\mathbf{P}_{NL}^{(2)} = \varepsilon_0 \chi^{(2)} (\mathbf{E}_1 + \mathbf{E}_2)^2 \quad (5)$$

Expanding equation (5) yields the following expression:

$$\begin{aligned} \mathbf{P}_{NL}^{(2)} &= \frac{1}{4} \varepsilon_0 \chi^{(2)} \{2(|\tilde{E}_1|^2 + |\tilde{E}_2|^2) + \text{Re}(\tilde{E}_1^2 \exp(-i2\omega_1 t) + \tilde{E}_2^2 \exp(-i2\omega_2 t)) \\ &+ 2 \text{Re}(\tilde{E}_1 \tilde{E}_2 \exp[-i(\omega_1 + \omega_2)t]) + 2 \text{Re}(\tilde{E}_1 \tilde{E}_2^* \exp[-i(\omega_1 - \omega_2)t])\} \end{aligned} \quad (6)$$

The physical meaning of each term in equation (6) is clear: the first two terms are the self-phase modulation contributions; the next two terms represent the second-harmonic frequency generation; the 5th and 6th terms correspond to the sum and difference frequency generation, respectively. Equation (6) indicates that several new

frequencies could be potentially generated. However, not all of the aforementioned processes can be enhanced and efficiently produced. The efficiency of a new frequency generation depends on the so-called phase matching condition. To understand this, assuming \tilde{E}_1 and \tilde{E}_2 have the following forms:

$$\begin{aligned}\tilde{E}_1 &= E_1(r, t) \exp(ik_1 z) \\ \tilde{E}_2 &= E_2(r, t) \exp(ik_2 z)\end{aligned}\tag{7}$$

where $E_1(r, t)$ and $E_2(r, t)$ are the envelopes of the fields and varying slowly with both time and space. Taking the difference frequency term as the example, amplitude of the difference frequency is determined by the following term:

$$\tilde{E}_1 \tilde{E}_2^* = E_1 E_2^* \exp i(k_1 - k_2)z\tag{8}$$

As the optical waves propagate in the nonlinear medium, they develop a phase difference due to their different phase velocities. The difference frequency generation will be most efficient when the phase difference disappears (phase matching). The detailed analysis of phase matching will be given later; however, a straightforward physical picture may be obtained as following: when k_1 and k_2 differ significantly, a fast oscillation of the phase difference between the two waves will be developed during the propagation. Considering E_1 and E_2 are slowly varying functions of space, the product $E_1 E_2^*$ will be averaged out during propagation; on the other hand, when the difference between k_1 and k_2 is small, meaning the two waves are more or less in-phase during propagation, the contribution from $E_1 E_2^*$ will be accumulated and efficiently enhanced. Generally, phase matching is much more difficult for optical waves than for RF waves since optical waves have much shorter wavelengths, implying much faster phase

evolution. Thus phase matching of optical waves is a substantial work and generally needs specific design of dispersion properties, which will be discussed in this thesis in detail.

It is worth noting that, even though the previous discussion is for difference frequency generation, it applies generally to any nonlinear process, meaning that the efficiency of a nonlinear process depends on the corresponding phase matching condition of the particular process in addition to the strength (intensity) of the applied electric field.

1.4 Optical mixing mechanism

In our work we have investigated a practical optical mixing scheme for various applications in detail. The intention was to start from a relatively simple case, the small-frequency-shift mixing within the telecomm band. Then we have enlarged the frequency separation and investigated the possibility of translating from the telecom band to the visible band, which serves to address the original challenge associated with this work. Translation to the longer wavelength regime has focused on the telecom-to-MWIR translation, studied in chapter 6.

1.4.1 Nonlinear medium comparison

As discussed previously, a nonlinear medium is required for optical mixing. There are two types of common nonlinear medium, crystalline and amorphous optical materials. Nonlinear optics based on crystals has been investigated for over thirty years and the technology is considered mature^{27, 28}. As an example, doubling or tripling of Neodymium-doped host laser sources has been commercially available²⁹ for some time.

The sum frequency technique has been used to produce blue or UV light sources^{30, 31}. The disadvantage of crystal technology is also recognized: although the nonlinear coefficient is large, it is also difficult to fabricate nonlinear crystals to large dimensions³², making the interaction length in a nonlinear crystal small. The effort of enhancing the nonlinear response typically leads to either a pulsed operation in order to increase the peak intensity of the optical pump, or a cavity structure to increase the interaction length, as shown in Figure 5. Although these techniques are effective to enhance the nonlinear response, they also restrict the device bandwidth.³³

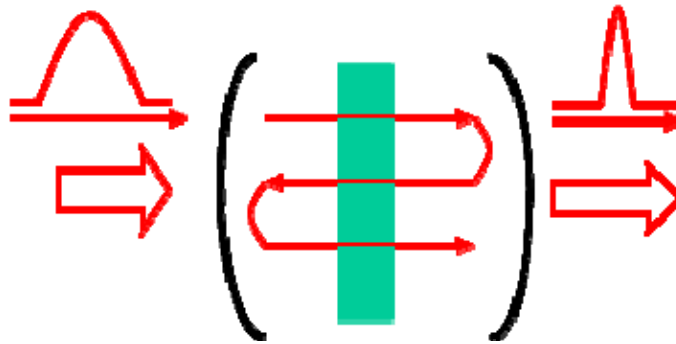


Figure 5 A cavity structure is generally used in crystal based nonlinear optics.

The optical fiber, as a prime example of an amorphous material device, addresses the above issues by a long interaction length. Fiber can be fabricated with small core size, resulting in a highly confined optical field, and be pulled fairly long to hundreds of meters or even kilometers of effective length³⁴. Therefore, even for a fiber fabricated with materials pertinent to a relatively small nonlinear coefficient (i.e., silica fiber), the long interaction length still results in significant nonlinear response^{35, 36}. As an example, the four wave mixing process (FWM) is one of the major impairment mechanisms in the long haul communication links^{37, 38}. Some specialty fibers possess fairly large nonlinear

refractive index (i.e., chalcogenide fibers), enhancing their nonlinear response further. Most importantly, nonlinear fiber enables one-pass structure that is truly transparent to the incoming IF signal. The response time of this structure is only limited by the response time of the nonlinear process, which is generally ultrafast (femtosecond level). All these attributes make nonlinear fiber a desirable platform for optical mixer construction, not only enabling high-speed transmission, but also extending its usage to fast optical processing and manipulation such as switching and routing³⁹.

1.4.2 Parametric process in fiber

Optical fibers do not normally exhibit second-order nonlinear effect due to the fact that $\chi^{(2)}$ vanishes in a material with a centro-symmetric molecular structure. The lowest order nonlinear effects in optical fibers originate from the third order susceptibility $\chi^{(3)}$, which is responsible for third harmonic generation, four-wave mixing (or parametric process) and nonlinear refraction. Among these nonlinear phenomena, the parametric process is of particular interests due to its ability to coherently map spectral bands. A typical parametric process in fiber is illustrated in Figure 6, in which two pump photons

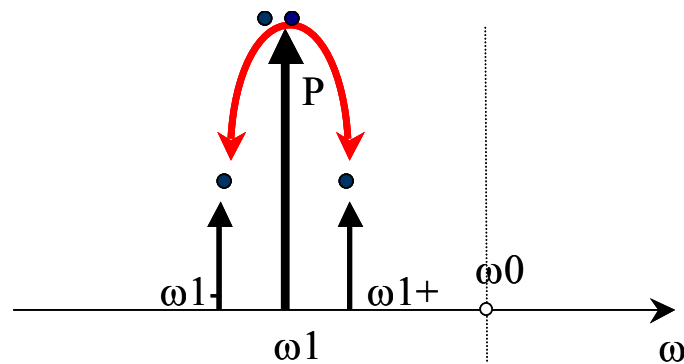


Figure 6 Illustration of parametric process in fiber.

at frequency ω_1 are absorbed and two sideband photons at ω_{1-} and ω_{1+} are subsequently generated^{40, 41}. Parametric exchange is a resonant process with both energy and momentum conserved. One can also understand the process from the classical electrodynamics point of view: the pump and signal wave continuously beat with each other as they co-propagate down the fiber. The beating tone then modulates the fiber refractive index at frequency $\omega_{1-}-\omega_1$ and this changing refractive index further modulates the phase of the pump wave and generates a new frequency component at $\omega_{1+}=\omega_1-(\omega_{1-}-\omega_1)=2\omega_1-\omega_{1-}$. The new frequency component will be enhanced if the phase of the interacting waves maintain their relationship.

To summarize, an efficient parametric process has to satisfy the following criteria:

$$\begin{aligned} 2\omega_1 &= \omega_{1-} + \omega_{1+} \\ 2k_1 &= k_{1-} + k_{1+} \end{aligned} \quad (9)$$

The first equation in (9) states the energy conservation and the second equation represents the phase matching condition (or momentum conservation). If an optical signal is seeded as a sideband ω_{1-} , not only that signal will be amplified, but the difference frequency ω_{1+} will be generated at the same time. The $\chi^{(3)}$ parametric process offers sub-picosecond response times, strict phase and quantum-state preservation over a wide spectral range, and high efficiency (high gain) provided that the phase matching condition is satisfied^{26, 42}. Therefore, the $\chi^{(3)}$ parametric process in fiber represents not only a good mechanism for optical mixer operation, but also embodies an effective optical amplifier and signal processor⁴³. Detailed analysis will be covered in the following chapters.

A practical parametric device may have some variations and therefore include more functions, which certainly complicate the construction, but at the same time provide advantages such as enhanced optical signal processing capability⁴³, equalized gain bandwidth⁴⁴ and so on, and therefore has drawn significant attention during the past ten years^{45, 46, 47}. An important variation is the two-pump parametric architecture shown in Figure 7. The two pump parametric interaction involves three major parametric processes, namely, modulation instability (MI), phase conjugation (PC) and bragg scattering (BS), which are tightly coupled and generate four sidebands that possess certain phase relations with each other⁴⁸.

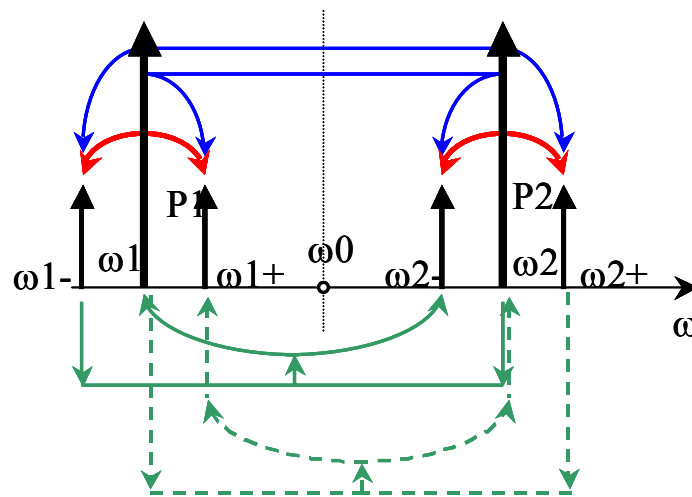


Figure 7 Two pump parametric interactions, in which three processes, namely, modulation instability, phase conjugation and bragg scattering, are coupled with each other and generate four sidebands with certain phase relations.

The MI process is the same degenerate process as that in the one-pump structure - each pump degenerates into two sideband photons as illustrated with the red arrow in Figure 7. As to the PC process, shown in Figure 7 with the blue arrow, each pump contributes one photon, and generates two sideband photons ($\omega_1 + \omega_2 \rightarrow \omega_{1-} + \omega_{2+}$ or

$\omega_1+\omega_2\rightarrow\omega_{1+}+\omega_{2-}$), that form a phase-conjugated pair; in the BS process, a pump photon combines with a sideband photon and generates the other pump photon and another sideband photon, shown with green arrow in Figure 7 ($\omega_1+\omega_{2-}\rightarrow\omega_{1-}+\omega_2$ or $\omega_{1+}+\omega_2\rightarrow\omega_1+\omega_{2+}$). In the BS process, the two interacting sideband photons are non-conjugated replicas of each other. The two-pump structure has considerably higher operational complexity than the one-pump structure. For example, the phase of the two pumps have to be aligned either in phase or out of phase to avoid excessive noise transfer to signal^{49, 50, 51}; polarization of the two pumps have also to be aligned for gain maximization⁴³ (or the two pumps are orthogonally polarized for polarization insensitive amplification^{52, 53}). However, the two-pump structure also provides operational flexibility – each pump can be individually controlled and manipulated and the pump separation can be finely tuned. Furthermore, the multi-band casting and multi-channel amplification and processing capabilities are important for many applications^{54, 55}. Detailed analysis and applications of the two-pump structure will be discussed in Chapter 2.

1.4.3 High-confinement fibers (HCF)

As discussed earlier, fibers could be used as an excellent nonlinear platform due to the highly-confined field and the long interaction length. In comparison to the regular single mode fiber (SMF), a high-confinement fiber has enhanced effective nonlinear coefficient that results from scaling down the core size. A high-confinement fiber normally needs special design of the transverse structure in order to simultaneously achieve single mode guiding and enhanced field-confinement. In this thesis, we divide

HCF into two types, namely, the highly nonlinear fiber (HNLF) and the photonic crystal fiber (PCF). HNLF generally has relatively simple step-index transverse structure. Two typical HNLF structures^{34, 56} are shown in Figure 8 Two typical HNLF transverse structures with 1) raised inner cladding and 2) depressed inner cladding.. In each case, a small cladding area near the core is doped such that its refractive index is different from both the core and the other cladding material: a raised inner cladding has a refractive index higher than its surroundings while a depressed inner cladding has a refractive index that is lower than its surroundings. The idea for a raised inner cladding design is to provide a barrier layer to prevent the field from extending further while a depressed layer design enhances the index contrast between the core and its immediate cladding surroundings.

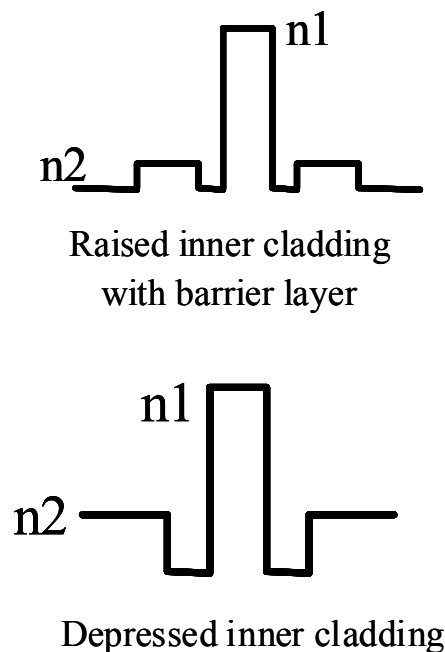


Figure 8 Two typical HNLF transverse structures with 1) raised inner cladding and 2) depressed inner cladding.

Photonic crystal fiber, on the other hand, has a nano-structured cross section⁵⁷. Although the pattern of the nano-structure could be designed arbitrarily^{58, 59}, we are particularly interested in the pattern that consists of a hexagonal silica core surrounded by a cladding with a honeycomb arrangement of circular air holes, as shown

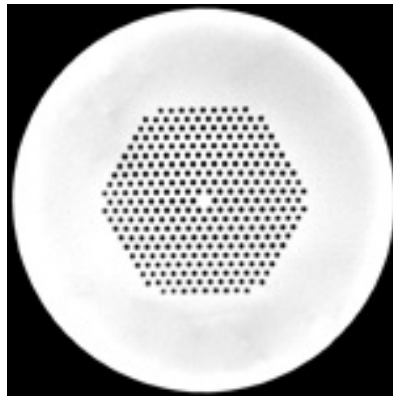


Figure 9 Transverse structure of a PCF consisting of a hexagonal silica core surrounded by a cladding with a honeycomb arrangement of circular air holes

in Figure 9. This structure is very useful in the parametric translation applications because it provides considerable freedom in the dispersion-engineering of the waveguide and therefore enables the phase matching capability. The dispersion property of this type of fiber is determined by the air-hole size and the period (or pitch) of the triangular pattern, the details of which will be covered in Chapter 3.

The reason we have to consider both HNLF and PCF fibers is due to their different dispersion properties. Although the parametric process could potentially provide large operational bandwidth, no single fiber can cover the whole optical spectrum: for different applications, various fiber platforms have to be chosen. In general, HNLF is highly efficient for parametric translation with a relatively small frequency shift (<20THz) while the PCF is suitable for distant band translation, such as NIR-to-visible or

NIR-to-MWIR translation. This is intuitively understood by observing the dispersion profiles of the silica HNLf and PCF shown in Figure 10. The dispersion profile of an HNLf, due to its relatively simple transverse structure, is linear-like in the vicinity of the zero-dispersion wavelength

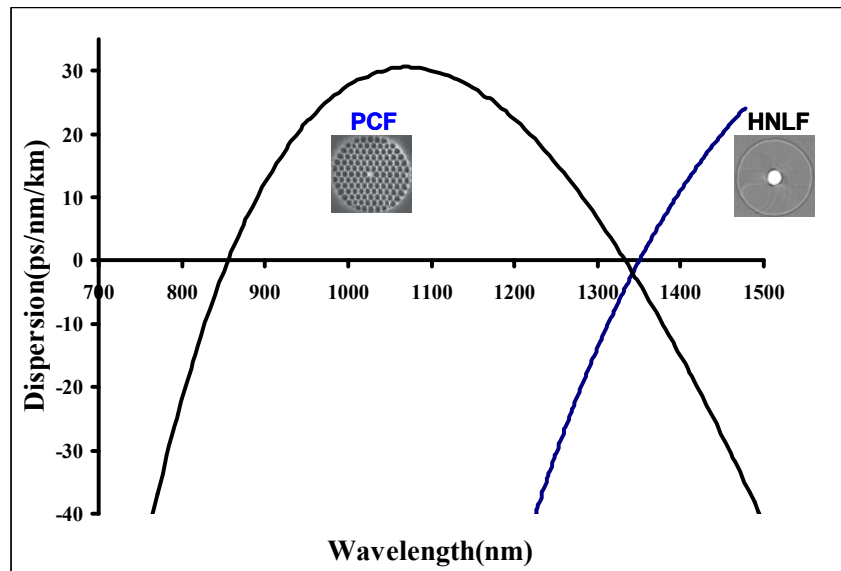


Figure 10 Comparison of the dispersion profile of silica HNLf and PCF

(ZDWL). Engineering the fiber transverse structure will vary the dispersion slope, and not be able to generate arbitrary high-order terms because of the weak waveguide dispersion in step-index fibers. The dispersion increases drastically as the wavelength moves away from the ZDWL, making distant-band phase matching difficult in HNLf. Phase matching however becomes considerably easier in the vicinity of ZDWL, where most HNLf based parametric devices operate^{60, 61}. On the other hand, PCF provides strong waveguide dispersion across a broad wavelength range and therefore is able to alter the total dispersion profile extensively. PCF described above normally has a

parabolic dispersion profile (see Figure 10) with two ZDWL, which makes phase matching of distant wavelengths possible.

Besides the fiber structure, different fiber materials are also of interest. The most widely used fiber material is, silica; however, silica fiber becomes very lossy when the wavelength approaches the SWIR band and beyond. Silica also has relatively small nonlinear index (n_2). Therefore, other materials such as Bismuth Oxide and Chalcogenide fibers have also been explored extensively^{62, 63, 64, 65}.

Table 1⁶⁷

Material	Nonlinear index*
Chalcogenide glass	~100 to 500
Bismuth Oxide	~55
Silicon	~170 ⁶⁶
Silica	1

* Relative to silica ($n_2=2.6 \times 10^{-20} \text{ m}^2/\text{W}$)

Table 1⁶⁷ shows the nonlinear property for several common nonlinear materials, among which chalcogenide glasses exhibit the highest nonlinear refractive indices. Indeed, chalcogenide glass PCF fiber was compared with silica in this work due to low

loss in the MWIR range and large nonlinear coefficient, which will be covered in Chapter 6.

1.5 Summary

To summarize, the goal of this work is to investigate optical mixing through the parametric process in high-confinement fibers. The mixing process must preserve the amplitude and phase information of the incoming signal. The 1.55 μm telecom band is chosen to serve as the optical IF signal at which signal processing including amplification, filtering, modulation and reception are performed. The optical IF signal is then translated to the target optical band, for example, other telecom frequency, visible, SWIR or MWIR bands through a $\chi^{(3)}$ parametric process. Both HNLF and PCF were studied for different applications. Besides the experimental demonstration of optical band translation, we have also performed the fiber transverse structure design for specific parametric translators. The thesis is organized as the following: Chapter 2 is dedicated to the theory and experimental work on parametric process in HNLF. In Chapter 3 computer modeling is detailed and includes effective index model, Fourier decomposition and beam propagation method in order to design the target PCF structure. Chapter 4 describes the experimental effort for NIR-to-visible translation using silica PCF. High-speed and high-fidelity translation is firstly demonstrated and the impairment mechanisms are measured and analyzed. In Chapter 5 we focus on the PCF structure design to address the impairment mechanisms based on the mathematical models established in Chapter 3. In Chapter 6 chalcogenide PCF design was explored for the purpose of NIR-to-MWIR

translation and compared to NIR-to-visible performance. We summarize our work and discuss future research opportunities in Chapter 7.

Chapter 2 Parametric Process in Highly

Nonlinear Fibers

2.1 Introduction

In this chapter, we describe both one-pump and two-pump parametric processes in HNLF. Indeed, research on one-pump parametric process in HNLF has been carried out for almost twenty years and has been demonstrated of high gain ($>70\text{dB}$)⁶⁸, wideband amplification⁶⁹ and wavelength conversion⁷⁰. The two-pump architecture has drawn increased attention in the last few years due to their enhanced ability and multi-band feature^{55, 71, 72}, resulting in great potential applications in the high-speed, bandwidth-demanding networks⁴³. Modeling of one-pump parametric process is firstly studied in order to understand the phase matching condition and the typical gain spectrum of the one-pump structure. The function of high-order dispersions in various conditions is discussed thereafter. In the subsequent section, the two-pump parametric process is investigated. A four-sideband model developed in previous work is conferred and, similarly, phase matching condition and gain spectrum are studied based on the established four-sideband model, including various high-order dispersion situations. The gain spectra between one-pump and two-pump structure are compared. Although the examples shown in the discussions refer to the HNLF, the modeling and discussion on both one-pump and two-pump parametric process are general and do not depend on the specific platform. As we show in Chapter 4, the same method can be applied to model the parametric process in PCF. The next three sections dedicated to three experimental and

theoretical works we have developed using silica HNLF, including the construction of record gain-bandwidth product parametric amplifier, implementation of the 40Gb/s optical switching and multicasting and modeling the impact of dispersion fluctuation using two-pump parametric systems.

2.2 One-pump parametric process

2.2.1 Phase matching condition

One-pump parametric scheme has been shown in Figure 6. A set of coupled-mode equations describing one-pump parametric process could be derived from the nonlinear Shrodinger equation²⁶. Although mathematically equivalent, two sets of equations were generally used in the past work. The first set of equations are given as follows^{26, 73}

$$\begin{aligned}
 \frac{\partial A_p(z)}{\partial z} &= i\gamma[|A_p|^2 A_p + 2(|A_s|^2 + |A_i|^2)A_p + 2A_i A_s A_p^* \exp(i\Delta\beta z)] - \frac{\alpha_p}{2} A_p \\
 \frac{\partial A_s(z)}{\partial z} &= i\gamma[|A_s|^2 A_s + 2(|A_p|^2 + |A_i|^2)A_s + A_p^2 A_i^* \exp(-i\Delta\beta z)] - \frac{\alpha_s}{2} A_s \\
 \frac{\partial A_i(z)}{\partial z} &= i\gamma[|A_i|^2 A_i + 2(|A_p|^2 + |A_s|^2)A_i + A_p^2 A_s^* \exp(-i\Delta\beta z)] - \frac{\alpha_i}{2} A_i
 \end{aligned} \tag{10}$$

in which γ and α are the nonlinear and loss coefficients, respectively.

$A_j (j = p, s, i)$ represents the complex field amplitudes of the pump, signal and idler. $\Delta\beta$ is the propagation constant²⁶ difference and has the form of

$$\Delta\beta = \beta_s + \beta_i - 2\beta_p \tag{11}$$

The equation (10) is obtained by directly expanding the $\chi^{(3)}$ term in the nonlinear polarization expression. The physical meaning of equation (10) is clear: in each equation, the first term represents the effect of self-phase modulation; the second and third terms are the cross-phase modulation contributions; the fourth term is the four-wave mixing term and the last term accounts for the loss. Other $\chi^{(3)}$ processes such as triple-frequency generation and sum frequency generation are generally not phase matched and therefore are neglected. The advantage of equation (10) is that it clearly states the physics involved in the parametric process and is easy for simulation. However, phase evolution of the parametric process is not explicitly illustrated in equation (10), which is sometimes important in order to understand the dynamics of the parametric process (i.e, predicting the energy flow direction). To address this, another equation set were developed as follows⁷⁴:

$$\begin{aligned}
\frac{dA_p}{dz} &= -2\gamma A_i A_s A_p \sin[\phi(z)] \\
\frac{dA_s}{dz} &= \gamma A_i A_p^2 \sin[\phi(z)] \\
\frac{dA_i}{dz} &= \gamma A_s A_p^2 \sin[\phi(z)] \\
\frac{d\phi}{dz} &= \Delta\beta + \gamma(2A_p^2 - A_s^2 - A_i^2) + \gamma \left[A_p^2 \left(\frac{A_s}{A_i} + \frac{A_i}{A_s} \right) - 4A_i A_s \right] \cos[\phi(z)]
\end{aligned} \tag{12}$$

Note that in equation (12) the complex field $E_j = A_j e^{i\phi_j}$ ($j = p, s, i$) and A_j and ϕ_j ($j = p, s, i$) represents the field amplitude and phase of pump, signal and idler, respectively. The last equation in (12) describes the parametric phase evolution, where

$$\phi(z) = \Delta\beta \cdot z + \phi_s + \phi_i - 2\phi_p \tag{13}$$

Equation (12) shows that the parametric phase shift has complex form. It, however, could be simplified by assuming a non-depleted pump during the process,

which is generally justified since a strong pump is typically used in a parametric system.

In this case, the phase equation becomes

$$\frac{d\phi}{dz} = \Delta\beta + 2\gamma P + 2\gamma P \cos[\phi(z)] \quad (14)$$

where P is the pump power. At the same time, the field amplitude coupled-mode equation reveals that the parametric gain for signal and idler could be written as:

$$G(z) = 2\gamma P \int_0^z \sin[\phi(\xi)] d\xi \quad (15)$$

where $G(z)$ is the decibel gain accumulated in length z . Equation (15) clearly reveals the power-flow direction of the parametric process: for ϕ in $2n\pi$ and $(2n+1)\pi$, power flows from pump to signal and idler; otherwise, power is given to the pump. Secondly, maximum gain is achieved when $\sin[\phi(z)]$ is maximized, that is when $\phi(z) = \pi/2$. This could be achieved by choosing $\phi(0) = \pi/2$ and making

$$\Delta\beta + 2\gamma P = 0 \quad (16)$$

Equation (16) is the well-known phase matching condition at which the parametric gain is maximized. Taylor expanding equation (16) gives the form of phase matching condition as the following:

$$\sum_{n=1}^{\infty} \frac{2}{(2n)!} \beta^{(2n)}(\omega_p) (\Delta\omega)^{2n} + 2\gamma P = 0 \quad (17)$$

where $\beta^{(2n)}$ stands for the $2n^{\text{th}}$ order dispersion of the fiber, defined as

$$\beta^{(2n)} = \frac{\partial^{(2n)} \beta}{\partial \omega^{(2n)}} \quad \text{and } \Delta\omega \text{ is the frequency shift equaling } \omega_s - \omega_p. \text{ Generally speaking, (17)}$$

implies that all even order dispersion terms contribute to the linear (dispersive) phase

shift. It is, however, impractical to include the contribution from all the high order dispersion terms in the calculation. Simplification of equation (17) is conducted by comparing the contribution of adjacent dispersion terms, for which purpose an α factor is defined as follows:

$$\alpha_{2n} = \frac{\beta^{2(n+1)}}{\beta^{2n}} \frac{\Delta\omega^2}{2(n+1)} \quad (18)$$

All terms pertinent to a small α factor ($\alpha \ll 1$) could be potentially neglected. As one can see from (18), the highest order dispersion term that needs to be accounted for is determined by the curvature of the dispersion profile and the frequency shift of the parametric process $\Delta\omega$. As an example, in a regular dispersion flattened HNLFF, $\beta^{(2)} \sim 1 \text{ ps}^2 / \text{km}$, and $\beta^{(4)} \sim 10^{-5} \text{ ps}^4 / \text{km}$ in the vicinity of ZDWL; as long as $\Delta\omega < 100 \text{ (THz} \cdot \text{rad)}$, $\alpha_2 \ll 1$, implying that the 4th order dispersion term is much smaller than the 2nd order dispersion and therefore only the latter needs to be considered in this case. Using the approximation that $\Delta\lambda(\text{nm}) \approx 1.27\Delta\omega \text{ (THz} \cdot \text{rad)}$, the above calculation indicates that, normally, in a regular HNLFF, as long as the wavelength shift is less than 120nm, only the second order dispersion term is important. In other words, 4th order dispersion or higher needs to be included if operating at wavelength shift larger than 120nm. On the other hand, for an specialized HNLFF with $\beta^{(4)}$ as high as $10^{-4} \text{ ps}^4 / \text{km}$, α factor calculation suggests the 4th order term becoming important when the wavelength shift is larger than 32nm.

Practically speaking, for HNLFF operating near ZDWL, high order dispersion terms ($n > 4$) become negligible⁷⁵. In the following discussions we only keep the second

order dispersion term with fourth order dispersion included only in some special cases, where either the fiber has a large dispersion slope⁷⁶ or the parametric frequency shift is large.

Equation (15) also indicates that, even when one is offset from the phase matching condition, parametric gain could still be obtained as long as the accumulated sine value of the parametric phase shift is positive; in this case, parametric process will gain an initial phase value that maximize the gain. In order to characterize the phase evolution under this condition, we define a unit length parametric phase shift (termed as parametric phase shift in the thereafter text) as

$$\kappa = \Delta\beta + 2\gamma P \quad (19)$$

In which we have made the assumption that the parametric phase $\phi \sim \pi/2$ so that $\cos[\phi(z)] \sim 0$.

It is instructive to take a look at the parametric phase shift κ versus the wavelength shift, shown in Figure 11a, where only second order dispersion is taken into

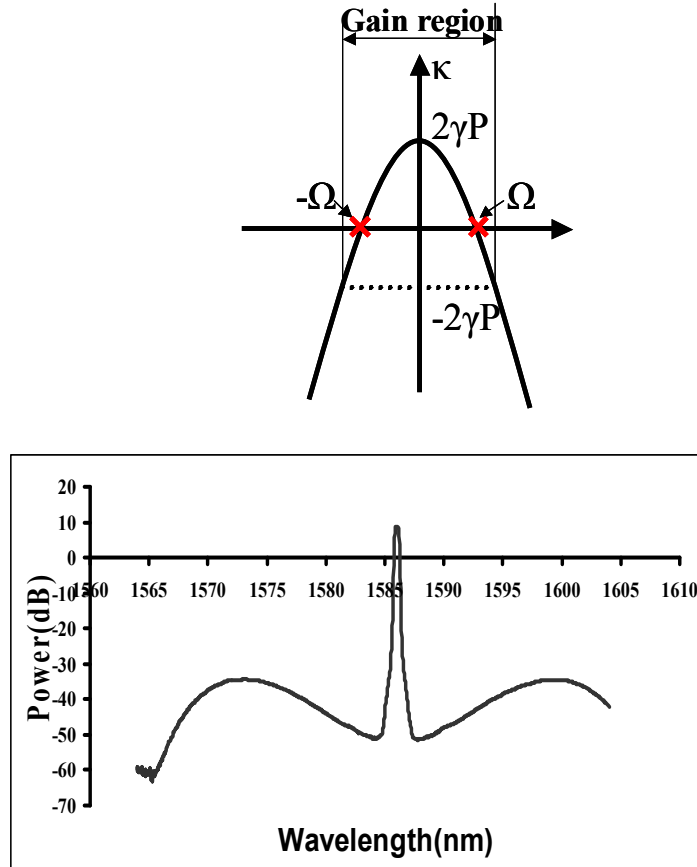


Figure 11 a) wavenumber mismatch parameter and b) experimentally measured power spectrum for one-pump parametric scheme.

account. In order to achieve phase matching, β_2 has to be negative to balance the nonlinear phase shift, meaning the pump has to be placed in the anomalous dispersion regime. In this case, κ is a parabolic curve facing downward with the maximum value at $2\gamma P$. The gain region is the wavelength section where κ falls in between $-2\gamma P$ and $2\gamma P$, with the (perfect) phase matching point at $\pm\Omega = \pm \sqrt{\frac{2\gamma P}{|\beta_2|}}$. Therefore, two gain humps symmetric to the pump position ought to be observed. In Figure 11b, we show a typical experimentally measured ASE spectrum, agreeing with the prediction. The bandwidth of

the gain region is $4\sqrt{\frac{\gamma P}{|\beta_2|}}$, shrinking as the pump moving away from the ZDWL. On the other hand, as the pump moving towards the ZDWL, second order dispersion contribution decreases and nonlinear induced phase shift becomes dominant, potentially resulting in reduced gain. Also, high order dispersion terms turn out to be important as the pump approaches ZDWL. Therefore, there is generally an optimum pump position at which maximum gain-bandwidth product is achieved. This is confirmed by the experimental observation shown in Figure 12: when the pump is placed in the normal dispersion region, there is very little gain; as we move the pump into the anomalous dispersion region, the gain profile begins to develop and reaches maximum as the red curve.

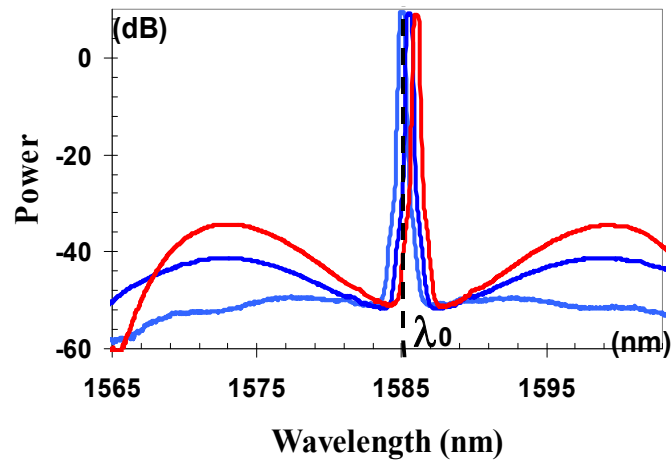


Figure 12 One-pump parametric gain versus the pump wavelength

2.2.2 High-order dispersion contribution

High-order dispersion plays important role for large frequency shift operation and highly curved dispersion profiles. The influence of high order dispersion term is

somewhat complicated. It generally bends the κ curve, potentially rendering additional phase matching regions. For example, parametric phase shift including fourth order dispersion becomes

$$\kappa = \frac{\beta_4}{12}(\Delta\omega)^4 + \beta_2(\Delta\omega)^2 + 2\gamma P \quad (20)$$

The discussion could be generally divided into three situations, briefed as follows:

(1) $\beta_2 < 0$ and $\beta_4 < 0$. The parametric phase shift and gain profile have typical shapes as shown in Figure 13 similar to what we have observed previously. β_4 results in reduced gain bandwidth.

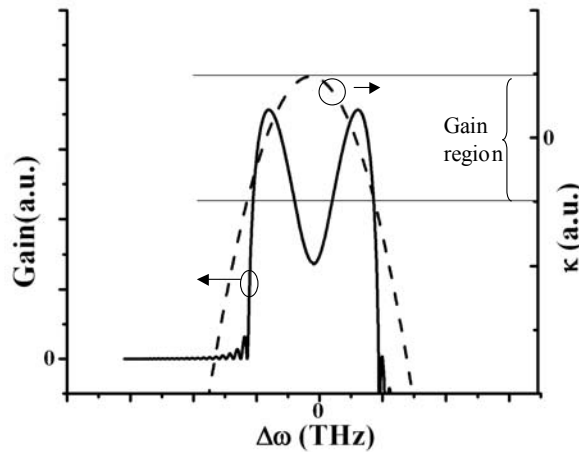


Figure 13 Parametric phase shift and corresponding gain shown in the same plot for $\beta_2 < 0$ and $\beta_4 < 0$. Fourth order dispersion change does not change the profile of parametric phase.

(2) $\beta_2 < 0$ and $\beta_4 > 0$. The parametric phase shift and gain profile have typical shapes as shown in Figure 14. New phase matching regions appear at relatively further band positions with narrow bandwidth due to the prominent 4th order dispersion. This case is of particular interests because it indicates the possibility of phase-matching distant

bands by resorting to high order dispersions, which remains an important strategy to reach distant bands into the visible, SWIR or mid-IR range. The nonlinear phase is usually small in this distant band region and the phase matching points are at

$$\pm\Omega = \pm\sqrt{\frac{12|\beta_2|}{\beta_4}} \quad (21)$$

The bandwidth of the distant gain region could be estimated as the following:

Define $\Delta\omega = \Omega + \delta\omega$, in which $\delta\omega$ stands for the frequency shift from the phase matching point. Therefore,

$$\begin{aligned} \Delta\omega^2 &= (\Omega + \delta\omega)^2 = \Omega^2 + 2\Omega\delta\omega + \delta\omega^2 \approx \Omega^2 + 2\Omega\delta\omega \\ \Delta\omega^4 &= (\Omega^2 + 2\Omega\delta\omega)^2 = \Omega^4 + 4\Omega^3\delta\omega + 4\Omega^2\delta\omega^2 \approx \Omega^4 + 4\Omega^3\delta\omega \end{aligned} \quad (22)$$

Since parametric gain develops when $\kappa \in [-2\gamma P, 2\gamma P]$, using gives

$$\delta\omega \leq \frac{2\gamma P}{|\beta_2| \cdot \Omega} \quad (23)$$

Therefore, the bandwidth of the distant-band gain-hump is

$$BW_{distant-band} = \frac{4\gamma P}{|\beta_2| \cdot \Omega} \quad (24)$$

(24) clearly shows the bandwidth is inverse proportional to the frequency shift of the distant-band phase matching point.

The inner gain hump (close to ZDWL) should have increased bandwidth due to the fact that 4th order dispersion could cancel part of the 2nd dispersion in this region provided 4th order dispersion is important in this region at all.

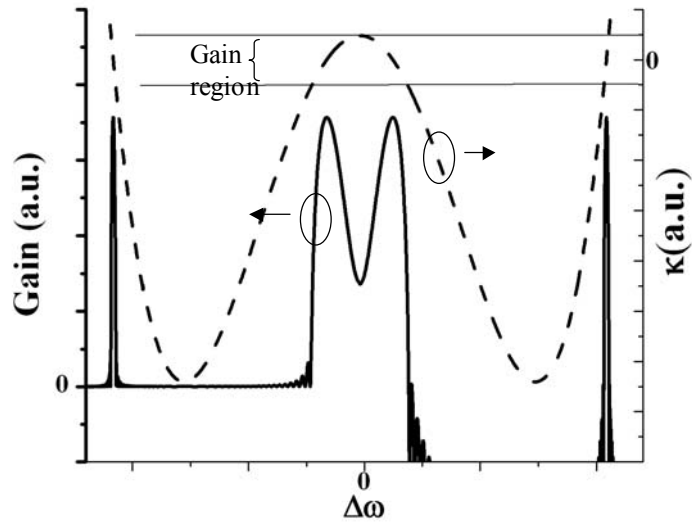


Figure 14 Parametric phase shift and corresponding gain shown in the same plot for $\beta_2 < 0$ and $\beta_4 > 0$. Fourth order dispersion introduces additional phase matching region

(3) $\beta_2 > 0$ and $\beta_4 < 0$. The parametric phase shift and gain profile have typical shapes as shown in Figure 15, indicating two phase-matching regions at further band positions, a similar situation to what has been observed above. However, the gain region close to the ZDWL depends heavily on the detailed information of β_2 and β_4 value

All above cases are useful for understanding the gain behavior and have been experimentally observed in a one-pump parametric structure. It is worth noting that while the above analysis only includes fourth order dispersion, it applies to higher order dispersion as well. In the next chapter, we will find out that the phase matching in PCF is very similar to case 2 described above. The difference is that in a PCF, even higher order dispersion terms need to be considered and phase matching is mainly due to the balance between these high order dispersions.

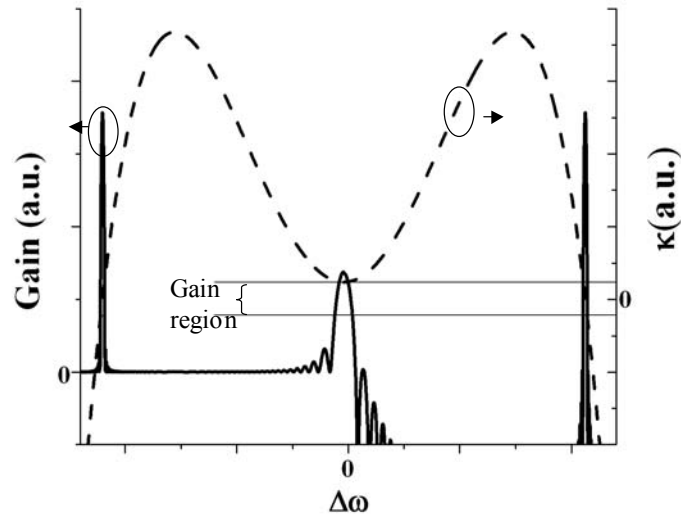


Figure 15. Parametric phase shift and corresponding gain shown in the same plot for $\beta_2 > 0$ and $\beta_4 < 0$. Fourth order dispersion creates phase matching region for normal-positioned pump.

2.2.3 Parametric gain discussion in a one-pump structure

Analytical solutions for the non-depletion case was derived previously^{26, 73}. Here we focus only on the maximum and minimum parametric gain in order to understand the gain characteristics:

$$\begin{aligned} G_{\max} &= 1 + \sinh^2(\gamma Pz) \\ G_{\min} &= 1 + (\gamma Pz)^2 \end{aligned} \quad (25)$$

One-pump parametric scheme provides exponential gain when phase matched, while the gain becomes quadratic at the edge of the gain region, indicating a relatively steep falling in gain profile. As we shall see in the next section, this rapid gain drop-off could be corrected using two-pump scheme, in which both the maximum and minimum gain has the exponential form, rendering more uniform bandwidth.

For depleted pump operation, either equation (10) or (12) has to be solved numerically. Applications of one-pump parametric scheme in HNLF has been studied and covered in numerous past references^{68, 69, 70} and is not going to be further discussed in this thesis.

2.3 Two-pump parametric structure

2.3.1 Four-sideband couple-mode equations

Mathematical description of two-pump parametric structure uses four-sideband analysis developed by C.J. McKinstrie et al.⁴⁸. The coupled-mode equations have the following form:

$$\begin{aligned}
d_z B_{1-}^* &= -i(\delta\beta_{1-} + \gamma P_1)B_{1-}^* - i\gamma P_1 B_{1+} - i2\gamma(P_1 P_2)^{1/2} B_{2-}^* - i2\gamma(P_1 P_2)^{1/2} B_{2+} \\
d_z B_{1+} &= i\gamma P_1 B_{1-}^* + i(\delta\beta_{1+} + \gamma P_1)B_{1+} + i2\gamma(P_1 P_2)^{1/2} B_{2-}^* + i2\gamma(P_1 P_2)^{1/2} B_{2+} \\
d_z B_{2-}^* &= -i2\gamma(P_1 P_2)^{1/2} B_{1-}^* - i2\gamma(P_1 P_2)^{1/2} B_{1+} - i(\delta\beta_{2-} + \gamma P_2)B_{2-}^* - i\gamma P_2 B_{2+} \\
d_z B_{2+} &= i2\gamma(P_1 P_2)^{1/2} B_{1-}^* + i2\gamma(P_1 P_2)^{1/2} B_{1+} + i\gamma P_2 B_{2-}^* + i(\delta\beta_{2+} + \gamma P_2)B_{2+}
\end{aligned} \tag{26}$$

where B_j ($j=1-, 1+, 2-, 2+$) are the complex field amplitudes of the four sidebands. P_1 and P_2 are the two pump powers, assumed to be non-depleted during the process. $\delta\beta_j$ ($j=1-, 1+, 2-, 2+$) represent the propagation constant difference having the following form:

$$\begin{aligned}
\delta\beta_{1\pm} &= \beta_{1\pm} - \beta_1 \\
\delta\beta_{2\pm} &= \beta_{2\pm} - \beta_2
\end{aligned} \tag{27}$$

Equation (26) clearly shows that the four sidebands are strongly coupled to each other and it is impossible to distinguish which sideband photon is generated through which process.

2.3.2 Two-sideband analysis

In this section, we briefly discuss the two-sideband model that has been developed in the past and illustrate that although two-sideband results give physical insights in some aspects, they are generally incomplete to fully account for the parametric interactions in the two-pump parametric structure. The parametric phase shifts for MI, BS and PC processes, respectively, were developed in previous work and have the following form⁴⁸:

$$\begin{aligned}
 \kappa_{MI} &= \sum_{n=1}^{\infty} \frac{2}{(2n)!} \beta^{(2n)}(\omega_j) (\Delta\omega)^{2n} + 2\gamma P_j \quad (j=1,2) \\
 \kappa_{PC} &= \sum_{n=1}^{\infty} \frac{2}{(2n)!} \beta^{(2n)}(\omega_a) [(\Delta\omega)^{2n} - \omega_a^{2n}] + \gamma(P_1 + P_2) \\
 \kappa_{BS} &= \Delta\beta_{BS} + \gamma(P_2 - P_1)
 \end{aligned} \tag{28}$$

where $\omega_a = (\omega_1 + \omega_2)/2$ is the central position of the two pumps while $\omega_s = (\omega_1 - \omega_2)/2$ is the half pump separation. $\Delta\omega$ in the κ_{MI} expression refers to the frequency shift from signal to the pump while $\Delta\omega$ in κ_{PC} is the frequency shift from signal to the pump center ω_a . We do not expand the $\Delta\beta_{BS}$ term because BS process does not provide net gain, as pointed out in the past⁴⁸. BS process could however be interesting when used in noise reduction applications^{77, 78}.

In the two-pump structure, each pump individually develops the MI parametric interaction. However, the MI process is not prominent for the shorter-wavelength pump

since it is typically placed in the normal dispersion regime. The MI process for the longer-wavelength pump is more pronounced since it is normally set at the anomalous dispersion region. The MI behavior has been understood in the previous one-pump structure analysis.

PC process is a non-degenerate process that differentiates the one-pump and two-pump schemes. As observed in equation (28), the two pumps' central position and the pump-separation could be simultaneously adjusted, resulting in more operation flexibility, as shown in Figure 16. For example, the parametric phase could be flattened by decreasing the maximum phase profile (which is not possible in the one-pump structure), resulting in much flatter gain profile in broader bandwidth comparing to the one-pump structure.

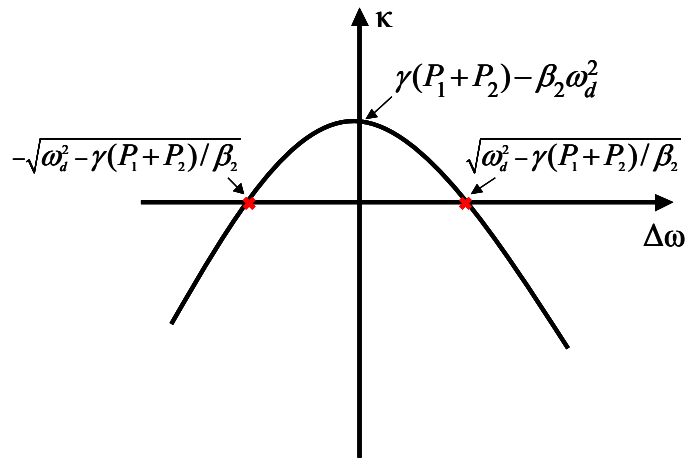


Figure 16 Parametric phase shift of a PC process.

Indeed, the maximum and minimum gain of a PC process has the following form⁴⁸:

$$\begin{aligned}
G_{\max} &= 1 + \sinh^2[\gamma(P_1 + P_2)z] \\
G_{\min} &= 1 + 4 \sinh^2\left[\frac{\sqrt{3}}{2} \gamma(P_1 + P_2)z\right]/3
\end{aligned}
\tag{29}$$

The maximum gain has exponential form in a PC process, similar to that in a MI process. Note that the minimum gain maintains the exponential form in the PC process, indicating a much more slowly gain-drop than in the MI process, an attribute that could be potentially used for gain equalization, as we have investigated in section 2.3.2.

Two-sideband analysis based on PC process was often used in the past to predict the two-pump parametric performance^{79, 80}. It gives good results in the PC dominated region. The problem for two-sideband model is that, first, it fails to predict the behavior of all four-sidebands; second, the gain profile predicted by two-sideband model is not correct in non-PC dominated region, and mostly in the near-pump regions. As an example, assume the following condition: $\gamma=12\text{km}^{-1}\text{W}^{-1}$, fiber length $L=200$ meters, $\beta_3=0.12\text{ps}^3/\text{km}$, $\beta_4=2.5\times 10^{-5}\text{ps}^4/\text{km}$, $P_1=P_2=1\text{W}$, pump position $\omega_1=-20\text{THz}$, $\omega_2=20\text{THz}$. The gain profile predicted by two-sideband PC based model is shown in Figure 17:

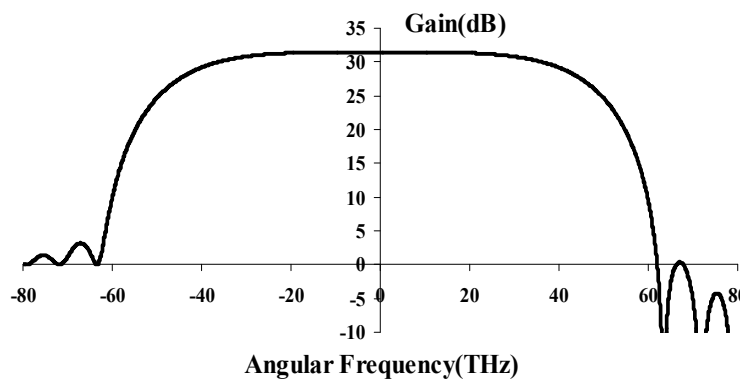


Figure 17 Phase conjugation gain for a two-pump parametric system with the operation condition illustrated in the text.

On the other hand, the complete gain analysis for all four sidebands for the same problem is shown in Figure 18, which shows qualitative difference from the two-sideband results. This example exemplifies the need for a more complete four-sideband model to precisely describe the two-pump parametric process.

2.3.3 Four-sideband analysis

In this section, we study the two-pump parametric gain profile under different pumping conditions based on the four-sideband analysis. The simulations are based on the following parameters that exemplify typical experimental conditions: fiber length $L=200$ meters, $\beta_3=0.12\text{ps}^3/\text{km}$, $P_1=P_2=1\text{W}$. Pump position and β_4 are subject to variation.

- Low β_4 case: $\beta_4=2.5\times 10^{-5}\text{ps}^4/\text{km}$

(1) $\omega_1=-20\text{THz}$, $\omega_2=20\text{THz}$; pumps are centered at ZDWL

As we see from Figure 18, PC process dominates the gain when the signal is far from the pumps ($>5\text{nm}$). As the signal approaches either pump, the MI process takes over and signal gain is reduced. It is also clear from Figure 18 that three idler-bands are generated simultaneously. The 2+ idler gain always matches the signal (defined as 1-) gain since it is the phase-conjugation pair of the signal. The other two idlers' (2- and 2+) gain profiles are generally very non-uniform. This can be explained as follows: the 1+ idler is mainly generated through the MI interaction with the 1- idler, whose parametric phase normally evolves fast in this case (because the pumps are normally away from ZDWL in the two pump structure) and crosses multiple numbers of π value as the signal wavelength changes, creating oscillation features in the gain profile. The 2- idler, however, is mainly generated through the phase conjugation with 1+ idler and therefore

almost exactly maps the gain profile of the 1+ idler. The non-equalized gain of 1+ and 2- idler is certainly not desirable in the applications such as multi-band casting, wavelength routing and sampling. Solution to this issue obviously requires a phase matched MI process in a broad range, which in turn demands an HNLF with smaller dispersion slope.

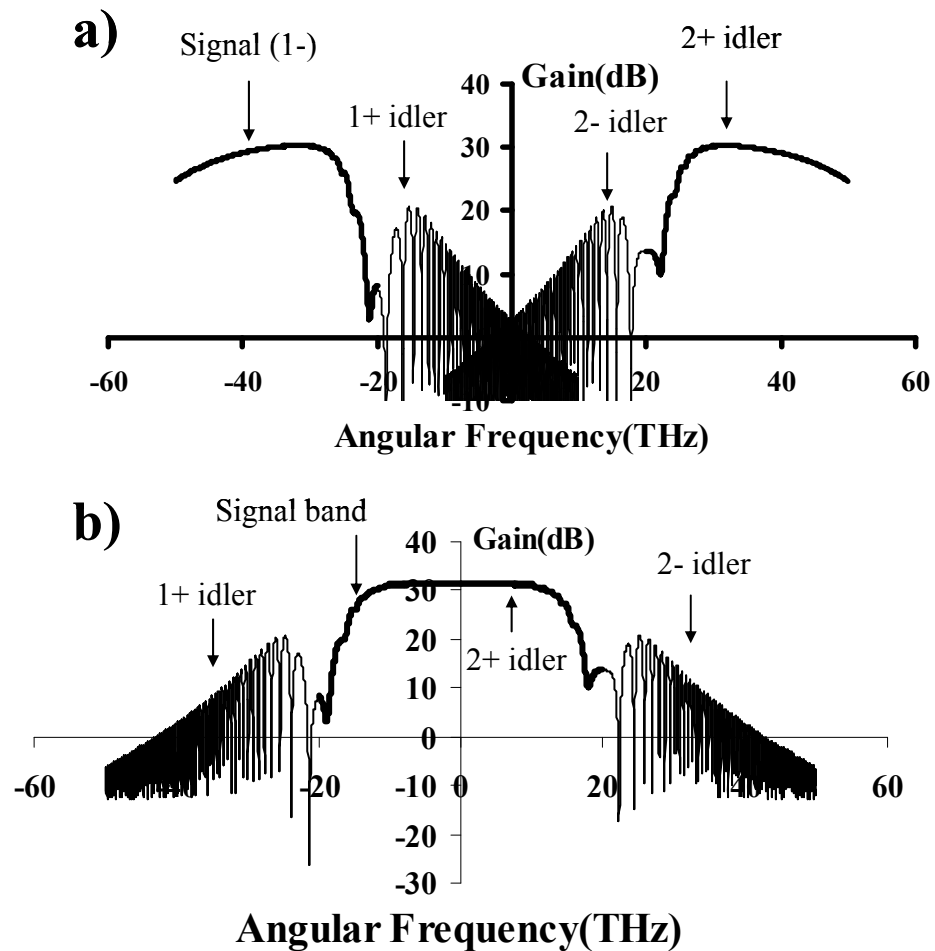


Figure 18 Four-sideband gain when a) signal injected at outer band and b) signal injected at inner band. Pumps are centered at ZDWL.

(2) $\omega_1 = -20$ THz, $\omega_2 = 21$ THz; pumps are centered at normal dispersion regime

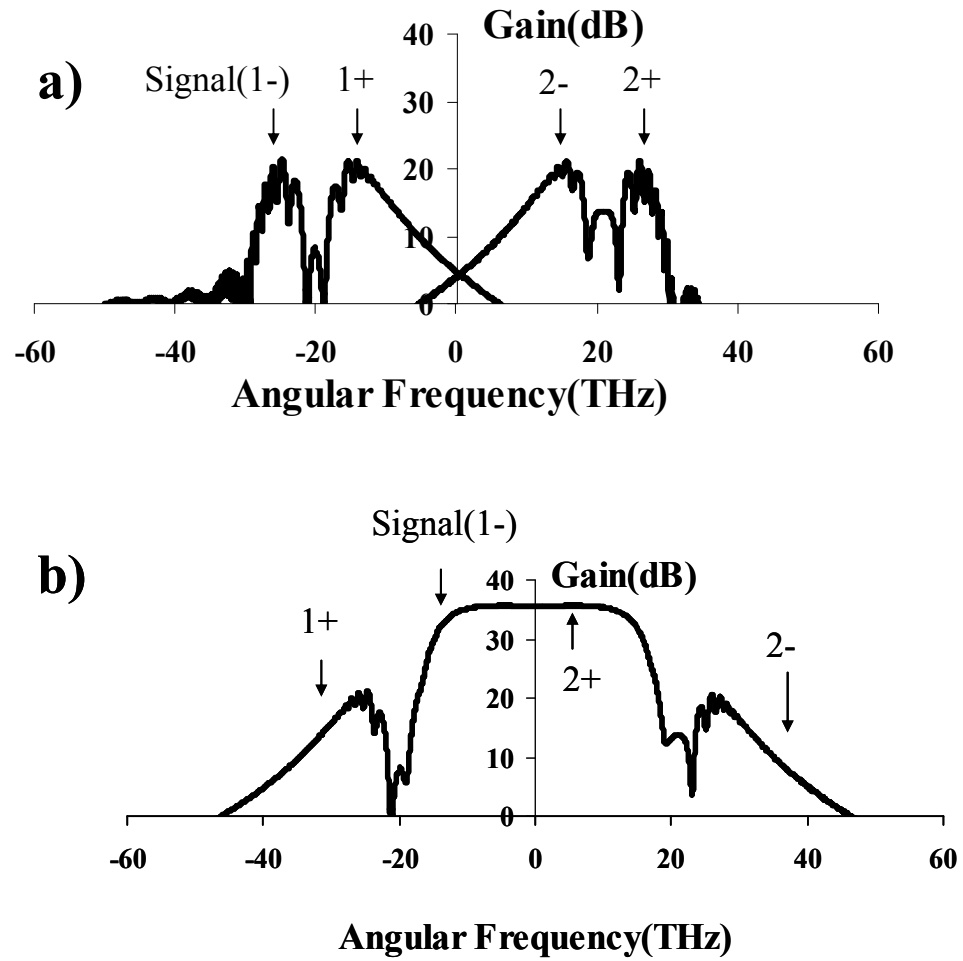


Figure 19 Four-sideband gain when a) signal injected at outer band and b) signal injected at inner band. Pumps are centered at normal dispersion regime.

(3) $\omega_1 = -21$ THz, $\omega_2 = 20$ THz; pumps are centered at anomalous dispersion regime

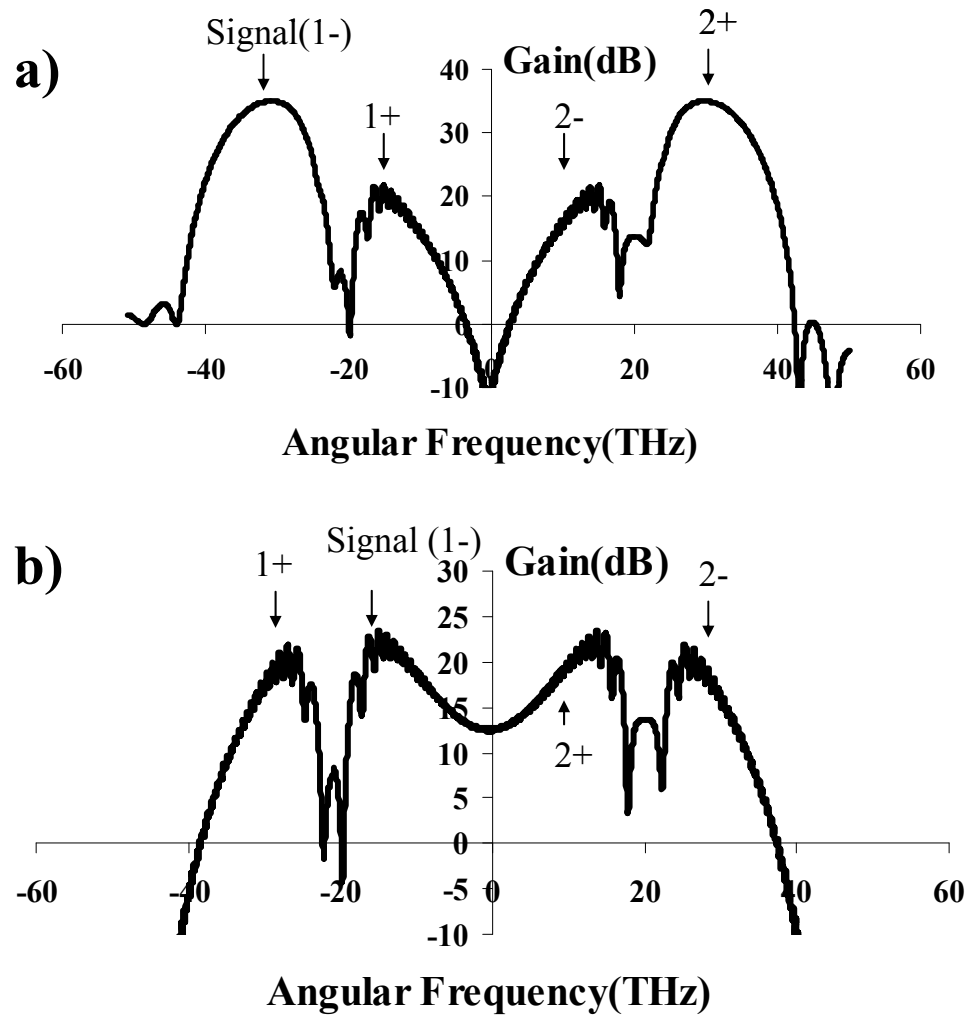


Figure 20 Four-sideband gain when a) signal injected at outer band and b) signal injected at inner band. Pumps are centered at anomalous dispersion regime.

Case 2: high β_4 : $\beta_4=2.5 \times 10^{-4} \text{ps}^4/\text{km}$

(1) $\omega_1=-20\text{THz}$, $\omega_2=20\text{THz}$; pumps are centered at ZDWL

The outer signal gain profile is narrowed due to the high β_4 . On the other hand, the inner-band signal gain does not vary too much since the 4th order dispersion contribution is small due to the small frequency shift in this region.

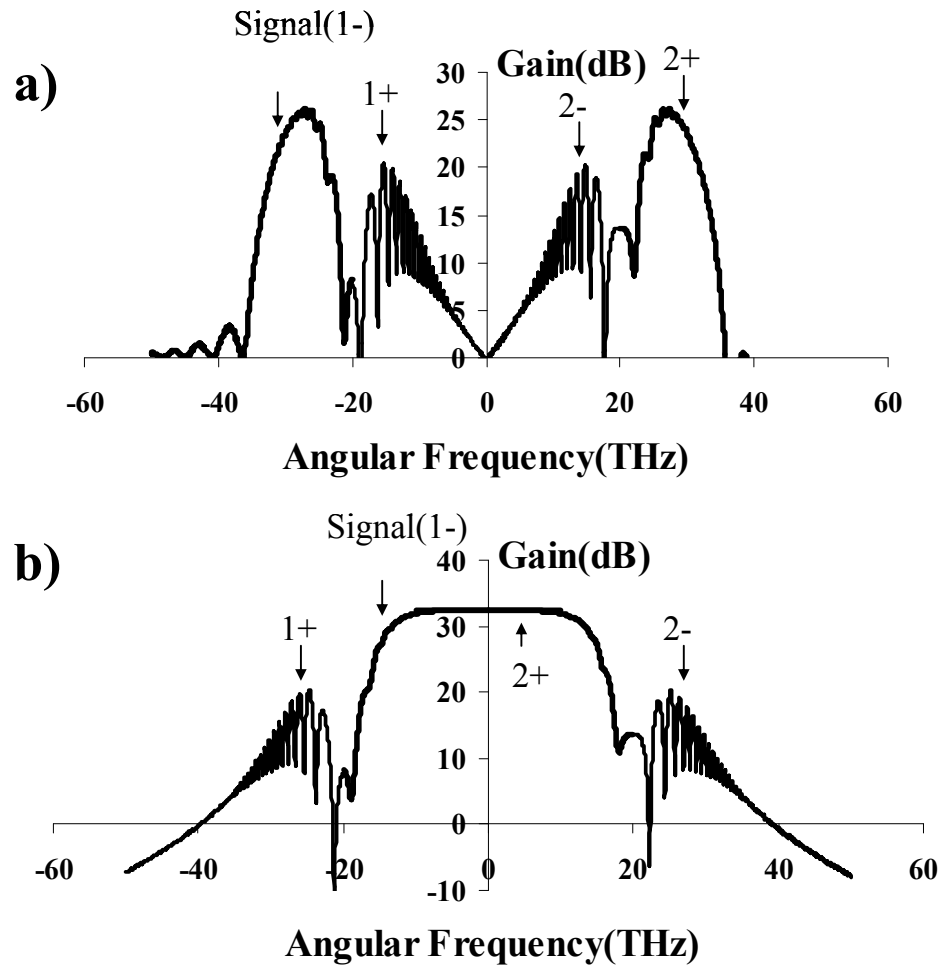


Figure 21 Four-sideband gain when a) signal injected at outer band and b) signal injected at inner band. Pumps are centered at ZDWL.

(2) $\omega_1 = -20$ THz, $\omega_2 = 21$ THz; pumps are centered at normal dispersion regime

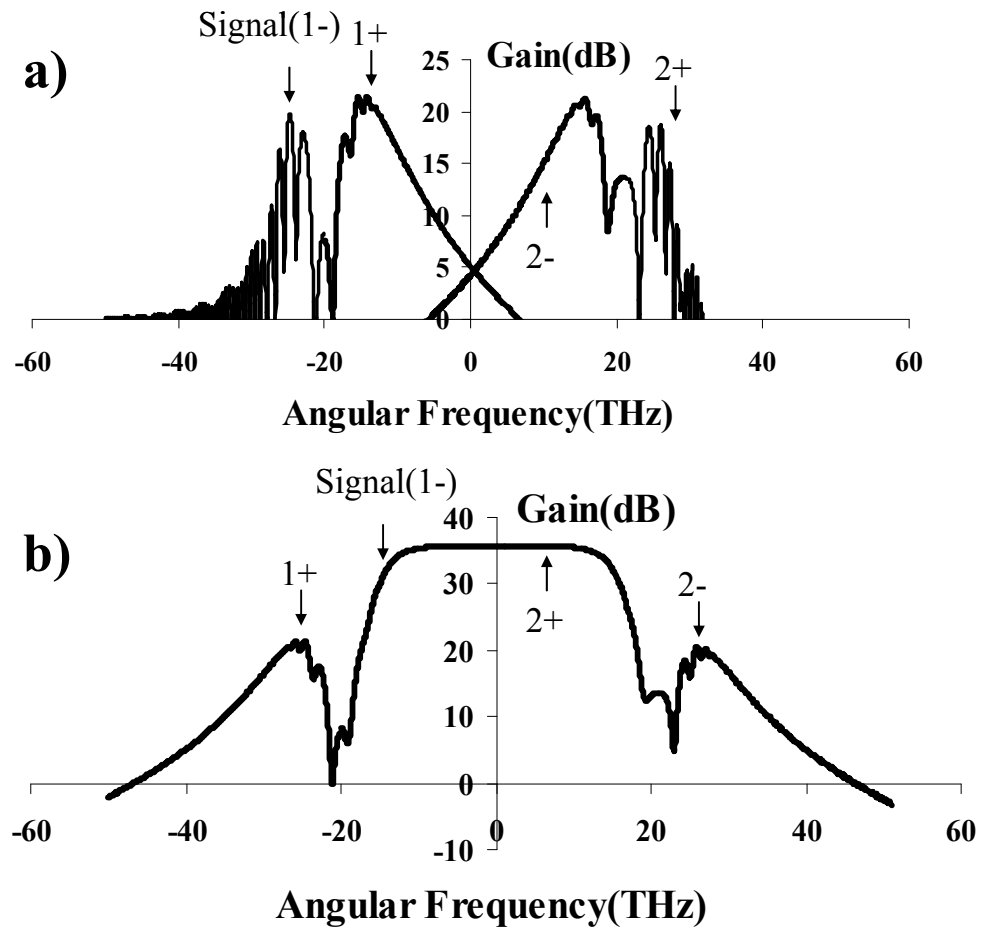


Figure 22 Four-sideband gain when a) signal injected at outer band and b) signal injected at inner band. Pumps are centered at normal dispersion regime.

(3) $\omega_1 = -20$ THz, $\omega_2 = 21$ THz; pumps are centered at anomalous dispersion regime

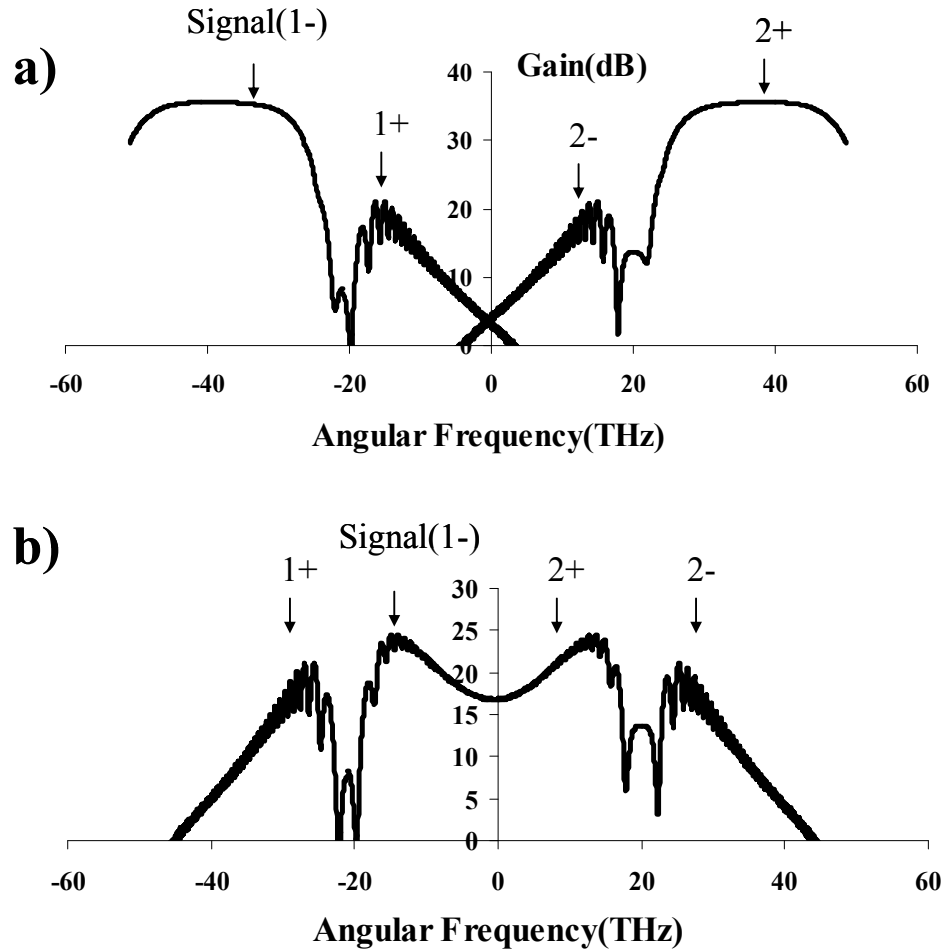


Figure 23 Four-sideband gain when a) signal injected at outer band and b) signal injected at inner band. Pumps are centered at ZDWL.

2.4 Optimizing the bandwidth of two-pump amplifier

High gain, large bandwidth amplifier is desirable not only for telecom applications to compensate the fiber loss, but also in sensing structure for increased sensitivity. Comparing to erbium doped fiber amplifier (EDFA), parametric amplifier could potentially provide larger bandwidth and create mixed frequencies (sidebands) that preserve the amplitude and phase information, which finds important applications in

optical tunable delay line⁸¹ and WDM networking⁴². The bandwidth of CW operated one-pump parametric amplifier is usually limited to 10-20 nm⁶⁹. Furthermore, parametric amplifier usually requires a phase-dithered pump for stimulated Brillouin scattering (SBS) suppression in the HNLF, rendering reduced idler noise performance in one-pump scheme⁵⁰. Two-pump parametric scheme could be successfully used to generate broadband, equalized gain profiles critical for telecom-grade amplification, wavelength conversion, all-optical signal processing and switching^{43, 82, 83}. Moreover, by dithering the two pumps either in phase or out of phase, we can reduce the pump noise transferring for the chosen idler bands⁴⁹. In this section, we describe the construction of a parametric amplifier measured to have more than 40dB of gain and 50nm of equalized bandwidth, spanning from 1550.68nm to 1601.26nm. This, to the best of our knowledge, is the largest equalized bandwidth for a two-pump parametric amplifier operating in continuous-wave (CW) mode reported at the time of this effort.

Two-pump experimental setup is illustrated in Figure 24 C-band and L-band pumps were seeded by the external-cavity lasers ($\lambda_{1,2}$), and were phase modulated using long ($2^{31} - 1$) 10Gbps pseudo-random bit sequence (PRBS) to suppress the SBS generated in the HNLF. The pumps were subsequently amplified and filtered to reject the amplified spontaneous emission (ASE). Combined pumps were launched to HNLF segment using the 90 port of a 10/90 coupler. The polarization controllers PC5 and PC6 were used to align the pump along the principal polarization axis of the HNLF section. Optical spectrum analyzers OSA1 were used to observe the spectrum after the HNLF; OSA3 was used to monitor the back-reflection from the HNLF.

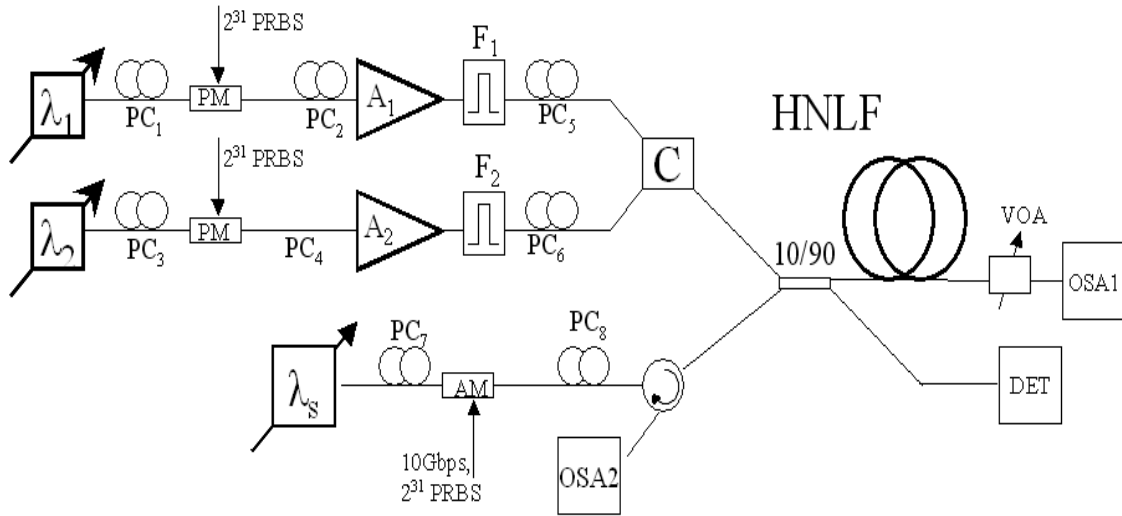


Figure 24 Experimental setup of two pump parametric amplifier. λ_1 : C-band pump at 1539.5nm; λ_2 : L-band pump at 1614nm. λ_s : tunable signal; DET could be either a power meter or an OSA;

Before the HNLF, the pumps' spectrum and power were measured using an OSA or a power meter. The setup was built around a 200m long Sumtomo Electric HNLF segment, with the nonlinear coefficient γ of $25 \text{ W}^{-1}\text{km}^{-1}$ and dispersion slope of 0.019ps/km/nm^2 . The zero dispersion wavelength of the fiber was measured at 1576nm. To maximize the bandwidth, we placed the L band pump at 1614nm, coinciding with the upper-limit of the wavelength operating range for the L-band amplifier. The C band pump was positioned at 1539.5nm. The maximum power launched into the HNLF was 1.4W for the C band pump and 400mW for the L band pump. The pump powers were not balanced throughout the experiment due to the limited L-band EDFA output at the band edge. As a consequence, the C-band pump also acted as a Raman pump, transferring the power to the L-band pump. The small signal (λ_s) power into the HNLF was -28dBm .

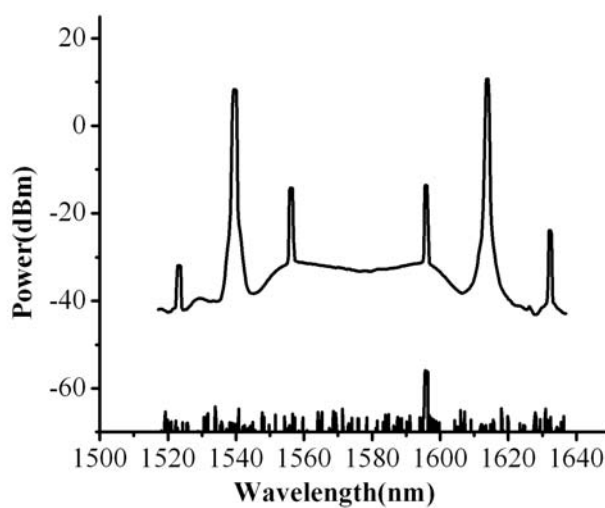
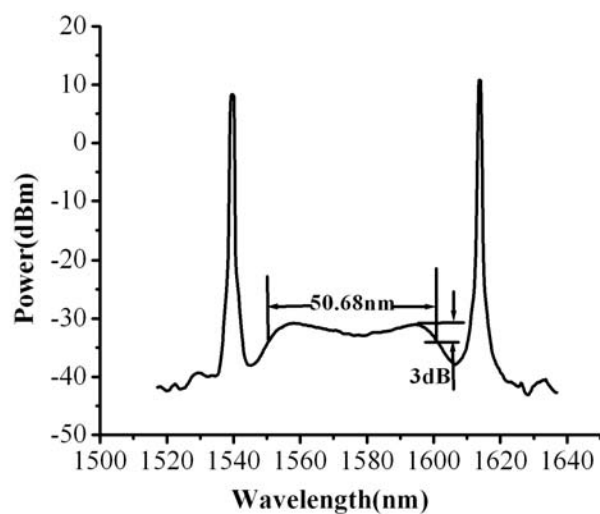


Figure 25 a) ASE spectrum of the two-pump parametric amplifier; the measured 3dB bandwidth is 50.68nm b) Typical amplified signal and four-sideband spectrum. 40dB of gain is observed

Figure 25a shows the measured ASE spectrum of the two-pump parametric amplifier while Figure 25b illustrates the typical amplified signal and three idlers that are generated by the parametric process.

In Figure 26, we show the measured gain spectrum together with the theoretical fit (based on coupled mode equations that do not incorporate dispersion fluctuations in HNLF⁴⁸) at different pump power levels. In the first example, 1.5W C-band pump and 0.4W L-band pump were launched to HNLF, resulting in 3dB-equalized bandwidth of 50.28nm (1550.68nm - 1601.26nm), covering the extended L-band. Two separate examples, defined by 1.1W/0.325W and 0.92W/0.27W pump power levels, have still maintained 50nm equalized bandwidth with corresponding gain of 32dB and 26dB, respectively. The measured results were fitted using the following set of parameters provided by Sumitomo Electric: $\gamma=25/(W^{-1}km^{-1})$, $\beta_3=0.03ps^3/km$ and $\beta_4=0.2\times 10^{-4} ps^4/km$ and an effective interaction length of 162m. In all cases, the measurements agreed well with the theoretical calculations. We note that an increase in pump power resulted in more equalized gain response. The latter is expected due to the zero dispersion wavelength fluctuation within the HNLF, which are not included in the coupled mode analysis, as noted previously. At high pump powers, the nonlinear phase shift dominates over the dispersion fluctuations⁴⁴, as demonstrated by the improved flatness of gain spectrum central region in Figure 28 (P1= 1.4W, P2=0.4W). At lower pump powers, the dispersion induced phase shift carries more weight, thus dominating the parametric amplifier response, inducing non-uniformity in the central region of the gain spectrum.

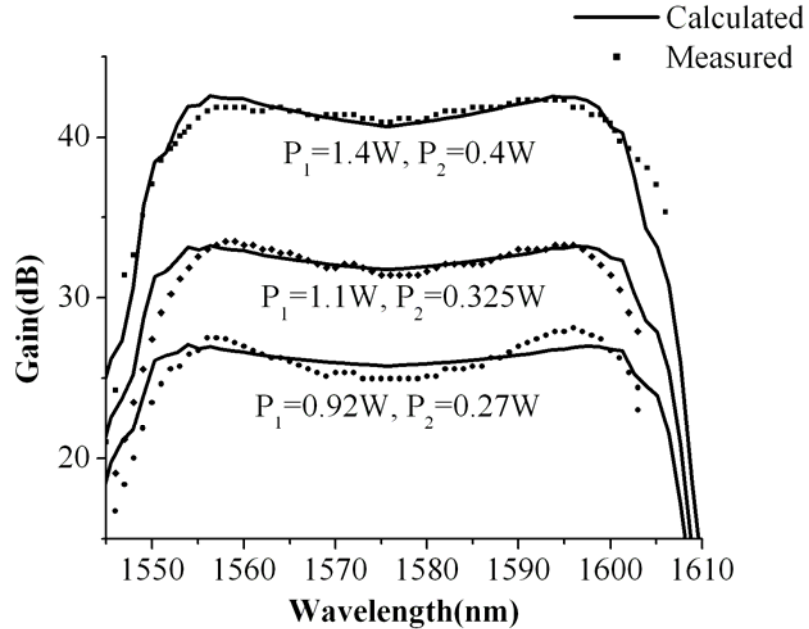


Figure 26 Measured gain spectra at different pump power levels. 50.28nm bandwidth with 41.5dB average gain is obtained. The pumps are at 1539.5nm and 1614nm, respectively. The resolution bandwidth is 2nm for all cases.

The calculation also showed that wider bandwidth is expected provided the two pumps could be separated further. Using the same parameter, the couple mode equations predict that one can achieve 100nm gain bandwidth by placing the pumps at 1510nm and 1647.5nm, respectively, with 1W incident power for both pumps. The result is shown in Figure 27.

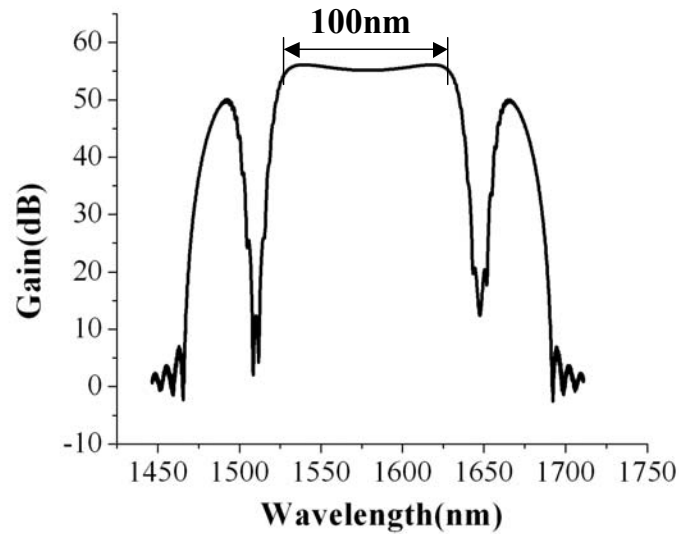


Figure 27 Predicted gain profile with the pumps placed at 1510nm and 1647.5 nm, respectively, with 1W incident power for both pumps.

In conclusion, we have demonstrated the record two-pump performance of 40dB of CW gain and 50.28nm 3dB-equalized bandwidth using third-generation 200-meter long highly nonlinear fiber. The attained gain bandwidth was limited by the available pumps' spectral and power tuning ranges. Our calculations indicate that HNLF is capable of even wider amplification response, given the extended wavelength range of the available components. Exceptional HNLF uniformity and high nonlinear parameters are identified as the key parameters characterizing the latest fiber generation

2.5 Impact of dispersion fluctuation on parametric systems

Dispersion fluctuation stands as a major limitation to the performance of parametric devices, preventing an arbitrary two-pump parametric design. It is well known that parametric process requires phase matching among pump, signal and idler waves. Dispersion fluctuation along the fiber, however, introduces random walk-off to the

parametric phase shift, and consequently reduces the gain. Impact of dispersion fluctuation has been previously studied in both one-pump⁸⁴ and two-pump structures⁸⁵. The reported work on two-pump structure was a two-sideband model based on phase-conjugation process. However, as has been pointed out, in the two-pump structure, three physical processes, namely, modulation instability (MI), Bragg scattering (BS) and phase conjugation processes, interact with each other, and generate four sidebands. A two-sideband model produces less accurate results for not accounting for the real physical processes. A complete model based on four-band analysis is required for the prediction of a practical performance of a two-pump parametric device⁸⁶. In this section, we first discuss dispersion fluctuations in fibers and try to obtain a physical insight into the problem. Then we will develop a stochastic four-sideband model, simultaneously accounting for the aforementioned three parametric processes under dispersion fluctuated HNLF. Numerical simulation models are discussed thereafter. Four-sideband analytical results were firstly compared to the two-sideband ones, and then to the numerical simulations. Due to the random nature of dispersion fluctuation, it is generally hard to compare the theoretical calculations to the experimental measurements unless a longitudinal dispersion profile is available for the HNLF. Therefore, only a set of qualitatively experiments was conducted for the justification of the developed model.

2.5.1 Phase matching under dispersion fluctuation

Longitudinal dispersion fluctuation in fiber could originate from dopant level fluctuation (resulting in index contrast fluctuation) or fiber transverse structure variation. Dispersion fluctuation results in random offset from the phase matching in a parametric

process, the details of which would require solving couple-mode equations. A simple explanation based on the parametric phase shift, however, provides very useful physical insight. Parametric phase shift could be generally written as²⁶:

$$\kappa = \Delta\beta + \Delta\phi_{NL} \quad (30)$$

where $\Delta\beta$ stands for the propagation constant difference, representing the linear phase shift per unit length and $\Delta\phi_{NL}$ denotes the nonlinear phase contribution. In an ideal case, κ maintains zero ed along the fiber and maximum gain is therefore obtained. When offset from the phase matching condition, parametric phase ϕ is driven by the integration value $\int \kappa(z)dz$ and a reduced gain is expected. In particular, once ϕ is shifted by a value of $\pi/2$ from the optimum value, power is transferring back from signal and idler to the pump. Dispersion fluctuation induced effect is thus easily understood with Figure 28: κ equals 0 initially and phase matching condition is satisfied. At position z_0 , because of the local dispersion variation, κ jumps to κ_0 until z_0+l point from where the dispersion is back to normal. The impact of this local dispersion fluctuation between $[z_0, z_0+l]$ is determined by the parametric phase evolution within this region, namely, κ_0l : if κ_0l is small ($\ll \pi$), signal/idler experiences a reduced gain during the rest of the propagation; signal/idler starts to see loss (meaning power flows back to pump) once κ_0l approximate π .

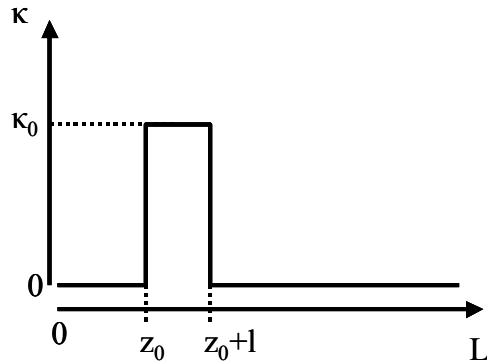


Figure 28 A schematic illustration of parametric phase mismatch number κ along fiber length. κ jumps from 0 to κ_0 during the region $[z_0, z_0+l]$ due to dispersion fluctuation.

The above discussion illustrates that two parameters, namely, the amplitude of dispersion variation (which results in κ varying from 0 to κ_0) and its ‘interaction length’ (l), together determines the effect of a local dispersion fluctuation. In practice, the overall performance of a parametric process could be viewed as an integrated result of many sections with random local dispersion variations. In literatures, the effect of dispersion fluctuation is modeled by considering a random longitudinal deviation from ZDWL and the correlation length of that deviation^{85,86}. While the treatment is standard for random data, physical meanings of these two parameters are observed in the parametric phase jump κ_0 and interaction length l , respectively. The illustration in Figure 28 is practically useful as well. Sometimes a fiber may have a large local dispersion variation due to the imperfect manufacturing process. This imperfection will not bring significant influence as long as the dispersion variation is very localized so that the induced parametric phase shift is less than $\pi/2$. A consequent conclusion is that, a shorter interaction length l is desirable, resulting in better tolerance of dispersion deviation. This agrees with the

previously reported result that a short period dispersion variation is less harmful than a long period variation does⁸⁵. A more rigorous analysis is illustrated in Figure 29 where two adjacent dispersion variation regions causing opposite sign of parametric phase shift are shown. Dispersion variation induced negative phase shift in the region $[z_0+l_1, z_0+l_2]$ could be partially compensated by the phase shift introduced by its preceding region $[z_0, z_0+l_1]$ and result in reduced overall parametric phase shift. For short period dispersion fluctuation, there exist a large number of local dispersion fluctuation sections, which statistically average out the parametric phase walk-off due to dispersion fluctuation and results in larger overall gain than that of a large period variation does.

The effect of dispersion fluctuation depends also on the location of a dispersion variation. Assuming that z_0 in Figure 28 is close to the input end of an HNLF and the dispersion fluctuation in the region $[z_0, z_0+l]$ quickly shifts the parametric phase to π , parametric gain would maintain a low level along the following fiber section ($[z_0+l, L]$) due to the unfavorable parametric phase even if the rest section satisfies the phase matching condition locally. Simply flipping the fiber input-output would significantly increase the parametric gain: parametric process is well phase matched and results in significant gain before the interacting waves hit the local dispersion jumping $[z_0+l, z_0]$. Although the gain value would be reduced in the following section ($[z_0, 0]$), a significantly improved overall gain is still obtained at the output. Indeed, a gain difference of 5dB as well as the gain spectra change is frequently observed in the experiments by simply flipping the fiber coil.

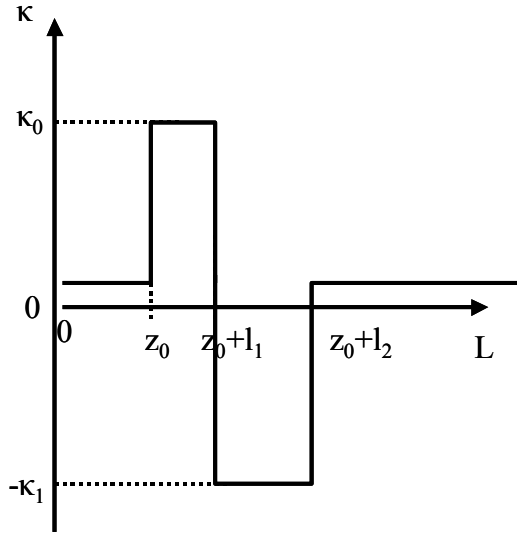


Figure 29 Illustration of a random pattern of dispersion fluctuation along the fiber.

Dispersion fluctuation induced negative parametric phase shift in region $[z_0+l_1, z_0+l_2]$ was partially compensated by the positive phase shift introduced in region $[z_0, z_0+l_1]$.

2.5.2 Dispersion fluctuation in one- and two-pump parametric structure

We have discussed dispersion fluctuation effect based on parametric phase shift in the preceding section. On the other hand, phase matching conditions for degenerate and non-degenerate parametric process are different, and therefore impact of dispersion fluctuation to these two processes are different as well. Here we restrain the discussion to continuous wave (CW), non-depleted condition, therefore nonlinear phase shift is kept constant. Without losing generality, we neglect the high order terms temporarily. In a degenerate parametric process, the linear phase matching relation could be written as²⁶

$$\Delta\beta = \beta_2(\omega_p) \cdot \Omega^2 \quad (31)$$

where ω_p is pump's angular frequency (will be called frequency in the thereafter context). While in a non-degenerate process, for example, PC process has its linear phase matching relation as follows⁴⁸:

$$\Delta\beta = \beta_2(\omega_a)(\Omega^2 - \omega_d^2) \quad (32)$$

where $\omega_a = (\omega_1 + \omega_2)/2$ and $\omega_d = (\omega_2 - \omega_1)/2$ (ω_1, ω_2 are the two pumps' frequency, $\omega_1 < \omega_2$); $\Omega = \omega - \omega_p$ in the degenerate and $\Omega = \omega - \omega_a$ in the non-degenerate process describe the frequency shift of a signal.

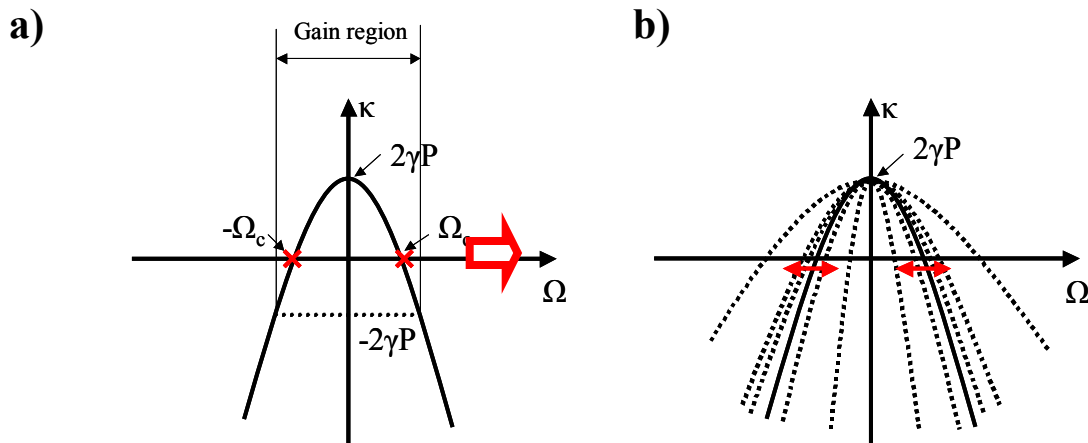


Figure 30 Parametric phase shift versus frequency shift in the MI process (one-pump structure) in a) an ideal condition and b) with longitudinal dispersion fluctuation

Some quick observations could be obtained by observing equation (31) and (32). Parametric phase shift κ for a degenerate process is plotted in Figure 30a, which is a parabolic function of frequency shift Ω with maximum value κ_{\max} equaling $2\gamma P$ and the parabolic opening proportional to $1/|\beta_2(\omega_p)|$. $\pm\Omega_c = \sqrt{2\gamma P/|\beta_2|}$ are the frequency shifts

of maximum gain. Dispersion fluctuation introduces additional phase shift $\delta\beta_2\Omega^2$, implying that the κ - Ω curve would vary longitudinal with the maximum point fixed at $(0, 2\gamma P)$ while with the parabolic opening and $\pm\Omega_c$ changes randomly. The overall effect is that the average gain would be reduced while the bandwidth could be maintained or even be broadened. This observation has been reported in⁷⁴, and experimentally utilized to achieve a flat, broadband operation by deliberately introducing a ZDWL variation in fiber^{87, 88}.

A PC process has a similar κ - Ω curve as shown in Figure 31a. However, the maximum value κ_{\max} and the gain-maximum frequency $\pm\Omega_c$ are now modified by the pump separation value ω_d , as shown in the following formulas:

$$\kappa_{\max} = -\beta_2(\omega_a)\omega_d^2 + \gamma(P_1 + P_2) \quad (33)$$

and

$$\Omega_c = \sqrt{\omega_d^2 - \frac{\gamma(P_1 + P_2)}{\beta_2(\omega_a)}} = \sqrt{-\frac{\kappa_{\max}}{\beta_2(\omega_a)}} \quad (34)$$

To simplify the discussion here, we assume the pumps are centered in the anomalous dispersion regime, namely, $\beta_2(\omega_a) < 0$. As $|\beta_2(\omega_a)|$ increases, κ_{\max} increases while Ω_c is reduced. However, the phase curves always cross two fixed points at $(-\omega_d, \gamma(P_1+P_2))$ and $(\omega_d, \gamma(P_1+P_2))$ where the two pumps are placed. As the interacting waves propagate longitudinally, the parametric phase curves change randomly as Figure 31b

shows, resulting in wildly variations of Ω_c and thus reduces the maximum gain. Furthermore, since PC process maintains exponential form across its gain region, a random change of κ_{\max} develops significant non-uniformity in the gain spectrum, as has been reported in previous literatures. An easy solution is seen by reducing the pump separation ω_d , which subsequently reduces the random dispersion fluctuation induced parametric phase shift ($\propto \delta\beta_2\omega_d^2$). This observation has been reported in previous work with two-sideband model. We will show later that four-sideband couple-mode equation results in the same conclusion.

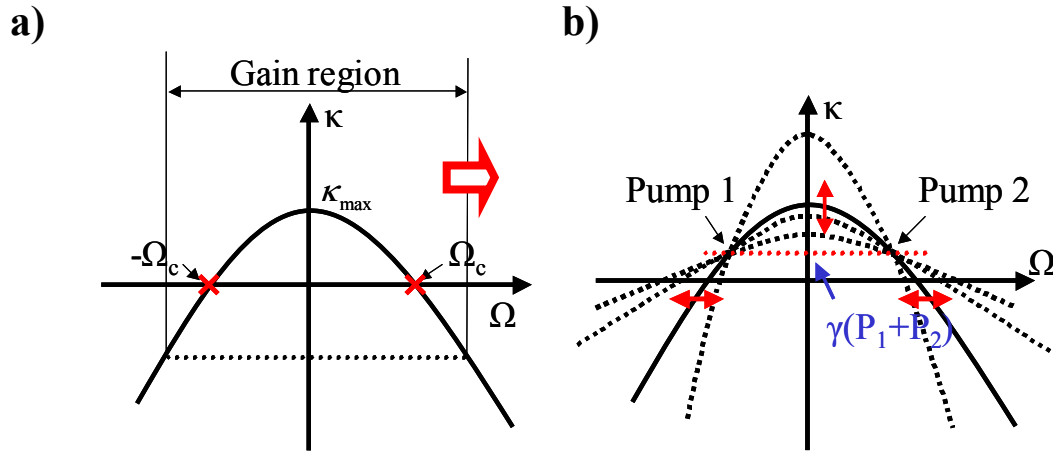


Figure 31 Parametric phase shift versus frequency shift in the PC process in a) an ideal condition and b) with longitudinal dispersion fluctuation

2.5.3 Mathematical description of dispersion fluctuation in fiber

Dispersion fluctuation results in β_2 to be a function of both ω and z , as shown in Figure 32. As one can see, as light wave travels from position 1 to position 2, not only the ZDWL moves, but also the dispersion slope, namely, β_3 varies, detailed in Figure 32b. A mathematical expression for the aforementioned case could be written as

$$\begin{aligned}\omega_0 &= \langle \omega_0 \rangle + \delta\omega_0 \\ \beta_3 &= \langle \beta_3 \rangle + \delta\beta_3\end{aligned}\quad (35)$$

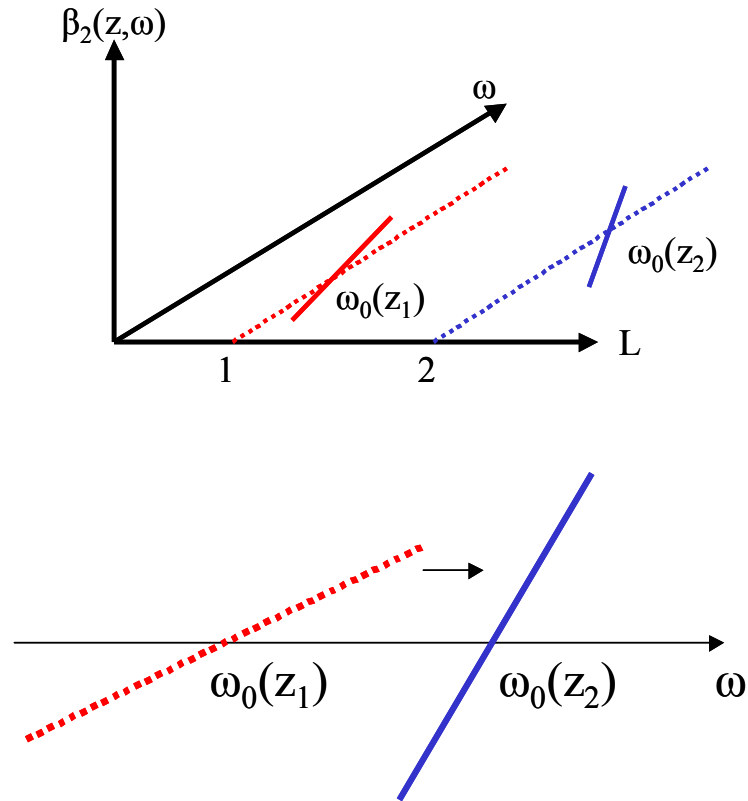


Figure 32 Illustration of β_2 as a function of both ω and z . Dispersion fluctuation offsets the ZDWL and changes the dispersion slope.

One can incorporate as many as possible the high-order dispersion terms for the modeling; however, the complexity would also be increased. While a numerical simulation could in principle take into account the random fluctuations of ZDWL and the dispersion slope simultaneously, it is generally difficult to do so for an analytical model. In the following work, we assume dispersion slope fluctuation is less significant than the ZDWL fluctuation and keeps constant along the fiber length.

It is instructive to ask, once the fiber is drawn, its dispersion property and parametric performance determined, why, then, it is important to study the problem with a statistical method? Indeed, a precise prediction of an HNLF's performance depends on complete knowledge of the longitudinal distribution of the dispersion, which requires dispersion mapping with meter scale resolution for hundreds meters long HNLF. Before such technique is available, dispersion fluctuation in HNLF can only be treated as random. Moreover, an analytical model, predicting an average parametric performance, provides a physical insight on the impact of dispersion fluctuation, and a criterion on the required fiber parameters for a desired performance. More importantly, a numerical model, by incorporating both ZDWL and dispersion slope variation locally, provides a potential for dispersion mapping: a set of parametric gain spectra could be measured experimentally, and iteratively approached by applying a random distribution of ZDWL and dispersion slope to the couple-mode equations until a best fit is achieved.

2.5.4 Stochastic Four-sideband Model

A non-depleted, two-pump interaction could be generally described as a set of four-sideband equations as follows⁴⁸:

$$\frac{dB}{dz} = iDB \quad (36)$$

in which $B = [B_{1-}^* \ B_{1+} \ B_{2-}^* \ B_{2+}]^T$ is the complex field of the four sidebands generated in the two-pump parametric interactions; and

$$D = E + F \quad (37)$$

where

$$E = \begin{bmatrix} -\delta\beta_{1-} & 0 & 0 & 0 \\ 0 & \delta\beta_{1+} & 0 & 0 \\ 0 & 0 & -\delta\beta_{1-} & 0 \\ 0 & 0 & 0 & \delta\beta_{2+} \end{bmatrix} \quad (38)$$

and

$$F = \begin{bmatrix} -\gamma P_1 & -\gamma P_1 & -2\gamma(P_1 P_2)^{1/2} & -2\gamma(P_1 P_2)^{1/2} \\ \gamma P & \gamma P_1 & 2\gamma(P_1 P_2)^{1/2} & 2\gamma(P_1 P_2)^{1/2} \\ -2\gamma(P_1 P_2)^{1/2} & -2\gamma(P_1 P_2)^{1/2} & -\gamma P_2 & -\gamma P_2 \\ 2\gamma(P_1 P_2)^{1/2} & 2\gamma(P_1 P_2)^{1/2} & \gamma P_2 & \gamma P_2 \end{bmatrix} \quad (39)$$

$\delta\beta_{1-}$ and $\delta\beta_{1+}$ are the propagation constant mismatch between 1-/1+ waves and the pump ω_1 and $\delta\beta_{1-}$ and $\delta\beta_{1+}$ are the mismatch between 2-/2+ waves and the pump ω_2 . P_1 and P_2 stands for the two pumps' power, γ is the nonlinear coefficient. The physical meaning of equations (36)-(39) is clear: \mathbf{E} represents the linear phase shift while \mathbf{F} is the nonlinear phase shift induced by self-phase modulation (SPM) and cross-phase modulation (XPM). Through mathematical manipulations, we can write:

$$\begin{aligned} \delta\beta_{1-} &= \beta_{1-} - \beta_1 \\ &= \delta\omega_0 \left\{ \frac{\beta_3}{2} (a^2 - b^2) - \frac{\beta_4}{6} (a^3 - b^3) \right\} + \frac{\beta_3}{6} (b^3 - a^3) - \frac{\beta_4}{24} (b^4 - a^4) \end{aligned} \quad (40)$$

where the dispersion terms $\beta_3 = \beta_3(\omega_0)$ and $\beta_4 = \beta_4(\omega_0)$ and \mathbf{a} and \mathbf{b} are frequency shift terms defined as $a = \omega_1 - \langle \omega_0 \rangle$, $b = \omega_{1-} - \langle \omega_0 \rangle$. We assumed $\delta\omega_0 \ll \omega_0$ in deriving (40). Similarly, $\delta\beta_{1+}$, $\delta\beta_{2-}$ and $\delta\beta_{2+}$ could be derived. Matrix \mathbf{E} then could be written as

$$\mathbf{E} = \mathbf{E}_1 + \delta\omega_0 \cdot \mathbf{E}_2 \quad (41)$$

Equation becomes

$$\frac{dB}{dz} = i[D_1 + \delta\omega_0(z) \cdot \mathbf{E}_2]B \quad (42)$$

where $\mathbf{D}_1 = \mathbf{E}_1 + \mathbf{F}$. The equation (42) is remarkable in its form since it clearly separates physical mechanisms responsible for two-pump parametric exchange in stochastic nonlinear waveguide such as HNLF. The matrix \mathbf{D}_1 incorporates the linear static phase shift (\mathbf{E}_1), as well as the nonlinear phase terms formed by SPM and XPM (\mathbf{F}). In contrast, \mathbf{E}_2 scales the fluctuating HNLF dispersion $\delta\omega_0$ and is independent of its nonlinearity (γ) and the pump powers.

Unfortunately, solving the equation (42) is not a trivial task since $\delta\omega_0$ represents longitudinally varied function. In case when \mathbf{D}_1 and \mathbf{E}_2 commute, the closed-form solution is readily written as:

$$B(z) = \exp i(D_1 + E_2 \cdot A(z))B(0) \quad (43)$$

where $A(z) = \int_0^z \delta\lambda_0(z') dz'$. In a more general case when \mathbf{D} and \mathbf{E}_2 do not commute, the solution is written as:

$$B(z) = \lim_{\delta z \rightarrow 0} \left(\prod_{i=1}^N \exp i(D_1 + \delta\omega_{0i} E_2) \delta z \right) B(0) \quad (44)$$

A real distribution of $\delta\omega_0$ could be quite complicated. To obtain some physical insight on the impact of dispersion fluctuation, a simple assumption is that $\delta\omega_0(z)$ being a δ -correlated Gaussian process. In addition to providing the algebraic tractability, the Gaussian assumption is justified by experimental observations and the random nature of HNLFF drawing process. Physically, $\delta\omega_0$ becomes δ -correlated when its correlation length is much shorter than the propagation length L in fiber, namely,

$$\langle \delta\omega_0(z) \rangle = 0; \quad \langle \delta\omega_0(z) \delta\omega_0(z - \xi) \rangle = \sigma^2 l_c \delta(\xi) \quad (45)$$

At the same time, under the δ -correlation assumption, equation (43) becomes the valid analytical solution. For a more complicated random distribution, one may solve for an approximate analytical solution by referring to equation (44) and applying Taylor operator expansion⁸⁷. Practically, one may feel more natural by considering λ_0 fluctuation instead of ω_0 . The two approaches are equal by noticing that in the vicinity of 1550nm region, $\delta\lambda[nm] = 1.27 \delta\omega[THz]$.

Parametric gain (conversion efficiency) represents an important figure of merit used to evaluate any two-pump device. Consequently, we concentrate on the effect of $\delta\omega_0$

variations on the parametric gain. As is assumed to be a Gaussian process, the integral $B(z)$ in equation (43) is also a Gaussian process, allowing a simple expression for power evolution as the following:

$$\langle B(z) \rangle = \exp(iDz - \frac{E_2^2}{2} \langle A^2 \rangle) B(0) \quad (46)$$

and $\langle A^2(z) \rangle = R_A(0) = \int_0^z \int_0^z R_{\delta\omega_0}(\xi_1, \xi_2) d\xi_1 d\xi_2 = 2z\sigma^2 l_c$, whereas $R_{\delta\omega_0}(\xi_1, \xi_2)$ is the statistical autocorrelation function of $\delta\omega_0$. The average gain under dispersion fluctuation is then readily to be obtained as

$$G = \left| \exp(iD - E_2^2 \sigma^2 l_c) z \right|^2 \quad (47)$$

Accuracy estimation of the four-sideband model is obtained by comparing the results to rigorous NLS solution, which will be treated in the next section. The four-sideband model is firstly compared to a simpler (two-sideband) calculation by considering the impact of dispersion fluctuations under the conditions stated in Figure 33. The results of the two models are nearly identical in the central region between the pumps that is dominated by PC process. In contrast, a significant difference is observable within the outer bands as the two-band model is incapable of capturing the processes in this region, overestimating the available bandwidth. The four-sideband model, however, fully accounts for MI, PC and BS interplay. Indeed, we note the increasing importance of degenerate MI process in immediate pump proximity, accounting for larger discrepancy between two- and four-sideband models. More importantly, a four-sideband model is

easily to be adjusted to two-sideband models accounting for MI, BS or PC processes specifically.

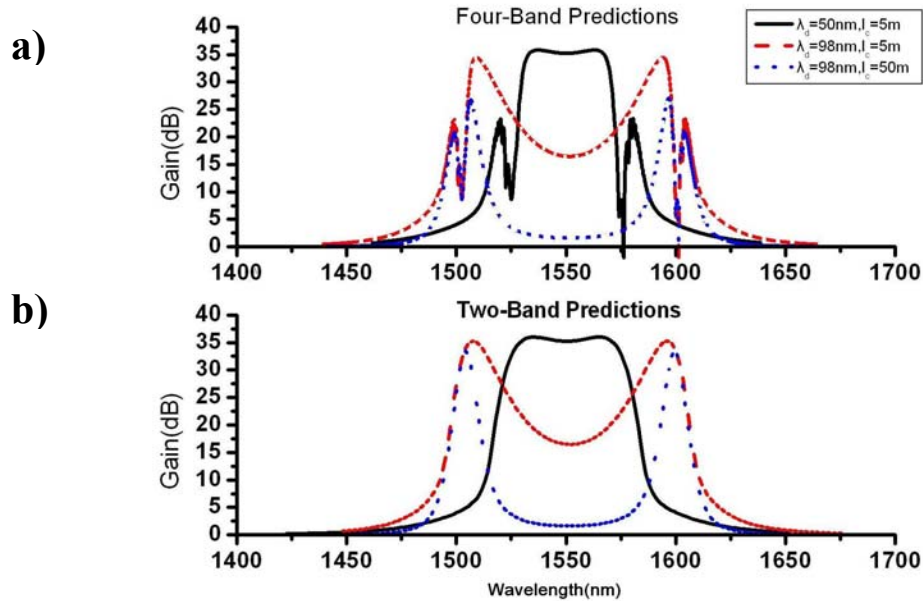


Figure 33 Comparison of the four-band and two-band model results on the impact of the dispersion fluctuation on two-pump gain profile. Pumps changed from 1575.12/ 1525.12nm (solid curve) to 1602.6/1500.6nm (dashed curve). λ_d refers to the two-pump separation and l_c is the correlation length.

2.5.5 Numerical simulations

A numerical simulation is to model a fiber with large numbers of small sections with constant dispersion and apply couple-mode equations to each section of fibers. While a stochastic model could predict the average performance of a set of fibers with physical insights, a numerical model is needed in accurately synthesizing the parametric performance, e.g., the gain spectrum. Numerical simulations could deal with complicated

distributions of ZDWL fluctuation and incorporate dispersion slope fluctuation as well. A schematic illustration for numerical simulations is shown in Figure 34.a. A local ZDWL fluctuation (e.g at $z+\Delta z$ section) could result from a local random fluctuation (called stochastic part in the figure) and the legacy of the fluctuation from previous section z , which is somewhat ‘deterministic’ as referring to section $z+\Delta z$. The stochastic part is Gaussian distributed, as mentioned previously.

The deterministic part depends on the correlation function. In a δ -correlation assumption (which we made in the previous section), a simple treatment is to make Δz equal l_c and the deterministic part vanishes. In another case of exponential–correlation assumption, we obtain that:

$$\Delta\omega_0(z + \Delta z) = \Delta\omega_0(z) \cdot \cos(\varphi) + \text{Gaussian}(0; \delta_{\omega_0}) \cdot \sin(\varphi) \quad (48)$$

where $\cos(\varphi) = \exp(-\Delta z / l_c)$.

We are now ready to use numerical simulations to verify the previously developed analytical four-sideband solutions. A comparison of three typical cases of different correlation length is shown in Figure 35. In the calculations, the two pumps are placed at 1575.12 nm and 1525.12 nm, respectively. Fiber parameters are stated in the figure caption. The numerical simulation results are the average value of 200 realizations. Figure 35 shows very good match between the numerical and analytical solutions, particularly in the case of short correlation length. Discrepancies begin to show up at

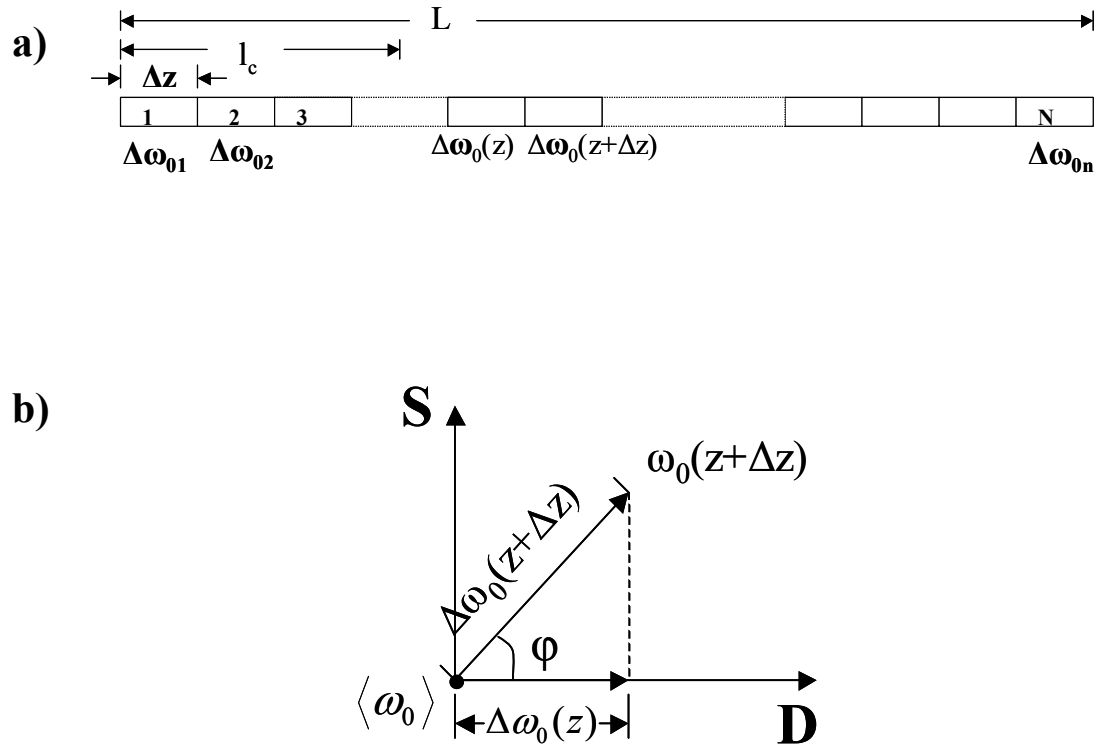


Figure 34 (a) Schematic of fiber sections for numerical simulations. L : fiber length; l_c : correlation length; Δz : section length within which dispersion is constant. (b) ZDWL offset at $z+\Delta z$ section determined by both the influence from the pervious section (D) and the local fluctuations (S). D : deterministic part; S : stochastic part.

longer correlation length ($l_c > 0.1L$), which is due to the unsuitable δ -correlation assumption in long-correlation length condition. Results could be improved by using a more complicated solution of equations (44) and (48). An important observation from Figure 35 is that a reduced correlation length results in an improved gain spectrum, which agrees with the previous conclusion from section 2 that a short period dispersion fluctuation is less harmful than a long period fluctuation does. Dispersion slope fluctuation could be treated in the same way, which is omitted in this work. Practically, it

is important to incorporate both ZDWL fluctuation and dispersion slope fluctuation to fit or synthesize an experimentally measured gain spectrum.

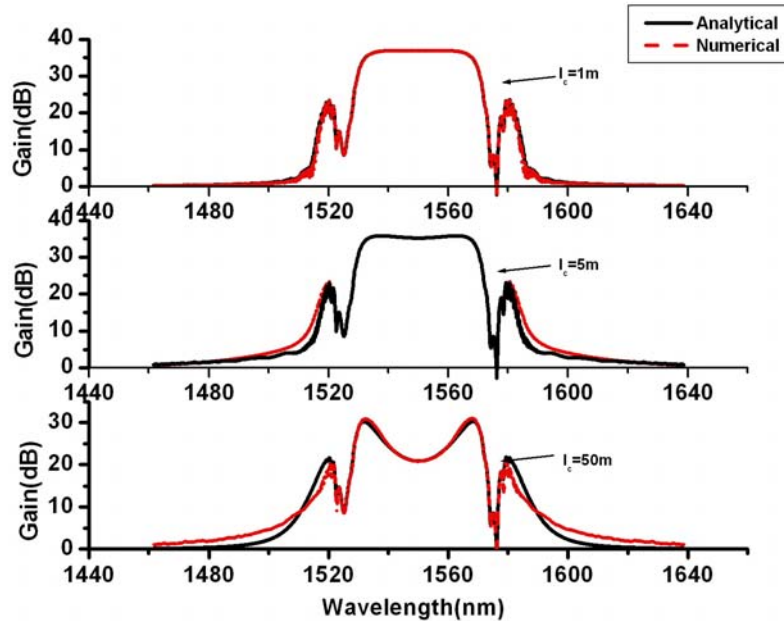


Figure 35 Comparison of the numerical simulations and analytical results for different correlation lengths with two pumps at 1575.12nm and 1525.12nm respectively. l_c denotes correlation length. Other fiber parameters: $\gamma=10/\text{km}/\text{W}$, $\langle\lambda_0\rangle=1550\text{nm}$, $\beta_3=0.12\text{ps}^3/\text{km}$, $\beta_4=10^{-4}\text{ps}^4/\text{km}$, $L=500\text{ m}$, $P_1=P_2=0.5\text{W}$

Figure 36 plots changes in the gain spectrum for several pump-separations. Parametric responses of both isotropic (Figure 36.a) and dispersion fluctuating HNLFF (Figure 36.b) are displayed in order to emphasize the stochastic effect of the gain profile. We note again the increasing importance of degenerate MI process in immediate pump proximity, accounting for larger discrepancy between two- and four-sideband models. As the two pumps are brought closer to each other, their relative strength of modulation

instability significantly grows resulting in gain spectrum that substantially departs from equalized, PC-driven response. Another observation is that reducing pump separation mitigates the impact of dispersion fluctuation within the inner band signal. Specifically, when pump separation is reduced below a critical value (50nm this case), the impact of dispersion fluctuations is drastically reduced. In contrast, an isotropic HNLFF always provides an equalized response, provided that proper pump spectral placement is chosen^{48, 85}. This observation agrees with the previously reported results and is consistent with the physical prediction discussed in section 2. A third observation is that distant outer-band gain humps that appear in the isotropic condition are smoothed or even ‘washed out’ in the fluctuation case, which has also been discussed in section 2 and is readily to be understood by observing equation (31) and (32). Parametric phase shift is a high order (at least 2nd order) polynomial function of frequency shift, which becomes extremely sensitive to dispersion variation at large frequency shift and makes distant band phase-matching much harder than the near-ZDWL region phase matching, agreeing with the experimental observations.

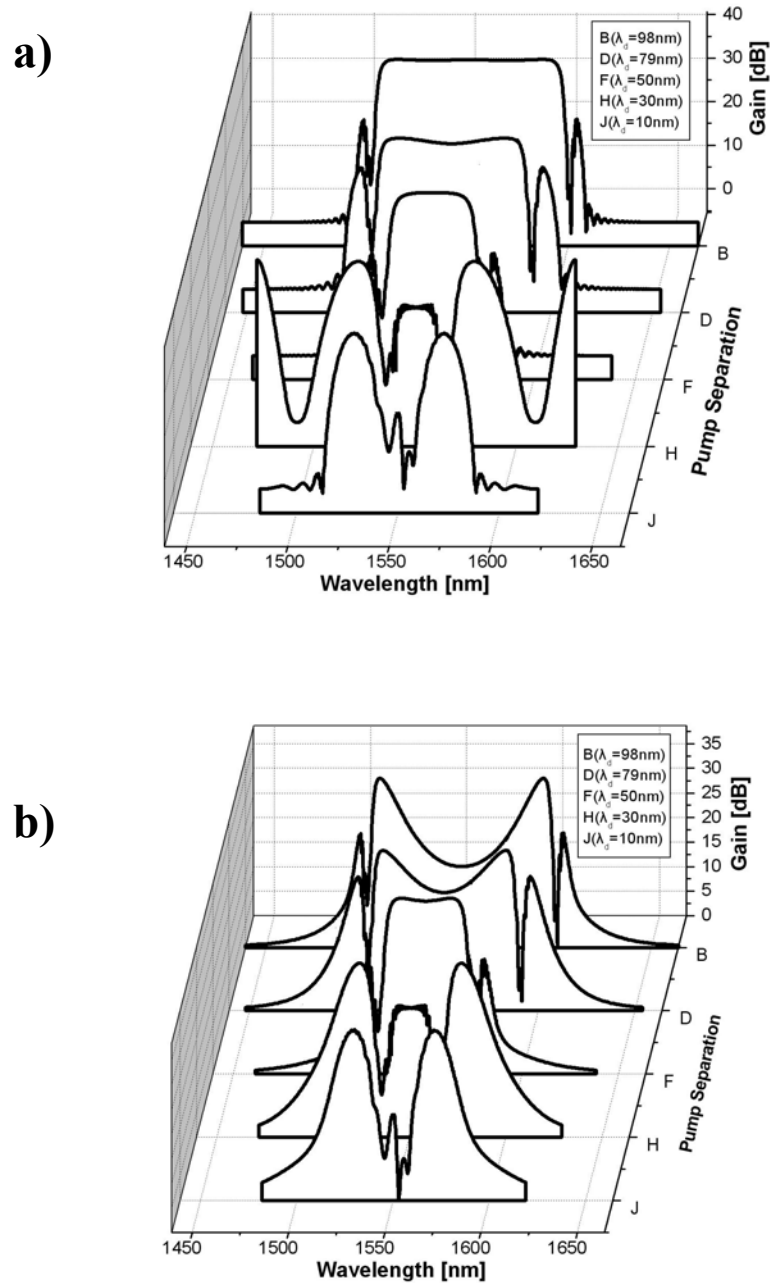


Figure 36 Calculations of gain profiles for different pump separations without (top plot) and with (bottom plot) dispersion fluctuations using four-band model. Reducing pump separations mitigates the impact of dispersion fluctuation in the inner band region. Calculations were performed assuming the following parameters: $\lambda_{sd} = 1\text{ nm}$, $l_c = 5\text{ m}$, $L = 500\text{ m}$, $\beta_3 = 0.1\text{ ps}^3/\text{km}$, $\beta_4 = 10^{-4}\text{ ps}^4/\text{km}$; $\gamma = 10/\text{km/W}$, and $P_1 = P_2 = 0.5\text{ W}$.

The afore-mentioned observations could be verified experimentally. Three HNLF coils that originated from the same draw process were investigated: a single 500-meter, and two 1000-meter coils, referred to as coil A and coil B in the following discussion. All three coils have nearly identical *average* ZDWL measured at 1583nm and *average* dispersion slope of 0.02ps/nm²/km. We emphasize that the average ZDWL value was obtained using a conventional method possessing limited spatial resolution (~100m) and accuracy in measuring very low dispersion values⁸⁹. The parametric experimental setup used is identical to the configuration previously reported⁷². The pump wavelength was centered near ZDWL (1583nm) in the anomalous dispersion region. Probe (signal) was inserted to measure and calibrate four-band response, generating three idlers, as illustrated in Figure 37. In accordance to model expectations, measured gain spectra becomes more equalized with closer pump spacing. An optimal pump spacing (in terms of gain flatness) was measured at 1569.00nm and 1597.0nm, for normal- and anomalous-regime pump wave, respectively. Excessive reduction in pump separation reduces PC-dominated region, allowing the modulation instability to develop non-uniformity within the inner band gain spectrum as well as developing higher order four-wave mixing tones. Throughout the experiments, no distant-band spectral features were observed. The same phenomenon was observed for the other two coils (not shown here).

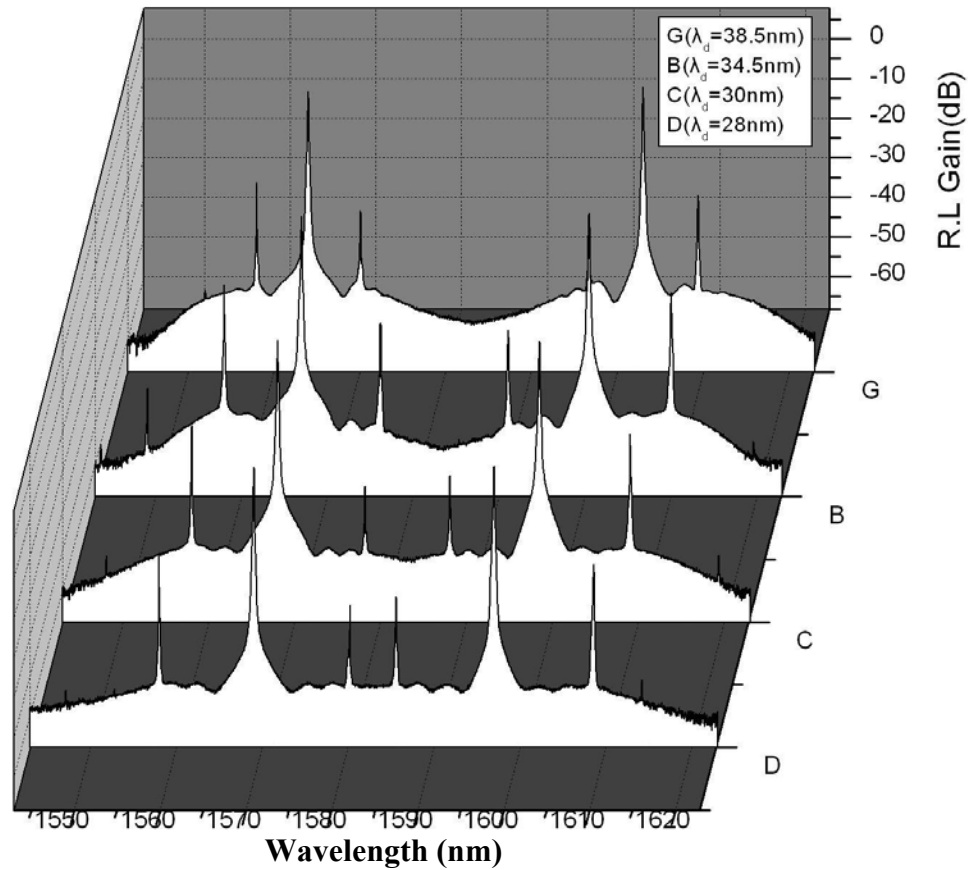


Figure 37 Experimental results of the gain profile of two pump parametric process with different pump separations. Signal and idlers are shown to illustrate four-sideband nature of the two-pump interactions. It is demonstrated that reducing pump separations does flatten out the gain spectrum in the inner band region. Experimental condition: C band pump: $\lambda_c=1569\text{nm}$, $P_1=0.5\text{W}$, L band pump: $\lambda_L=1597\text{nm}$, $P_2=0.5\text{W}$; Fiber length $L=500\text{m}$; average ZDWL $\lambda_0=1583\text{nm}$; average dispersion slope $S=0.02\text{ps/nm}^2/\text{km}$.

As an important practical implication, the four-sideband analytic model can be used to estimate the dispersion fluctuation in a given HNL fiber, thus providing a critical tool in selecting high-performance HNL fiber spools. Figure 38 shows the gain spectra for all three fibers for pumps positioned at 1569.0 nm and 1597.0 nm. The 500 m coil exhibited

the most uniform gain spectrum of the three coils under investigation. In addition, the gain spectrum corresponding to the coil B is considerably more uniform than that of the coil A, implying the smaller magnitude of dispersion fluctuations.

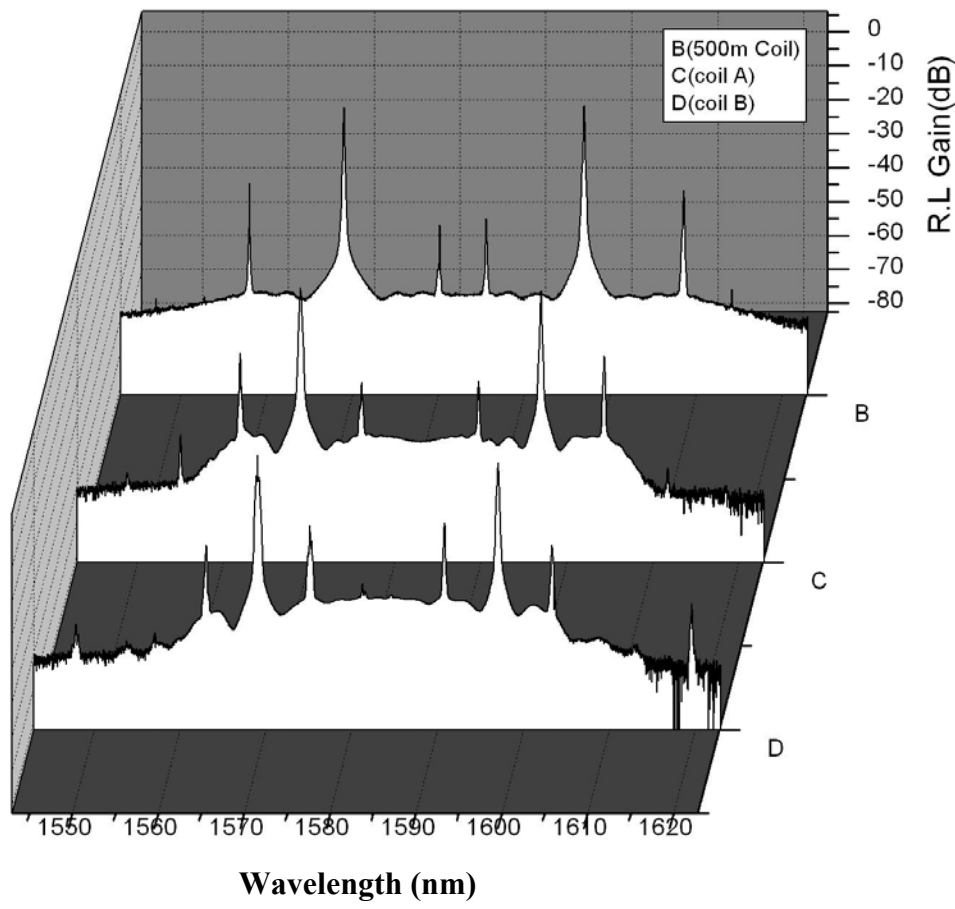


Figure 38. Experimentally measured gain profiles of the two-pump parametric process with the equal pump positions and input power. Results are shown for 3 different HNL fiber coils drawn from the same process. B is the result for a 500m coil, whereas plots C and D correspond to coils A and B in the text, both with length of 1000m. The 500m coil is the best in terms of dispersion fluctuation.

In conclusion, we have discussed the impact of dispersion fluctuation in two-pump driven parametric processes. An analytical, four-sideband parametric model incorporating all FPM processes and across four frequency bands in a two-pump parametric interaction has been derived. The stochastic model includes realistic fluctuations within the nonlinear waveguide. A numerical model that could account for a generally more complicated situation has been developed as well, which is potentially useful for synthesizing parametric performance. Both models predict that a proper pump separation can greatly mitigate the impact of the dispersion-fluctuation-induced gain non-uniformities for two pump schemes. In contrast to previously reported two-sideband model, we were able to predict an accurate parametric gain in vicinity of pumps and within the outer parametric bands. The experimental findings are in an excellent qualitative agreement with the predictions of the newly developed model.

2.6 Practical implementation of two-pump interaction:40Gb/s switching

Two-pump parametric (TPP) scheme can be used for numerous applications; here we illustrate its versatility by constructing ultrafast optical switch. The mechanism for two-pump parametric switching is illustrated in Figure 39. Since the C-band pump is placed at the normal dispersion regime, parametric response for this pump is negligible if L-band is not present. On the other hand, as the L-band is turned on, the two pumps couple through parametric process and results in wideband, large parametric gain. Therefore, turning the L-band pump on-and-off will switch the parametric gain on-and-

off. Since the parametric response is ultrafast, High-confinement fiber potentially allows for terabits/second switching rates, bit-level manipulation is ultimately limited by the speed of pump control which needs to be comparable to input data rates.

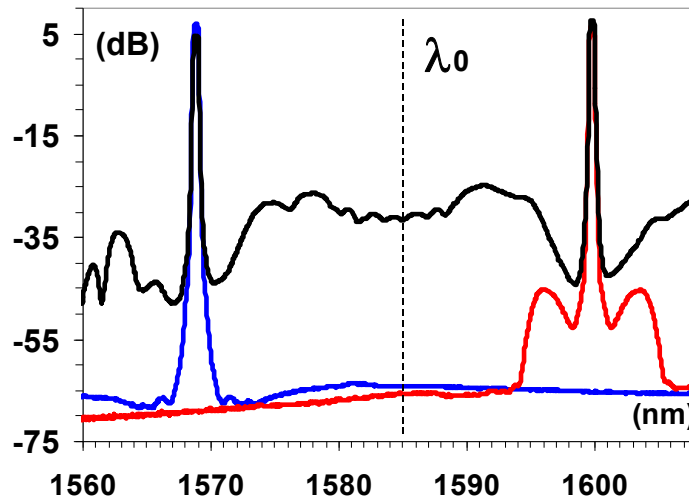


Figure 39 Optical switching of the two-pump parametric gain by switching the L-band pump on and off.

This section demonstrates, for the first time to our knowledge, multiple-band 40-Gb/s switching with a conversion efficiency of at least 21.2 dB and an extinction ratio exceeding 25.0 dB. The two-pump parametric configuration was used to achieve multicasting and 40-Gb/s bit-level signal processing within four operational bands. More importantly, the feasibility of subrate pump control was demonstrated for OC-768 signal processing.

Our two-pump experimental setup is shown in Figure 40. Two continuous-wave (CW) tunable lasers ($\lambda_1=1568.5\text{nm}$; $\lambda_2=1598.0\text{ nm}$) served as the pump seeds, and were amplified and filtered by two 0.25-nm filters (TF1 and TF2) to reduce the amplified

spontaneous emission (ASE) prior to the booster amplifier. The anomalous pump was controlled using a programmed nonreturn-to-zero (NRZ) bit sequence in both packet and bit-level switching experiments. A tunable optical delay line was used to adjust the relative delay between the pump and the signal. The two pumps were counterphased using a 5-Gb/s pseudorandom bit sequence to suppress stimulated Brillouin scattering generated inside both the booster amplifier [erbium-doped fiber amplifier (EDFA)] and the highly nonlinear fiber (HNLF). The EDFA booster provided an average output power of 2.3 W, measured prior to the ASE-filtering section (dashed box in Figure 40). The booster ASE was filtered out using two 1-nm tunable filters (TF3 and TF4) in order to guarantee pump spectral purity⁴² greater than 75 dB (measured within 0.2-nm bandwidth). A third tunable CW laser served as the signal. It was modulated using a 40-Gb/s NRZ pattern and was inserted into the HNLF through a 10/90 coupler. PC7, PC8, and PC9 were all adjusted to achieve a copolarized SOP for the pumps and the signal inside HNLF. The 520-m HNLF used in the experiments had an effective area of 11 μm^2 , a dispersion slope of 0.025 ps nm km⁻¹, and a zero-dispersion wavelength of 1582 nm. The four sidebands were individually selected using a 2-nm-wide optical filter (TF5) and observed using a fast oscilloscope (37-GHz response).

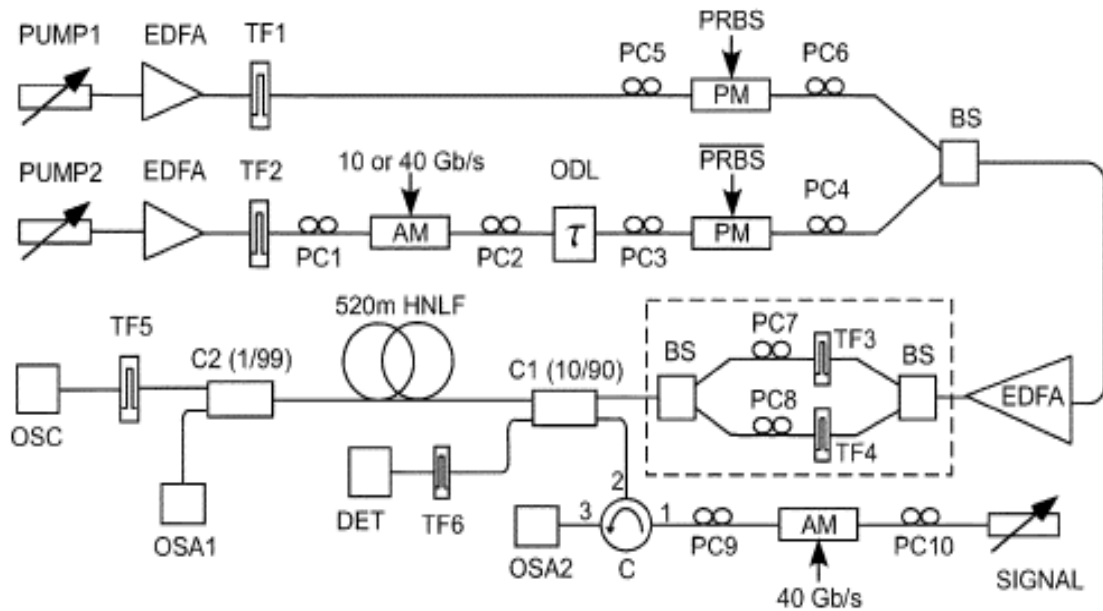


Figure 40 Experimental setup. TF: tunable filter. PM: phase modulator. AM: amplitude modulator. PC: polarization controller. ODL: optical delay line. OSA: optical spectrum analyzer.

OSC: oscilloscope. BS: band splitter. C1: 10/90 coupler. C2: 1/99 coupler. C: circulator. DET: detector; it can be either an OSA, an OSC, or a power meter used for characterizing the input signal, C- or L-band pump. OSA2 is used for monitoring Brillouin scattering of the pumps.

As a first goal of this study, we investigated the performance of arbitrary-bit-sequence (packet) extraction from the input OC-768 stream. Unlike the previously reported result³⁹, the switching of the OC-768 sequence required precise control beyond that of the OC-192 rate. Indeed, while the length of the switched sequence (1000 ps, see experiments below) allows for slow pump control, extraction with zero guardband does require speed comparable to the input data rate (OC-768) or faster. However, parametric generation inside an HNLF helps to reduce significantly such requirement on the pumps because the output signal/idler powers are related to the pumps by an exponential gain function. For simplicity, if the parametric process is assumed to be dominated by a single

phase-matched FPM process, the true switching rise–fall time is determined by the parametric response as $\tau_{\text{eff}} = \tau_{\text{pump}} / \sqrt{G}$, where τ_{pump} represents the effective pump power, defined as $P_{\text{eff}} = P_{\text{pump1}} + P_{\text{pump2}}$ for the nondegenerate (two-pump) interaction and $P_{\text{eff}} = P_{\text{pump}}$ for the degenerate (one-pump) interaction; L is the HNLF length and $\chi^{(3)}$ is the nonlinear parameter. For a parametric gain of 20–30 dB, this formula yields a parametric response two to four times faster than the corresponding pump rise–fall time.

In general, the single-pump configuration exhibits faster response⁹⁰. However, dual-pumping provides more functional sidebands and, thus, enables wavelength multicasting. The parametric rise–fall time associated with 10-Gb/s pump control (25 ps rise–fall time) was indistinguishable from that of the 40-Gb/s sequence in practice. This indicates that 10-Gb/s pump control could be effectively used to achieve the practical packet switching at OC-768 rates. Consequently, it allowed a control of the anomalous pump by a 10-Gb/s, rather than a 40-Gb/s, programmed sequence.

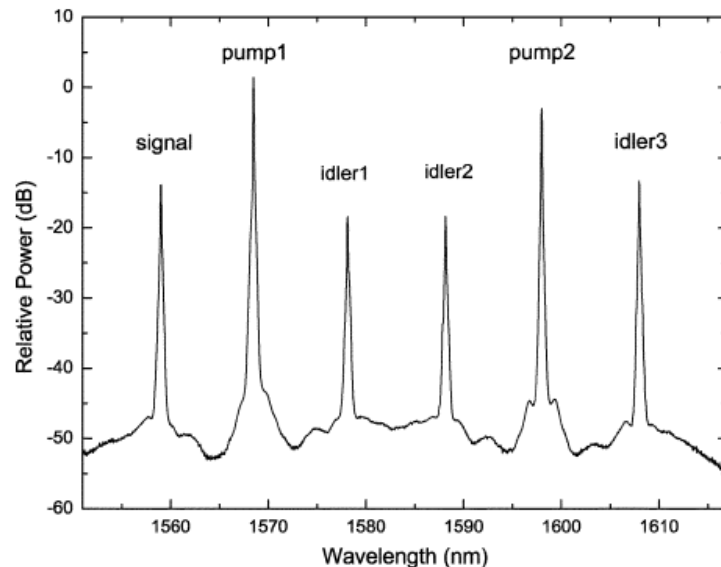


Figure 41 Optical spectrum measured at the output of HNLF, recorded with 0.2-nm resolution when a 1559-nm signal is launched. Other details are given in the text.

To demonstrate OC-768 packet switching, the long-wavelength pump was modulated using a 1-ns-long rectangular pulse (composed of ten successive logical ones at 10 Gb/s, corresponding to 40 bits at 40 Gb/s) in order to extract a selected sequence from the data stream of the small input signal ($P_{in}=-14\text{dBm}$). The average pump powers launched into the HNLF were 545 and 155 mW for the normal (L-band) and anomalous (S-band) pumps, respectively. The TPP spectrum is shown in Figure 41, illustrating three new switched wavelengths at 1578.1, 1588.1, and 1608.0 nm. The input signal at 1559.0 nm is simultaneously amplified by 25.2 dB (“ON–OFF” value, measured at the HNLF output) and multicasted with conversion efficiencies of 21.2, 21.4, and 25.9 dB, respectively, covering a spectral range of 49 nm. The corresponding 0.2-nm optical signal-to-noise ratios were measured to be 33.6 dB (1559.0 nm), 28.5 dB (1578.1 nm), 28.9 dB (1588.1 nm), and 34.8 dB (1608.0 nm). The absence of higher order wave⁹¹ in the vicinity of the switched sidebands confirms the linear TPP operation required for crosstalk-free waveband switching.

The temporal waveforms of the four sidebands and the L-band pump are shown in Figure 42. The input signal had a mark density of 1/2 [Figure 42a], with the extinction ratio limited by the electronic driver used for the 40-GHz AM modulator. Figure 42b shows the square waveform imposed on anomalous pump used for OC-768 sequence extraction. Switched packets were obtained from all four parametric bands. That at the signal wavelength (1559.0 nm) is shown in Figure 42c, and the corresponding idler packets at 1578.1, 1588.1, and 1608.0 nm are shown in Figure 42 (d)–(f), respectively. Switched packet traces were recorded by a simple tuning of the output (TF5) filter, since high power (5 dBm) in any of the four streams eliminated the need for post-

amplification. The switching is realized with low noise and high extinction ratio: No artifacts were observed in the immediate vicinity outside the switched window [indicated by an arrow in Figure 42c], in spite of the dense bit content carried by the input signal in this region. The higher noise levels seen with innerband packets (1578.1 and 1588.1 nm) are attributed to lower conversion efficiencies and the fixed input level used with the oscilloscope; no attempt was made to adjust the power levels to reduce the receiver noise. Physically, a high extinction ratio stems from the exponential dependence of the parametric gain on the pump powers. For example, in the phase-matched region, the parametric gain (in decibels) produced via nondegenerate FPM scales with pump powers as $\sqrt{P_1 P_2}$. In contrast, neither is the signal amplified nor are the idlers created in the absence of -band pump, since the -band CW pump located in the normal-dispersion region produces negligible FPM. Clearly, high parametric gain guarantees switching with high extinction ratios in all four sidebands.

The TPP process allows for arbitrarily long packets to be switched simply by varying the time interval in which both pumps are simultaneously present. More importantly, the effective compression of rise–fall time allows the use of slow pump control to achieve precise bit control. Indeed, the pump rise–fall time of 25 ps in this experiment was sufficient to achieve zero guardband packet switching. To demonstrate this capability, the anomalous pump switching window was shifted to cover the selected “1” bit, as indicated by Arrow 1 in Figure 42a. The switched packet is shown in Figure 43: It can be seen clearly that the selected “1” was switched in, with the preceding bits eliminated completely. At the same time, the last bit in the sequence, “1” indicated by

Arrow 2, was steeply carved out from the successive logical ones. Clearly, the instantaneous parametric response of FWM dramatically reduces the requirement of the

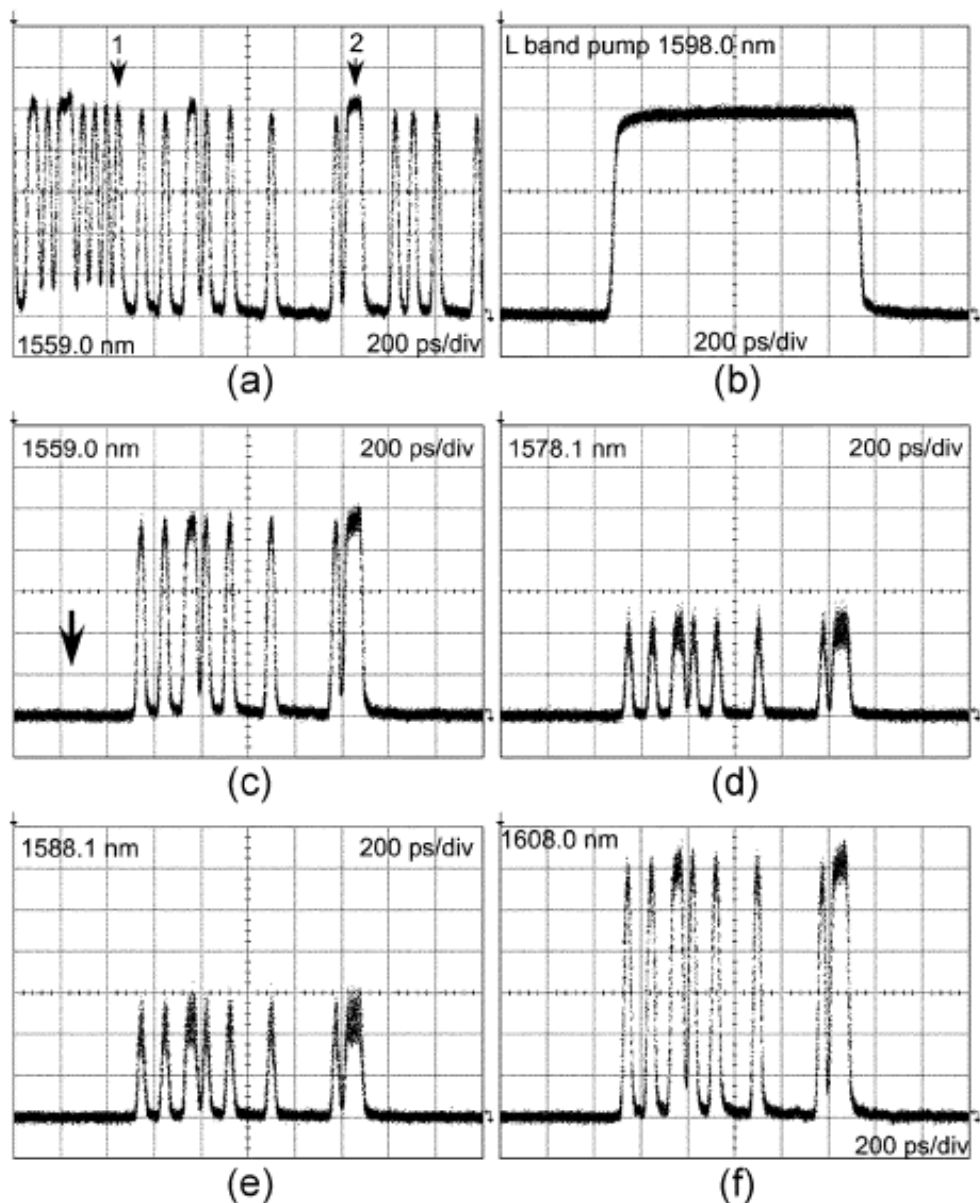


Figure 42 Temporal waveforms showing packet switching. A fixed input level was used in the oscilloscope for all signal/idlers waves. (a) Input 1559.0-nm signal; (b) L-band pump; (c) amplified signal; (d) switched 1578.1-nm idler; (e) switched 1588.1-nm idler; (f) switched 1608.0-nm idler.

guard time for packet switching⁹² and, thus, would help to increase the efficiency of optical processing schemes required in transparent networks.

As a second goal of this study, we demonstrated optical switching at the bit level. The input signal is modulated with a 40-Gb/s NRZ bit pattern, as shown in Figure 44a (other bit patterns can also be used). The anomalous pump was controlled by an isolated bit, as illustrated in Figure 44b. The pump was used to select the bits of a logical “0” and a logical “1” from the input sequence, as indicated by arrows in Figure 44a. High extinction ratio is demonstrated by comparing the contrast between switched “0” [inset in Figure 44c] and switched “1” [Figure 44c]. When the selected bit represents a high logical level, the signal is simultaneously amplified and replicated to three idler waves. Bit-level wavelength casting at 40 Gb/s is illustrated in Figure 44d, corresponding to translation of the selected bit “1” in the sequence to the outer parametric band (1559 →1608 nm).

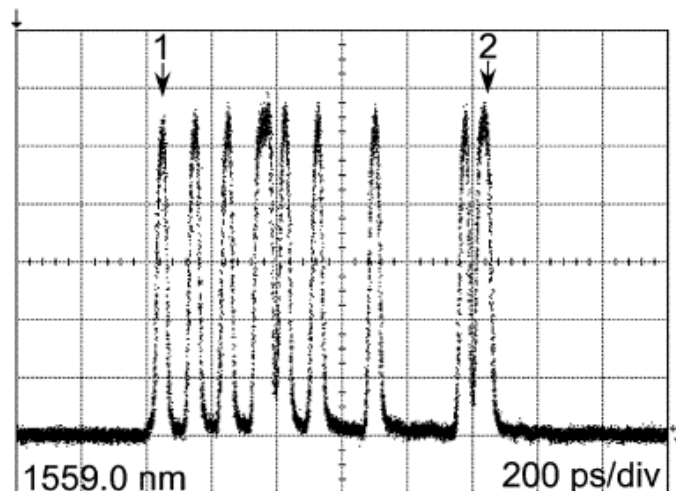


Figure 43 Amplified 1-ns packet of the 1559.0-nm signal when the L-band pump is temporally shifted in such a way that its leading edge coincides with the signal bit marked by arrow 1 in Figure 42a.

Similar switched bits (with smaller amplitudes) were obtained for the two inner bands. The switched bits had full-widths at half-maximum of 20 ps (1559.0 nm), 17 ps (1578.1 nm), 16 ps (1588.1 nm), and 20 ps (1608.0 nm), clearly indicating compression with respect to the original bits in the input sequence. The two inner bands had higher compression ratios, as expected by the different contributions of degenerate and nondegenerate FPM. Such pulse compression can be used to reshape the switched pulse and provide an efficient way for signal regeneration within the routing node itself.

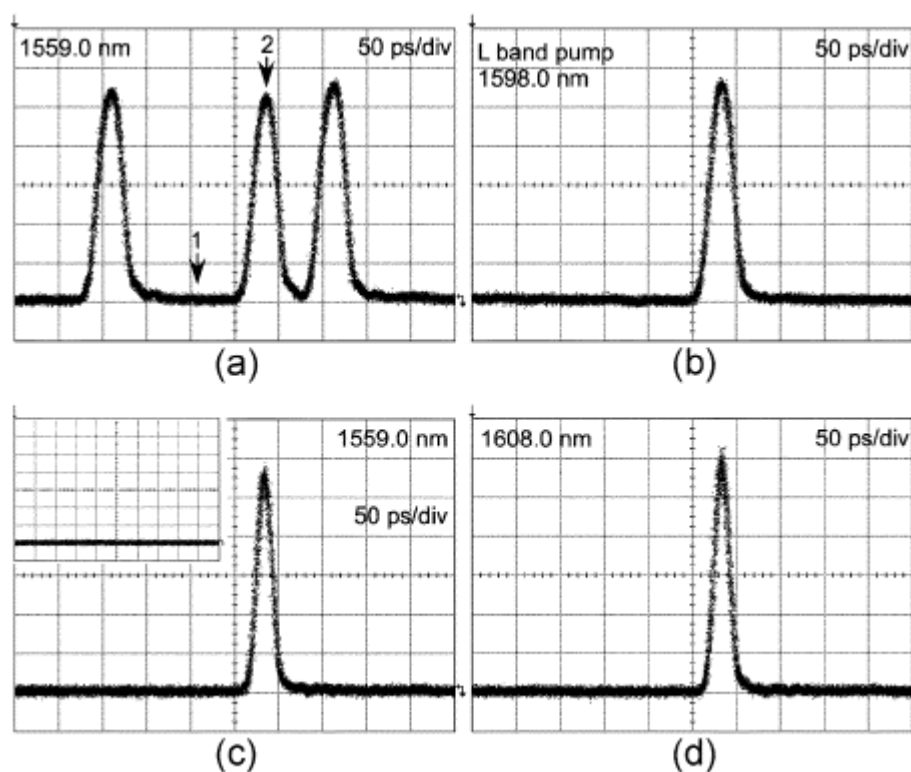


Figure 44 Temporal waveforms showing bit-level switching. (a) Input 1559.0-nm signal; (b) L-band pump; (c) amplified signal bit when the pump bit is located at Position 2. The inset shows the signal waveform when the pump bit is located at Position 1. (d) Switched bit for the outer-band idler at 1608.0 nm.

In conclusion, we have demonstrated optical switching with wavelength conversion at 40 Gb/s by using a TPP architecture. The scheme realizes packet switching for arbitrary packet lengths with negligible guard-time requirements and subrate pump controls. The experiment validated TPP performance that was sufficient to switch individual bits at 40 Gb/s, while maintaining high extinction ratios and conversion efficiencies above 20 dB. We note that the architecture also possesses an inherent ability to selectively conjugate a switched packet or bit sequence, thereby enabling the possibility for applications involving simultaneous high-speed switching and transmission-impairment mitigation.

Chapter 3 Photonic Crystal Fiber as Parametric Platform

3.1 Introduction

Photonic crystal fiber (PCF), distinguished from HNLF by the transverse microstructure, is probably one of the most important inventions in fiber optics during the past decade^{57, 93, 94}. PCF manufacturing technology, even though still under improvement, has been mature enough to enable commercial products at present time⁹⁵. The state-of-the-art techniques allow for manufacturing the microstructure in air-glass PCF to the accuracy of 10nm on a 1 μ m scale^{96, 97}. PCF has received remarkable attention because of its enormous control freedom on optical properties such as waveguiding⁹⁸, birefringence^{99, 100}, dispersion^{98, 101, 102, 103}, and nonlinearity^{104, 105}. The silica PCF platform has reached maturity, with significant progress made in understanding its nonlinear behavior such as nonlinear enhancement supporting four-photon mixing (FPM)^{106, 107}, self- and cross-phase modulation (SPM/CPM)¹⁰⁸ and supercontinuum generation¹⁰⁹. In variety of reports, the term ‘PCF’ includes both hollow-core photonic bandgap fiber (PBG) and solid-core photonic crystal fiber. In this thesis, we refer only to the latter type as PCF.

The idea of PCF was motivated by the limit of step-index Single Mode fibers (SMF). Regular SMF has a core-cladding refractive index $\Delta \sim 0.4\%$ ³⁴ and a core diameter of about 4-5 μ m. Designed for long-haul transmission link, SMF has several severe drawbacks in specialized applications. Firstly, the small index difference results in weak

guiding in the core¹¹⁰ and suffers severe loss when the fiber is bended to large curvature, preventing all-fiber integration. Secondly, the small index difference leaves limited room for fiber dispersion engineering⁸. Regular SMF is not suitable for a nonlinear application unless a long fiber spool is used - the weak Kerr effect and large core size results in small nonlinear coefficient. Lastly, the single-mode guiding wavelength region is limited in SMF. When the optical wavelength scales down from the designed operation wavelength, it will be transition to high order modes³⁴, preventing efficient distant-band optical mixing experiments. HNLF increases effective nonlinearity by decreasing the fiber core diameter to $\sim 2\mu\text{m}$ ³⁶.

PCF addresses these limitations: The index contrast can be maximized because the air-hole interface has the minimal refractive index (1). At the same time, the transverse structure provides enhanced single-mode guiding region^{111, 112, 113} and considerable freedom for dispersion design,^{104, 114}. The effective nonlinear coefficient can also be enhanced by 50 times with respect to SMF, and 5-10 times to that of a regular HNLF. We will discuss these properties in detail in the following sections.

PCF can guide optical waves in single mode across a wide spectral range. When designed properly, it can even guide across the whole optical spectrum in single mode - a so-called endlessly single-mode guiding state¹¹⁴. A first look-at the periodic structure of a PCF might imply that PCF guides light via a band-gap effect. A PCF actually guides light through total-internal-reflection¹¹², a similar mechanism as in a SMF fiber. Keeping in mind that the PCF cladding structure could potentially act as a waveguide, the guiding property of a PCF could then be understood in simple intuitive terms: optical wave within the core, experience an effective cladding layer whose refractive index depends on the

propagation property of the same optical wave in the cladding structure; to be more specific, the effective cladding index equals the effective index of the lowest guiding mode in the cladding – termed fundamental space filling mode (FSM)^{115, 116}. The FSM

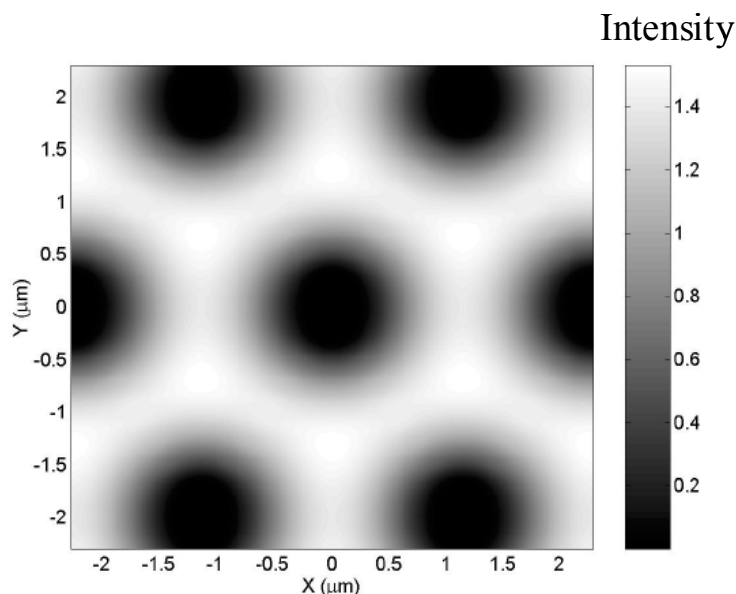


Figure 45 Fundamental space filling mode of a PCF cladding structure.

of a typical PCF cladding structure is shown in Figure 45, with the intensity peaked at the interconnections of the glass wire and a small part penetrates and decay to 0 in the air holes. The short wavelengths are well confined in the glass area while the long wavelengths tend to extend into the air holes. The effective cladding index (that is, the effective index of the FSM) is smaller than the core index and therefore the optical waves could be guided through total internal reflection once the incident angle is larger than the critical angle. Unlike in SMF, the effective cladding index is not constant but depends on the optical wavelength. Therefore, PCF could be viewed as an equivalent step-index structure whose cladding index is adaptive to the incident optical waves. For example, when the wavelength is short, the cladding effective is large because the FSM is well

guided in the glass region and the index contrast between the core and cladding is small, resulting in a weak guiding. On the other hand, when a long wavelength propagates in the PCF, the effective cladding index is smaller because the FSM now ‘sees’ a smeared glass-air region and the index contrast between the core and cladding is larger, leading to a strong waveguiding. Therefore, when the PCF parameters are chosen properly, optical waves could be guided in single mode at all wavelengths – an important property that distinguishes PCF from SMF or HNLF and has been experimentally verified.

High nonlinearity of PCF is easily understood by looking at the nonlinear coefficient²⁶

$$\gamma = \frac{n_2 \omega}{c A_{eff}} \quad (49)$$

where n_2 is the nonlinear refractive index, ω is the angular frequency of the optical wave, c is the speed of light and A_{eff} stands for the guiding mode area. It is easy to see that by scaling down the guiding mode area, one can achieve higher effective nonlinearity. Indeed, PCF core could be scaled down to $\sim 1\mu\text{m}$ diameter and results in a γ value as large as $100\text{W}^{-1}\text{km}^{-1}$ within target spectral range.

PCF is also recognized for its dispersion engineering capability, which is attributed to the strong waveguide dispersion in PCF⁹⁸. That is, the waveguide dispersion in PCF is so strong that altering waveguide dispersion will significantly change the overall dispersion; while in SMF or HNLF, the total dispersion is dominated by material dispersion and dispersion engineering many times has to resort to doping technique, which is much more complicated and costly. Engineering waveguide dispersion is done

through fine tuning the period and air-filling ratio (defined later in this section) of a PCF structure.

In this chapter, we outline modeling of the specialized PCF, with particular interests in the guiding property and dispersion calculation. In chapter 5, we design fiber structures relevant to proper dispersion profiles that are able to phase-match the target parametric processes, using the tools/models developed in this chapter. Three models, namely, the effective index model (EIM), the scalar two-dimensional (2-D) Fourier analysis (FA) and full-vector beam propagation method (BPM), will be discussed in detail. Accuracy and the computational time will serve as major considerations. In comparison, EIM model is fast, but is only a rough model that gives less accurate results. The FA is accurate since it takes into account the true PCF transverse structure. However, FA method calculates not only the fundamental mode in the core, but also all the transverse modes - including the cladding modes, resulting in significant computation error. This might be undesirable since not all the modes are of interests - most of the transverse modes are lossy and thus do not propagate in the fiber. The full vector BPM method, on the other hand, simulates the physical process of a wave propagating in a fiber or waveguide and consumes moderate computational time. In this thesis, EIM and BPM are the mostly used two methods: EIM is generally used for qualitative estimation and fast searching and scanning of PCF structures while BPM is applied when an accurate dispersion profile is required.

Before getting into detailed calculations, we shall define the PCF structure to avoid any ambiguity. In this chapter, we only discuss the symmetric transverse structure,

which could be solely defined by two parameters, that is, the period or pitch (Λ) size and air-filling ratio (d/Λ), showing in Figure 46

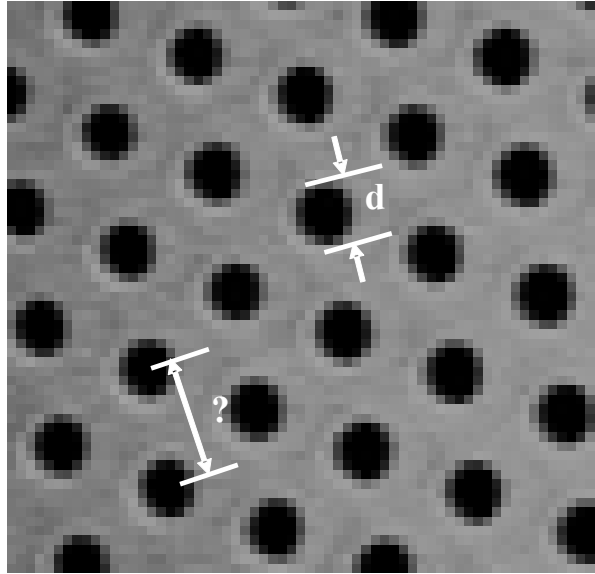


Figure 46 Illustration of typical PCF parameters. Λ , being the distance between the air holes is usually called period or pitch, and d is the diameter of the air holes.

Asymmetric structure that could result in shape-induced birefringence will be dealt with in the next two chapters. Furthermore, the PCFs in our discussion, intended for distant-band parametric process, generally have a core diameter between 1-2 μm , resulting in high nonlinearity, and air-filling ratio between 0.4 and 0.6 - higher air-filling ratio (>0.6) can potentially lead to multi-mode guiding at short wavelength, which is undesirable; On the other hand, a small air-filling ratio (<0.4) does not provide enough waveguide dispersion. A typical PCF in this work has a cross-section shown in Figure 47.

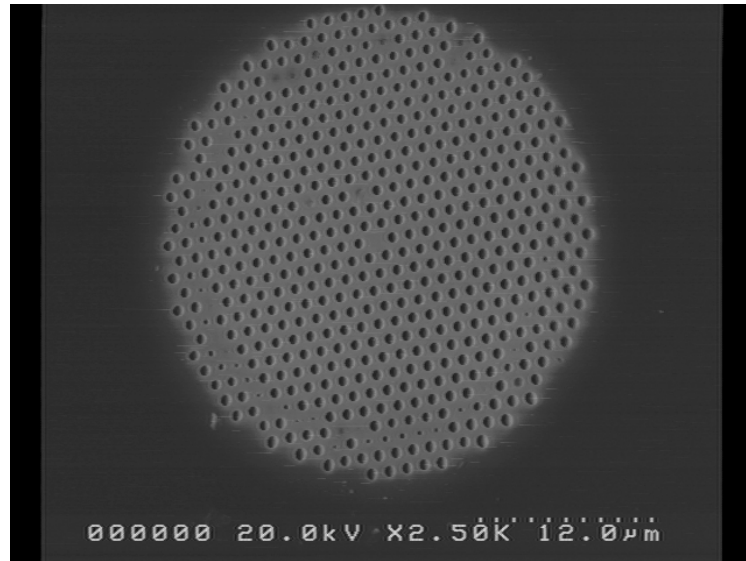
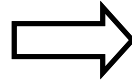
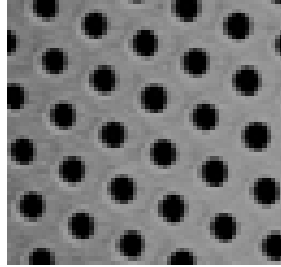


Figure 47 SEM scanning picture of a PCF structure with period $\Lambda=1.2\mu\text{m}$ and $d/\Lambda=0.6$.

3.2 Effective Index Model

EIM model is identified as the simplest PCF modeling technique^{114, 117}. However it is not accurate enough for precise PCF modeling in general case. Nevertheless, it is the most intuitive model that relates the guiding nature of a PCF and is very illustrative for understating PCF properties. The EIM model effectively approximates a PCF having complicated transverse structure with a step-index fiber, in which a strand of silica core is surrounded by a uniform cladding . In this approximation, the cladding's index is the effective index of the FSM of the periodic PCF cladding, which depends on the operating wavelength.

Step 1: solving for effective cladding index n_{eff}



Step 2: solving for the guiding mode

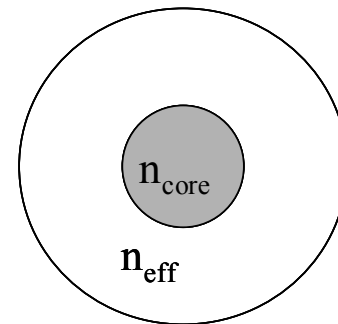


Figure 48 Two steps for modeling a PCF with EIM: a) Acquiring the effective cladding index n_{eff} by solving the FSM of the periodic cladding structure; b) The PCF is simplified to an equivalent step-index whose cladding index equals n_{eff} . n_{eff} is a function of λ .

The methodology of EIM model is illustrated in Figure 48. Mathematical tools for calculating the effective cladding index have been well developed in previous work^{116, 117}. The PCF with primitive triangular pattern could be divided into infinite numbers of the following hexagon unit cells shown in Figure 49. The characteristic equation for the FSM is as follows¹¹⁶:

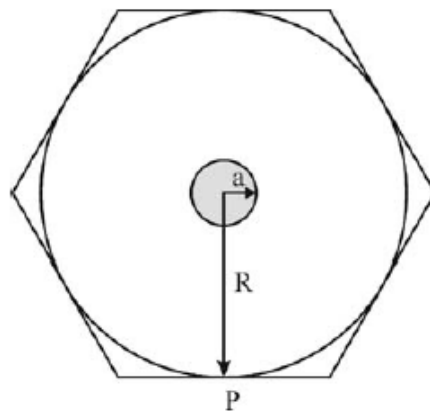


Figure 49 Equivalent circular unit cell of a hexagonal one for a PCF

$$w \frac{I_1(wa)}{I_0(wa)} [J_0(ua) - Y_0(ua) \frac{J_1(uR)}{Y_1(uR)}] = -u [J_1(ua) - Y_1(ua) \frac{J_1(uR)}{Y_1(uR)}] \quad (50)$$

where $u^2 = n_{silica}^2 k^2 - \beta^2$, $w^2 = \beta^2 - n_{air}^2 k^2$, $a = d/2$ is the air hole radius, R is the radius of the equivalent circular unit cell, I_l is the modified Bessel function of the first kind of order l , and J_l and Y_l are Bessel functions of the first kind and second kind of order l , respectively.

The boundary condition is $\left. \frac{\partial \varphi}{\partial r} \right|_{r=R} = 0$ (ρ is the radial component in cylindrical coordinates), which is based on the fact that the field φ is symmetric at point P on the circle, and that the field and its derivation are continuous on the air-silica border.

Li¹¹⁸ has compared the scalar analytical approach with the plane wave method and found good match when the radius of the equivalent circular cell is properly chosen. Analytical solution for the step-index model has been well developed and can be found in past work⁴

An important use of EIM is to predict the guiding property of a PCF. It is easy to come to the conclusion that for an effective guided wave, the following criteria has to be satisfied:

$$\beta_{FSM} < \beta_{eff} < nk_0 \quad (51)$$

where β_{FSM} is the propagation constant of the cladding FSM mode, β_{eff} is the effective propagation constant of a guided core mode while n denotes the core index and

k_0 stands for the vacuum wavevector. The maximum transverse wavevector of a guided mode has to satisfy:

$$k_{j,\max} = \sqrt{(nk_0)^2 - \beta_{FSM}^2} / 2 \quad (j = x, y) \quad (52)$$

Assuming the core diameter is ρ , the smallest transverse mode separation in k -space is $1/\rho$. Considering equation (52), the total number of modes that could be guided in a PCF is determined by¹¹⁴

$$\begin{aligned} V_{\text{eff}} &= \frac{k_{\max}}{1/\rho} = \rho \sqrt{(nk_0)^2 - \beta_{FSM}^2} / 2 \\ &= \frac{\pi\rho}{\lambda} \sqrt{n^2 - n_{\text{cl}}^2} \end{aligned} \quad (53)$$

where n_{cl} is the effective cladding index. We note that equation (53) defined a V_{eff} parameter that has the same form as the V number of a step-index fiber and could be used to quantify the number of guiding modes in PCF – the single-mode guiding criterion is $V_{\text{eff}} < 2.405$.

There are some well developed shortcuts in applying the EIM to specific geometry analysis. EIM does not model the true transverse structure; therefore, the core size that gives the best result in EIM is not necessarily the boundary of the first ring layers Λ . In the calculation process, the core size is usually finely tuned to match the true dispersion profile of a PCF (sometime even the air-filling ratio is also finely tuned). In other words, for EIM to have good results, a guess close to the correct solution has to be stated. One can also see a paradox here: it is not possible to obtain the accurate result without knowing the true PCF behavior; however, if one has already obtained the reference, why use the EIM model? Indeed, an EIM model was never utilized for

accurate modeling of a PCF, but only for qualitative verification of a PCF's guiding and dispersive properties. However, one should not underestimate the importance of the EIM because it provides physical insight into the PCF property, as we have seen in understanding the endless guiding behavior and will further see in understanding the dispersion property in PCF.

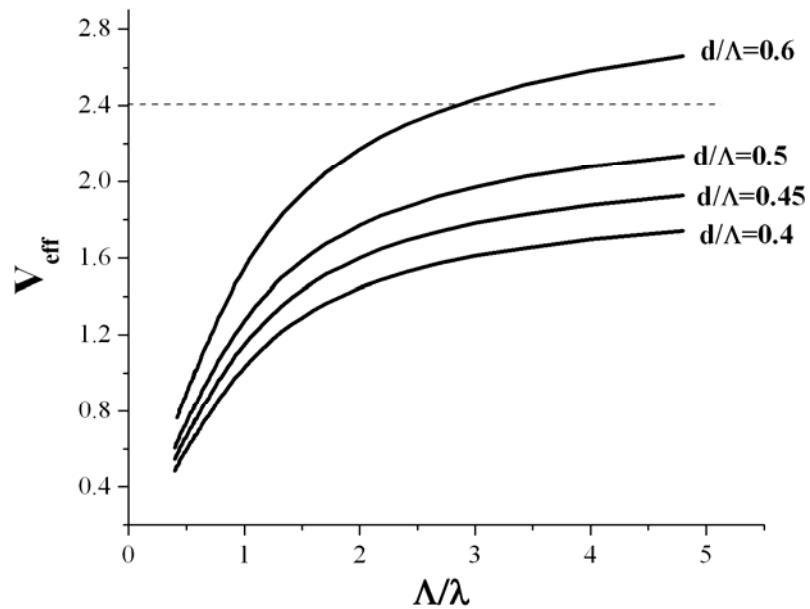


Figure 50 Guiding properties of several PCF structures. V_{eff} curve versus the normalized frequency were calculated.

We calculate a set of V_{eff} versus Λ/λ curves for the PCF structures with $\Lambda=1.2\mu\text{m}$ and various air-filling ratios. The results are shown in Figure 50. The dash line in figure shows the border of the single-mode guiding region. For the optical spectrum we are interested in (visible to NIR), all the structures with $d/\Lambda < 0.5$ guide light in single mode; however, for $d/\Lambda=0.6$ structure, part of the visible spectrum can guide high-order modes,

which agrees with the experimental measurements, detailed in Chapter 4. EIM has also been used to estimate the dispersion property of a PCF structure¹¹⁸. In Figure 51, we show three sets of calculations in which d/Λ is fixed at 0.55 while Λ varies from 1.1 to 1.3 μm . EIM predictions are compared against the MIT photonic band (MPB) model¹²⁶, a widely accepted computational package for nano-structure modeling, under different conditions. EIM model gives reasonable approximations to the true dispersion profile.

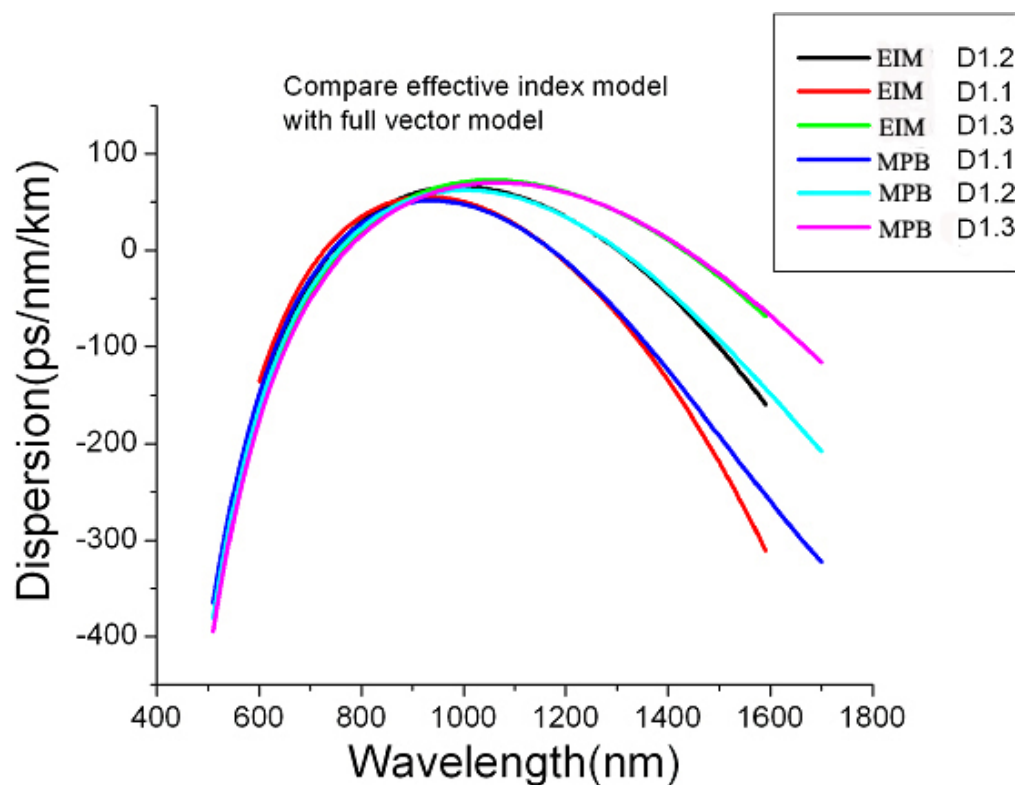


Figure 51 Comparison of EIM results against the MPB method. EIM results closely resembles the MPB results provided proper effective fiber parameters are chosen. In all calculations, $d/\Lambda=0.55$ while period varies from 1.1 μm to 1.3 μm .

In all the calculations the material dispersion is accounted for by using a Sellmeier model, which is also conducted in all the thereafter calculations²⁶.

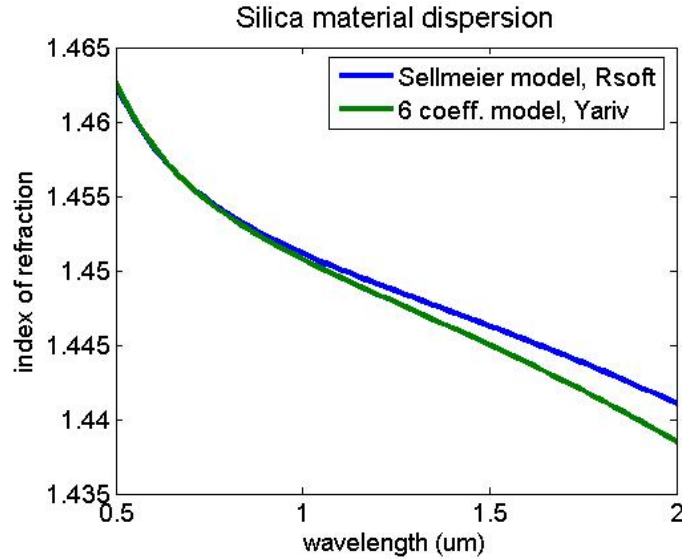


Figure 52 Comparison of Sellmeier's model with the 6 order polynomial model¹¹⁹ accounting for the silica material dispersion

3.3 2-D Fourier Analysis

The nonlinear Schrödinger equation, when arranged with β^2 as eigenvalue, takes the following form⁹⁸:

$$(\nabla^2 + k_0^2 \varepsilon(\vec{r}_T) + [\nabla \ln \varepsilon(\vec{r}_T)] \times \nabla \times) \vec{E}_T = \beta^2 \vec{E}_T \quad (54)$$

where $\vec{E} = \vec{E}_T(r_T) e^{-j\beta z}$, $\varepsilon_T(\vec{r}_T)$ is the dielectric constant, $\vec{r}_T = (x, y)$ is the position in the transverse plane, and $k_0 = \omega/c$ is the vacuum wavevector. Written out explicitly in Cartesian coordinates, (54) yields two equations relating E_x and E_y as follows:

$$\begin{aligned}
\frac{\partial^2 E_x}{\partial y^2} + \frac{\partial^2 E_x}{\partial x^2} - \frac{\partial \ln \varepsilon}{\partial y} \left(\frac{\partial E_x}{\partial y} - \frac{\partial E_y}{\partial x} \right) + (\varepsilon k_0^2 - \beta^2) E_x &= 0 \\
\frac{\partial^2 E_y}{\partial x^2} + \frac{\partial^2 E_y}{\partial y^2} - \frac{\partial \ln \varepsilon}{\partial x} \left(\frac{\partial E_x}{\partial y} - \frac{\partial E_y}{\partial x} \right) + (\varepsilon k_0^2 - \beta^2) E_y &= 0
\end{aligned} \tag{55}$$

and a third differential equation relating magnetic field components H_x , H_y and H_z , which is, however, not required to solve (55).

In the paraxial approximation, the second operator term in (55) coupling between the vector components of the field can be neglected, yielding the following scalar equation:

$$\nabla^2 \vec{E}_T + (k_0^2 \varepsilon(\vec{r}_T) - \beta^2) \vec{E}_T = 0 \tag{56}$$

Unlike EIM model, plane wave method calculates the real PCF transverse structure described by the distributed dielectric constant $\varepsilon_T(\vec{r}_T)$. The FA encloses the whole PCF transverse structure within a rectangular area that is large enough to ensure that the fields of the guided modes of interest are zero at the boundary. The field is then expanded in a double Fourier series in which the sinusoidal basis functions are zero at the boundary. This expansion converts the scalar wave equations into a set of homogeneous linear equations for the Fourier coefficients. The eigenvalues and coefficients of the bound modes are then found by solving the matrix eigenvalue problem.

The mathematical description of the FA is as follows^{120, 121}:

We then expand $E(x, y)$ using basis functions which are products of sine functions with zero at the boundaries $x=0, L_x$, and $y=0, L_y$. The basis function are given by

$$\phi_i(x, y) = \frac{2}{(L_x L_y)^{1/2}} \sin\left(\frac{m\pi x}{L_x}\right) \sin\left(\frac{m\pi y}{L_y}\right) \quad (57)$$

where $m, n = 1, 3, 5, \dots$ are even modes and $m, n = 2, 3, 6, \dots$ are odd modes about the center of selected rectangular region with dimensions L_x and L_y . These basis functions are orthogonal to each other.

$$\langle \phi_i(x, y) \phi_j(x, y) \rangle = \delta_{ij} \quad (58)$$

The bracket here denotes integration over x and y . The field can be expanded as

$$E(x, y) = \sum_j a_j \phi_j(x, y) \quad (59)$$

Substituting $E(x, y)$ into the scalar wave equation (56) and by some mathematical manipulations, one can arrive to matrix equation

$$\sum_j (A_{ij} - k^2 n_{eff}^2 \delta_{ij}) a_j = 0 \quad (60)$$

where

$$A_{ij} = (K_x^2 + K_y^2) \delta_{ij} + k^2 \langle \phi_i(x, y) n(x, y)^2 \phi_j(x, y) \rangle \quad (61)$$

One can use other functions, for example Bessel functions, as the basis functions, but this will not change the form of the final eigenvalue equation. The accuracy of this method obviously depends on the grid numbers on the transverse plane and the number of basis functions that determines the resolution of this method. Increasing both numbers

will surely increase the modeling accuracy, but also will increase the computational time. We used FA method to calculate the mode field diameter (MFD) and compared to the experimentally measured results and found a good match. In Figure 53, the MFD of 530nm and 1550nm waves are shown. In this calculation, 20 even modes and 20 odd modes were used.

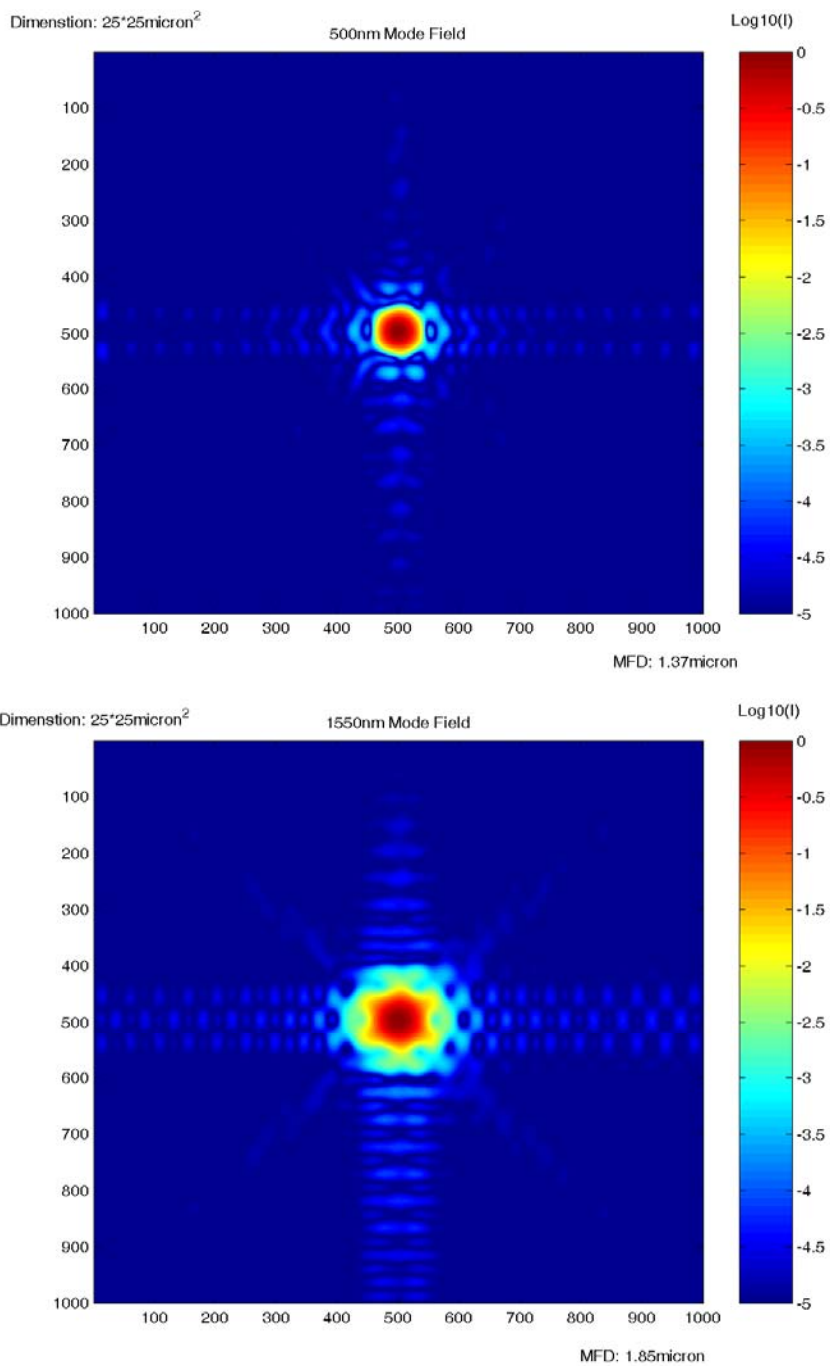


Figure 53 Calculated and measured field diameter for three waves. MFD: mode field diameter

FA can calculate all the modes that could be guided in a PCF, including all the cladding modes.

3.4 Beam Propagation Method

BPM uses the exact wave equation describes monochromatic wave, and solves the resulting equations numerically^{122, 123}. BPM is generally an efficient method and allows its complexity to be adjusted by considering the number of the grid points and the convergence criteria. BPM is readily applied to complex geometrical structures without the need for development of the specialized versions of the method. Finally, BPM automatically includes the effects of both guided and radiating fields as well as mode coupling. BPM is divided into scalar and vector versions as well. In this section, we will firstly illustrate the BPM through a scalar wave equation. We will prove then that for the accurate modeling of a PCF, a vector BPM has to be used.

A scalar wave equation can be written in the following form²⁶:

$$2i\bar{\beta} \frac{\partial u}{\partial z} + \frac{\partial^2 u}{\partial x^2} + \frac{\partial^2 u}{\partial y^2} + (\beta^2 - \bar{\beta}^2)u = 0 \quad (62)$$

where $u(x,y,z)$ is the well-known slowly varying envelope function of the optical field. Equation (62) can be written in the following form

$$\frac{\partial u}{\partial z} = \frac{i}{2\bar{\beta}} \left(\frac{\partial^2 u}{\partial x^2} + \frac{\partial^2 u}{\partial y^2} + (\beta^2 - \bar{\beta}^2)u \right) \quad (63)$$

Equation (63) states that by knowing the optical fields in one transverse plane, one can predict the fields at the following plane and is the basic BPM equation in three-dimension (3-D).

It is important to recognize the value that has been gained and lost in the above approach. Firstly, factoring of the rapid phase variations allows for slowly varying field to be represented numerically on a longitudinal grid (i.e. along z) that can be much coarser than the wavelength for many problems, contributing in part to the efficiency of the technique. Secondly, the iteration analysis can be solved by simply integration of the above equation along the propagation direction z . This latter point is also a major factor in determining the efficiency of BPM, implying a time reduction by a factor of at least of the order of N_z compared to the full numerical solution of the wave equation.

However, slowly varying envelope approximation limits consideration to fields that propagate primarily along the z axis (i.e. paraxial cases), and also places restrictions on the index contrast (more precisely, the longitudinal rate of change of index which is a combination of index contrast and propagation angle.) In addition, fields that have complicated phase variation, such as in multimode devices, may not be accurately modeled if the rapid phase variation is critical to device behavior.

Because of PCF's complicated transverse structure and high index contrast, polarization coupling between TE and TM modes cannot be neglected. Therefore, the vector form of the nonlinear Schrödinger equation has to be implemented in the transverse structure calculation. In other words, wave equation in the form of (63) has to be applied, which could be reduced to the following form for a BPM implementation¹²⁴:

$$\begin{aligned}\frac{\partial u_x}{\partial z} &= A_{xx}u_x + A_{xy}u_y \\ \frac{\partial u_y}{\partial z} &= A_{yx}u_x + A_{yy}u_y\end{aligned}\tag{64}$$

where A_{xx} , A_{xy} , A_{yx} , A_{yy} are the operators whose detailed forms could be found in [124]

We used RSoft BeamProp package¹²⁵ to implement the aforementioned BPM method. Figure 54 shows the calculated dispersion profiles using scalar and full-vectorial BPM model, comparing against the MPB results. A significant discrepancy between the scalar and full-vectorial models is observed. Implementation vectorial model is required in order to precisely predict the dispersion properties of a PCF.

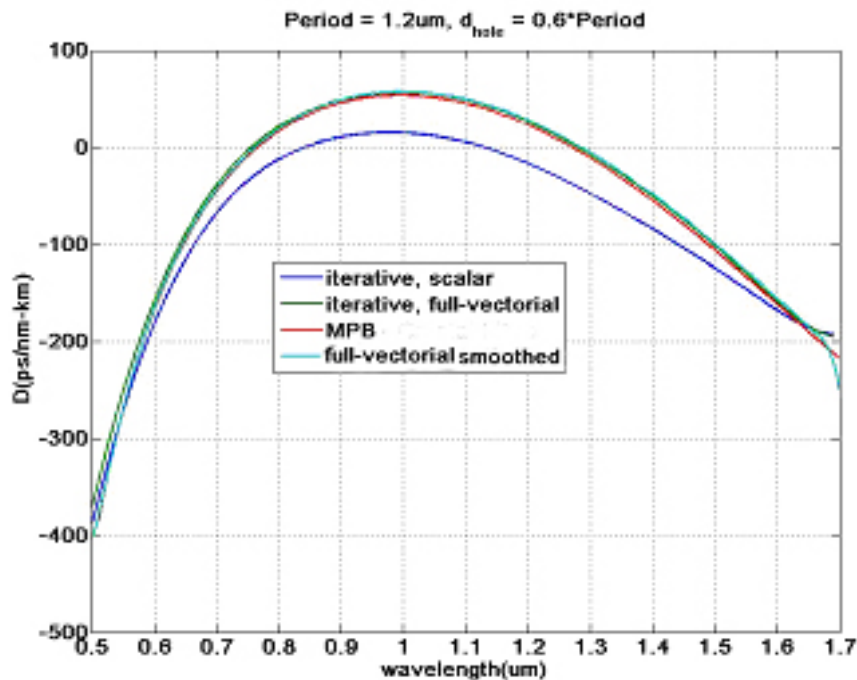


Figure 54 Both scalar and full-vectorial iterative BPM are computed against the MPB results. In the plot, we also show the smoothed full-vector results. Calculation shows that full-vectorial method must be used (due to high index contrasts)

The plots also show that there is good agreement between BPM and MPB results¹²⁶. Our implemented model is further validated by comparing more simulations to MPB results, as shown in Figure 55.

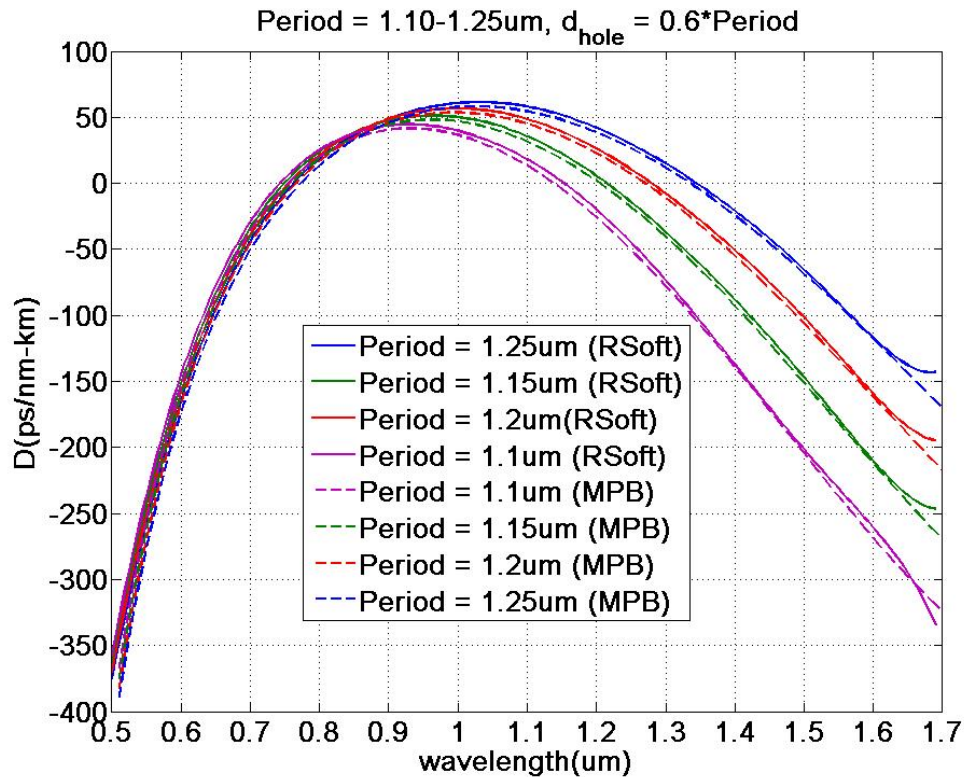


Figure 55 Comparison of RSoft BPM implementations and MPB results – good agreement achieved.

3.5 The relationship between transverse structure and dispersion profile

It is important to understand the relationship between the PCF transverse structure and the corresponding dispersion profile. We perform two sets of simulations to observe the dispersion profile variations by altering the transverse structure and discuss the

physics behind these variations. The period and air-filling ratio are changed systematically: first, the air-filling ratio is fixed at 0.5 and the period is swept from 1.2 μm to 1.4 μm , illustrated in Figure 56. The plots show that variation of the period has very little influence on the dispersion profile at the short wavelength side – for example, the first ZDWL is almost unchanged as the period changes – but has significant impact on the long wavelength – the second zero dispersion wavelength shifted to the shorter wavelength side by around 250nm when the period changed from 1.2 μm to 1.4 μm , and accordingly, the maximum dispersion decreased from 30ps/nm/km to 5ps/nm/km. This phenomenon is readily understood with EIM model. Firstly, as the period increases, the core size increases, leading to stronger waveguide dispersion in the core. On the other hand, increased PCF period results in a stronger waveguiding in the cladding structure in the same time, which in turn induces an increased effective cladding index. The index contrast between the cladding and the core therefore becomes smaller, rendering weaker waveguide dispersion in the core. In short, there exist two counter effects to the dispersion profile in the core as the period increases. The former effect is more significant to the long wavelength while the latter one is more prominent at the short wavelength side than at the long wavelength side. Therefore, the overall effect embodies as the dispersion increases at the long wavelength side but decreases at the short wavelength side. There exists a wavelength position that the dispersion does not change with the varying period and this position is generally in the vicinity of the first ZDWL.

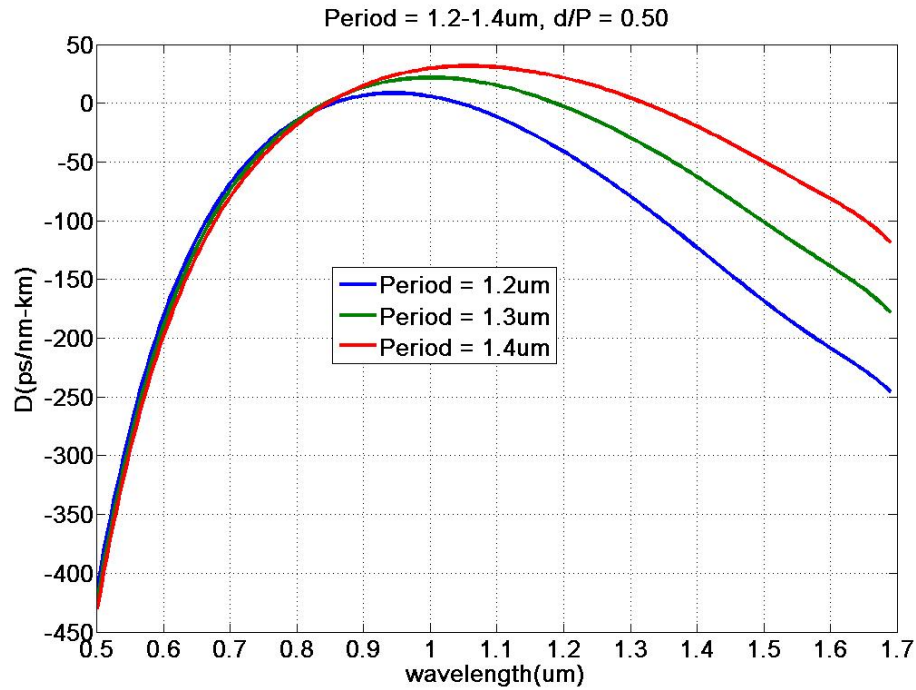


Figure 56 Dispersion profiles with fixed air-filling factor but various period values.

In the next set of tests, the period is fixed at 1.2um and the air-filling ratio is swept from 0.45 to 0.6, illustrated in Figure 57. In this case, dispersion profile is leveraged across the optical spectrum as the air-filling ratio increases. This is because increasing air-filling ratio generally leads to smaller effective index at all wavelengths because the waveguiding in PCF cladding structure becomes weaker. The globally enhanced refractive index contrast between the core and the effective cladding results in stronger waveguiding dispersion, leading to leveraged total dispersion across the whole optical spectrum.

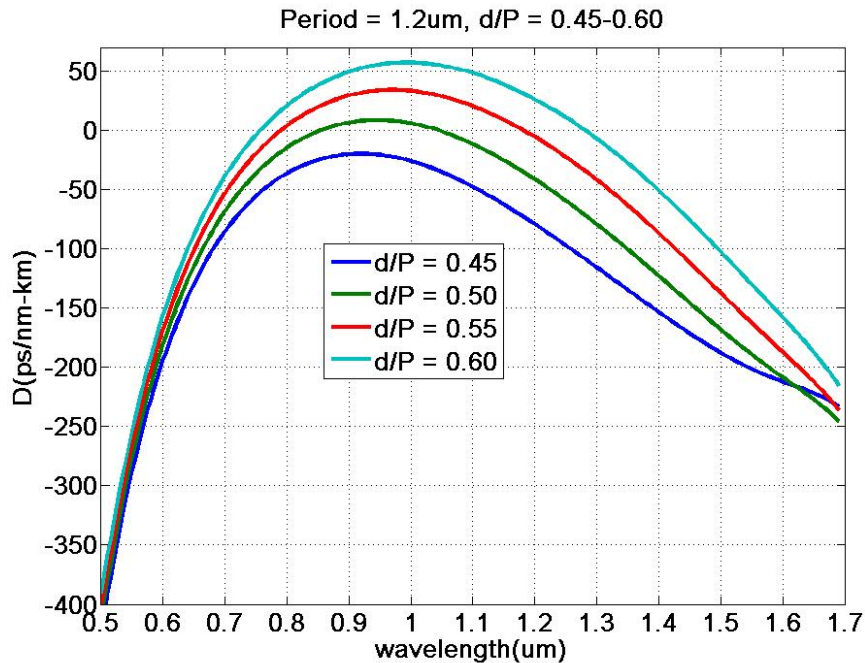


Figure 57 Simulated dispersion profile with fixed period value but various air-filling factors

3.6 Polarization maintaining (PM) PCF

In many cases, variations are introduced into the PCF structure in order to bring more functionality. One such important variation is the introduction of structural asymmetry. Figure 58 illustrates this case: two opposite air holes in the innermost ring layer are deliberately made larger than other air holes. This variation will not only introduce birefringence to the fiber, but also change the dispersion profile, which could be used in the fiber design as well. The birefringence property of PCF will be discussed in detail in Chapter 4. The influence of introducing asymmetry to the dispersion is significant: not only that the dispersion profile is changed, but also the dispersion profile becomes polarization dependent. That is, dispersion profiles for TE and TM waves would be different. In Figure 59, we show the split of dispersion profiles for TE and TM waves

caused by the introduction of the PM holes. At the same time, the dispersion profiles shift away from the corresponding symmetric structure. The calculations also indicate that changing PM holes will impact more on the TE wave than the TM wave. As we will see in Chapter 4, the separation of dispersion profiles induces non-negligible separation of the phase matching conditions for TE and TM waves as well. In Chapter 5, we discuss the utilization of PM holes to aid the design of the target dispersion profile.

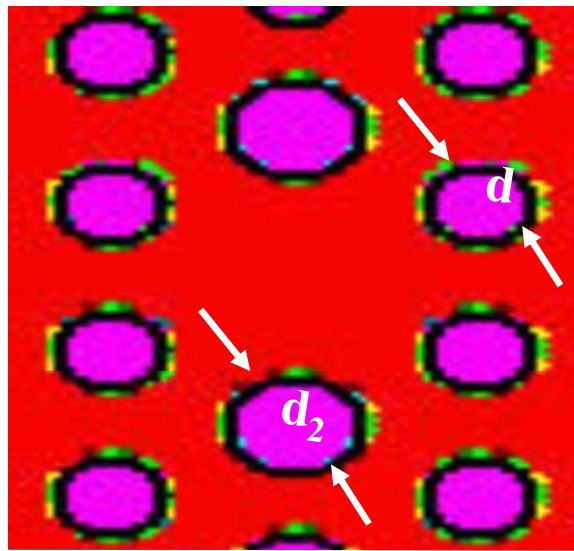


Figure 58 Cross section of a PM PCF in which two opposite holes in the innermost ring layer are deliberately made larger than other air holes, introducing birefringence and changing dispersion profile.

3.7 Conclusion

We described three methods that effectively model the PCF properties including wave-guiding and dispersion. EIM and BPM methods are most frequently used in this work, in which the EIM is used for qualitative verification and understanding of the

afore-mentioned properties. The BPM method, however, provides quantitative results and has been verified to match the tools used by the commercial PCF structures. In the following work, these methods will be used to solve the inverse problem, that is, the transverse structure design. We will first specify a desirable dispersion profile and find a way to synthesis the PCF structure that pertains to the target dispersion profile.

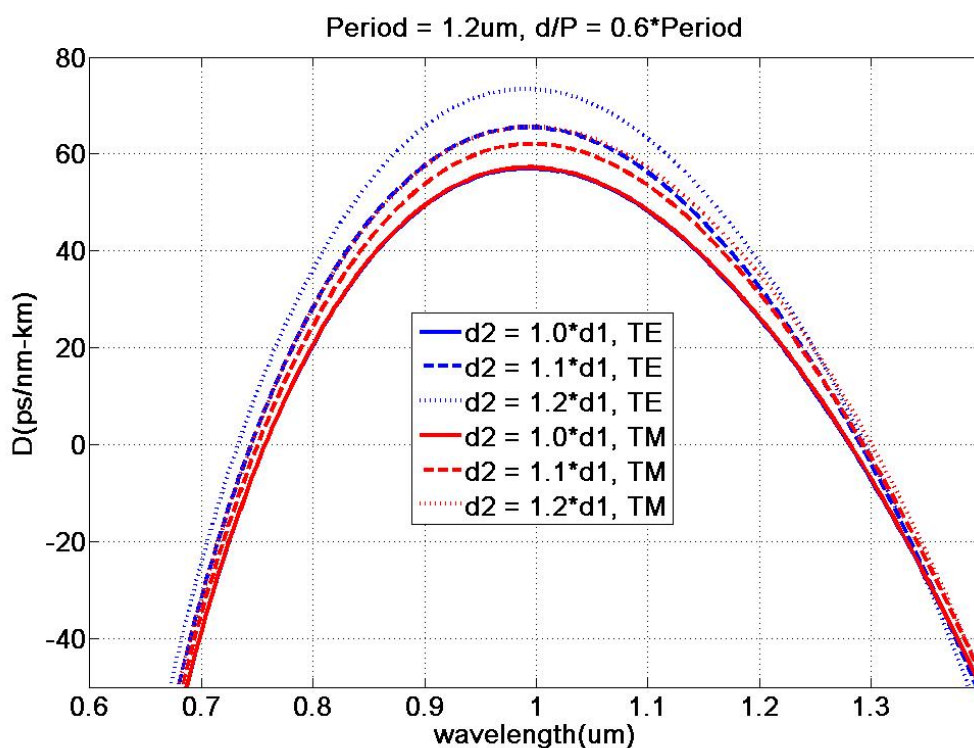


Figure 59 Illustration of the impact of PM-hole size onto dispersion profile.

Chapter 4 NIR-to-Visible Translation in Silica Photonic Crystal Fiber

The application of parametric devices should not be confined to conventional telecom (NIR) band. The inherent principles allows the implementation of parametric process in any optical bands and therefore leverages the telecom band technologies across the entire optical spectrum⁸. The coherent nature of parametric process allows the phase information to be preserved during the translation process^{8, 26, 127}, which is an important attribute for an optical mixer operation. Even though the work conducted in Chapter 2 focuses on telecom band application due to the HNLFF limit, the basic idea could be extended to other optical bands when different fiber platforms are applied. In the following two chapters of this thesis, we will study the telecom-to-visible band translation using silica PCF. In particular, Chapter 4 will be dedicated to the experimental effort of demonstrating the feasibility of such distant band translation. Before conducting such experiments, coupling optics is studied to resolve the issue of inputting light into a small core PCF (1.0 μm to 2.0 μm diameter). The biggest challenge is simultaneous coupling of 780 nm pump and 1550 nm signal with acceptable coupling efficiency. Since a general microscopic objective (MO) is not chromatically corrected for these two wavelengths, special coupling techniques were investigated.

In the following section, we study the phase matching condition in PCF, taking into account the high order dispersion terms. Then a set of parametric conversions using several different PCF coils were measured and phase matching contours were extracted. The experimentally acquired phase matching contours were then compared with the

calculated results and found to be in good agreement. PCF with proper dispersion profiles were then selected and used for the demonstration of the telecom-to-visible parametric translation. Both amplitude and phase coded signals within telecom band were translated to visible idler in error free manner. Impairment mechanisms for the parametric translation in PCF were subsequently measured and quantified. In Chapter 5, we investigate the design issue in PCF, in effort to address the observed impairment mechanisms.

4.1 Coupling optics

A general coupling schematic is shown in Figure 60.

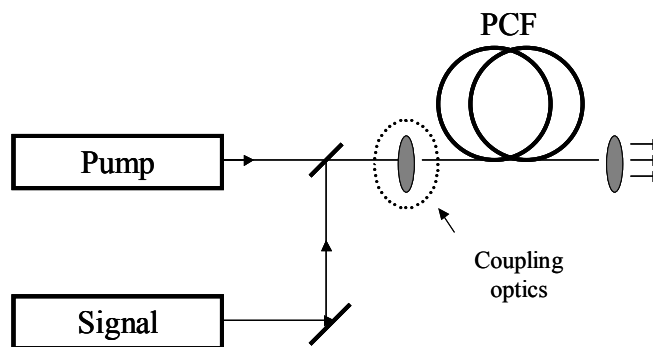


Figure 60 Schematics of the experimental setup

As mentioned in Chapter 3, the PCF used throughout the experiments all have very small core size ($1.8\mu\text{m}$ diameter typical). Therefore, even though a all-fiber setup is desirable, it was avoided throughout the experiments due to the following reasons: first, there is no regular SMF fiber that can guide such distant waves as 800nm pump, 1550nm signal and 500nm idler simultaneously. Moreover, the extremely small PCF core renders mode matching between regular SMF and PCF impossible. A tapered fiber could potentially mode match with PCF, however, again, no tapered fiber could guide the pump and signal waves at the same time. Indeed, the first test experiment was done by splicing

both ends of PCF to a 980 nm SMF and combining the pump and signal with either a 980nm/1550nm WDM coupler or a 90/10 fused coupler. The scheme was found to be very lossy at both wavelengths. Therefore, we resorted to free space coupling scheme, in which both pump and signal were firstly collimated to free space. After manipulating polarization and beam size of each wave, the pump and signal were then combined with a dichroic mirror and coupled into PCF through a high numerical aperture (NA) microscopic objective (MO).

4.1.2 Free-Spacecoupling

A general focusing scheme using lenses is illustrated in Figure 61.

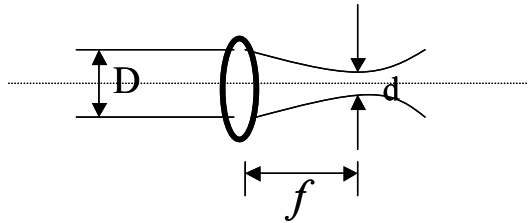


Figure 61 A lens focusing optics. D is the incident beam size and d is the focusing spot size

The focusing spot size d of an incident plane wave is given by the size of the airy-disk¹²⁸:

$$d \approx 1.22 \frac{f\lambda}{D} \leq 0.61 \frac{\lambda}{NA} \quad (65)$$

where λ is the wavelength, NA stands for the numerical aperture of the MO, D is the incident beam size and f is the focal length of the MO. Equation (65) indicates that for tight focusing, a high NA MO is desirable. In practice, both f and NA are functions of λ , which has to be taken into account in our experiments due to the large frequency shift between the pump and signal wave and will be dealt with later. However, for the moment

we assume that f and NA are constant. For an efficient coupling, the focal spot has to be smaller than the PCF core size. Therefore, a rough estimation of NA is as follows (assuming $d_{\text{core}}=1.8\mu\text{m}$).

$$\text{For } \lambda = 780 \text{ nm, NA} \geq 0.26;$$

$$\text{For } \lambda = 1550 \text{ nm, NA} \geq 0.52.$$

We note again that mode size in PCF is different for 780 nm and 1550 nm waves. Therefore, the requirement for focal spot size is different for pump and signal waves. Here we use the PCF core size as the general criterion for focusing, which provides good estimation of coupling efficiency. Following the above calculations, in order to couple the pump and signal simultaneously, an MO with NA larger than 0.52 has to be chosen. During the experiment, we usually chose 40× (NA=0.65) or 60× (NA=0.85) MO. On the other hand, NA of the focused beam has to be smaller than that of PCF to avoid the light penetration into the cladding. However, calculation and measurement both show that the PCF we used have numerical aperture ~ 0.46 , which is smaller than 0.52, indicating that there always will be coupling loss for the signal wave even if the mode is matched.

More importantly, the focal length f is a function of λ , resulting in a severe degradation of coupling efficiency due to the chromatic aberration. For example, a 40× MO generally has a focal length of 4 mm at 800nm and its focal length is shifted to 4.05 mm at 1550 nm range. Coupling each wave at its own focal plane is not acceptable due to the significant loss. If the focused beam is considered Gaussian, its beam size and intensity is then determined by the following expression²⁰:

$$w(z) = w_0 \sqrt{1 + \left(\frac{z}{z_0}\right)^2}$$

$$z_0 = \frac{\pi w_0^2}{\lambda} \quad (66)$$

$$I(r, z) = I_0 \left(\frac{w_p}{w(z)}\right)^2 \exp\left(\frac{-2r^2}{w^2(z)}\right)$$

Assuming that beam waist w_0 to be $1.8\mu\text{m}$ and that 1550nm wave is focused at $f_{1550}=4.05\text{mm}$ while the PCF tip is placed at $f_{780}=4\text{mm}$, for the 1550nm wave, the Rayleigh range $z_0=6.57\mu\text{m}$ and beam size $w(50\mu\text{m})=13.82\mu\text{m}$. Therefore the coupling efficiency for 1550nm is estimated to be only a few percent ($\sim(1.8/13.82)^2=1.7\%$).

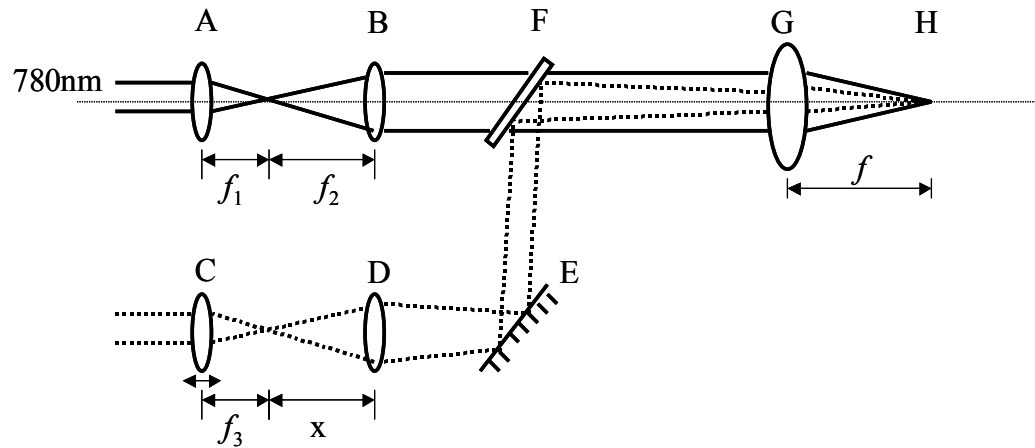


Figure 62 System for simultaneously coupling 780 nm and 1550 nm waves. Telescope system in 780 nm is regular configuration while the telescope in 1550 nm arm is made into a focusing structure so that the focal spot of both 780nm and 1550nm are at position H. The dimension parameters are defined as the following: d_1, d_2, d_5, d_7 are the 780nm wave's beam diameter at position A, B, G, H; d_3, d_4, d_6, d_8 are the 1550 nm wave's beam diameter at position C, D, G, H; the optical path from position D to G is L, assuming all the optics components are thin elements.

It is then important to manipulate pump and signal individually before overlapping them. The coupling setup we used during the experiments is illustrated in Figure 62. The telescope system in 780 nm is afocal construct while the telescope in 1550 nm arm is focusing so that the focal spot of both 780nm and 1550nm are at position H, the focal point of MO (G) at 780nm. We can then write the following relations:

$$d_2 = d_5 = \frac{f_2}{f_1} d_1; \quad (67)$$

$$d_7 = 1.22 \frac{f}{d_5} \lambda = 1.22 \frac{f f_1 \lambda}{f_2 d_1} < d_{core}$$

The typical experimental condition was described by: $d_1=d_2=1.5\text{mm}$; $f_{780\text{nm}} = 4\text{mm}$ and $f_{1550\text{nm}}=4.05\text{mm}$ ($45\times$ MO), $L \approx 300\text{mm}$. Since $d_7 < d_{core}$, we have

$$1.22 \frac{4\text{mm} \cdot 0.78\mu\text{m}}{1.5\text{mm}} \frac{f_1}{f_2} < 1.8\mu\text{m} \quad (68)$$

$$\Rightarrow \frac{f_2}{f_1} > 1.41$$

on the other hand, $\text{NA}_{\text{focus}} < \text{NA}_{\text{PCF}}$, therefore,

$$\frac{d_5/2}{f} < 0.46 \Rightarrow \frac{f_2}{f_1} \cdot d_1 \frac{1}{2f} < 0.46 \quad (69)$$

$$\Rightarrow \frac{f_2}{f_1} < 2.45$$

By combining (68) and (69), we can select $f_2/f_1 = 2$.

Calculation of d_6 and d_8 is more complicated. The optical path of signal arm could be combined as shown in Figure 63.

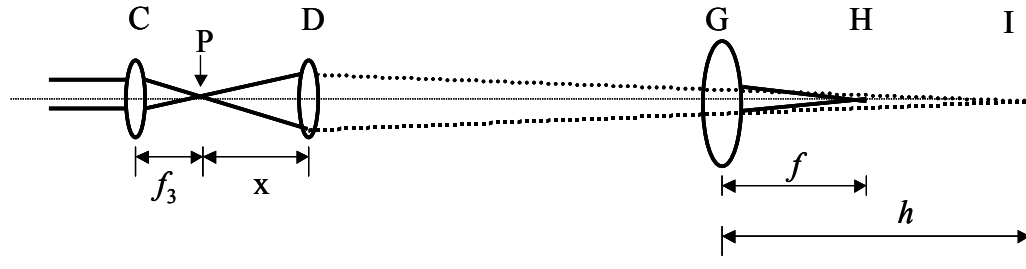


Figure 63 Schematics of optical path of 1550nm wave.

With the help of Figure 63, one can easily derive the following conditions:

$$d_4 = \frac{x}{f_3} d_3;$$

$$\frac{1}{x} + \frac{1}{L+h} = \frac{1}{f_4};$$

$$\frac{d_6}{d_4} = \frac{h}{L+h};$$

$$\frac{d_I}{d_p} = \frac{L+h}{x}; d_p = 1.22 \frac{f_3}{d_3} \lambda;$$

$$\frac{1}{-h} + \frac{1}{f} = \frac{1}{f_{1550}};$$

$$\frac{d_8}{d_I} = \frac{f}{h}; d_8 \leq d_{core} \quad (70)$$

Firstly, it is easy to select $h = 324\text{mm}$. Then we have

$$\frac{f}{h} d_I \leq d_{core}, \Rightarrow d_I \leq 145.8 \mu\text{m} \quad (71)$$

therefore

$$\begin{aligned}
d_p \frac{L+h}{x} &\leq 145.8 \mu\text{m}; \\
\Rightarrow 1.22 \frac{f_3}{x} \lambda \frac{L+h}{d_3} &\leq 145.8 \mu\text{m} \\
\Rightarrow \frac{x}{f_3} &\geq 5.4;
\end{aligned} \tag{72}$$

We also note that , $\text{NA}_{1550} < \text{NA}_{\text{PCF}}$, thus:

$$\begin{aligned}
\frac{d_6/2}{f_{1550}} < 0.46 &\Rightarrow d_4 < 7.176 \text{mm} \\
\Rightarrow \frac{x}{f_3} < 4.8
\end{aligned} \tag{73}$$

Equation (72) and (73) indicate conflicting requirements. Therefore, for 1550nm arm it is impossible to simultaneously focus within the core size and the NA of the PCF, resulting in inefficient coupling. A quick estimate could be made regarding the coupling loss due to unmatched NA:

Assuming the focal spot is within the core, one can calculate $d_8=1.8\mu\text{m}$ and $x/f_3=5.4$. Furthermore in this case $d_6=5.05\mu\text{m}$ and $\text{NA}_{\text{focusing}}=0.62$. The coupling efficiency is only $\sim \left(\frac{0.46}{0.62}\right)^2 = 55\%$. Therefore, simultaneous coupling 780nm and 1550nm waves into PCF with reasonable efficiency poses a challenge. It requires an MO that corrects the chromatic aberration at pump and signal wavelengths that are widely spectrally separated. The coupling efficiency are further degraded by other aberrations of the MO at 1550nm, resulting in relatively low resolution. For example, we observed the resolution of a typical $45\times$ MO at 1550nm is around $3.0\mu\text{m}$.

In the experiments, optimized coupling is realized by mounting lens C on a translation stage and fine-tuning the position of lens C until maximum coupling for signal is achieved.

Detailed coupling protocol and coupling conditions are reported in the appendix.

4.2 Phase matching in PCF

With significant amount of pump and signal power coupled in PCF, parametric generation is ultimately limited by the phase matching condition of the PCF. Recall that in Chapter 2 we discussed phase matching in HNLF, obtaining the conclusion that phase matching contour could be acquired by solving the following equation

$$\kappa = \sum_{n=1}^{\infty} \frac{2}{(2n)!} \beta^{(2n)}(\omega_p) (\Delta\omega)^{2n} + 2\gamma P \quad (74)$$

The high order dispersion terms ought to be considered is determined by the α factor defined previously. In this section, we further study the phase matching condition in PCF. As mentioned previously, phase matching calculation in PCF is more complicated because high order dispersion terms can not be neglected any more. As an example, in Figure 64, we show a PM PCF with period $\Lambda=1.4\mu\text{m}$ and air-filling ratio $d/\Lambda=0.525$. d_2 in the figure stands for the PM hole size .

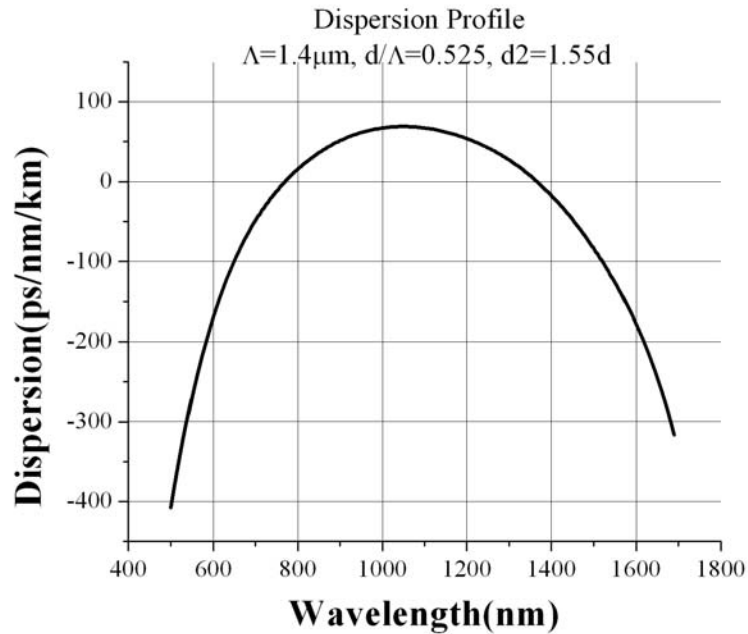


Figure 64 Dispersion profile of a typical PCF. The PCF parameters are shown in the figure.

Calculation shows that 6th order dispersion is important for an experimental operation with

$$\lambda_p=780\text{nm and } \Delta\omega \sim 1000\text{THz}$$

By recalling previously introduced parameters, it is possible to write:

$$\alpha_4 = \frac{\beta^{(6)}}{\beta^{(4)}} = 10^{-5} \text{ ps}^2 \quad (75)$$

$$\alpha_6 = \frac{\beta^{(8)}}{\beta^{(6)}} = 10^{-7} \text{ ps}^2$$

at 780nm pump, which indicates that for a frequency shift of

$$\Delta\omega = 1000 \text{ (THz} \cdot \text{rad)}, \quad \frac{\beta^{(6)}}{\beta^{(4)}} \frac{\Delta\omega^2}{6} \sim 1 \quad \text{while} \quad \frac{\beta^{(8)}}{\beta^{(6)}} \frac{\Delta\omega^2}{8} \ll 1, \text{ up to 6}^{\text{th}} \text{ order dispersion}$$

should be considered. The 8th order dispersion, however, should be included if operating beyond 1000THz frequency shift. Noting that the curvature of different dispersion

profiles is very different for various PCF, each PCF design has to be calculated individually to decide how many dispersion terms ought be included.

The dispersion profile of PCF is usually not easy to obtain. Generally, there are two ways of acquiring an accurate dispersion profile. One can experimentally measure the high order dispersion coefficient using white light interferometry, which has been carried out for both bulk media and fibers^{129, 130, 131}. While a Fourier interferometry allows mapping of high-order dispersion coefficients independently¹²⁷, most methods measure the total dispersion and mathematically derive the dispersion coefficients of different orders⁷³. The question here, is what the measurement accuracy is, which becomes problematic for high order terms. The other way is to measure the transverse structure of a PCF and calculate the dispersion profile using the numerical methods developed in chapter 3. This however, assumes that the transverse structure could be measured very accurately (measurement error <1%); furthermore one has to assume that the transverse structure does not vary longitudinally, which, as we will see later, is not generally true. The first method is always preferred if a direct measurement of dispersion profile is available since the measurement resembles the true global dispersion of the fiber.

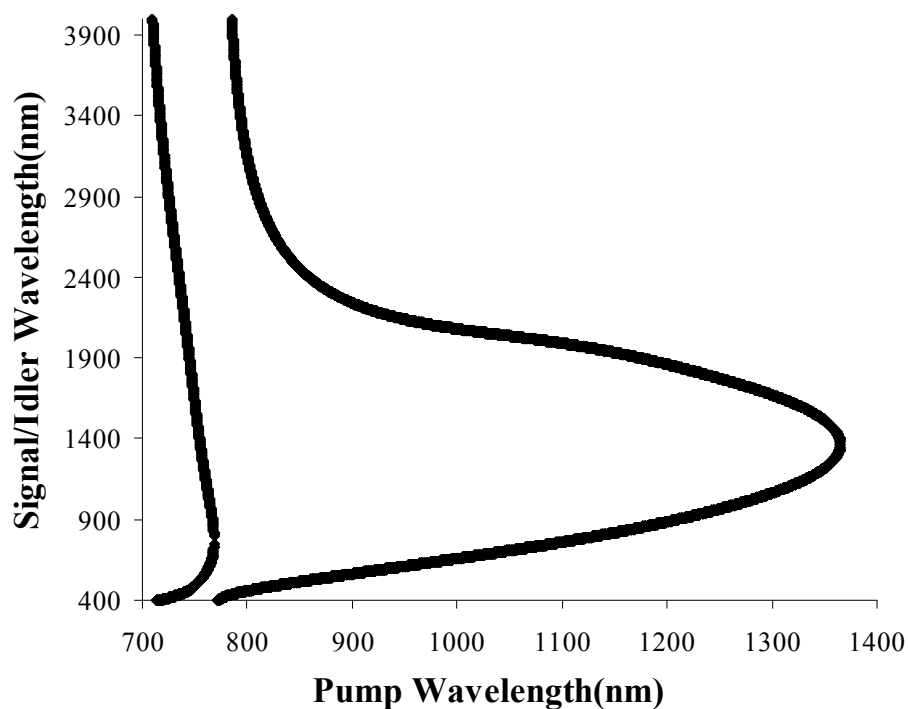


Figure 65 Phase matching contour corresponding the dispersion profile in Figure 64.

One important application of dispersion profile is to predict the phase-matched wavelengths of certain PCF, which again requires solving high order polynomial equations (74). Phase matching condition in PCF is typically presented as a phase matching contour, which is a contour plot that each pump wavelength value on the abscissa corresponds to a phase-matched signal and idler pair on the ordinate. For example, the phase matching contour of PCF in Figure 64 is shown as Figure 65. One can read from the contour that for a pump placed at 800nm, a phase-matched pair 1550nm signal and 540nm idler could be generated.

Phase matching contour calculation is utilized to predict the performance of a PCF and to design the PCF. Once a fiber is obtained, phase matching contour could be

measured by directly observing the parametric generation from noise photon, the details of which is discussed in the next section.

4.3 Parametric generation in PCF

A first set of experiment is dedicated to characterize the phase matching condition in PCF, during which only the pump was coupled into the PCF¹³². The phase matching contour extraction was achieved by measuring the modulation instability (MI) spectra generated from the amplified spontaneous emission (ASE) photons in the visible band. At each pump wavelength, the MI band at 500 nm region was recorded by a visible spectrometer, and the matched wavelength at the near-infrared band was then calculated based on the energy conservation relation. The positions of the ASE bands, calculated near-infrared wavelengths and known pump spectral position were used to reconstruct the PCF phase matching contour. The experimental setup is shown in Figure 66. In the one-pump parametric structure, a diode laser with 1.4W maximum output, 500kHz linewidth and 766-786 nm tunable range was used as a pump. The pump beam was s-polarized with 30dB polarization extinction ratio.

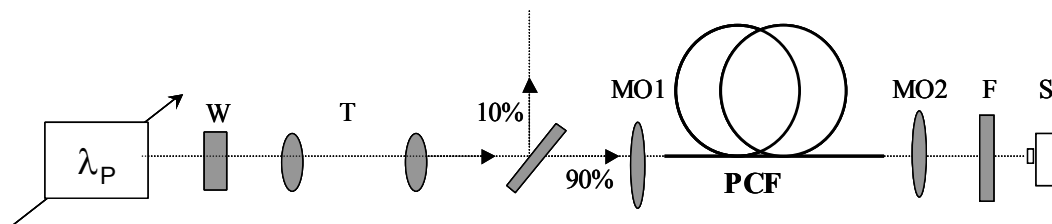


Figure 66 Experimental setup. W: half-waveplate; T: telescope; MO1-MO2: microscopic objective; F: filter; S: spectrometer. The 90/10 tap is used for pump power and back-reflecting spectrum monitoring

It was then sent through a half-waveplate to achieve alignment with one of the principle axes of the PCF. A telescope system was used to adapt the beam size to the coupling-in objective MO1. A 90/10 beam splitter was placed after the telescope to monitor the pump power level and the back-reflecting spectrum from the PCF. The pump was then coupled into the PCF through a high numerical aperture (NA) objective MO1. The output of the PCF was collimated by another high NA objective MO2, and received by a spectrometer (S). A band pass filter in the visible region (F) was placed before the spectrometer to suppress the pump at the output. The pump diode current was directly-driven by a $\sim 5V$, 10MHz harmonic tone to suppress the stimulated Brillouin back scattering from the PCFs (see section 3.6.1). This allowed coupling of approximately 350mW pump into the PCF. Due to the limited tunability of the pump laser, the phase matching contours were measured in the vicinity of the 780 nm region.

Table 2 PCF structure

	$\Lambda(\mu\text{m})$	d/Λ
1	0.81	0.57
2	0.81	0.58
3	1.03	0.58
4	1.25	0.58
5	1.35	0.58
6	1.02	0.64
7	1.06	0.63

We tested seven distinct coils of PCF, each of which with about 10 meters long. Before observing the parametric generation, the PCF transverse structures - the air-hole period (Λ) and air-filling ratio (d/Λ) – were obtained using scanning electron microscope (SEM), shown in Table 2.

Except for coil 4 and 5, which had 9 air hole layers, all the PCF coils transverse structure contained 12 air hole layers. Figure 67a shows the measured phase-matching contours in the visible region for the 2 principal axes of all the PCF coils. The phase matching in the coils covers different parts of the visible band, jointly encompassing almost the entire visible region. The measurement of the near infrared (NIR) portion of the phase matching contours was hindered by the wavelength selectivity of the optical components in the output portion of the setup, optimized for the visible band. However, the NIR sidebands could be determined from the photon energy conservation relation. The corresponding calculated contours are displayed in Figure 67b. Figure 67 indicates that a small change in PCF transverse structure could result in significant shift in the measured parametric-sideband contour.

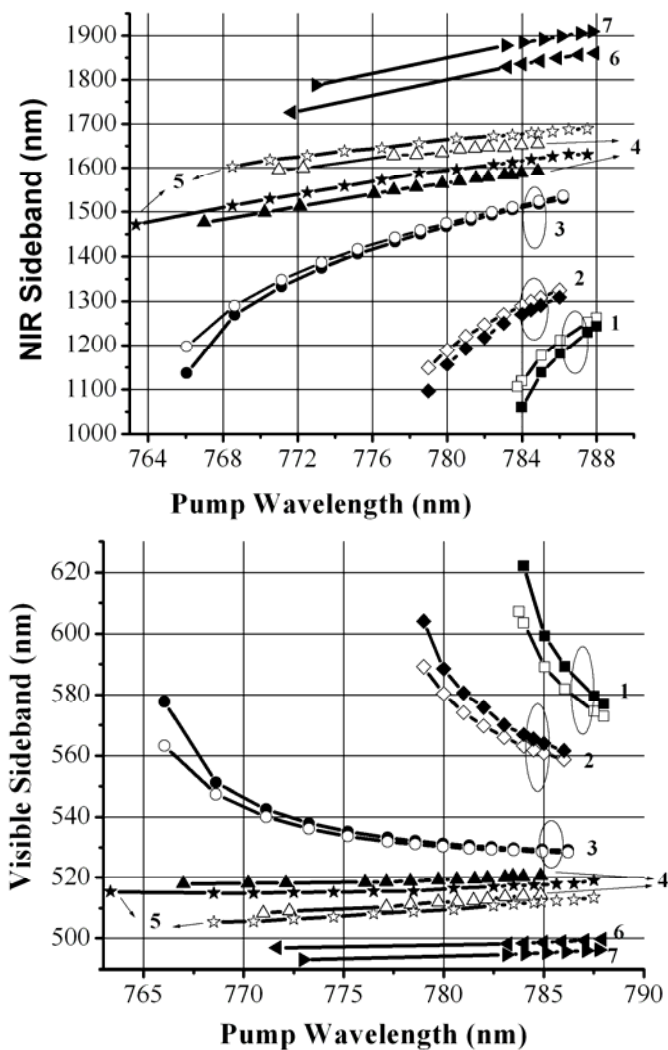


Figure 67 Measured and calculated Phase-matching contours of the parametric generation at a) visible range (measured) and b) near-infrared range (calculated). The two contours circled together represent two polarization states, with the filled marker corresponding to slow axis and open marker fast axis.

More importantly, the asymmetric transverse structure of PCF results in different phase-matching contour plots for different input polarization state. Indeed, coil 1 to 5 show significantly different contour plots for the two principal axes. In particular, coil 4 and 5 have two air holes in the innermost air-hole layer deliberately made about 1.2 times

larger than other holes, resulting in a relatively larger contour plot separation between the two principal axes. Coils 6 and 7, on the other hand, have more symmetrical transverse structures and show negligible difference in the two principle axes phase matching. It is important to notice that coils 1, 2 and 3 have steeper tuning slope than others: a small tuning of pump wavelength results in much broader sweeping of the parametric sidebands. As an example, coil 2 allows the parametric sideband sweep over more than 40nm in the visible band by tuning the pump for 7nm only. It is generally possible to design the PCF structure so that the parametric sidebands have much steeper tuning slope; the whole visible band could thus be covered with a single piece of PCF¹³³. In the NIR band, tuning is more efficient – tuning the pump for 15nm results in 400nm tuning from 1150nm to 1550nm.

The measurements on coil 4 and 5 are particularly interesting, clearly showing the phase matching among ~780nm pump, telecom-band signal and visible band idler and therefore the potential for telecom-to-visible band translation. We therefore take a closer look at this fiber. Again, the measurements of phase-matching contours were conducted for both PCF principal axes due to the asymmetry of the PCF transverse geometric structure and the results are separately illustrated in Figure 68. Notice that the phase-matching contours along the two principle axes (P1 and P2) are separated by 10 nm in the visible range and 100 nm in the 1550 nm range, indicating an asymmetric transverse structure of the PCF. As an example, when the pump is centered at 780 nm and its polarization is aligned along P1 axis, the 518.3 nm idler and 1575.5 nm signal waves are phase-matched; conversely, the 511.4 nm idler and the 1663.9 nm signal waves are matched if pump polarization is realigned along the P2 axis. Figure 68 also implies

approximately 10nm of continuous tunable range in the 500 nm region and a 100 nm tunable range in the near infra-red (NIR) region, as the pump is tuned from 765 to 785nm. The tunable range can be optimized by using different fiber structures and/or the wider pump tuning. A tunable range as wide as 450nm from visible to NIR band has been achieved in a previously published work with a pulsed pump at 650 nm range, operating at the normal dispersion regime of a PCF with high air-filling ratio¹³⁴.

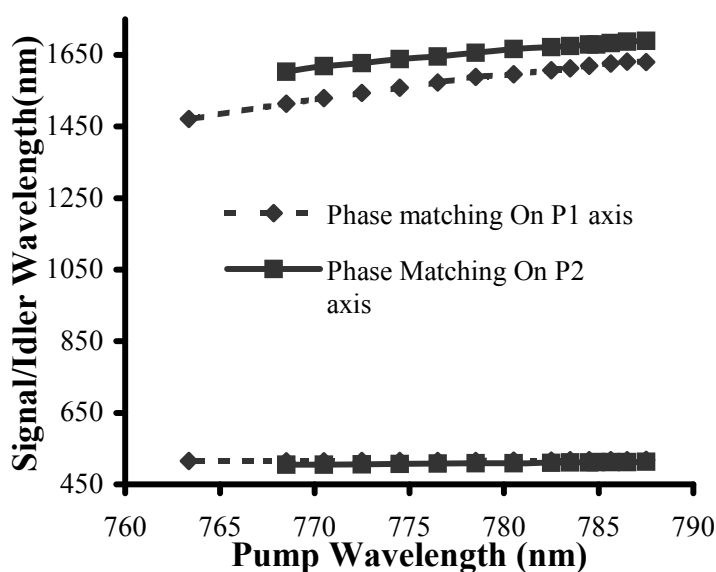


Figure 68 Measured phase matching contour for the two principle axes of the PCF. The asymmetric PCF transverse structure results in the phase matching condition difference for the two polarizations.

We also compared the phase-matching-contour measurement method with the calculation. In Figure 69a, dispersion profiles measured by white light interferometry of the two fibers were shown, while in Figure 69b, measured and calculated phase matching contour were overlapped within the same plot. Note that the calculation covers a much broader pump range than the measured one does; the latter one is limited by the available

pump tuning range. The measured contours are otherwise overlapped very well with their calculated counterparts.

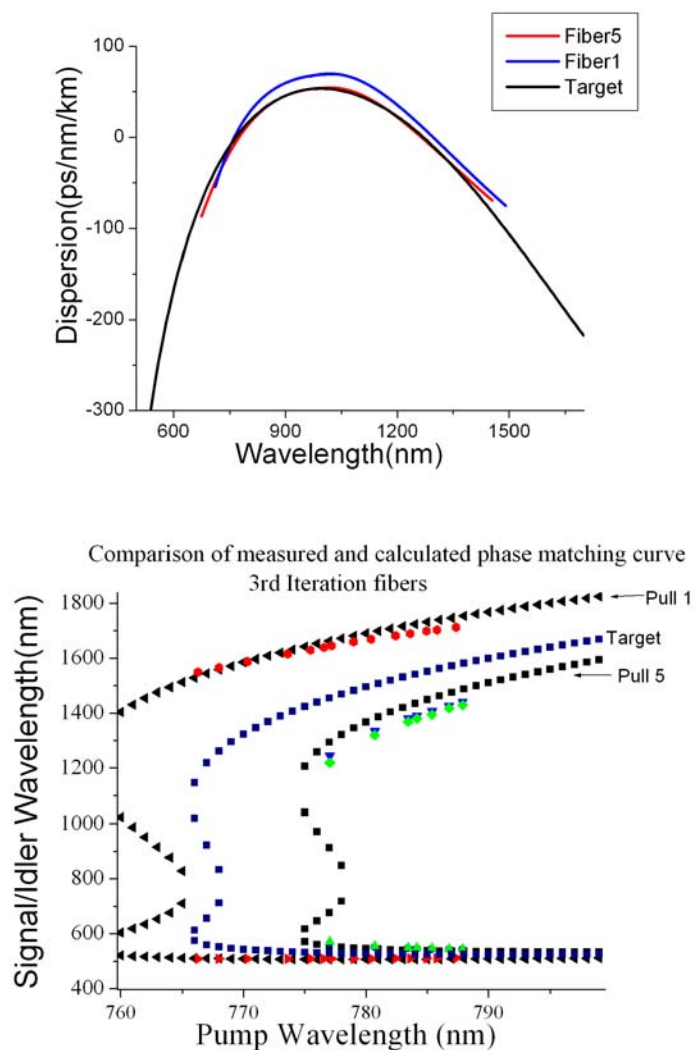


Figure 69 Two PCF with their dispersion profile shown in a) and phase matching contour shown in b). We observe that the measured results agrees well with the calculations.

In conclusion, the continuous-wave parametric generation spanning the entire visible region was measured for the first time. The measurements demonstrated that small changes in the PCF transverse structure had significant impact on parametric generations.

Distinct phase-matching contours were observed for the fast and slow axes. Experimental measurements agree well with the calculated results. The availability of high power laser diode in the 780-nm region could enable the construction of a fiber-based continuous-wave parametric oscillator in both visible and near infrared regions⁴³. The matched parametric sidebands can potentially enhance the wavelength conversion efficiencies¹³⁵. In the following, we will focus on the telecom-to-visible translation based on the experimental results shown above.

4.4 Amplitude modulation translation from telecom to visible band

One important attribute of the parametric process is that the signal and idler form a phase conjugate pair and therefore the modulation imprinted on signal will be translated to idler with high fidelity, and vice versa. The implication for submarine communication is obvious: one needs to modulate NIR wave only to obtain modulated visible signal. In the sensing structure, information received from the environment or sample could be translated back to telecom band for high sensitivity detection. In the following two sections, we demonstrate experimentally high-speed amplitude and phase modulation translation from telecom to visible band^{136, 143}. At the same time, we also demonstrate WDM channel translation and demultiplexing at the visible band¹³⁷.

The PCF structure used in this section is a standard commercial product designed for supercontinuum generation at 800nm and consists of a hexagonal silica core with 1.6 μm diameter, surrounded by a cladding with a honeycomb arrangement of circular air holes, as illustrated by the micrograph shown in Figure 70. By controlling the ratio of the

air-hole size and adjacent cell distance, it is possible to support single-mode propagation in bands separated by hundreds of nanometers. More importantly, the variation of the same parameters can be used to synthesize balanced higher-order dispersion terms and achieve phase matching for spectrally distant signal-pump-idler waves (see chapter 2).

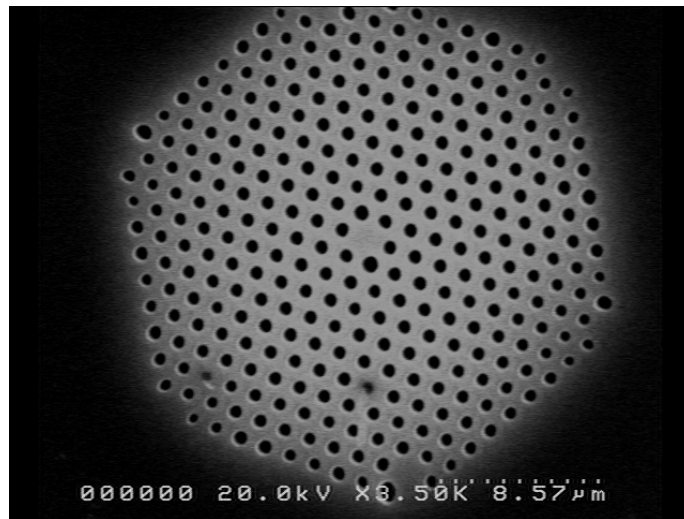


Figure 70 *Scanning electron microscope image of the commercial photonic crystal fiber used in this work.*

Figure 71a shows the dispersion curve of the PCF used in the experiment. The PCF is characterized by two ZDWs, at 750nm and 1260 nm, and a maximum dispersion of 69.5ps/km-nm at 1001 nm. The nonlinear parameter was estimated to be $70 \text{ W}^{-1}\text{km}^{-1}$ near 800 nm. The large curvature of the dispersion curve requires the inclusion of terms upto 8th order in the corresponding Taylor expansion, in order to provide an accurate description of phase-matching and parametric interaction.

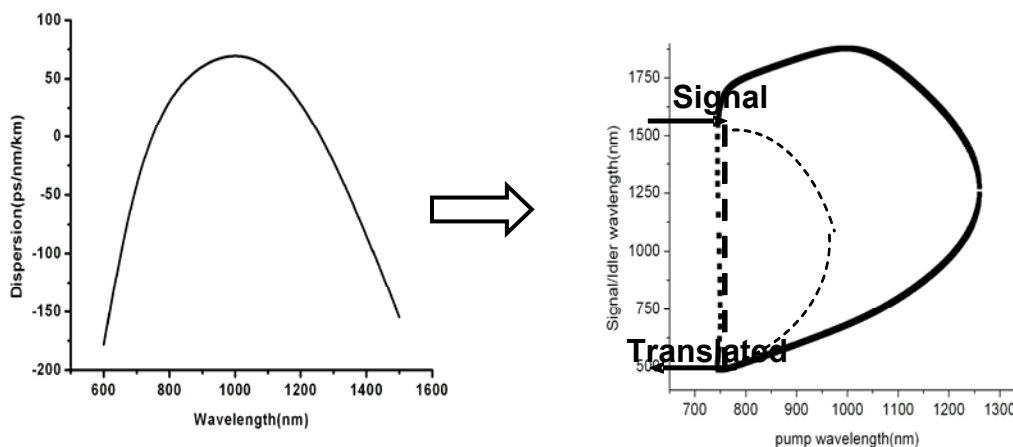


Figure 71 a) dispersion curve of the PCF with two zero dispersion wavelength at 750nm and 1260nm respectively, b) Phase matching contour of the PCF shown on the right.

Figure 71b plots the phase matching contour corresponding to the dispersion curve in the case of negligible nonlinear phase mismatch, in agreement with the experimental condition of this work. By tuning the pump, indicated by the vertical dashed line, two intersections with phase-matching loci define paired signal and idler wavelengths. A commercial 780-nm diode pump allows the standard telecommunication band at 1550 nm to be matched with the submarine communication window at 500 nm. We note that the ideal pairing of signal and idler waves on the phase-matching contour guarantees the maximal conversion efficiency, even in the case of low pump powers. As the pump power increases, the phase-matching condition can also be altered by the interplay of linear and nonlinear phase shift in the region near the pump wavelength, as the regular modulation instability (MI) contribution, positioned close to the pump wavelength, becomes important. Since the translation-paired sidebands, defined by 1550-nm and 500-nm waves in this case, are much further from the pump wavelength than

those affected by MI, their center wavelength as well as their spectral shape is less sensitive to the pump power fluctuations.¹⁴ On the other hand, for the same reason, the outer sidebands are very sensitive to dispersion fluctuations, which tend to be significant for fibers with such small cores.

The performance of the translator is defined in significant way by the effective bandwidth^{10,11}. While the translation of low-rate, single channel communication can, in principle, be accomplished by cavity-aided, crystalline devices^{138, 139}, a general UBT should be capable of mapping the entire WDM band. The effective bandwidth of the PCF translator can be controlled by precise tailoring of local PCF dispersion curvatures at signal, pump and idler wavelengths. An important design consideration is related to the high PCF dispersion experienced by the signal modulated at a high rate. Indeed, a signal modulated at Gb/s or faster, is expected to sustain high intersymbol interference (ISI) in a high-dispersion waveguide. While it is possible, at least in principle, to synthesize the dual-ZDW PCF to simultaneously provide spectrally distant phase matching and limited local dispersion at the signal (idler) bands, it is unlikely that this approach would be required for any practical data rates. The high PCF nonlinear parameter ($\gamma \sim 100 \text{ W}^{-1} \text{ km}^{-1}$) dictates the use of relatively short fiber segment (<20 m), which limits the total dispersion within the signal band to approximately 3 ps/nm. This small but finite dispersion is beneficial at practical channel rates (<40 Gb/s) since it alleviates constraints on the WDM signal grid: the channel spacing can be made considerably smaller than that in the HNLF-based system, while maintaining low inter-channel FPM crosstalk.

A one-pump parametric device was constructed as shown in Figure 73. A single-frequency continuous-wave (CW) Ti:Sapphire laser, tunable between 780 and 840 nm,

served as a parametric pump and operated in the anomalous dispersion region of the PCF coil. The polarization-dependent nature of the PCF required the use of a half-waveplate (W1) to align the pump polarization to a principal axis of the PCF. A dichroic beam splitter (M2) was used to combine the pump and signal (1550-nm) bands into a high-numerical-aperture (NA) coupling objective (MO1). A standard microscopic objective optimized for visible transmission was used here, and the transmission for both the pump and signal were only 75%. Ideally, an IR objective should be used.

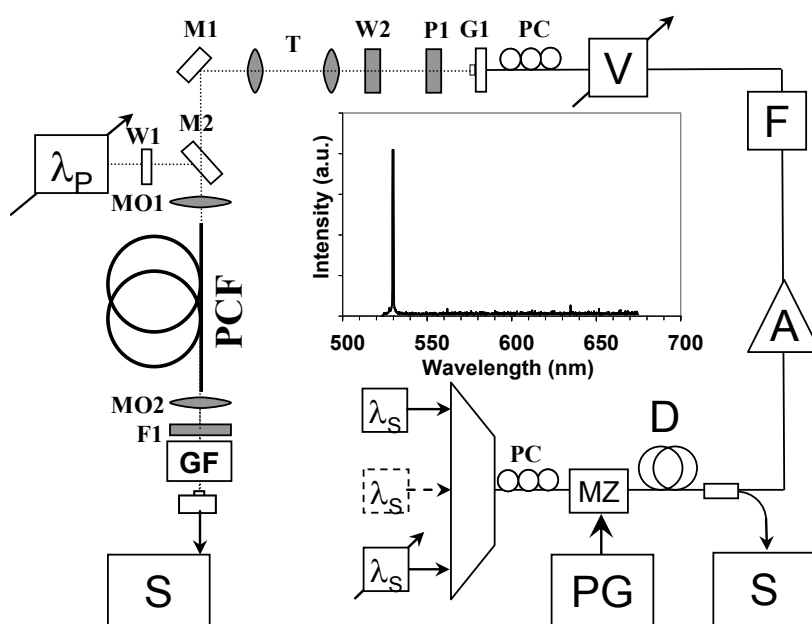


Figure 72 Experimental Setup; symbols as defined in text. Inset indicates typical visible (converted) single-channel spectrum. PC- Polarization Controller; MZ- Mach-Zehnder Amplitude modulator; PG- pattern generator; D- fiber decorrelator; S- Scope; A- Amplifier; F- filter; V- Variable Optical Attenuator; P1- Polarizer; W1-W2: $\lambda/2$ waveplate; T: Telescope; M1-metallic mirror; M2- Dichroic mirror; MO1-MO2: Microscopic Objective; GF-Grating Filter.

The first set of experiments was performed using a single external cavity laser (ECL) signal source tuned from 1530 to 1600 nm. The source was modulated using a

Mach-Zehnder (MZ) modulator driven by either a harmonic or a pseudo-random pattern generator, with varied pattern length (from 2^7-1 to $2^{31}-1$ bits) and modulation speeds of 50, 155.52, 200 and 400 MHz. The initial modulation speed was limited by the slow response (100MHz bandwidth) of the visible detector. The modulated signal was boosted (A) and filtered (F) in order to reject excess amplified spontaneous emission (ASE) from the EDFA. A fiber polarization controller (PC) was used to maximize the gradient-index (GRIN) lens (G1) coupling to the free-space signal arm (G1-M1). The combination of a linear polarizer (P1) and a half-wave plate (W2) was used to align the pump and signal polarizations prior to insertion in the PCF, with minimal coupled powers of 20.5dBm and 10dBm, respectively, throughout the experiment. A dedicated telescope (T) segment collimated the signal beam before it was coupled into the PCF by the objective (MO1). A metallic mirror (M1) was used to steer the signal arm to overlap with the pump. Two 20-meter coils of PCF that have the same claimed dispersion curve were used to compare the performance. The PCF output was collimated using a second objective (MO2 40 \times) and filtered by a 600-nm low pass dichroic element (F1), which separated the idler band from the pump and the signal bands. All the waves were observed in fundamental mode at the PCF output. The final (visible) idler had sufficient power in all experimental configurations (single channel and WDM) to overcome the output coupling losses (MO2, F1) and was well above the sensitivity threshold of the receiver. In the second set of experiments, the single tunable source was replaced by four WDM channels, which were modulated and decorrelated prior to the booster (A). The visible channels were then dispersed by a grating filter (GF), selected by a spatial filter and detected by either a fast oscilloscope or the visible detector. In both sets of experiments, the input signal channels

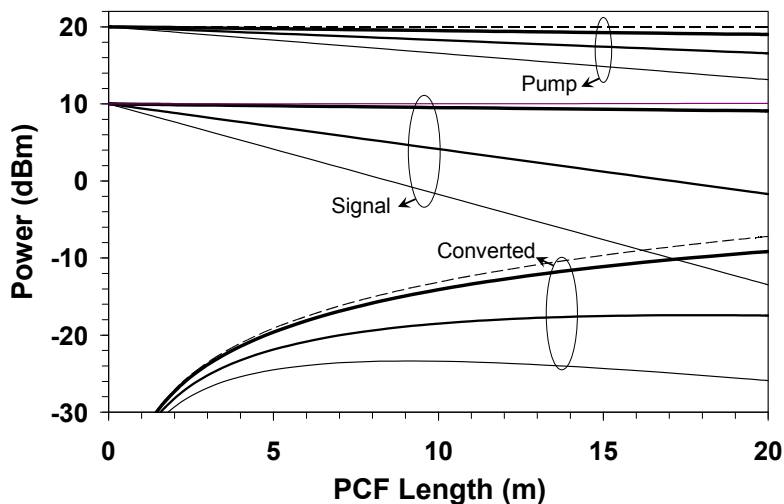


Figure 73 Pump (800nm), signal (1550nm) and idler (539nm) evolution in case of lossless (dashed curve) and lossy PCF. Corresponding losses for signal/pump/idler bands in dB/km: 50/50/50 (heavy curve), 600/175/200 (medium curve) and 1200/350/400 (thin curve).

were monitored (C) prior to the booster stage using a fast oscilloscope (S). In the last set of experiments, the Ti:Sapphire pump was replaced by a continuous wave (CW) diode laser with high output power (~ 1 W) tunable over 768nm-786nm. A faster (1GHz bandwidth), but less sensitive receiver was used in this set of experiments. The translation of a 2^{31} -1 PRBS pattern modulated at 1Gbps rate, to 500nm-band idler was observed in error-free manner.

The experimental performance of the translator, particularly in terms of conversion efficiency, was limited by the fact that pump, signal and idler waves were not exactly phase matched. The phase matching contour, obtained from approximate manufacturer's dispersion data, shown in Figure 71b, indicates that a 780-nm pump needs to be paired with a 1550-nm signal. The Ti:Sapphire pump-power peak was offset from this wavelength, dictating operation in 800-nm vicinity. This departure from ideal phase

matching is further compounded by the fact that the commercial PCF sample was not designed to guide the standard 1550-nm telecom band. These experimental constraints were investigated using the coupled-mode equations (1)-(3) with excessive 1550-nm band loss. Figure 73 compares the typical power evolution estimates along the fiber for ideal (lossless) and lossy PCF samples. Relatively low pump power (20 dBm) and a weak input signal (10 dBm) lead to a -7 dBm translated wave at 500 nm. A moderate loss of 50 dB/km across all three bands decreases the conversion efficiency by 2 dB, as indicated by the thick curve. This case is of particular practical interest since it points to the operational efficiency that could be attained by current PCF manufacturing process. Any loss in excess of 50 dB/km has a significant impact on the translation efficiency, even for the short sample lengths used in this experiment: a total signal loss of 10 dB or more reduces the converted power to below -20 dBm. In the experiment, a -25 dBm 500 nm idler was converted from a 10 dBm 1550 signal, resulting in a conversion efficiency similar to that reported in [73]. Figure 74 illustrates a typical spectrum obtained by a visible-range spectrometer, recorded with a 0.5-nm resolution. The idler was tuned across the visible range to demonstrate the available translator bandwidth. The first coil under investigation allowed continuous tuning in the ranges 515-525 nm and 530-542 nm, whereas the second coil covered the ranges 515-525 nm and 565-580 nm. The observed gaps in continuous tuning range are attributed to the fact that the Ti:Sapphire laser exhibited large power variations during the tuning process. We observed Ti:Sapphire pump-power fluctuations of nearly 30% occurring across nm-scale tuning of the pump wavelength, thus preventing rigorous characterization of the equalized translator bandwidth. The idler power exhibited high sensitivity to the input pump polarization, in

agreement with previous observation.¹⁴ The rotation of the half-waveplate (W1) within the pump arm was used to demonstrate nearly-complete idler extinction.

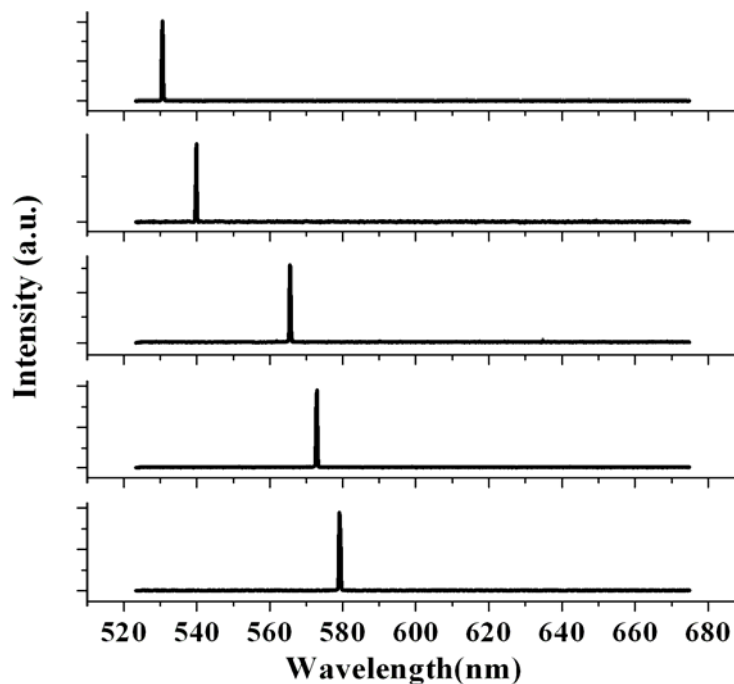


Figure 74 Typical idler spectrum tuned across the visible band and measured by the visible spectrum analyzer.

The first modulation experiment was performed with the pump and signal set at 790 and 1541 nm, respectively; the signal was modulated harmonically. The generated visible idler at 531 nm was received by a visible detector, with a cutoff frequency of 100 MHz, and was analyzed on the oscilloscope, as illustrated in Figure 75. Although the signal was modulated at rates up to 10 Gbps, the absence of a fast visible detector rendered any faster measurements (>200 Mb/s or 1.5 Gb/s in the later experimental stage) impossible. Modulated and translated waveforms at 50 and 200 MHz are shown in Figure

76a and Figure 76b, illustrating the fundamental limitation posed by the slow receiver.

The measured idler

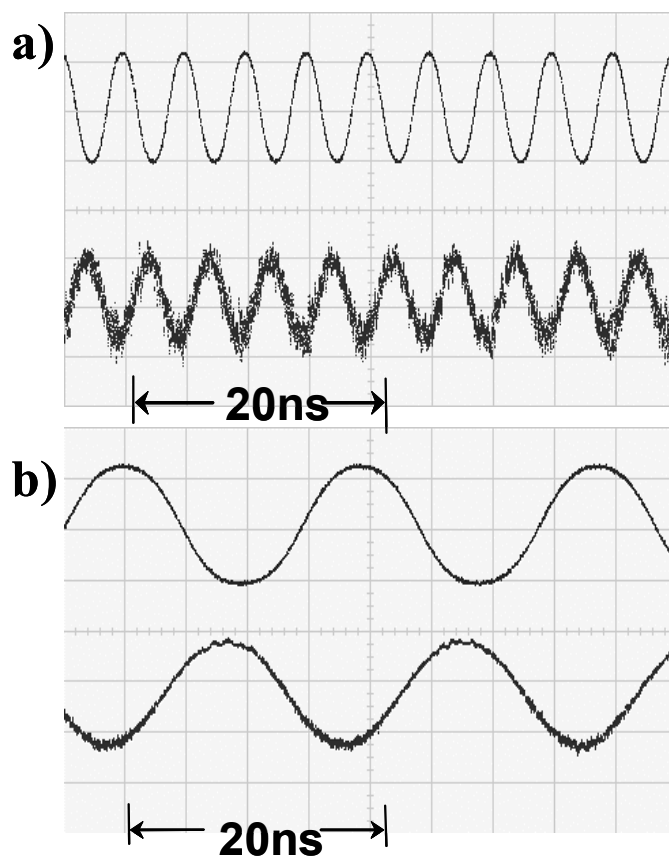


Figure 76 a) 200MHz harmonically modulated 1542nm signal (upper trace, 1550nm PIN receiver) and its translated waveform, corresponding to 3dB frequency rollover point of the visible receiver; b) 50MHz harmonically modulated 1541nm signal (upper trace) and its translated (531nm) waveform (lower trace);

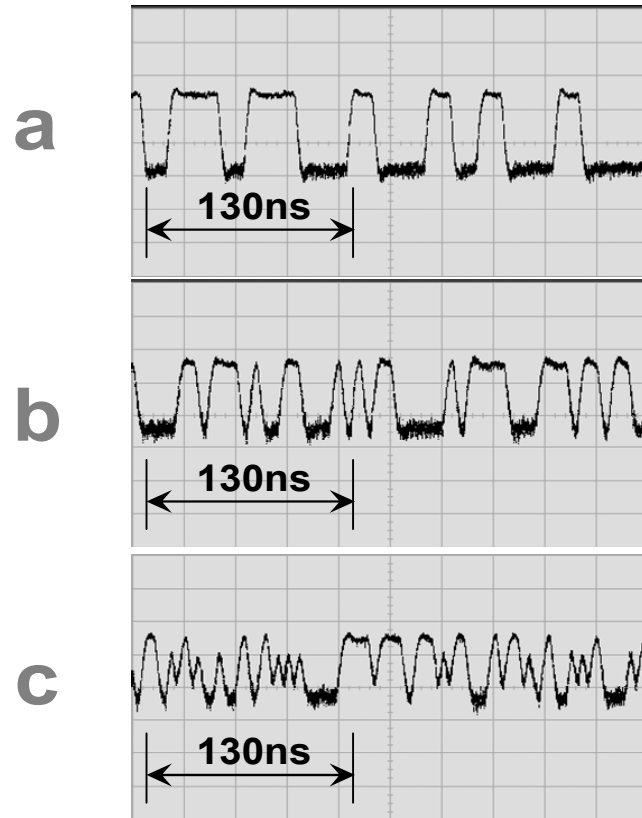


Figure 77 a) 50Mbps b) 155.52Mbps and c) 400Mbps modulated PRBS word received at 531nm;

power scaled linearly with signal power, as expected for a non-depleted, one-pump parametric interaction. The translated modulation measurement was dominated by the frequency response of the receiver. In the case of 50-MHz harmonic modulation, the recovered idler exhibited a high extinction ratio, with average low and high logic levels of 1 and 500 mV, respectively. Fast harmonic modulation at 200 MHz exceeded the 3-dB receiver rollover by many tens of MHz, resulting in the distortion illustrated in Figure 76a.

A second set of modulation experiments was performed using non-return-to-zero (NRZ) pseudorandom bit sequence (PRBS), in order to estimate the penalty induced by the translation process. The modulation rate was varied from 50, 155.52 (OC-3) and 400

Mbps, with short (2^7-1) and long ($2^{31}-1$) bit sequences. The idler waveforms were analyzed using both the sampling oscilloscope and the BER analyzer. Figure 77 illustrates typical received idler patterns at 2^7-1 pattern length. Both 50- and 155.52-Mbps patterns are nearly unimpaired, whereas the 400-Mbps pattern exhibits heavy inter-symbol interference (ISI) imposed by insufficient receiver bandwidth. Our PRBS modulation test was thereafter performed at 155.52 Mbps. Figure 78 shows a typical eye diagram with a measured

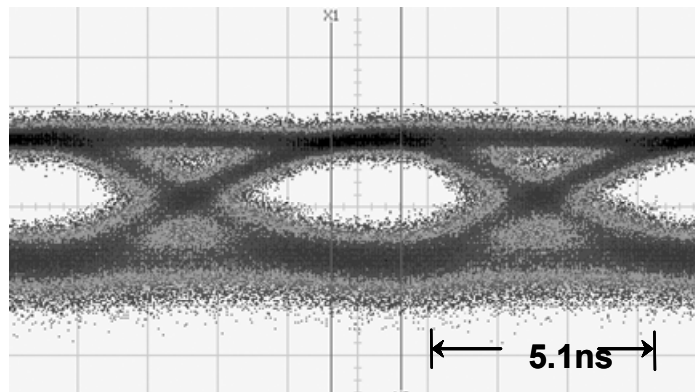


Figure 78 531nm eye pattern with 155.52Mbps NRZ modulation. The eye penalty is dominated by the operation of the visible receiver beyond 3dB rollover point.

Q-factor of 15.23dB at 155.52 Mbps. This translated performance incorporates the cumulative penalty associated with the operation of the visible receiver beyond its 3-dB rollover point, the noisy Ti:Sapphire pump and the excessive PCF loss at 1550 nm. The bit-error-rate (BER) measurements of short PRBS words ($<2^{10}-1$) indicated error-free performance; however, the longest PRBS sequence ($2^{31}-1$) pattern had a measured BER of 6×10^{-8} . This degradation increase is attributed to the patterning effect that originates from the unequalized frequency response of the detector, particularly near the DC region.

In addition to the translation of a single modulated channel at 1550 nm, we explored the feasibility of WDM (band) translation. Four channels positioned at 1541, 1549, 1555 and 1560 nm were translated using a fixed and tunable Ti:Sapphire pump. Figure 79 illustrates WDM band casting corresponding to parametric pumps positioned at 791, 800 and 802 nm. The longest wavelength channel (1560 nm) is mapped to either 529 nm (pump at 791 nm) or 540 nm (pump at 802 nm). Parametric WDM upconversion results in considerably denser channel spacing, with the highest-frequency channel separation just resolved by the visible spectrometer used in this setup. A 9-nm wavelength separation in the communication band was mapped to a 1-nm separation in the visible band. It is interesting to note that the ultradense WDM channel spacing of 0.2 nm (25 GHz) would correspond to a separation of only 0.02 nm in the visible band, which is well beyond the capabilities of the spectrometer used in this work. Down-conversion back to the 1550-nm band at the receiving end would ease the need for a high-resolution visible spectrometer.

The pump was then placed at 840 nm, and two visible channels converted from two WDM channels at 1565.5 and 1551 nm, respectively, were spectrally demultiplexed, as illustrated in Figure 80, with measured Q-factors of 10.9dB. The measurements indicate no significant crosstalk, in agreement with the modeled prediction.

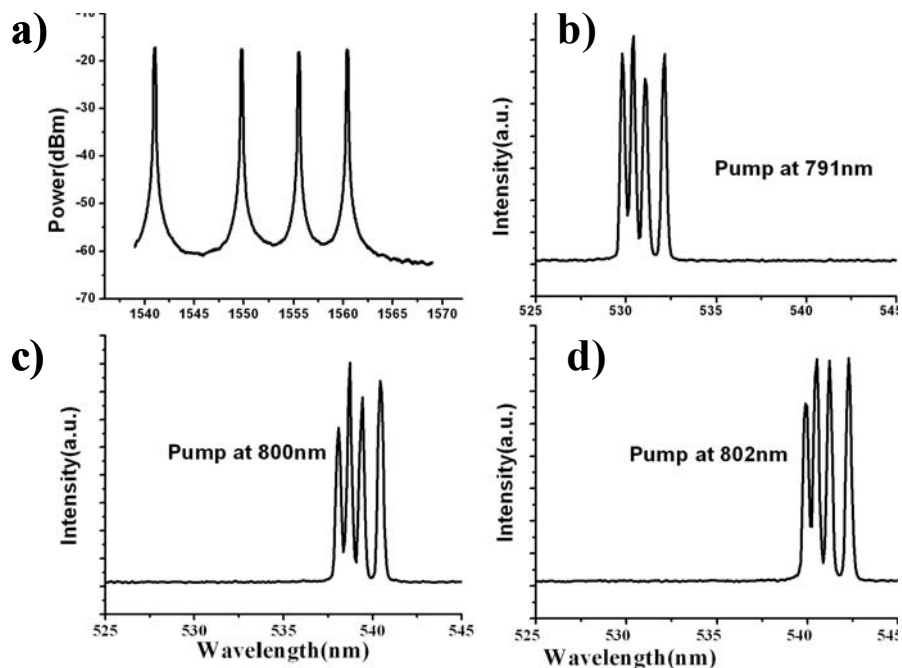


Figure 79 a) Four WDM channels at 1541nm, 1549nm, 1555nm and 1560nm are translated to visible spectral domain. Parametric pump is tuned to b) 791nm; c) 800nm and d) 802nm. Upper trace indicates visible (translated) and lower traces indicate 1550nm (signal) WDM band in all cases.

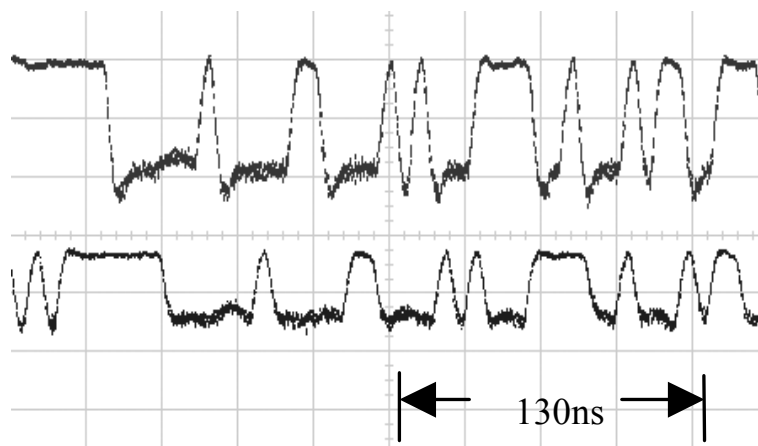


Figure 80 Channels demultiplexed after visible translation: 574nm (upper trace) and 576nm (lower trace).

In the final set of measurements, the Ti:Sapphire pump and 100-MHz visible receiver were replaced by a CW diode pump and GHz visible receiver, respectively. Faster modulation measurements were obtained using 20.7-dBm pump and 19-dBm signal coupled powers, yielding -16.7 dBm of visible power from the 5-m long PCF segment. The idler wavelength was tuned from 512 to 520 nm by sweeping the pump wavelength, similar to the Ti:Sapphire procedure described above. The NRZ modulated signal translation was thereafter demonstrated by setting the pump at 777.6 and 775.5 nm, respectively, and the signal at 1575 nm, resulting in idler wavelengths of 516.2 and 514.4 nm. The idler was received by the visible detector, which has a 3-dB rollover frequency of 1 GHz, and was subsequently observed using the fast sampling scope. The received 1-Gbps NRZ waveform and eye diagram are shown in Figure 81a. The corresponding Q-factor is 15.27 dB. The performance of the architecture was quantified by the BER, measured using a $2^{31}-1$ PRBS pattern to achieve error-free performance. Figure 82 shows the measured BER curve at the two different wavelengths, indicating that tuning did not influence the performance of the wavelength-conversion process. By increasing the NRZ rate beyond the receiver 3dB rollover frequency (1 GHz), the amplitude of the 1.5-GHz idler waveform was reduced and the measured Q-factor dropped to 13.26 dB, as shown in Figure 81b.

We then measured the detection margin by sweeping the detection threshold and detection time, the result of which is shown in Figure 83. The measured error-free detection threshold margin is one fourth of the eye opening and the error-free detection time margin is one half of the bit period.

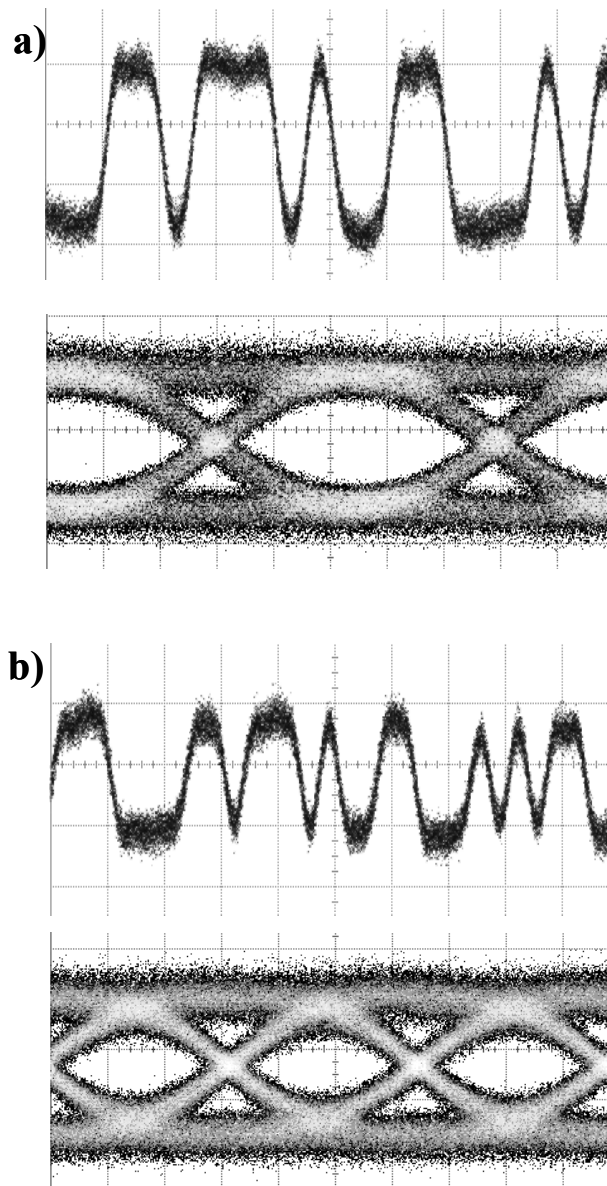


Figure 81 Measured waveform at a) 1Gbps and b) 1.5Gbps and corresponding eye diagrams.

Each division corresponds to 2ns for upper figures and 200ps for lower figures.

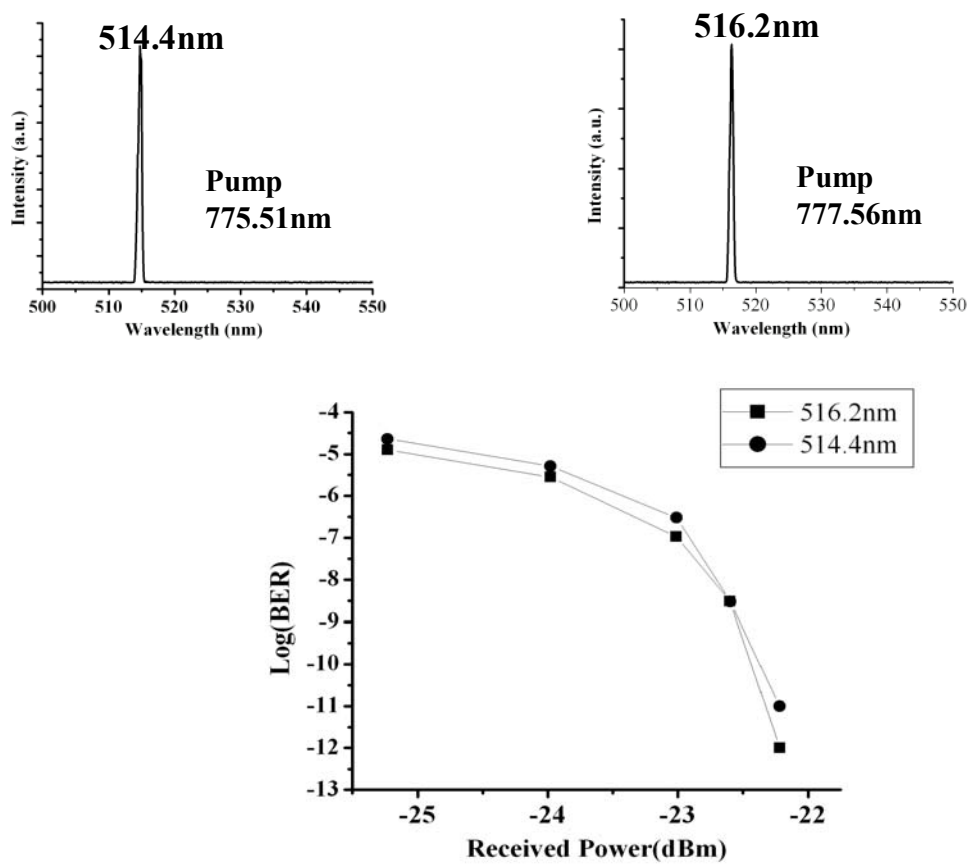


Figure 82 Measured BER curve for idlers at 516.2nm and 514.4nm, respectively.

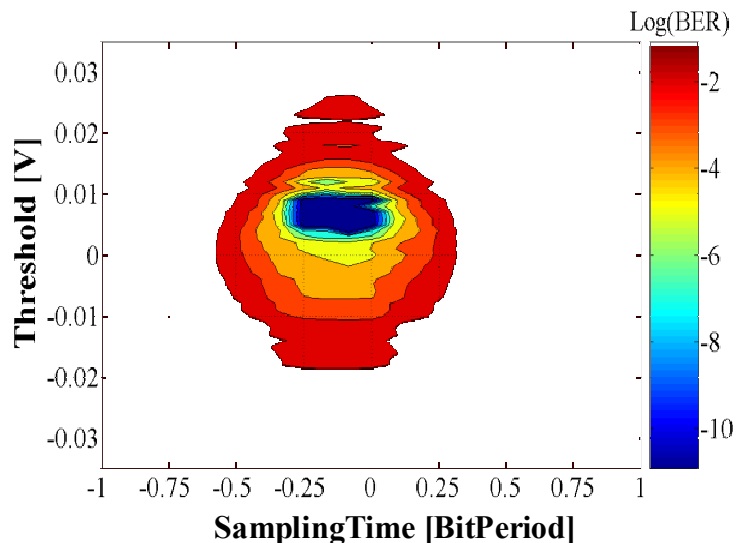


Figure 83 Contour plot indicating the detection margin. The measured error-free detection threshold margin is one fourth of the eye opening and the error-free detection time margin is one half of the bit period.

In summary, we have demonstrated the translation of single and multiple modulated channels between the standard near-infrared and visible bands. The reported conversion over 375 THz is a record for modulated channel translation in an all-fiber structure. Bit error-rates at 155 Mbps and 1 Gb/s were measured for the intensity modulated signals translated from near infrared to the visible spectrum. No significant impairment associated with the translation process was observed in either the single- or multiple-channel case. The experimental investigation was performed using commercial PCF coils, which were not designed to support 1550-nm guiding. Improved translation performance can be achieved by a combination of dispersion-optimized, low-loss PCF and higher power single-frequency pump, which represents a natural extension of the reported work. While a more sensitive and faster visible detector would certainly facilitate the optimization of the near-infrared to visible translator, its availability (or lack

thereof) is not a fundamental obstacle: a two-way, time-division architecture can be constructed using the same device, which allows performance characterization within the originating (near-infrared) band. We also believe that significant opportunity remains in further investigations that include multiple-pump parametric architectures and dual ZDW-PCFs tailored for nondegenerate FPM coupling. However, a significant challenge in quantifying the impact of spatial dispersion and polarization fluctuations in the PCF on the performance of the translator system is recognized.

4.5 Phase modulation translation from NIR to visible band

Phase modulation, in comparison to the amplitude modulation, has an increased detection sensitivity¹⁴⁰, which is an important attribute for communication link operation, under variable environmental disturbances, in e.g. submarine communication links. More importantly, the ability to modulate and detect phase information is critical in coherent spectroscopic applications. As an example, in interferometric coherent anti-Stokes Raman scattering (CARS) microscopy, a phase controllable anti-Stokes local oscillator is used for elimination of the nonresonant background^{141, 142}. On the other hand, Distant-band translation, due to the large frequency shift, is very sensitive to PCF dispersion fluctuation and phase noise from the pump or signal, hindering a high-fidelity phase translation process. In this section, we demonstrate an error-free parametric phase translation of 1Gbps pseudo-random bit sequence (PRBS) pattern from 1575 nm signal to 518 nm idler in a dual zero dispersion wavelength (ZDWL) PCF¹⁴³.

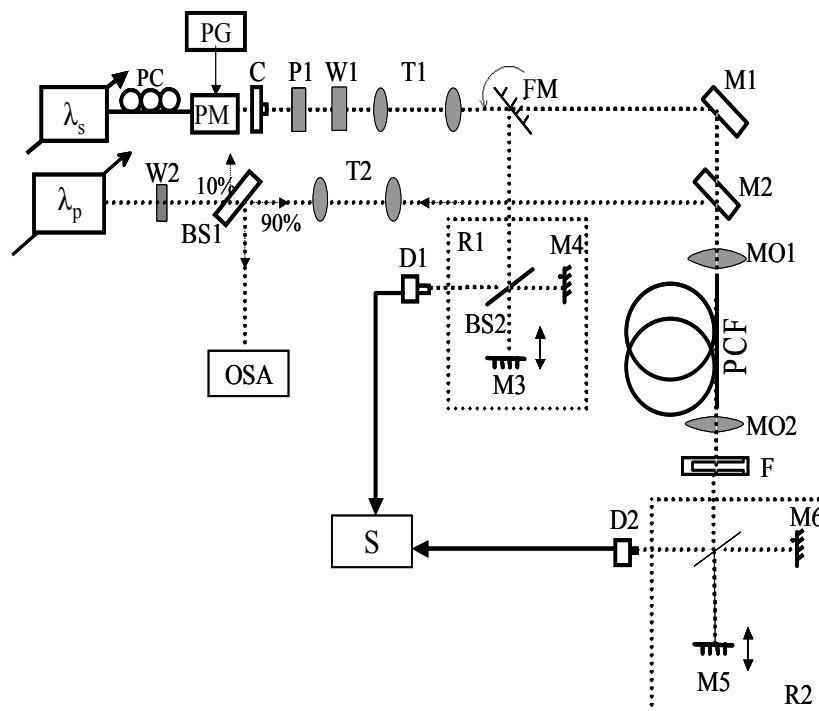


Figure 84 Experimental setup. λ_p : pump transmitter; λ_s : signal transmitter; PM – phase modulator; PG – pattern generator; C: collimator; P1 – polarizer; T1-T2: telescope system; M1 – M6: mirrors; W1-W2: half-waveplates; FM – flip mirror; BS1: 90/10 beam splitter; MO1-MO2 – microscopic objectives; D1-D2 – detectors; R1-R2: receivers; F: filter; S: oscilloscope; OSA: optical spectrum analyzer.

Figure 84 shows the experimental setup. A narrow linewidth (~ 500 kHz) semiconductor laser with 1.4 W maximum output power and a tuning range from 768 nm to 787 nm was used as a pump. After passing through the polarization tuning and beam shaping optics (W2 to T2), the pump beam was reflected by a dichroic beam combiner M2 and coupled into the PCF by a high numerical aperture (NA) ($40\times$) microscopic objective MO1. A 90/10 tap (BS1) was installed in the pump arm to monitor both the pump power level and the back-reflecting Brillouin scattering from the PCF. For the signal arm, the signal transmitter was constructed of an L-band tunable laser, an external

phase modulator, and a high power erbium doped fiber amplifier (EDFA). The modulated signal beam was sent through a free space polarization controller (P1 and W1) in order to facilitate the signal and the pump polarization alignment. Finally, the telescope system (T1) was used to adapt the beam size to the coupling-in objective MO1. The quality of the phase modulation on the signal was monitored by a flip-mirror (FM) before coupling into the PCF: With the FM flipped up, the signal was diverted to a 1550 nm one-bit delay Michelson interferometer; whereas the signal path was unaffected and overlapped with the pump beam into the PCF, with the FM flipped down. The fiber under test was inserted between the two objectives MO1 and MO2. Specifically, a 12-meter coil and a 5-meter coil were used in this experiment. Figure 85 shows the transverse structure of the PCF coils measured with scanning electron microscope (SEM). The measured period and air-hole diameters were $1.3\mu\text{m}$ and $0.685\mu\text{m}$, respectively. The innermost ring layer contains two opposite air holes that are 20% larger than other air holes, making the fiber polarization maintaining. The accuracy of the SEM measurements was 5%. The fiber has a parabolic dispersion profile, with two zero dispersion wavelengths at 750 ± 15 nm and 1250 ± 25 nm. The maximum dispersion was estimated to be 70 ps/km/nm at 1001 nm. The measured nonlinearity coefficient and birefringence of the fiber at 780nm were 70/W/km and 3×10^{-4} , respectively. The fiber was a commercial PCF, originally designed for supercontinuum generation at 800 nm range with a relatively low loss (~ 80 dB/km) at 780 nm. The PCF, however, exhibited high loss at both 1550 nm and 500 nm range, estimated to be in the order of 1000 dB/km and 400 dB/km, respectively. A previous work detailed the impact of PCF loss on the conversion efficiencies²¹. Further more, the

fiber was estimated to have a cut-off wavelength at about 600nm. The fiber was, thus, far from optimized for the purpose of the intended translation experiments .

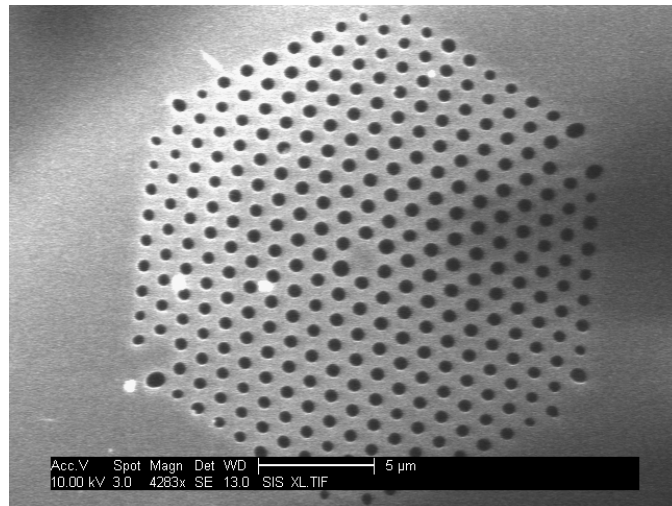


Figure 85 Transverse structure of the PCF used in the experiment. The core, formed by missing one air hole in the center, is about 1.8 μ m diameter.

The power coupled into the fiber core was discussed earlier in section 4.1. The coupling throughout the experiment was optimized for the pump, which, consequently, compromised the coupling efficiency for the signal wave. At the output of the PCF pump, signal and idler were collimated by a high NA objective (MO2). A 3-millimeter thick bandpass filter (F) in the visible range was used to block both the pump and signal at the output. The separated idler was finally directed to a spectrometer or a visible photo-detector block, which contained a visible one-bit delay Michelson receiver R2 (shown in Figure 84) that was used to receive and decode the idler DPSK stream, converting the phase encoded information into intensity modulation. The decoded waveform was finally sampled using a digital oscilloscope and/or received by the analyzer section of the bit-error-ratio tester (BERT) to verify error-free translation performance.

The signal beam was phase-modulated with a short word pattern, or 2^{23} long non-return-to-zero (NRZ) pseudo-random bit sequence (PRBS) at 1Gbps. A 5-meter coil was chosen for the phase translation experiment, for its high SBS threshold and less overall loss (see section 4.6.1). The pump was positioned at 779.6 nm and the signal at 1575 nm for the best phase matching. 174 mW (22.4 dBm) of pump and 120mW (20.7dBm) of signal were coupled into the PCF and generated 35 μ W (-14.55 dBm) idler at 518 nm. Considerable radiative loss, in the form of green luminescence along the entire PCF length, was observed. We note that this observation was to be expected from the high PCF loss in the visible band. Consequently significantly more idler-power generation should in principle be possible by reducing the fiber loss in the visible region. The idler power was then kept constant at -14dBm in the subsequent experiments. The DPSK data transmitted on the signal wave were translated to the visible idler and the performance of the DPSK translation was then measured. At first, three short binary-phase word patterns were imprinted onto the signal, and were recovered at the idler band, as shown in Figure 86. The interferometer was biased to introduce a π phase shift, which caused the output intensity pattern to be inverted relative to the originally transmitted sequence. A simple micrometer adjustment provided the non-inverted receiver output. The signal was then phase coded with a long PRBS pattern. The received pattern in the visible idler band was decoded by the R1 receiver block, compared with the original pattern and the bit error rate (BER) was measured. The idler power incident

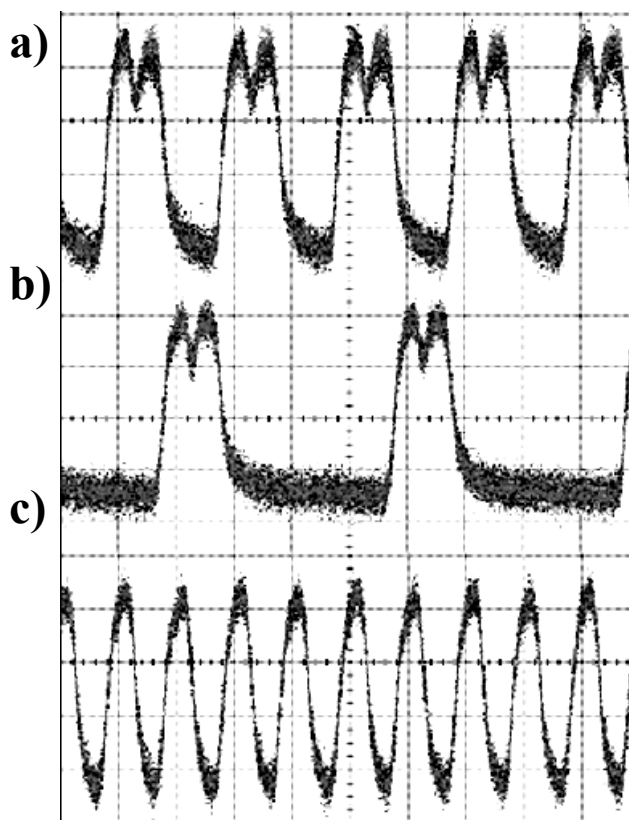


Figure 86 Received visible channel at 518 nm with 1575 nm signal phase coded by data
 pattern a) 1000 b) 1000 0000 c) 1100. Time scale: 2 ns/div

into the receiver was altered by tuning the neutral density filter in front of the receiver, which enabled the variation of the signal-to-noise (SNR) in the BER measurement. Figure 87 shows the received eye diagram and measured BER in subplots (a) and (b), respectively. With the received idler power of -19 dBm, the error-free performance was achieved. Finally, the BER contour plot of the eye diagram indicating the performance margin was measured, as shown in Figure 87(c). The BER contour plot indicates transient instabilities in the system performance over the five minutes' interval in which the performance was measured. The instability is attributed to the pump power fluctuation, in addition to the phase bias instability of the R1 receiver, both of which degraded the contrast between the decoded marks and zeros. A more stable pump, as well

as the setup integration into a compact package would undoubtedly increase the stability of the translation process. It is also worth noticing that a single-port Michelson interferometer receiver introduced an additional 3dB of loss; higher detection sensitivity

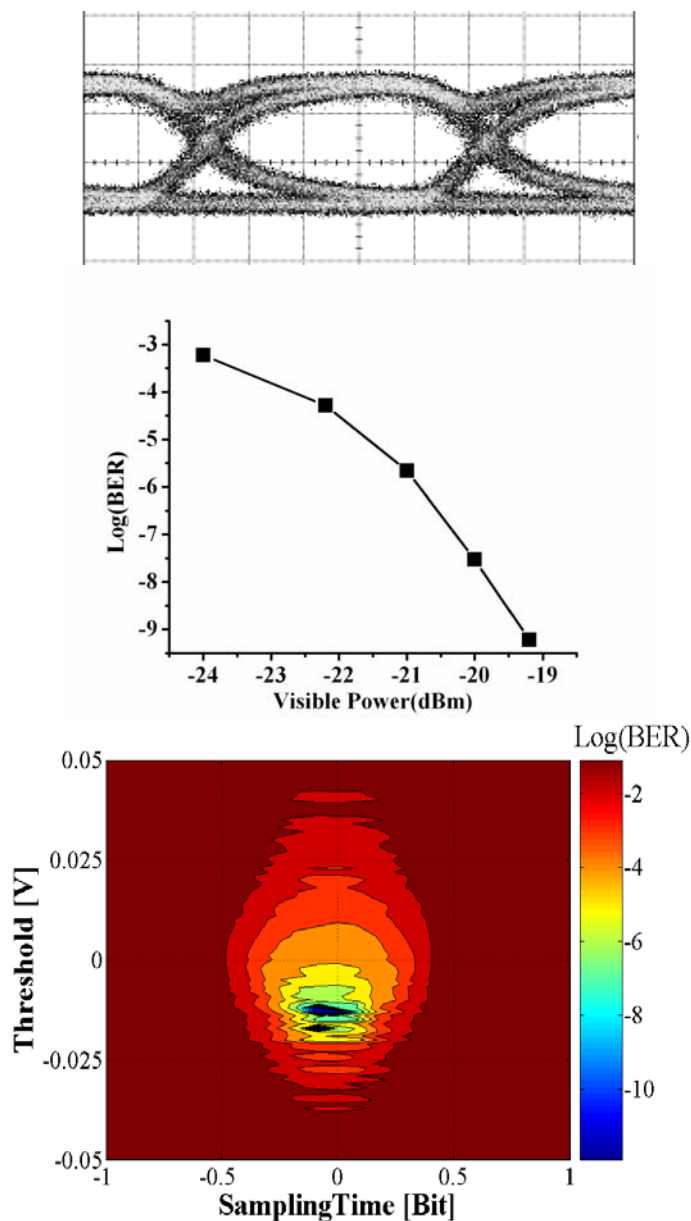


Figure 87 a) Measured eye diagram for the translated 1Gbps phase coded signal. Time scale: 200 ps/div; b) measured BER curve c) BER contour plot of the eye diagram

can be achieved by changing the receiver into a two-port Michelson or Mach-Zehnder configurations.

In conclusion, a translation of Gbps phase modulated signal from the conventional fiber-optic communication window (1550nm) to the visible band with error-free performance was demonstrated. -14.55 dBm of visible power was generated by a parametric mixing of 22.4 dBm of input pump power and 20.8 dBm of input signal, in a 5-meter PCF fiber designed for supercontinuum generation around the 800nm, with excessive (1000 dB/km) loss in the visible and the 1550 nm bands. Distinct phase matching contours were measured for the two principle axes, as a consequence of the asymmetric PCF transverse structure. The low SBS threshold in the PCF was identified to be the major limitation on the system performance, restricting the pump power coupling into the PCF and introducing both phase and intensity noise to the translation process. The SBS threshold was also found to be highly polarization dependent. A spectrally-broadened pump would certainly allow the coupling of more pump power increasing the attainable idler power. However, this, in turn, would also introduce additional phase noise to the translation process. A simple solution is seen in a counter-phased two-pump architecture, which combines the spectrally broadened pumps and narrow idler generation. The distant band phase-preserving translation from the communication to the visible band opens a new way for high capacity submarine communications and advanced visible spectroscopy techniques. Due to the spectral-invariant nature of the parametric process, the same technology could be applied to other spectral bands, such as the short-wavelength infrared (SWIR) and the mid-infrared (MIR) windows.

4.6 Characterization of Parametric Translation in PCF

In previous sections, parametric translation of over 400THz from 1550 nm band to visible band was described. Due to the coherent nature of the parametric process, the amplitude and phase coding was translated from telecom band to idler band in error-free manner, demonstrating a new transmitter technology in the visible band. However, the translation efficiency is low in the aforementioned experiments – the maximum power that has been reported is tens of microwatts, which corresponds to a conversion efficiency of ~0.03%. One reason of such low efficiency is the high loss of the PCF used. However, further testing regarding parametric generation in PCF are required in order to understand the system's behavior and find out the impairment mechanisms in order to enhance the performance by addressing the issues by either better system architecture or improved PCF structure design.

During the experiments, other than the significant fiber loss, four major impairment mechanisms were observed and quantified: Stimulated Brillouin Scattering (SBS), multimode guiding at short wavelength, the polarization decoupling among the interacting waves and the dispersion fluctuations, each of which will be studied in detail in the following subsections. Techniques to address each of the impairment mechanisms are discussed and implemented.

4.6.1 SBS in PCF

At first set of the experiments shown in section 4.3 indicated a sub-500mW SBS threshold in all launching conditions (fiber length ≥ 5 meters), imposing a hard limit on the overall conversion efficiency of the system. In this section we conduct a set of

experiments to examine the SBS properties on a 12-meter and a 5-meter PCF coils. The power transmission curve was measured with different input polarization states and the back-reflecting spectrum was monitored at all times. Since all the PCF used in our work has similar dimensions, their SBS properties are similar.

Due to the high PCF birefringence, the SBS threshold was observed to be highly polarization dependent during the experiment. Figure 88 shows the measured results for the 12-meter PCF coil. Figure 88a shows the measured power transmission curve, indicating the SBS threshold of 105 mW on the principal axes, and that of 210 mW, when the input pump polarization is rotated at 45° with respect to the principal axis. The 3dB difference between the two polarization states agrees well with previously reported results¹⁴⁴ and was previously predicted in¹⁴⁵. The SBS threshold for an arbitrary input polarization state was experimentally corroborated to be confined to the 105 - 210mW range, defined by the afore-mentioned two limiting cases. In Figure 88b, the reflected and the transmitted pump powers are shown, in agreement with the measured threshold shown in Figure 88a. As expected, at the onset of the SBS threshold, a sharp increase in the reflected power is observed at the fiber input. A typical back-reflected spectrum obtained with a 780.2nm pump is shown in Figure 88c. The pump power equaled 200mW and its polarization was aligned to one of the principle axes. A 20GHz downshifted Brillouin peak was observed to be 5dB higher than the Rayleigh back scattering, indicating an onset of an efficient SBS process in the PCF.

The Brillouin threshold can be estimated by a simple expression²⁶:

$$g_B P_{th} L_{eff} / A_{eff} \sim 21 \quad (76)$$

in which $g_B \sim 5 \times 10^{-11}$ m/W is the Brillouin gain coefficient, P_{th} is the SBS threshold, L_{eff} is the effective fiber length, and $A_{eff} \sim 2.5 \mu\text{m}^2$ is the effective mode area at 780 nm. The expression results in the SBS threshold of 111 mW in a 12-meter coil (loss adjusted), in excellent agreement with the experimental measurements. The measured Brillouin threshold for short (5- meter) coil showed similar behavior to the 12-meter coil with increased threshold value of 250mW on principle axes and 500mW at the polarization state 45° to the principle axes.

The onset of SBS greatly degrades the integrity of the translated modulation. In order to prevent the SBS in the PCF, the input pump power has to be maintained well below the SBS threshold. We studied the effect of SBS on the translation process by translating 1 Gbps intensity-modulated signal from 1575nm to 518nm by placing the pump at 779.6nm. It was found that for an input pump power as low as 74mW, aligned along the principle axis P1, the Brillouin impairment imposed on the translated idler (in the 12-meter coil) was non-negligible. Figure 89a shows the resulting translated intensity modulated pattern of the idler. Figure 89b shows the same waveform averaged by collecting 32 sampled traces. As demonstrated in Figure 89, the Brillouin effect resulted in a massive loss of the signal integrity. Consequently, the phase translation experiments were conducted using a short (5-meter) coil to operate far from the Brillouin induced impairment regime. Even though the SBS threshold for the 5-meter coil was at 250mW, the incident pump power was limited to 174mW in order to maintain sufficient guardband, and obtain impairment-free translated phase information on the idler.

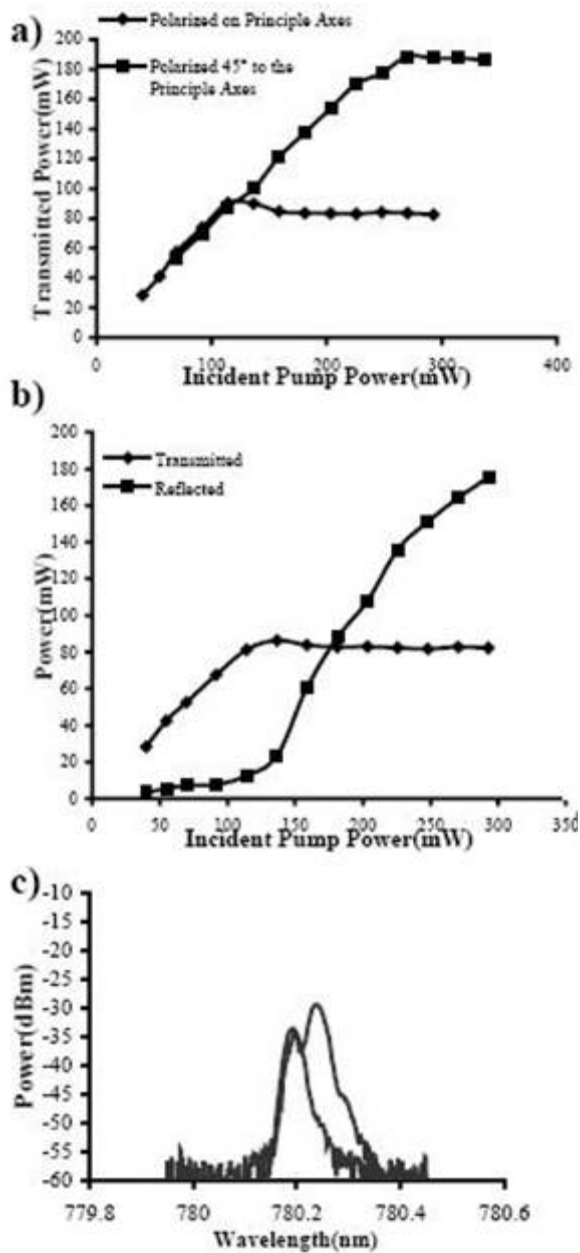


Figure 88. a) Power transmission curve for the cases when the pump input polarization is aligned with the principle axes (open markers) and rotated at 45° to the principle axes (solid markers); Incident pump power refers to the power that is coupled into the PCF input end; b) Measured reflected and transmitted power when the pump is aligned on the principle axes; c) Back-reflecting spectrum of 780.2nm pump at 50mW input power level (black curve) and at 200mW input power level (gray curve) and input polarization aligned to the principle axes.

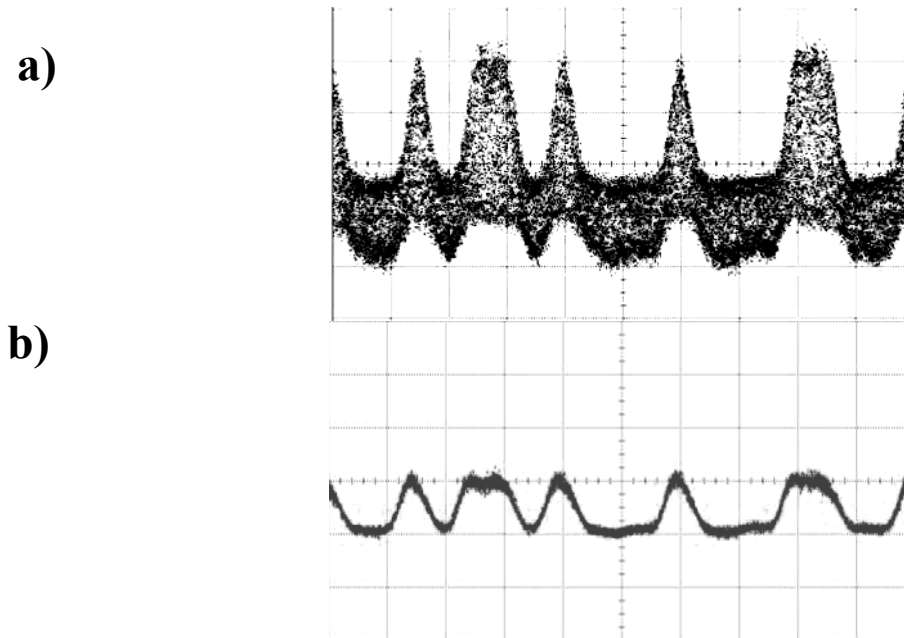


Figure 89 a) Translated 1Gbps amplitude shift keying signal with SBS onset b) the identical waveform recorded by time-averaging. Time scale: 2ns/div

Although the experiment described above implies that crossed pump polarization (45° with respect to the principle axis) allowed for higher SBS threshold, it was avoided due to the large birefringence difference between the pump and signal wavelength. If not aligned with the principle axes, the pump and the signal will experience different polarization evolution in the fiber, reducing the electrical field coupling between the two waves and resulting in an inefficient four-wave mixing process, which is discussed in detail in the following sub-section.

SBS could be alleviated through many ways, including temperature control of the fiber¹⁴⁶ and pump dithering^{50, 51}. In our experiments, dithering the pump phase is relatively easier. The diode pump we used, if operated at the longer wavelength side ($>780\text{nm}$), the cavity of which could be misaligned by offsetting the cavity mode and the

grating transmission peak, which will broaden the output laser linewidth above 1GHz. Using this linewidth broadened pump, the SBS could be effectively suppressed and more power could be coupled into the PCF. For example, we were managed to couple ~300mW pump into a 20-meter PCF, which boosted the idler (visible) power several tens of times.

The pump and signal are placed at 780 nm and 1575 nm, respectively, with maximum 270mW pump power and 200mW signal power coupled into the fiber. We first fix signal at 200 mW and vary the input pump power, the generated idler power is shown in Figure 90.

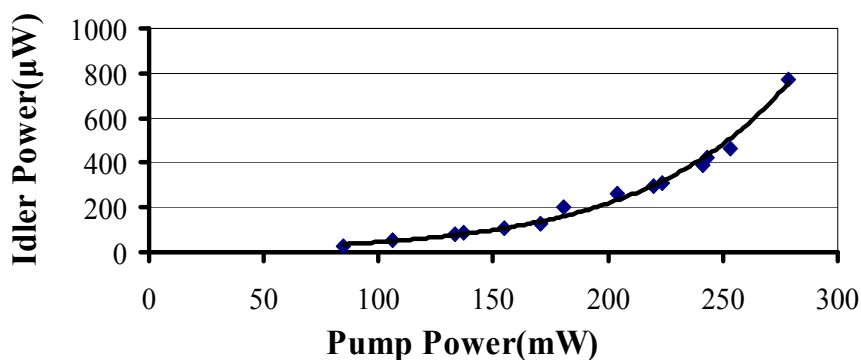


Figure 90 Measured (520nm) idler power with varying pump input. The signal power is fixed at 240mW. An exponential tendency was measured.

Figure 90 shows an exponential growth of idler power as the pump power is increased. When the pump power is maximized at 270mW, maximum of 800μW idler power was achieved, corresponding a conversion efficiency of 0.4%. This measured value is at least 13dB higher than previously reported results. However, the conversion

efficiency is still low, indicating other impairment mechanisms other than SBS also impacts significantly on the parametric process.

4.6.2 Polarization decoupling

The experiments demonstrated that PCF shows very different birefringent properties at pump, signal and idler wavelengths . As an example, for a PCF structure shown in Figure 91a, the mode field diameter (MFD) measurements showed that the 500 nm idler wave was well confined in the PCF core and therefore experiences nearly isotropic structure, suffering very little shape-induced birefringence. The 780 nm pump, however, has larger MFD and the mode edge experiences nearly two PM holes and suffers considerable shape induced birefringence. The 1550 nm wave had the largest MFD, and penetrates into more air-hole layers than the 780nm wave. Since the cladding structure is symmetric, the birefringence at 1550nm ought to be smaller than the 780nm wave. Moreover, since PCF transverse structure generally suffers severe longitudinal variation, the pump, signal and idler waves could also experience different PCF structural configuration during propagation, and, thus, exhibits different polarization evolution along the fiber, shown in Figure 91b. As a consequence, the polarization coupling between the pump and signal may vary with propagation, thus significantly reducing the four-wave mixing efficiency. Therefore, a careful study of the polarization properties of the PCF in the vicinity of 780 nm, 1550 nm and 500 nm range was warranted in order to optimize the conversion efficiency, or, equivalently, to maximize the received power in the idler band.

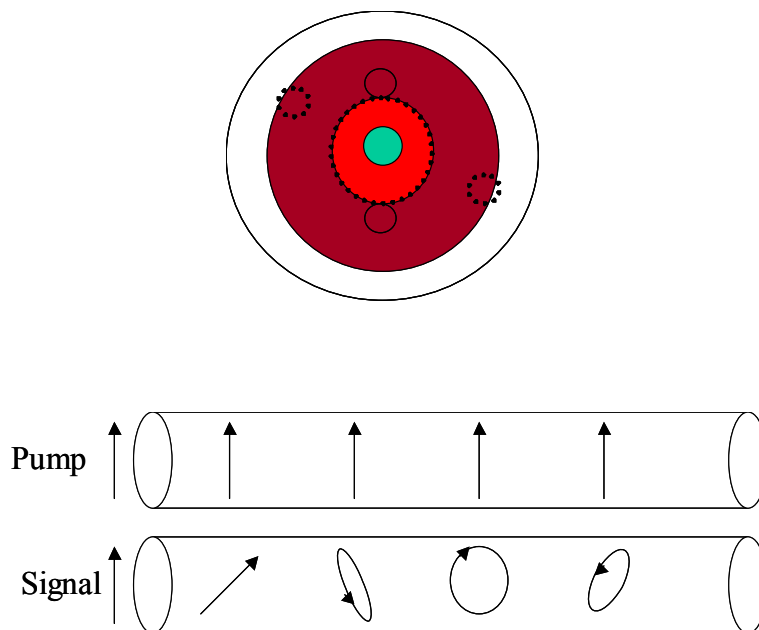


Figure 91 Illustration of a) MFD and b) polarization evolution of pump, signal and idler waves in PCF. Different MFD results in diverse polarization evolution of the three waves.

In first set of experiments only, the signal arm was active. We tested two representative fibers, namely, PCF B and C specified in subsection 4.6.4, which are 5-meter and 10-meter long respectively. As noticed earlier, PCF B is PM fiber containing two PM holes in the inner ring layer while PCF C were intended to be uniform, that is, polarization isotropic. We performed two sets of measurements on each fiber. In the first set of measurements, the differential group delays (DGD) at 780nm and 1550nm were measured and birefringence value were subsequently derived for pump and signal respectively. In the second set of experiments the degree of linear polarization was measured for the pump and the signal beams at both the input and output of the PCF in order to measure the polarization extinction of the fiber. The output from the pump laser was s-polarized and characterized with a 30dB polarization extinction ratio (PER), whereas the signal had 40dB PER. The degree of linear polarization after the PCF coil

was measured, after the output objective MO2, followed by a polarization analyzer. The setup is shown in Figure 92¹⁴⁷.

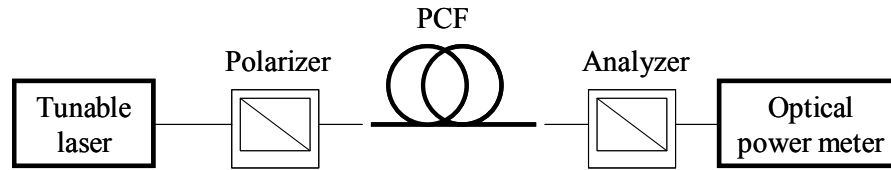


Figure 92 Setup for the fixed analyzer PMD measurement.

Measurements were firstly performed on PCF C with uniform structures. PMD measurements on DGD at both 780nm and 1550nm are shown in Figure 93a and Figure 93b, respectively. According to¹⁴⁵, the mean DGD $\langle \tau \rangle$ of the tested fiber can be determined by extrema counting from¹⁴⁵:

$$\langle \tau \rangle_{\lambda} = \frac{kN_e \lambda_{start} \lambda_{stop}}{2(\lambda_{stop} - \lambda_{start})c} \quad (77)$$

where λ_{stop} and λ_{start} are the ends of the wavelength sweep in meters, N_e represents the number of transmission extrema (peaks and valleys) that occur across the scan, and c is the speed of light. The unitless factor k is the mode-coupling factor that statistically accounts for the effects of the wavelength dependence of the principal states of polarization, generally between 0.6 and 1.

or alternatively,
$$\langle \tau \rangle_{\lambda} = \frac{(N_e - 1)k \lambda_{first\ extrema} \lambda_{last\ extrema}}{2(\lambda_{last\ extrema} - \lambda_{first\ extrema})c} \quad (78)$$

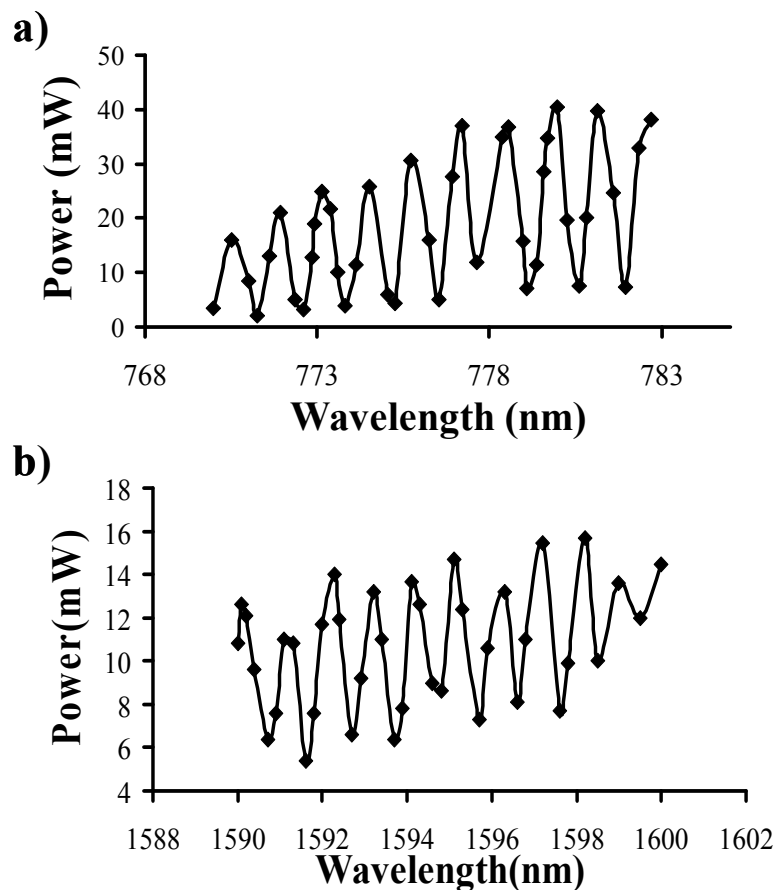


Figure 93 PMD measurement response for a) 780nm and b) 1550nm

The measurements showed that for the 10-meter PCF C, the DGD at 780nm is 1.4ps/10m while the DGD is 8.6ps/10m at 1550nm range, which results in the birefringence value to be 4.2×10^{-5} and 2.6×10^{-4} at 780nm range and 1550nm range, respectively, indicating a strong birefringence at signal and relatively weaker birefringence at pump. The measurements also indicate that PCF C is far from uniform structure – the imperfect manufacturing process results in strong birefringence, as pointed out in the chapter 2.

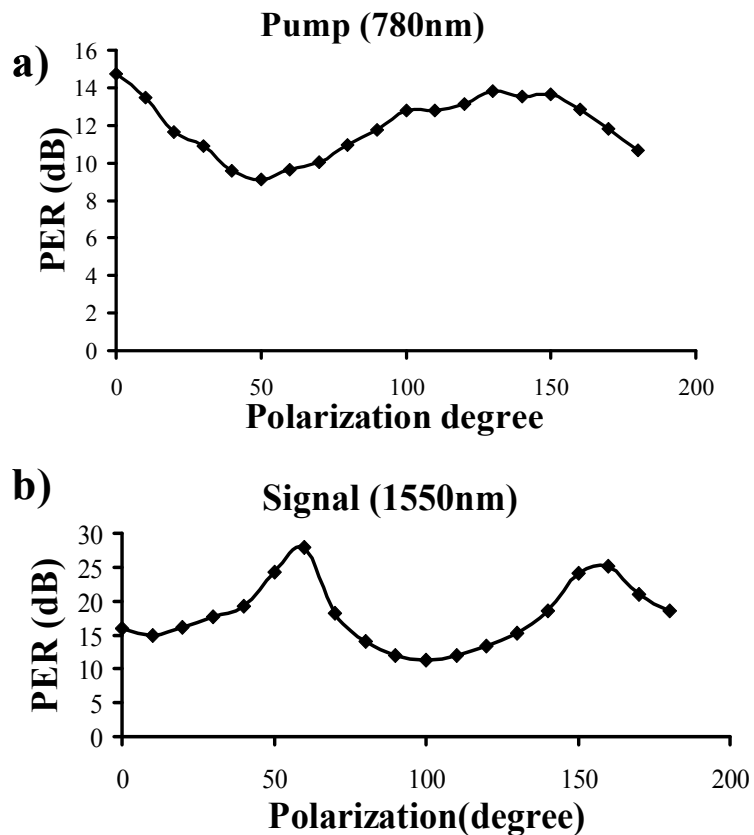


Figure 94 PER measurements for a) pump and b) signal, respectively. The results show that PER at signal wavelength is larger than that at pump wavelength, agreeing with the PMD measurements.

In the next set measurements, the polarization extinction ratio of PCF C was measured, the results of which are shown in Figure 94a and b, respectively. Figure 94 shows the measured degree of linear polarization for both the pump and the signal as their input polarization was varied, indicating the PCF having 14.5dB PER at pump wavelength and 30dB PER at signal wavelength. The measured results show that the fiber having high birefringence at 1550 nm and relatively low birefringence at 780 nm range and the principal axes for these two wavelengths almost overlap. Similar measurements were also done in the visible region by a 532nm source followed by a polarizer. The

measured PER curve, however, was degraded to less than 2dB (in the best case), and was characterized with poor contrast, suggesting a random birefringent nature of the PCF in the visible region. This result is easily understood as the 500-nm wave has a much smaller MFD and thus experiences significantly less shape-induced birefringence than the 780-nm and 1550-nm waves. The weak birefringence at 500-nm region implies non-perfect coupling among pump, signal and idler waves, resulting in considerably reduced conversion efficiency. A fiber optimized for parametric process therefore should maintain large birefringence at all three wavelengths.

We then performed the same measurements on a 5-meter PCF B. The measured birefringence value at 780 nm is 4×10^{-4} while the birefringence value becomes 8×10^{-5} at 1550 nm range, indicating a strong birefringent property at both pump and signal. Figure 95a shows the measured degree of linear polarization for both the pump and the signal as their input polarization was varied. The pump, launched with 30dB PER, was received with 28dB PER at the output, while the signal, which started with 40 dB PER, ended up with 22dB PER at the output of the PCF. The measured results show that the fiber maintains high birefringence at 1550 nm and that the principle axes at 1550 nm signal maintains the overlap with the principle axes of the 780 nm pump. Identical measurements were also done in the visible region by a 532nm source followed by a polarizer. The measured PER curve, however, was degraded to less than 5dB (in the best case), and was characterized with poor contrast, suggesting a random birefringent nature of the PCF in the visible region.

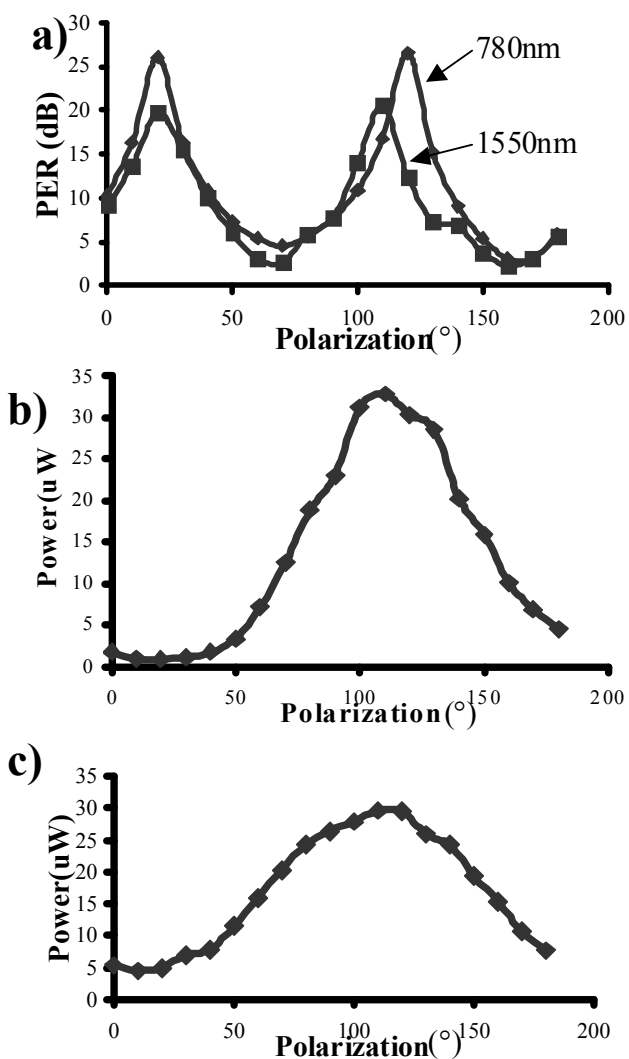


Figure 95. a) Measured degree of linear polarization at the output of the PCF for both the 780 nm and 1550 nm waves. b) Measured idler power (518 nm) when the signal (1575nm) input polarization is aligned to the P1 axis, and tuning the pump (780nm) input polarization; c) Measured idler power (518 nm) when the pump input polarization is aligned to the P1 axis, while the signal input polarization is varied.

A fiber optimized for parametric process therefore should maintain large birefringence at all three wavelengths. Figure 95b shows the measured visible idler power as the input polarization of the signal was held constant, and aligned with the principle

axis P1, while tuning the pump input polarization. Figure 95c illustrates the situation with the reversed roles: pump input polarization was held constant and aligned with P1 axis whilst the signal input polarization was rotated. In both cases, the pump and the signal were at 779.6 nm and 1575 nm, respectively. 174mW (22.4dBm) of pump and 120mW (20.7dBm) of signal were coupled into the PCF.

As expected, the most efficient generation of the visible idler was observed when the input polarization of both the pump and the signal were aligned along the same principal axis; in this case the two waves are phase-matched, maximizing the efficiency of the parametric process. On the other hand, in the case when the pump and the signal input polarizations are both aligned with the other principle axis, although still at the same wavelengths, the two waves do not mix efficiently resulting in no detectable idler power.

It is clear that polarization decoupling serves as one of the major impairment mechanisms, decreasing the parametric efficiency. This issue could be addressed by new PCF structure design, which renders high birefringence and therefore polarization maintaining across the optical spectrum, the details of which will be discussed in chapter 5.

4.6.3 Multimode guiding

As discussed in Chapter 3, PCF has the ability to guide light in single mode across broad optical spectrum. Indeed, during the experiments we observed that 1550nm signal and 780nm pump were guided in single mode in most PCFs, provided the input light is in Gaussian mode and the coupling plane is not tilted. However, we also observed that

500nm wave was guided in high order core modes or even cladding modes. There are two reasons of such guiding property at 500 nm band. First, the 500 nm wave is weakly guided in the core and easy to leak out of the core. Second, the cladding could also effectively guide this short wavelength due to the relatively large air-hole separation and large index contrast between the glass wire and air holes, as explained in Chapter 3. The guidance of short wavelength light is further complicated by the surface quality of the air-hole rings – a rough surface easily excites unwanted cladding modes. The guiding property across the optical spectrum could be studied by calculating the effective V number using the EIM mode, as shown in Chapter 3. Another useful method is to calculate (or measure) the cutoff length of PCF¹⁴⁸. Figure 96 is particularly instructive, showing the normalized guiding metrics¹⁴⁹. In the plot, x-axis is the air-filling ratio of a PCF while y-axis stands for the cutoff wavelength normalized to the period value. Wavelength region below the solid red curve is the single-mode guiding region and that above indicates the multi-mode guiding region.

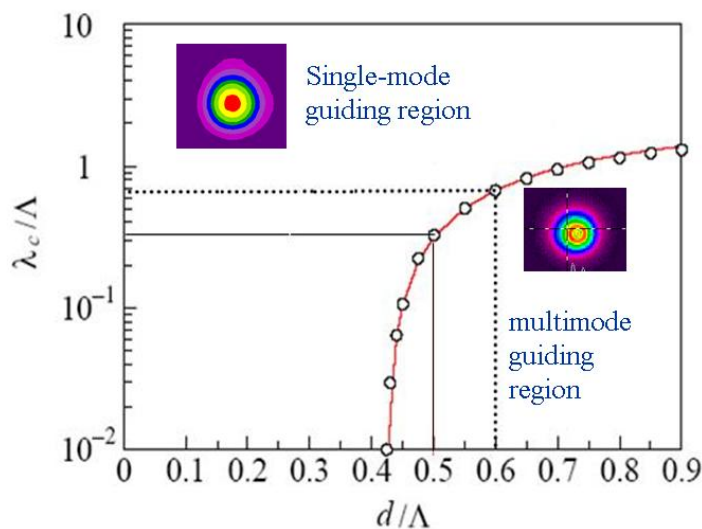


Figure 96 Guiding metrics of PCF

From Figure 96, we read that for a PCF with air-filling ratio 0.6 (d/Λ), the cutoff wavelength is $\sim 0.6\Lambda$ while the cutoff wavelength decreases to 0.25Λ for a 0.5 air-filling ratio structure (d/Λ). The PCFs used in our experiments had air-filling ratio between 0.5 and 0.6 and the period value between $1\mu\text{m}$ and $1.4\mu\text{m}$. As an example, PCF C in subsection 4.5 possess period $1.2\mu\text{m}$ and air-filling ratio 0.6, whose cutoff wavelength is about 780nm , indicating that both pump and idler could be guided in high-order mode. Indeed, we observed a second-order Hermite-Gaussian mode at pump wavelength when the coupling angle is oblique, shown in Figure 97. The transverse mode of 500 nm wave is more complicated, as shown in Figure 98. The effect can be explained by assuming that the outer six spots are the Fresnel pattern of the cladding mode, indicating that a large portion of the energy is not guided in the core. This is verified by observing the near field pattern of the transverse mode, which shows guided modes at the intersections of every three neighboring air-holes. These guided modes have certain phase relationship with each other. As we defocus the camera, we can observe the development of these modes and at some certain position the interference effect of these modes forms the outer 6 spots shown in Figure 98. As we defocus more, these 6 spots diverge quickly.

It is then important to measure the portion of light that is guided in single mode in the core, which really participated in the FWM process. A grating could be used to separate fundamental mode from high order core mode or cladding, the mechanism of which is shown in Figure 99 and Figure 100.

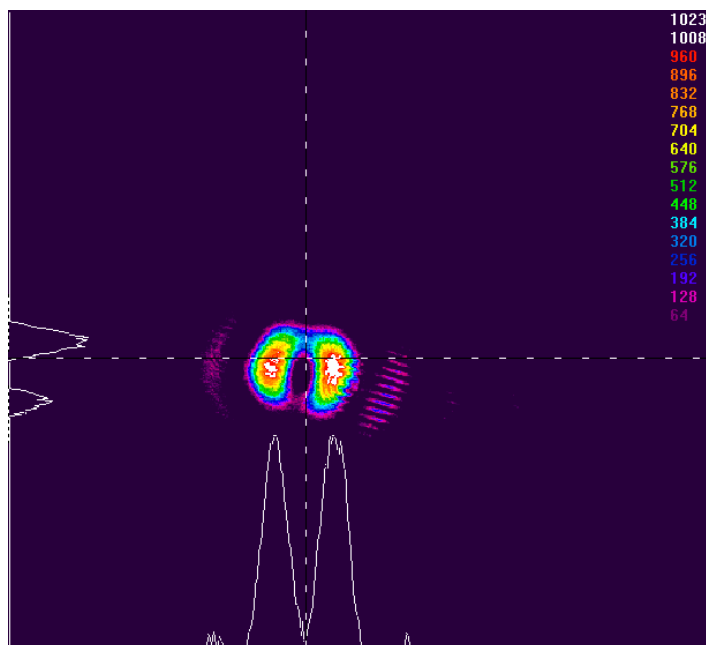


Figure 97 Near-field image reveals that PCF with $\Lambda=1.2\mu$ and $d/\Lambda=0.6$ can guide 780nm pump at second order transverse mode.

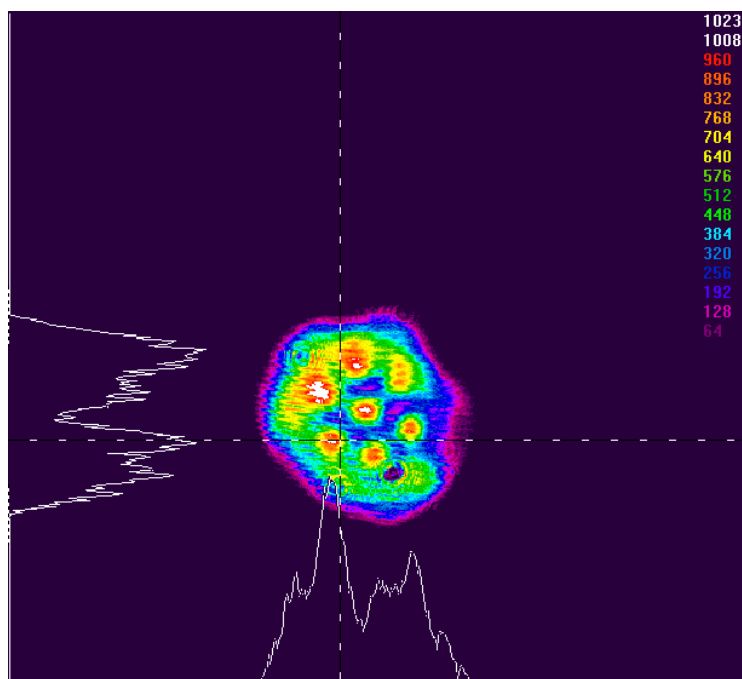


Figure 98 Near-field image of the transverse mode at 500 nm with the same fiber in figure

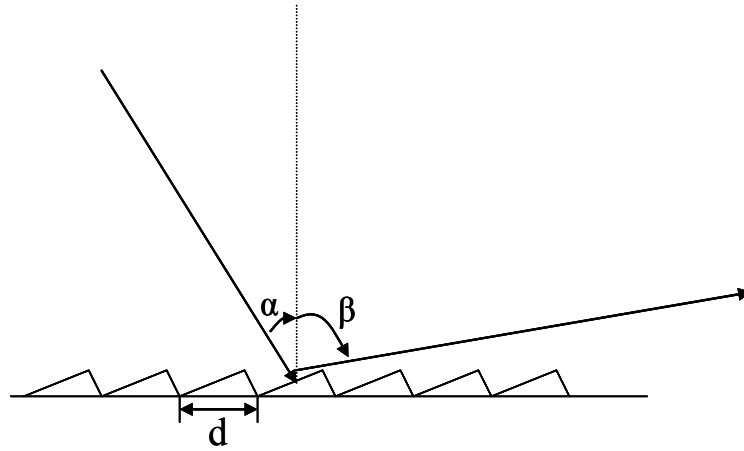


Figure 99 Grating schematics

When a plane wave incidents onto a grating with angle α , the grating equation has the following form:

$$n\lambda = d(\sin \beta - \sin \alpha) \quad (79)$$

On the other hand, a second order light could be view as two plane waves propagating with a small angle $2\Delta\alpha$ (see Figure 100) to each other. After diffracted by the grating, the angle between these two plane waves become $\Delta\beta$. When designed properly, $\Delta\beta$ becomes large, which helps separate the aforementioned two plane waves that forms second order mode (see Figure 100). In the same way, the grating could separate higher order mode from fundamental mode.

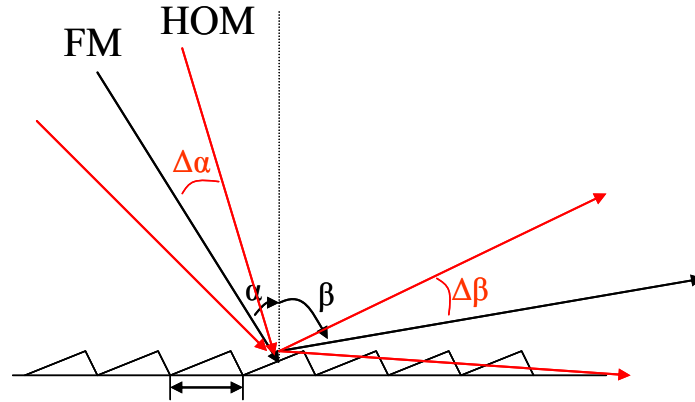


Figure 100 A grating helps separate high-order mode from fundamental mode. FM: fundamental mode; HOM: high order mode

In Figure 100, FM stands for fundamental mode while HOM means high-order mode. From (79), one can derive that

$$\begin{aligned} \frac{d\beta}{d\alpha} &= \frac{\cos \alpha}{\cos \beta} \\ \Rightarrow \frac{d\beta}{d\alpha} &= \frac{\cos \alpha}{\sqrt{1 - (\sin \alpha + n\lambda / d)^2}} \end{aligned} \quad (80)$$

(80) shows that by choosing incidence angle α , the grating parameter d and diffraction order properly one can obtain large ‘angular magnification’ such that the fundamental mode could be easily separated from the high-order modes. A set of calculations is shown in Figure 101a, in which $n=1$, that is, the first diffraction order is to be observed. We vary the grating parameter and showed that in all case, the angular magnification is significant once the incident angle approaches a certain value (graze incidence). In Figure 101b, we fix the grating parameter at $2\mu\text{m}$ and found that 2nd diffraction order light was needed in this case to observe 500nm wave. Using the above-

mentioned method, we measured that only 10-20% of 500 nm wave was in fundamental mode at the output of a 20-meter fiber generally.

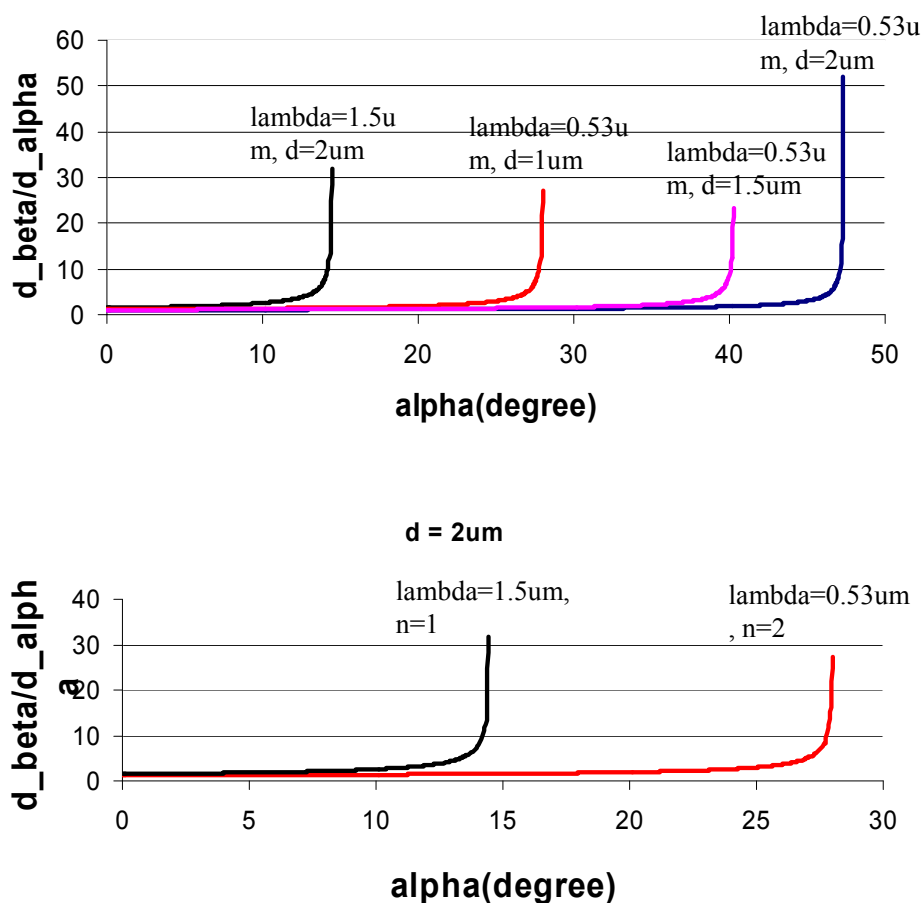


Figure 101 Two sets of calculations show that by properly setting the incident condition and the grating, separation of fundamental mode and high-order mode could be achieved.

The impact of multimodal guiding was then estimated by defining the coupling length as the length over which 10% of the power transferred from fundamental mode to high order modes. Using the coupled-mode equation stated in Chapter 2, we calculated the idler power evolution in PCF with various coupling length, shown in Figure 102 (pump power 250mW; signal power 200mW), indicating that idler generation becomes very inefficient as the coupling length becomes small. We estimated that the coupling

length is between 2-4 meters, resulting greatly reduced FWM efficiency comparing with the ideal case (all the light are in fundamental mode)

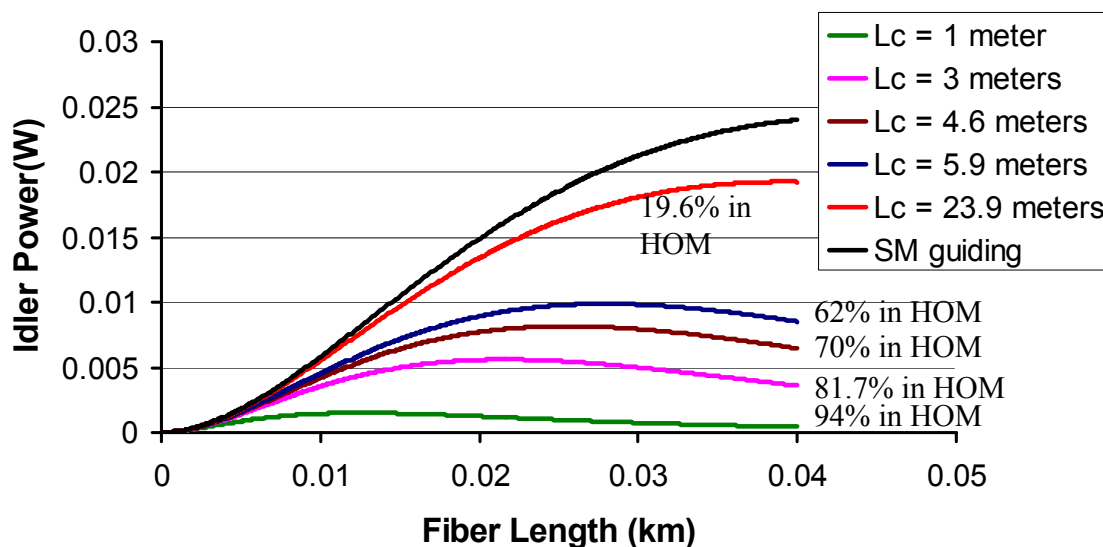


Figure 102 Impact of multi-mode guiding on the idler generation at various coupling lengths.

Multi-mode guiding is a server issue and not easy to be addressed. Straightening of the fiber could alleviate this issue to some extent. Figure 96 indicates that by selecting lower air-filling ratio, it is possible to render better guiding conditions. However, decreasing the air-filling ratio also means weaker waveguiding and therefore may result in undesirable dispersion response. We will discuss this issue further in chapter 5, where PCF design is studied in detail.

4.6.4 Dispersion fluctuation

Longitudinal dispersion fluctuations is generally considered as major impairment mechanisms in fiber parametric systems. In Chapter 2, we have discussed the impact of dispersion fluctuation on the two-pump parametric system, in which a four-sideband

model was established to predict the details of dispersion fluctuation effect. In this section, we will study the dispersion fluctuation in the telecom-to-visible translation parametric system both experimentally and theoretically. We first tested two PCF coils with various loss and dispersion condition (see Table 2). A set of cutback measurements was conducted and longitudinal structure variation induced dispersion fluctuation was identified to be one major impairment mechanism in the PCF parametric generation.

4.6.4.1 Experiments

The experimental setup is similar to that already described in sections 4.1-4.6 . Two PCF coils were marked with PCF B and C. Transverse structures of the two coils of PCF were shown in Figure 103a and b, respectively. Both coils contain small core surrounded by a triangular pattern of air holes. PCF B constitutes 10 ring layers with period equaling $1.35\mu\text{m}$ and air-filling ratio at 0.53. PCF C, on the other hand, has 14 ring layers with $1.2\mu\text{m}$ period and air-filling ratio 0.6. The structure parameters were measured with scanning electron microscope and maintain 3-5% measurement errors. PCF B have the loss condition as the following: 800 nm region: 100dB/km; 1550 nm region: 250dB/km; 500 nm region: 200dB/km. PCF C has improved loss condition as the loss in the above regions are 85dB/km, 100dB/km and 100dB/km, respectively. The improved loss condition for PCF C is due to the increased ring layers, offering better confinement of optical mode. PCF C has uniform structure while PCF B has two opposite air holes in the innermost ring layer that is 20% larger than other air-holes, leading to high birefringence of this fiber.

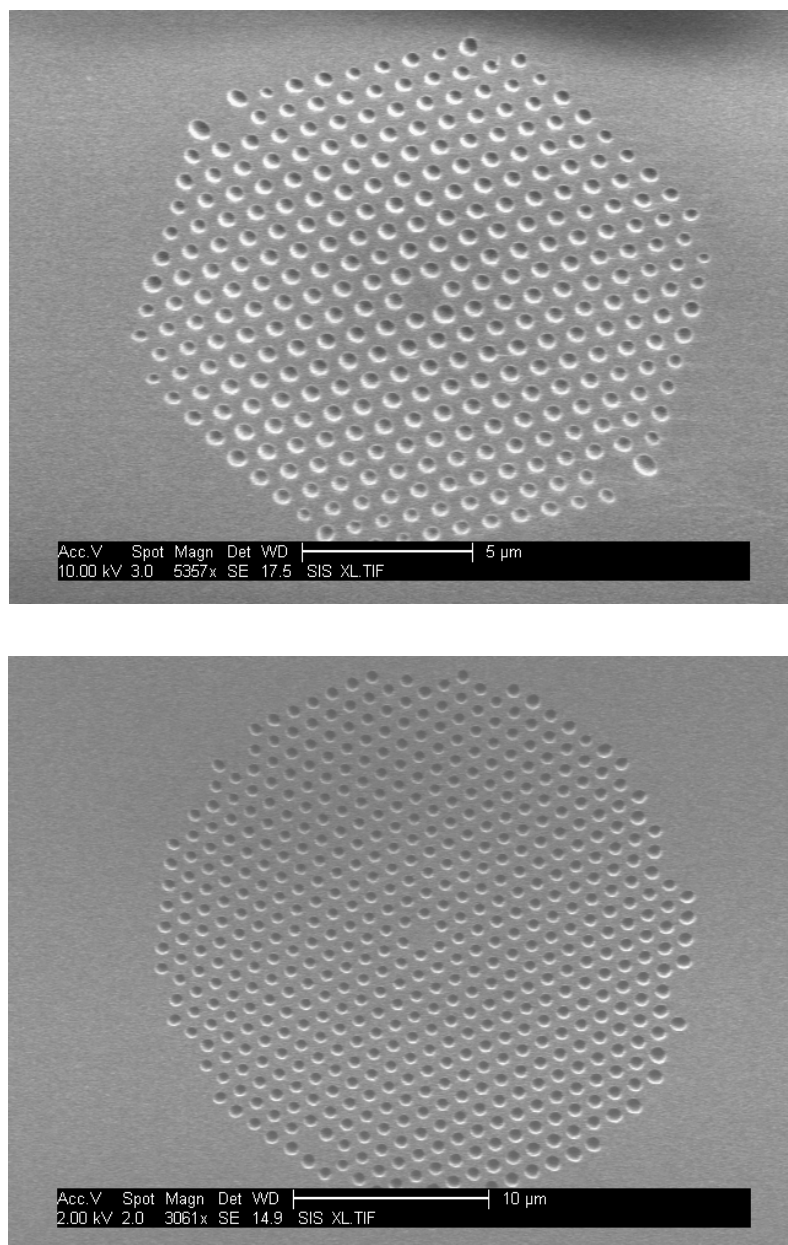


Figure 103 SEM image of the three PCF coils: a) PCF A b) PCF B c) PCF C tested in the experiments.

Table 3 Loss information of three tested PCF coils

PCF coil	Loss(dB/km)		
	800 nm	1550 nm	500nm
Coil B	~250	~100	~200
Coil C	~150	~70	~100

Original PCF B draw was 40 meter long. After measuring the idler power spectrum in the 40-meter fiber by tuning the pump from 779.5 to 785.5 nm, the fiber was cut to 35 meters, 30 meters, 20 meters and 10 meters step by step. During the cutback, one end of PCF was always fixed at the coupling-in setup while the cutback is done at the output end of the PCF to ensure that the input condition was not changed significantly during the cutback. At each length, the power spectrum measurement was then repeated. Throughout the experiment, the pump power was fixed at 250mW and the signal at 200mW. The measured results are shown in Figure 104. Two observations are important. Firstly, at all fiber lengths, the measured power spectrum is not continuous but shows fast oscillation features, an indication of quasi-phase matching instead of true phase matching behavior. Secondly, although the idler generation generally decreases as the fiber is cut shorter, the idler power shows saturation at the last 20-meter section – this saturation is particularly prominent at below 10 meters. Since we did not observe any pump or signal depletion throughout the experiment, this saturation behavior cannot be from the pump depletion process. The above two observations lead to the speculation that the dispersive fluctuation was significant in tested PCF samples. To test these assumptions, we performed the power spectrum measurements repeatedly with the final 10-meter section.

Subsequently, this 10-meter section was cut into two 5-meter sections and we repeated the same measurements on these two 5-meter sections as well, the results of which are shown in Figure 105.

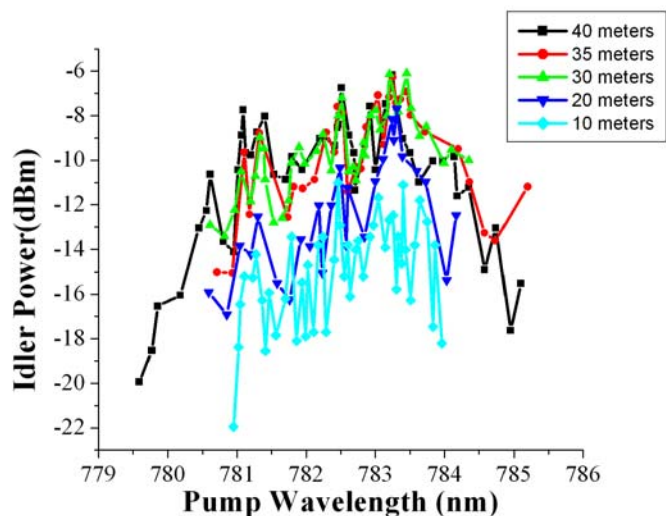


Figure 104 Cutback measurement results.

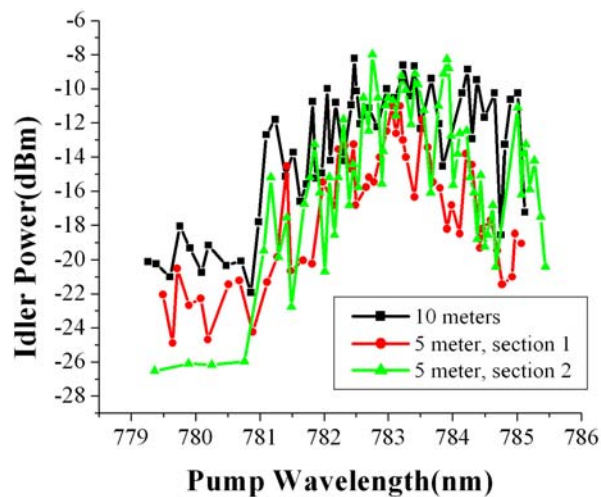


Figure 105 Cutback measurements of the last 10-meter section.

Besides the fact that the oscillating feature is observed repeatedly, Figure 105 also shows a surprising result that a 5-meter subsection, marked as green curve in the Figure

105, generates almost the same power as the 10-meter section does. On the other hand, for the other 5-meter section, marked as red curve, the generated idler was reduced by 3dB comparing to the previous 5-meter section under the same experimental conditions. The measurement confirmed that the dispersion fluctuation introduced by longitudinal fiber variation is a major impairment mechanism. To eliminate the possibility that PCF B is an exceptionally non-uniform fiber, we also tested another fiber coil PCF C. PCF C was originally 40-meter long as well and cut to a 30-meter and a 10-meter section. We repeated the above power spectrum measurements to these two sections. The result is shown in Figure 106. The same features were observed again – the 10-meter section almost generates the same power as the 30-meter section does. However, the 30-meter power measurement exhibited considerably larger continuity than that of the 10-meter section, attributed to the fact that the dispersion fluctuation impact is averaged over the longer section, resulting in a smoother tuning feature.

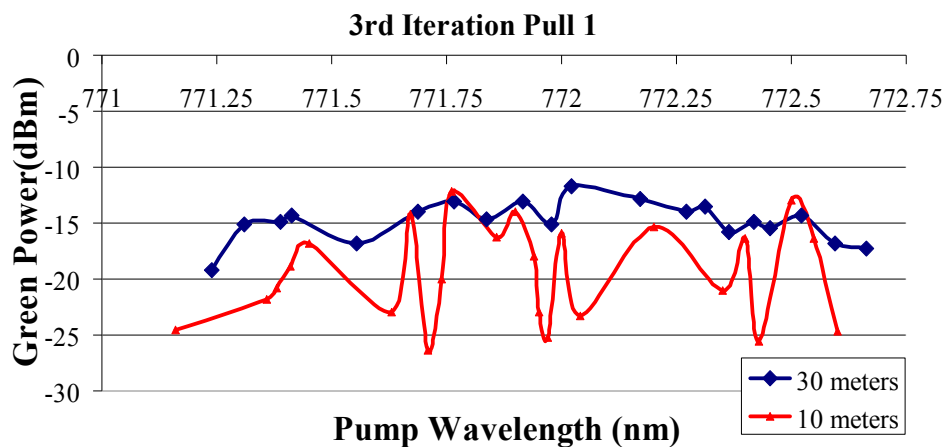


Figure 106 Power spectrum measurements for two-sections of a same PCF coil.

We have also performed SEM scanning of the cross-sections for all sections and observed no significant transverse structure variation. Considering the measurement

accuracy is only 3-5%, the global longitudinal variation ought to be below 3%, agreeing with the reported 1% PCF manufacturing precision⁵⁷.

4.6.4.2 Theoretical analysis and simulations

Simulation of the impact of dispersion fluctuation on the parametric generation in PCF has been previously studied based on an effective index model, which states that for a 0.02% core size variation over a 2-meter correlation length, the efficiency for a 100THz frequency shift parametric generation is 40dB lower than that of a ~0THz shift parametric generation¹⁵⁰. In the above experiments, parametric translation frequency shift is close to 200THz, therefore should suffer severely from the dispersion fluctuation. A simple estimation could be performed based on effective index model, detailed as follows.

We define a normalized frequency as $V = \frac{2\pi}{\lambda}a$, where λ and a are the optical wavelength and PCF core diameter, respectively. The phase mismatch number could be written as:

$$\Delta\beta = \beta_s + \beta_i - 2\beta_p \quad (81)$$

where β_j ($j = p, s, i$) is the propagation constant of the pump, the signal and the idler. Taylor expansion of (81) can then be written as:

$$\beta_p^2 \Delta\omega + \frac{2}{4!} \beta_p^{(4)} \Delta\omega^2 + \frac{2}{6!} \beta_p^{(6)} \Delta\omega^4 + \frac{2}{8!} \beta_p^{(8)} \Delta\omega^8 + \dots = 0 \quad (82)$$

As explained in previous sections, dispersion fluctuation introduces random parametric phase shift and destroys the designed phase matching condition. To study this effect, we define $\delta\beta$ as the phase mismatch number induced by the dispersion fluctuation and interaction length l_c as the effective interaction length over which the parametric phase changed from in phase to out of phase, that is¹⁵¹,

$$\delta\beta \cdot l_c = \pi \quad (83)$$

and

$$\begin{aligned} \delta\beta &= \Delta\beta|_{a+\Delta a} - \Delta\beta|_a \\ &= \Delta\beta_s + \Delta\beta_i - 2\Delta\beta_p \end{aligned} \quad (84)$$

in which $\Delta\beta_j$ ($j = p, s, i$) is the propagation constant changes due to the structural variation ($a \rightarrow a + \Delta a$) and has the following form:

$$\begin{aligned} \Delta\beta_s &= \beta_{a+\Delta a} - \beta_a \\ &= \frac{\Delta\beta}{\Delta a} \cdot \Delta a = \frac{\Delta\beta}{\Delta V} \frac{\Delta V}{\Delta a} \cdot \Delta a \\ &= V \left. \frac{d\beta}{dV} \left(\frac{\Delta a}{a} \right) \right|_s \end{aligned} \quad (85)$$

$\Delta\beta_i$ and $\Delta\beta_p$ could be derived in the same way. Subsequently, the parametric phase mismatch number $\delta\beta$ has the following form:

$$\delta\beta = \frac{\Delta a}{a} \left[\left(V \frac{d\beta}{dV} \right) \Big|_s + \left(V \frac{d\beta}{dV} \right) \Big|_p - 2 \left(V \frac{d\beta}{dV} \right) \Big|_p \right] \quad (86)$$

After simplification, the following could be derived:

$$\delta\beta = \frac{\Delta a}{a} \cdot \Delta\omega^2 (\beta_p^{(3)}\omega_p + 2\beta_p^{(2)}) \quad (87)$$

Equation (87) is remarkable since it states that the longitudinal phase mismatch number is proportional to the structural variation $\frac{\Delta a}{a}$, is quadratic with respect to the parametric frequency shift and depends on the global dispersion profile. Combining equation (87) with equation (83) yields the following expression:

$$l_c = \frac{\pi}{\frac{\Delta a}{a} \cdot (\beta_p^{(3)}\omega_p + 2\beta_p^{(2)}) \cdot \Delta\omega^2} \quad (88)$$

Generally, the pump is placed at anomalous dispersion region with small dispersion values. Assuming a typical operation that $\beta_p^{(2)}$ is $1\text{ps}^2/\text{km}$ and that $\beta_p^{(3)}$ equals $0.01\text{ps}^3/\text{km}$. Equation (88) can now be used to predict following conditions:

$$\text{if } \frac{\Delta a}{a} = 1\%, \quad l_c \sim 2 \text{ (centimeters)}$$

$$\text{if } \frac{\Delta a}{a} = 0.1\%, \quad l_c \sim 20 \text{ (centimeters)}$$

$$\text{if } \frac{\Delta a}{a} = 0.01\%, \quad l_c \sim 2 \text{ (meters)}$$

This result agrees well with previously reported results and indicates that parametric generation with large frequency shift poses high requirements on the fiber longitudinal variations. Considering the present PCF manufacturing technology that controls the manufacturing precision to about 1%, the interaction length of a typical PCF is only several centimeters.

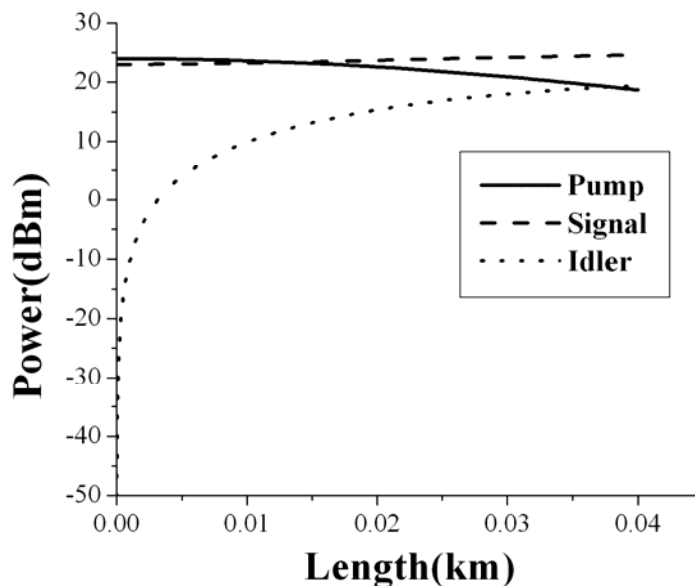


Figure 107 Prediction of power evolution of pump, signal and idler in 40-meter PCF.

However, simulation in Figure 107 shows that to obtain significant conversion efficiency, the PCF length has to be at least several meters long, which is much larger than the interaction length l_c , resulting in reduced gain due to many cycles of random parametric phase variation. Parametric process in PCF is then simulated by assuming a longitudinal core variation $\Delta a/a$ as 1% and the correlation length at 2 cm. The resulting idler power is shown in Figure 108, showing the same oscillating feature as we have observed in the experimental results, thus confirming that the longitudinal dispersion variation is the main impairment mechanism responsible for reducing the parametric efficiency.

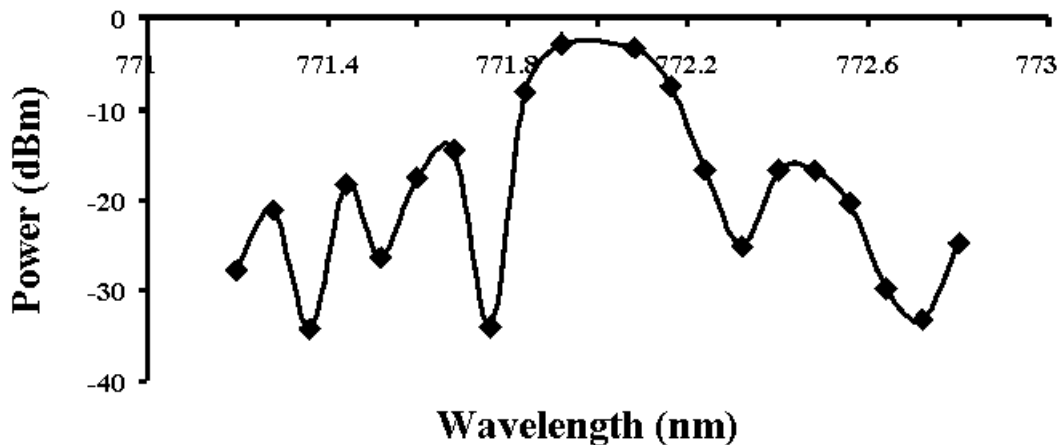


Figure 108 Idler power spectrum assuming a random longitudinal variation with $da = 1\%$ and correlation length 2cm.

Finally, we measured phase matching contours of the cutback sections in PCF B. The measured results are show in Figure 109. The phase matching contours of the different sections do overlap with each other, indicating that the correlation length of the dispersion fluctuation period is much smaller than a meter, agreeing with the previous prediction that the correlation length is centimeter scale.

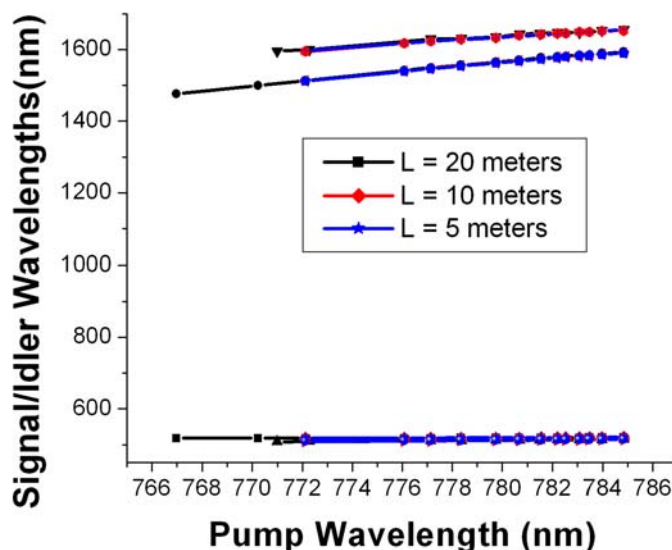


Figure 109 Measured phase matching contours of a 5-meter, a 10-meter and a 20-meter section of the same PCF coil B. The phase matching contours overlap with each other, indicating the dispersion fluctuation period is much less than meter scale, agreeing with the cm-scale prediction.

In conclusion, we performed rigorous cutback measurements on two distinct coils of PCF fibers and concluded that longitudinal structure variation induced severe dispersion fluctuation. The latter is identified as a main impairment mechanism for distant-band parametric translation in PCF. Theoretical analysis and numerical simulations confirmed the assumption, introducing severe requirements on the longitudinal precision of PCF manufacturing. The requirement can be alleviated by using a strong pump that renders the usage of a shorter fiber, which in turn requires material with high nonlinearity, such as, bismuth or chalcogenide.

4.7 Temperature dependence of the parametric translation process

The temperature dependence of the parametric translation process remains a large practical consideration. It is clear that temperature variation introduces two effects: firstly, the refractive indices of fused silica changes with temperature. Secondly, the thermal expansion of fused silica changes the dimensions of the fiber, altering the waveguide dispersion subsequently. The variation of dispersion will modify the phase matching conditions of the parametric process and could potentially harm the parametric translation efficiency.

Thermal expansion of fused silica obeys the following rule¹⁵² :

$$\frac{\Delta L}{L} \sim 0.55 \times 10^{-6} / K \quad (89)$$

Where ΔL is the thermal expansion. For regular PCF with $d \sim 600\text{nm}$ and $\Lambda \sim 1.4\mu\text{m}$, the thermal expansion introduces less than 1 pm dimension variation per Kelvin temperature change, which imposes negligible waveguide dispersion variation.

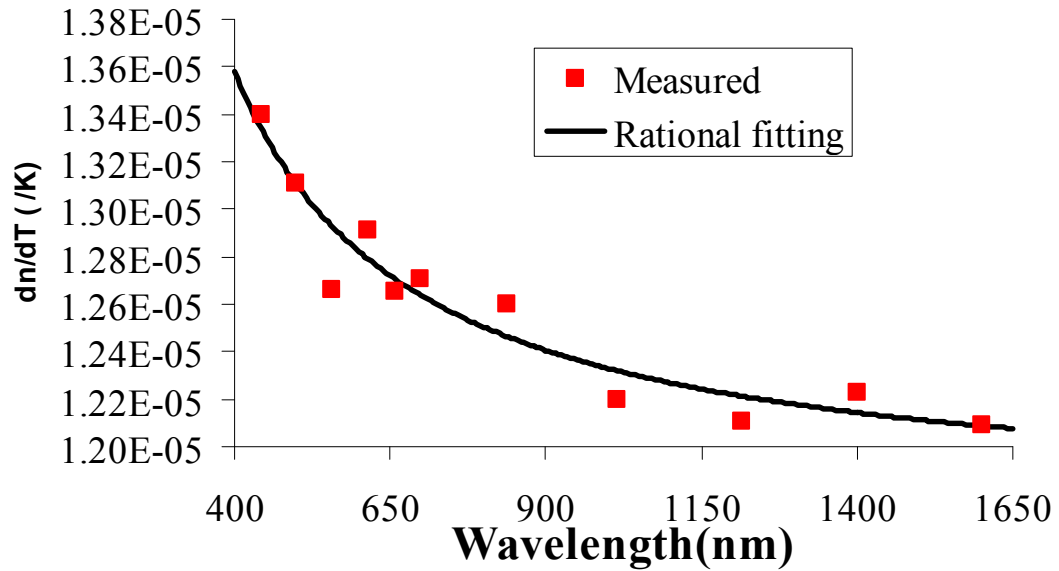


Figure 110 Dependence of the average thermal coefficient of refractive index of fused silica dn/dT on wavelength λ

Thermal induced refractive index variation requires more complex consideration. The dependence of the thermal coefficient of refractive index of fused silica on wavelength was measured previously¹⁵³, shown in Figure 110. We fitted the measurement with rational function, overlapped in the same plot with the measured data. Recall that the phase matching condition could be written as:

$$\begin{aligned} \Delta\beta &= \beta_s + \beta_i - 2\beta_p \\ &= \sum_{n=1}^{\infty} \frac{2}{(2n)!} \beta^{(2n)}(\omega_p) (\Delta\omega)^{2n} \end{aligned} \quad (90)$$

Therefore, the impact of temperature variation on the phase matching could be found as the following:

$$\frac{d\Delta\beta}{dT} = \sum_{n=1}^{\infty} \frac{2}{(2n)!} (\Delta\omega)^{2n} \frac{d\beta^{(2n)}(\omega_p)}{dT} \quad (91)$$

Taking the second order term as an example, we have

$$\begin{aligned}\beta_2 &= -\frac{\lambda^3}{2\pi c^2} \cdot \frac{d^2 n(T, \lambda)}{d\lambda} \\ &= -\frac{4\pi^2 c}{\omega^3} \cdot \frac{d^2 n(T, \lambda)}{d\lambda}\end{aligned}\quad (92)$$

Therefore, the second order term in equation (91) renders the following result:

$$\begin{aligned}\beta_2 \cdot (\Delta\omega)^2 &= -(\Delta\omega)^2 \cdot \frac{4\pi^2 c}{\omega^3} \cdot \frac{d^2 n(T, \lambda)}{d\lambda} \\ &= -\frac{4\pi^2 c}{\omega} \cdot \left(\frac{\Delta\omega}{\omega}\right)^2 \cdot \frac{d^2 n(T, \lambda)}{d\lambda}\end{aligned}\quad (93)$$

Based on Figure 110, we have the following results

$$\begin{aligned}at \quad \lambda = 500nm, \quad \frac{d^2}{d\lambda^2} \left(\frac{dn}{dT}\right) &\sim 1.77 \times 10^{-11}; \\ at \quad \lambda = 800nm, \quad \frac{d^2}{d\lambda^2} \left(\frac{dn}{dT}\right) &\sim 3.25 \times 10^{-12}; \\ at \quad \lambda = 1550nm, \quad \frac{d^2}{d\lambda^2} \left(\frac{dn}{dT}\right) &\sim 3.61 \times 10^{-13};\end{aligned}\quad (94)$$

Since

$$\frac{\Delta\omega}{\omega} \ll 1 \text{ and } \frac{4\pi^2 c}{\omega} < 1 \quad (95)$$

It is then clear that the second order dispersion contribution in equation (91) is a very small number. Repeating the same analysis shows that contributions from other terms (higher order dispersion contribution) are also very small, rendering the conclusion that thermal induced refractive index variation will have negligible impact on phase matching process either.

To summarize, thermal effect neither changes waveguide dispersion nor the material dispersion significantly. Therefore, thermal process will not hurt the phase matching and the parametric translation.

4.8 Reverse translation: Visible to NIR Conversion

Previous work focused on translation from 1550nm range to visible range, constructing a transmitter that leverages the telecom-band technologies to distant spectral range. Similarly, the universal band translator is also capable of translating light back to 1550nm in order to take advantage of the EDFA and high-sensitivity receiver in telecommunication band. In this section, we report on a visible-to-telecom band parametric translation with a dual zero dispersion wavelength (ZDW) PCF. The translated wavelength in telecom band was tuned by adjusting the pump wavelength.

In Figure 111, experimental setup for visible-to-NIR translation is illustrated. The signal transmitter was fixed 532nm source with 80mW output power. A 50dB polarizer was placed directly after the source, followed by a half-waveplate W1 to align the signal polarization to one of the principal axis of the PCF. A telescope system was used to adapt the signal beam size to the coupling-in objective MO1 and the PCF core size. The pump laser was a high power semiconductor laser with a maximum output of 1.4Watts and tuning range from 768nm to 786nm. The pump beam was passing through optics similar to that of the signal arm and reflected by MO2, overlapping with the signal beam. A 10-meter PCF coil was inserted in between the coupling-in and out objective MO1 and MO2. During the experiment, 200mW of pump and 20mW of signal were coupled in the PCF. The output beam consisting of pump, signal and telecom band idler were collimated

in free space and passed through 1300nm bandpass pass filter. The idler wave was then received by an optical spectrum analyzer

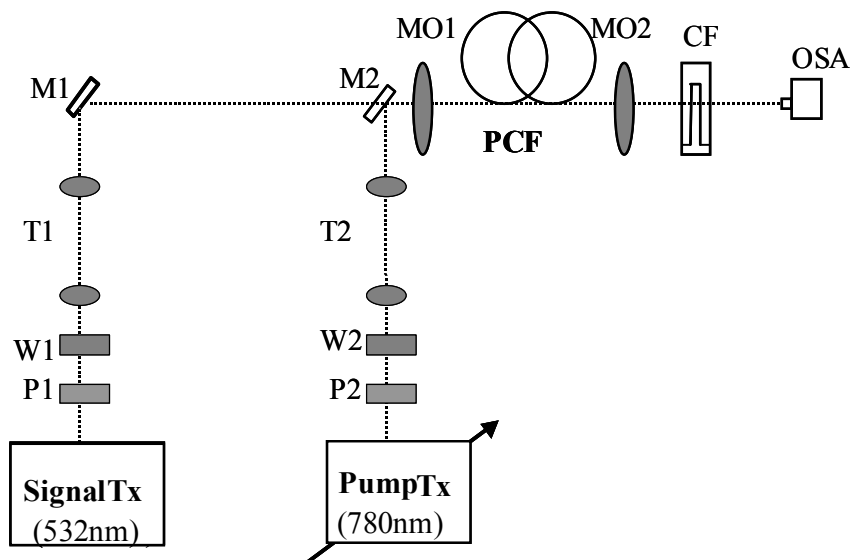


Figure 111 Experimental setup. P1-P2: polarizer; W1-W2: half-waveplate; T1-T2: telescope system; M1-M2: mirrors; MO1-MO2: microscopic objectives; F: filter; OSA: optical spectrum analyzer.

Figure 112 shows the input signal spectrum with three peaks at 531.9nm, 532.08nm and 532.26nm respectively, representing three longitudinal cavity modes and barely distinguished by a visible spectrometer (0.5nm resolution). Figure 113 shows a set of translated telecom band idlers as the pump wavelength is tuned from 776.6nm to 780.1nm. The three peaks of signal, not very discernable with a visible spectrometer, were translated into three discrete spectral lines in telecom band. A maximum of -21 dBm idler power was achieved by placing pump at 778.18nm, corresponding to -36 dB signal-to-idler conversion efficiency.

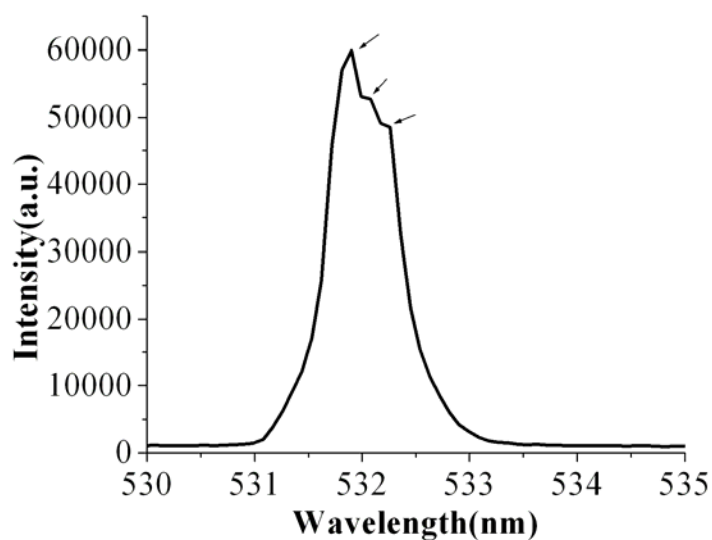


Figure 112. Signal spectrum with 3 peaks at 531.9nm, 532.08nm and 532.26nm.

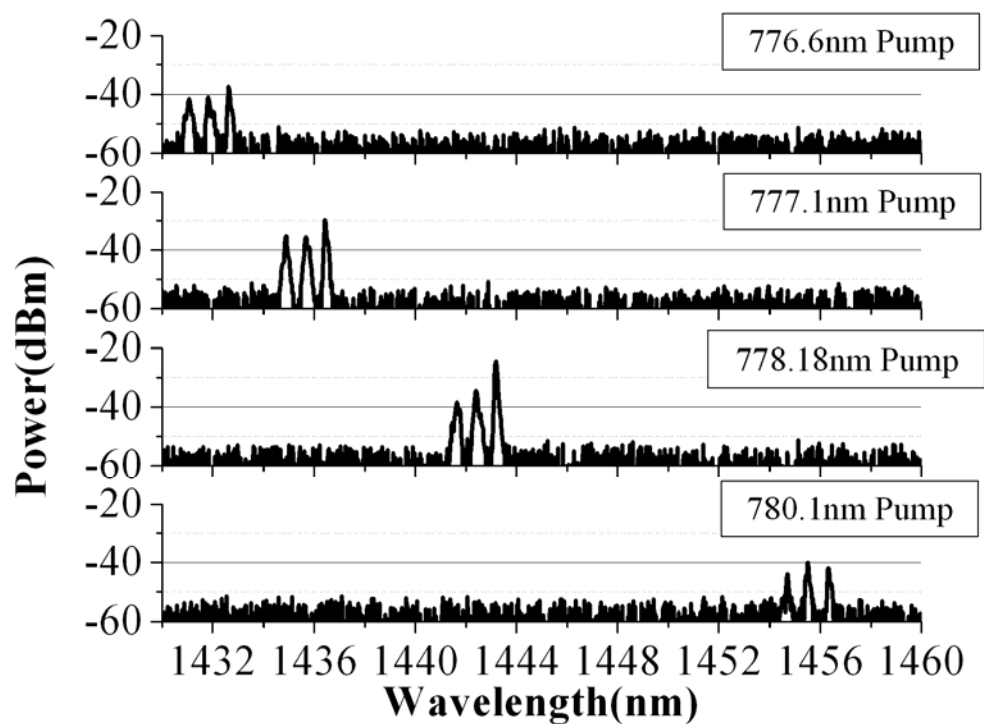


Figure 113 Translated telecom -band idler at various pump wavelengths.

4. 9 Conclusion

In this chapter we performed experimental demonstration and testing of the telecom-to-visible translation. Record translation was performed on Gb/s amplitude and phase modulated channel with error free performance. 1mW continuous power at visible range was obtained for the first time, 20 times higher than what has been reported to date. We also identified four major impairment mechanisms, namely, the polarization dependent SBS, multi-mode guiding at short-wavelength range, polarization decoupling of the interacting parametric waves and dispersion fluctuation, which have been both experimentally characterized and theoretically modeled. The modeling agrees very well with the experimental characterization. Solutions to the impairment mechanisms were then proposed and will be discussed in detail in the following chapter. Finally, we performed visible-to-telecom reverse translation experiment, demonstrating fully reciprocity of the universal band translator concept.

Chapter 5 Silica PCF design

5.1 Introduction

This chapter is dedicated to fiber structure design that aims to address the impairment mechanisms of parametric conversion. According to the discussion in Chapter 4, major impairment mechanisms include polarization dependent SBS, polarization decoupling, multimode guiding and dispersion fluctuations. The issue of SBS could be solved by spectrally broadening the pump, which suppresses the SBS onset by decreasing the power spectral density. Although this may introduce phase noise to the translation process, the penalty would be negligible as long the as the broadened pump linewidth is still much smaller than the transmission bandwidth. Dispersion fluctuation is determined by the manufacturing process and inherent to fiber once a fiber is drawn. The other two impairment mechanisms, namely, polarization decoupling and multimode guiding could at least in principle be solved by a PCF design.

An initial guess of the three design parameters – PCF transverse period, air-filling factor and PM hole size is required to start the calculating process. Among the three parameters, the air-filling factor is the dominant one and ought to be determined first. Choosing air-filling factor sets the intended guiding property of the PCF as desirable to have pump, signal and idler in single mode propagation. Therefore, the cut-off wavelength (as illustrated in Figure 96) of the designed PCF ought to be smaller than 500nm. Based on chosen air-filling factor, we then sweep the period values of the PCF structure and obtain a set of corresponding dispersion profiles. Phase matching contours are subsequently calculated for each dispersion profile. A proper design is finally

identified if a suitable phase matching contour is obtained. Otherwise, we choose a period that is closest to the target phase matching condition and continue sweeping of the PM parameter with the air-filling ratio and the structure period fixed. PM holes not only introduce birefringence, but also change dispersion. For each selected PM ratio, the dispersion profile and corresponding phase matching condition are obtained. The search process is terminated once a proper phase matching is obtained. Otherwise, we then choose an optimal PM ratio and update the air-filling factor. The process is iterated until a proper PCF structure is found. The flow-chart illustration of the design procedure is illustrated in Figure 114.

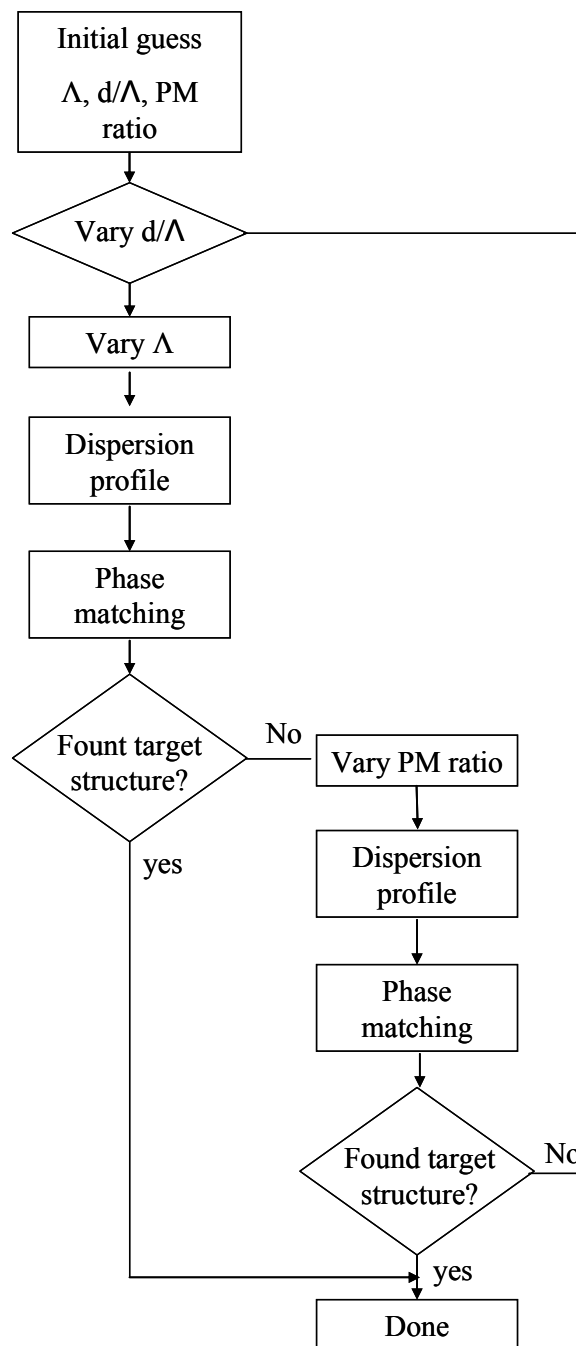


Figure 114 Flow chart illustrating the search procedure to find a proper PCF structure with targeted phase matching contour, air-filling factor and birefringence.

5.2 PCF design for telecom-to-visible translation

In this section, the work is to find a PCF structure that aims to phase match 780nm pump, 1550nm signal and 500nm idler. The air-filling factor cannot be too large ($d/\Lambda > 0.6$) since otherwise the cutoff wavelength will be long, which renders the fiber suffering from multi-mode operation. On the other hand, the air-filling factor is better not to be too small so to suffer from weak waveguiding. The silica's material ZDWL is at ~ 1300 nm. However, in our case the pump wavelength is at 780nm. In order for the pump to experience anomalous dispersion, the first ZDWL of the PCF has to be less than 780nm, which poses a strong waveguiding dispersion requirement on the PCF. Therefore, the air-filling factor is better to be greater than 0.4. A first guess sets the d/Λ at 0.5. A quick observation on Figure 96 shows that with $d/\Lambda = 0.5$ and period value between 1 and $2\mu\text{m}$, the cut-off wavelength is approximately 450nm, satisfying our single-mode guiding requirement. We then fix the air-filling factor and vary the period from 1.2 to $1.4\mu\text{m}$, assuming an isotropic fiber (No PM holes). The dispersion profiles for each structure are subsequently calculated, shown in Figure 115.

As expected (discussed in subsection 3.4 of chapter 3), varying the period does not significantly shift the first ZDWL, which in all cases is above 800nm. However, the $1.4\mu\text{m}$ -period structure has the leveraged dispersion profile at longer wavelength and is closest to the previous design that phase-match the three waves (780nm, 1550nm, 500nm). We then vary the PM-hole size, the results of which are shown in Figure 116. It is found out that increasing the PM-hole size shifts the dispersion profile towards the shorter wavelength side, which benefits us in two aspects: it is possible to shift the first

ZDWL below 780nm without significantly changing the second ZDWL, as varying air-filling factor or period generally does; the fiber also becomes highly birefringent due to the large structural asymmetry. The fiber could thus potentially be polarization maintaining at all three wavelengths, which is desirable to alleviate the polarization decoupling issue that is discussed in Chapter 4.

All the dispersion profiles are thereafter translated into a set of phase matching contours. Comparison of different phase-matching contours results in an optimum structure with $d/\Lambda=0.5$, $\Lambda=1.4\mu\text{m}$ and PM-hole $d_2=1.55d$ (d is the regular air-hole size), whose dispersion profile is shown in Figure 117a. In Figure 117b, corresponding phase matching contour is shown.

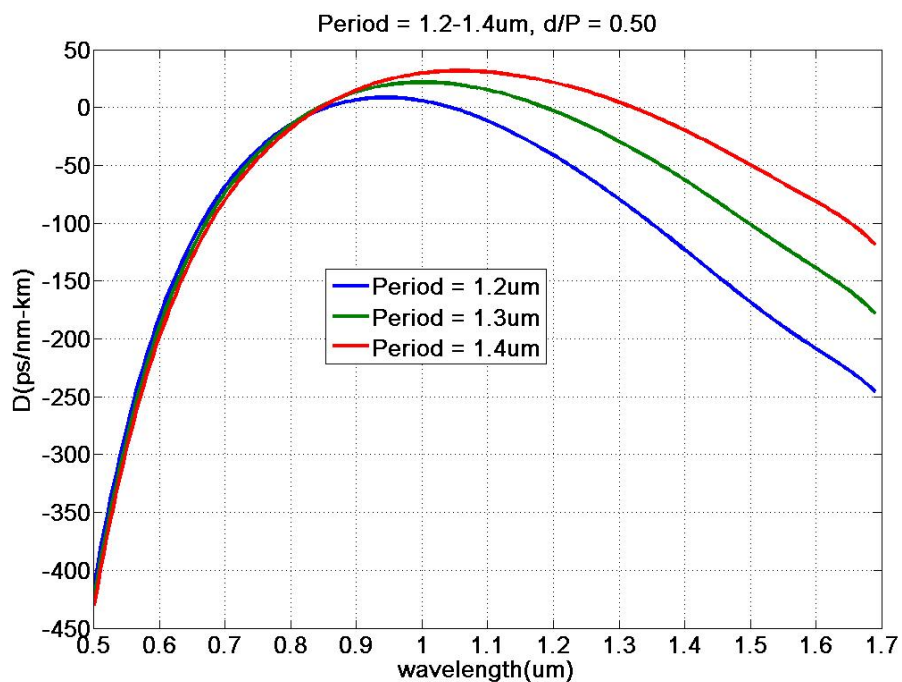


Figure 115 Dispersion profiles of PCF with $d/\Lambda=0.5$ and various period values.

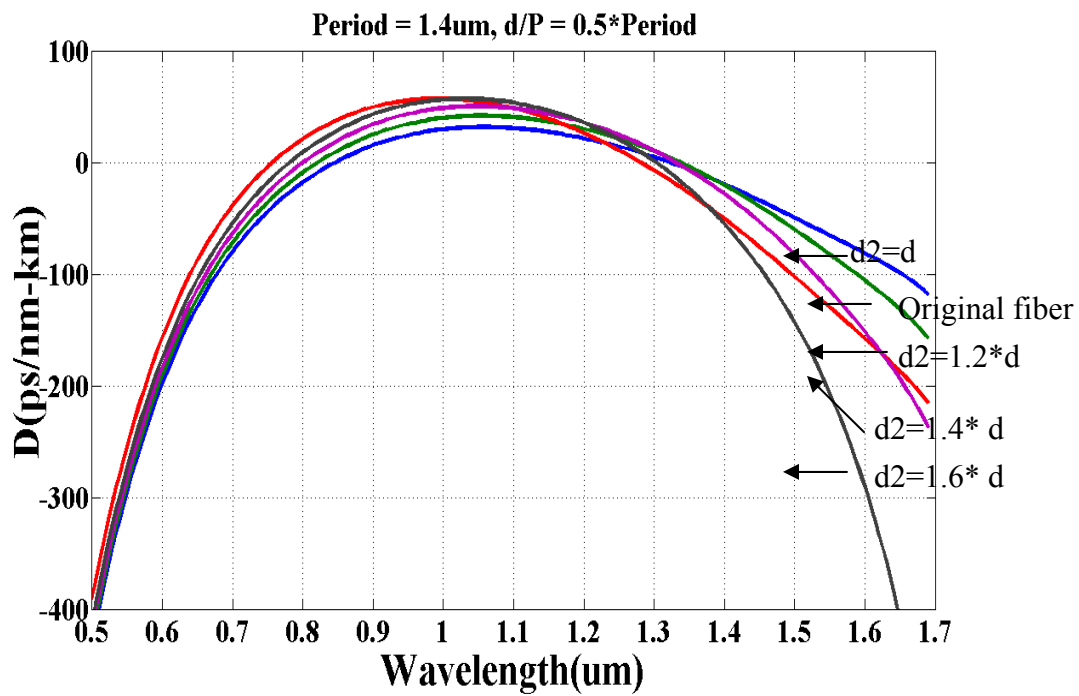


Figure 116 Dispersion profiles of PCF with $d/\Lambda=0.5$, period = 1.4 μ m and various PM-hole sizes

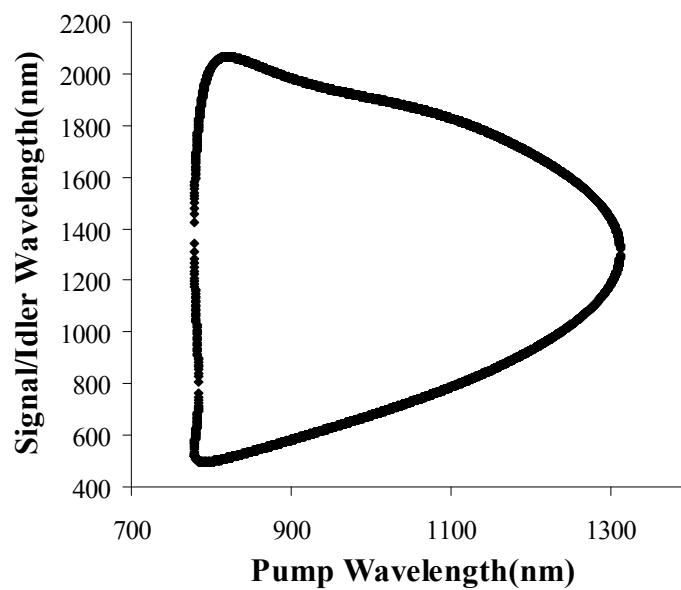
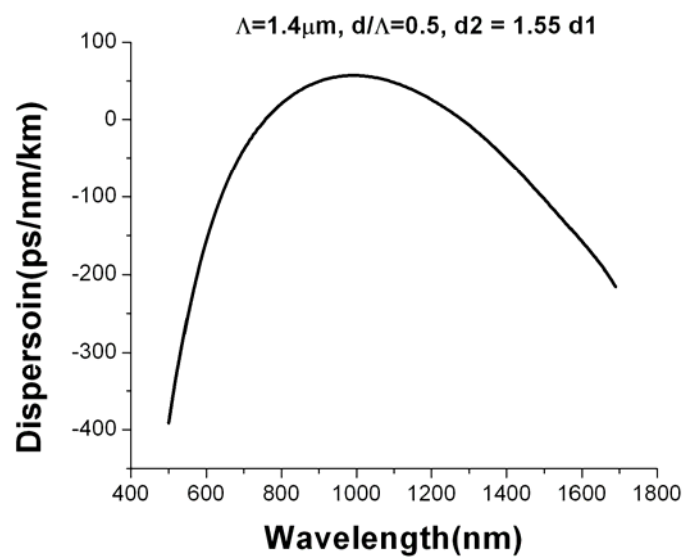


Figure 117 a) optimum dispersion profile for telecom-to-visible band translation and b) the corresponding phas- matching contour

5.3 Discussion of structure variation

It is known that PCF structure variation impacts significantly on the phase matching. To study this effect on the new design, we perturb each parameter (air-filling factor, period and PM-hole size) by $\pm 5\%$ from the original design while fixing the other two parameters and compare the resulting phase matching contour with the target phase matching contour. In Figure 118, we show the structure with the period and air-filling factor fixed at 1.4 μm and 0.5, respectively, but the PM-hole size is perturbed $\pm 5\%$ from the design. Figure 118a shows the complete phase-matching contours overlapped in one plot. We then zoom in into 1510-1610nm region in Figure 118b. The simulations show that the phase-matching contour is sensitive to the PM-hole size, and it is estimated that 1% of PM hole size change results in 1.5nm shift of the phase matching curve. It is generally required that the pump laser has some tunability, and the wider the tunable range, the more robust it is to the PM-hole size offset. Figure 118 also implies significant phase-matching bandwidth: for a fixed pump wavelength, it is possible to phase match the whole telecom band signals.

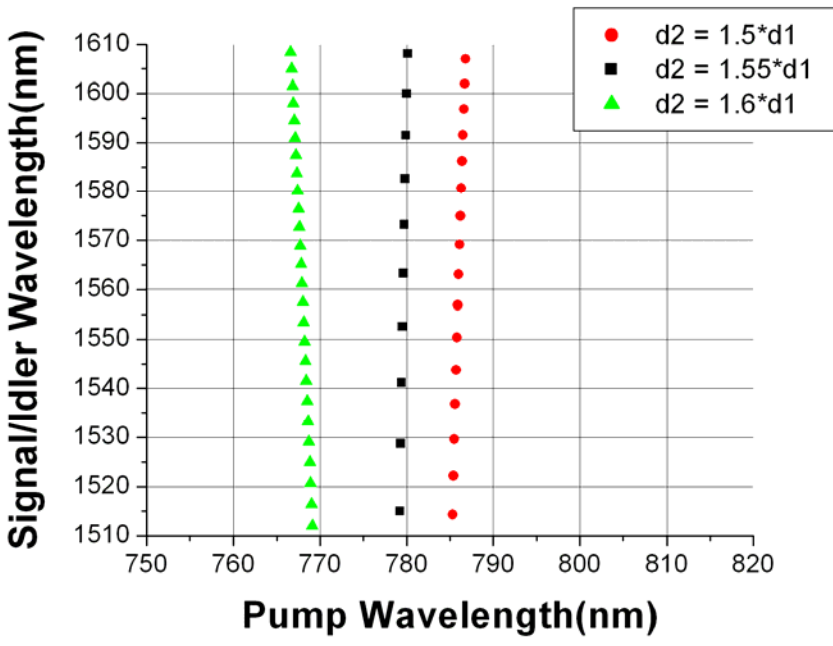
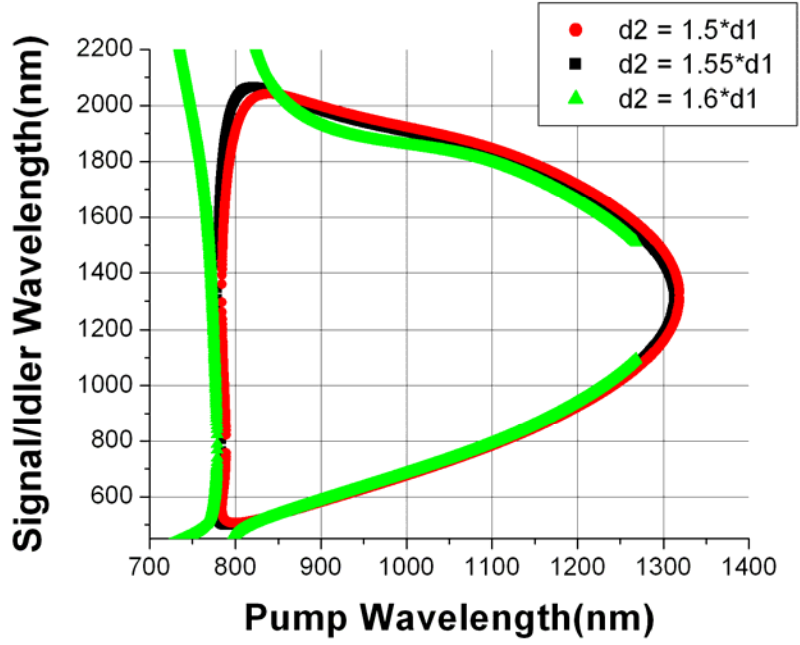


Figure 118 Phase matching contour with fixed period = 1.4um and air-filling factor at 0.5 and various PM hole size

We then fix the air-filling factor at 0.5 and PM-hole size $d_2=1.55d$. The period is then perturbed $\pm 5\%$ around 1.4 μm , the results of which are shown in Figure 119. Again, the subplot a shows the complete phase-matching contours and the zoom-in image at $\sim 780\text{nm}$ pump region are overlapped in subplot b. Since changing the period does not significantly change the dispersion profile at the short wavelength side but impact heavily on the long wavelength range (see Chapter 3), the phase matching contours vary drastically at the long wavelength range while changes less significantly at the short wavelength side. Figure 119b indicates variation at the smaller period value is more severe than the larger period case. Again, pump lasers with tunability will increase the tolerance to the period offset.

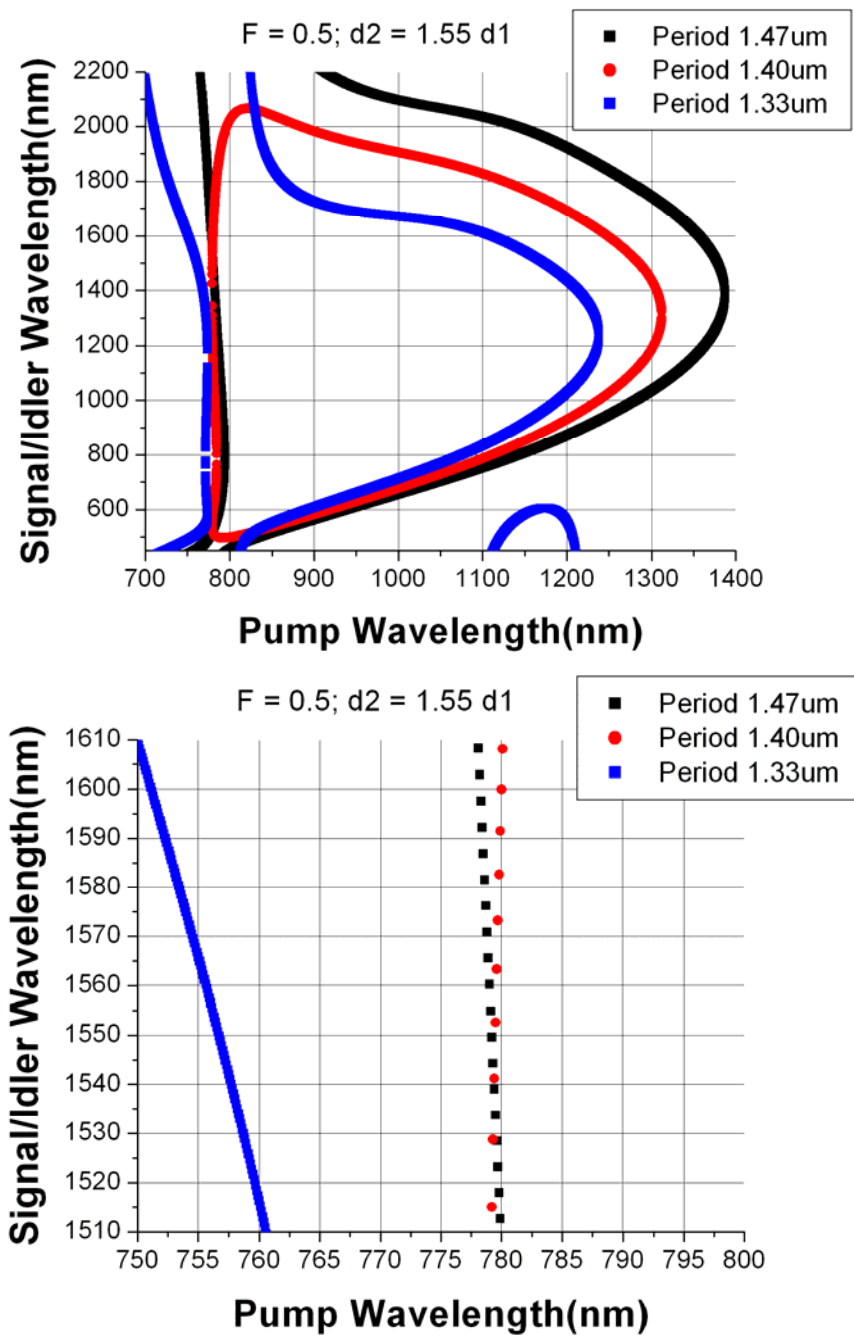


Figure 119 Phase matching contour with fixed air-filling factor at 0.5, PM hole size $d_2=1.55d$ and various period values.

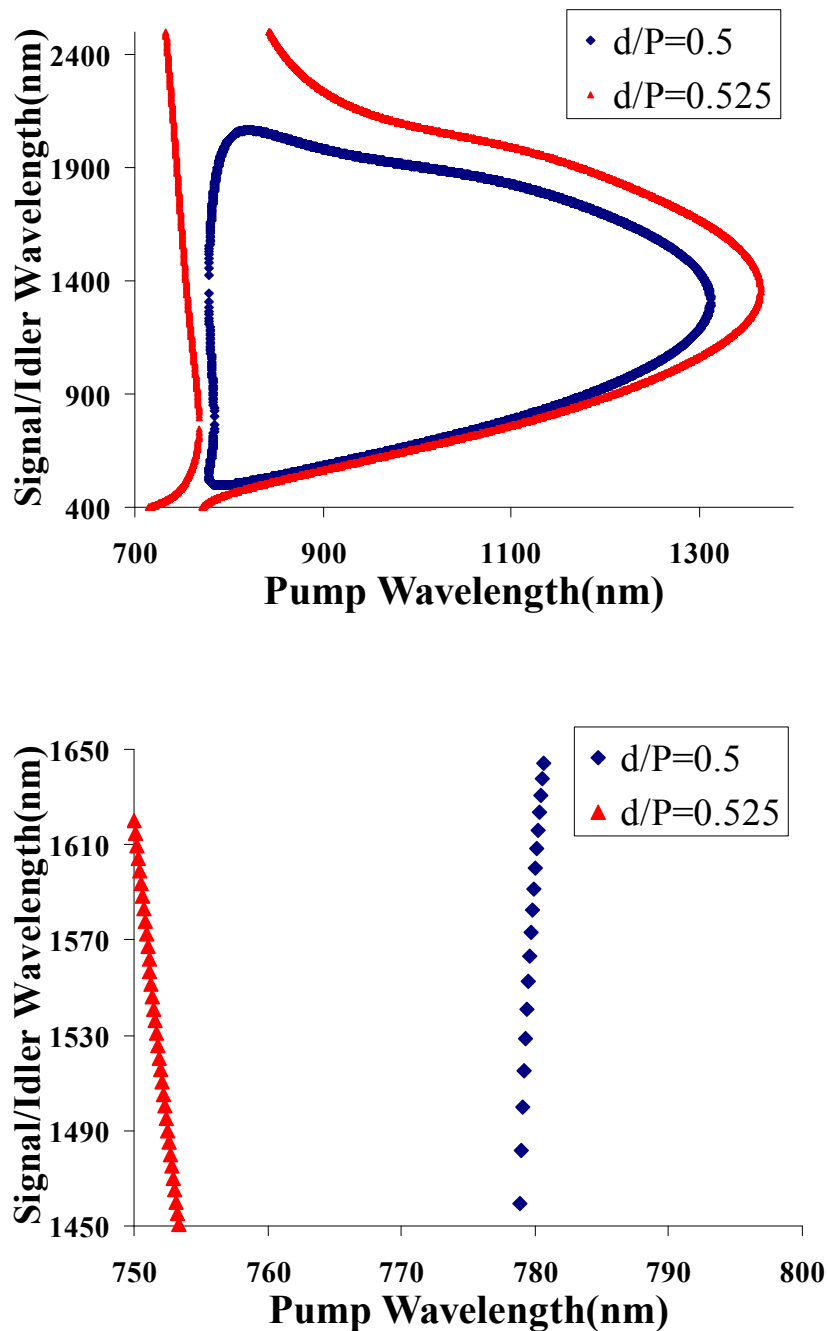


Figure 120 Phase matching contour with $\Lambda=1.4\mu\text{m}$, PM hole size $d_2=1.55d$ and altering air-filling factor.

Lastly, we investigate the impact of the air-filling factor perturbation on the phase matching contour. One can expect that the air-filling factor is the most sensitive in the

transverse structure parameters because it significantly alters the dispersion profile in all wavelength range (see chapter 3), and therefore the whole phase-matching contour is supposed to scale up or down depending on whether the air-filling factor is increasing or decreasing. The calculation is then done for fixed period at 1.4 μ m and PM-hole size $d_2=1.55d$, but the air-filling factor is now perturbed 5% around the average value 0.5. The results are shown in Figure 120a and b.

As expected, perturbation of air-filling factor has significant influence on the resulting phase matching contour, which renders high requirements on the manufacturing process that always introduces some manufacturing perturbation (~3%) on all fiber parameters. The situation is further complicated by the fact that the variation is random along the fiber length, which introduces dispersion fluctuation (discussed in chapter 4) and significantly shifts the phase matching condition from section to section in fiber, resulting in low conversion efficiency.

5.4 Experimental results on new fiber

The new design was sent for manufacturing and was tested thereafter. The transverse structure of the new fibers were measured and shown in Figure 121. Two PM-holes are prominent, indicating a strong asymmetrical structure. There were three coils drawn, the fiber parameters of which are shown in Table 4.

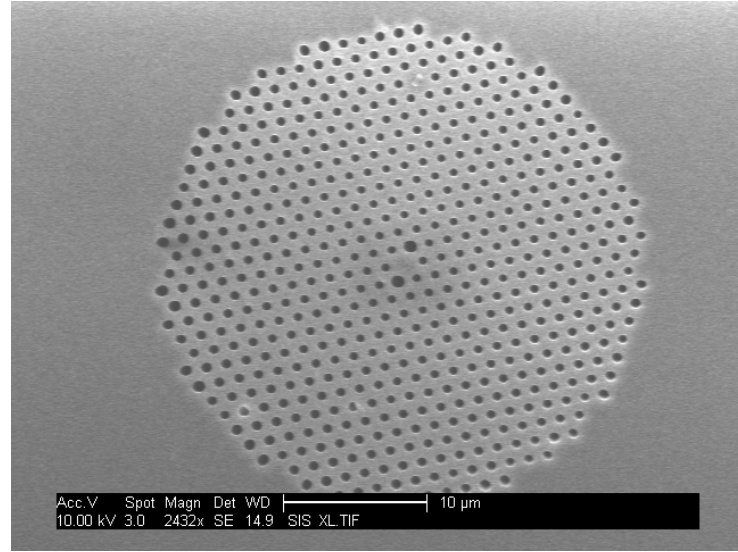


Figure 121 Typical structure of the newly-drawn fibers.

Table 4 Fiber parameters of the new-drawn fiber

Fiber coil	Λ	d/Λ	d_2/d
1	1.28	0.45	1.41
2	1.32	0.42	1.65
3	1.35	0.46	1.54

The measurements show that the parameters of the new fiber are far from the original design and therefore do not satisfy the desired phase matching condition. Indeed, when inserting a strong pump within 767-787 nm, no parametric generation (ASE peaks) were observed, indicating no phase matching within this pump region. Further measurements show that the multi-mode guiding and polarization decoupling are partially addressed. For the multi-mode guiding issue, the grating method revealed that 40%-50% (depending on fibers) of the energy was in fundamental mode for 500-nm wave, tripled the value that is observed in the old fibers. Furthermore, the polarization extinction ratio for the 500-nm was leveraged to 10-12dB, which could be considered as quasi-

polarization maintaining. No translation experiment was performed due to the improper phase matching condition.

5.5 Conclusion

In this chapter, we designed new fiber structure that pertains to proper phase matching condition and partially addresses the impairment mechanisms. The impact of structural variation to the phase-matching condition was studied as well. New fibers were drawn; however, the offset of the fiber structure from the original design renders no proper phase matching. However, measurements do show that the structure alleviates the impairment mechanisms regarding the multi-mode guiding at short wavelength and the polarization decoupling. Therefore, manufacturing PCF resembles our design is expected to enhance the conversion efficiency.

Chapter 6 Chalcogenide PCF design

6.1 Introduction

In previous chapters, we studied telecom-to-telecom and telecom-to-visible band translation (chapter 2) using silica HNLF and PCF. Located at the long wavelength side, the middle wavelength infrared (MWIR) spanning from 3 μ m to 6 μ m, in particular the 3.4 μ m spectral line, is interesting to many applications. This spectral window overlaps the atmosphere transportation window and is a desirable wavelength range for free-space communication and sensing¹¹. The vibrational energy level of most molecules lies within this spectral range, making it important in molecular spectroscopy⁹. Aircrafts and missiles have strong thermal signature in this window, and therefore it is desirable to develop transmission, detection and sensing techniques in this range. However, the problem here is similar to what we were facing in constructing underwater communication system: there are no suitable optical sources within this range – some quantum well lasers operate at this range^{154, 155}; however, they are yet to be reliable for the practical application. Neither mature modulation nor reception technologies are available in this spectral range. A possible solution is seen in the idea of band translator. Again, modulation and signal processing are conducted at telecom band, which is to be translated to the MWIR band through a parametric processor, illustrated in Figure 122. The telecom band is now used as both the pump and the modulation/information carrier. When seeded with a 980 nm continuous wave, the parametric band translator will translate the modulation coded on the telecom-band pump to the MWIR band idler.

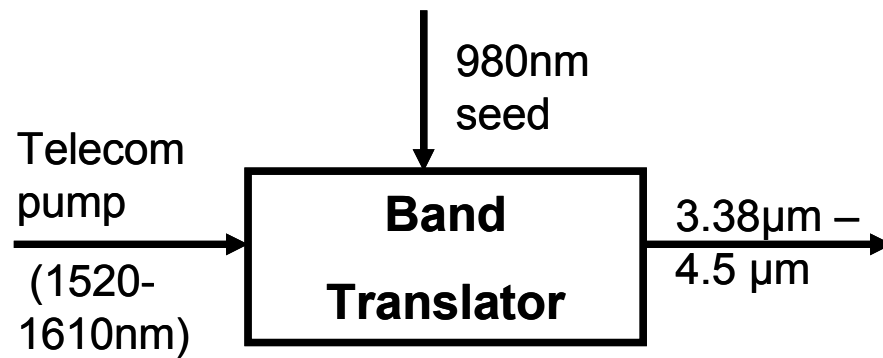


Figure 122 Band translator that translates telecom band pump to MWIR idler. Modulation and processing is conducted on the tunable telecom pump. 980 nm is seeded as signal.

6.2 Chalcogenide glass

Conducting such a translation from telecom to MWIR band requires different materials other than silica. Silica fiber has been demonstrated lossy for light waves longer than 2.4 μm . Chalcogenide glasses, on the other hand, have low absorption at MWIR band, which has made chalcogenide glasses useful for a wide range of applications: i.e. as fiber for transmission high power MIR lasers such as Er:YAG (2.94 μm)¹⁵⁶, CO (~5 μm)¹⁵⁷ and CO₂ (10.6 μm)¹⁵⁸ and remote sensing and as bulk glass for manufacturing MWIR windows, lenses and other optical components. In Figure 123¹⁵⁹, the absorption spectrum of typical chalcogenide glasses components are illustrated, showing a broad band transmission at MWIR and far-IR range from 2 μm to 12 μm . Approximate transmission windows of several chalcogenide glasses are detailed in Table 5¹⁶⁰.

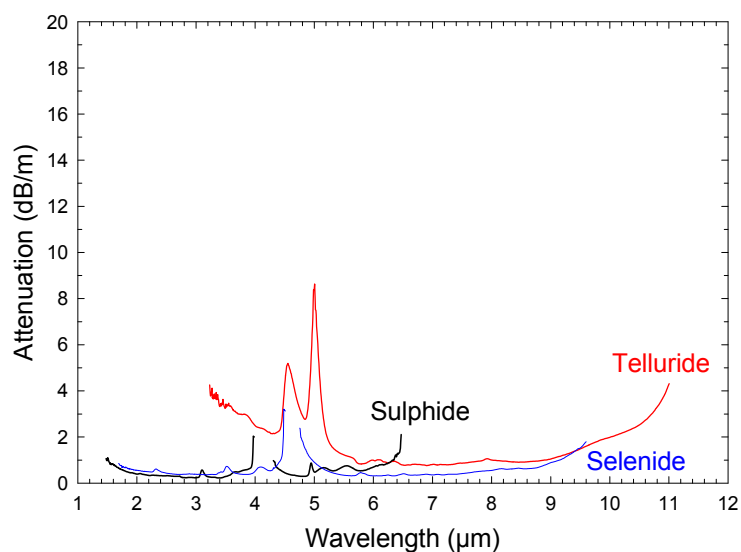


Figure 123 Attenuation curve of chalcogenide glass, which shows a broad band transmission from 2-12 μm .

Table 5 Approximate transmission windows of some chalcogenide glasses

Glass	Typical composition	Transmission window ($\alpha < 1\text{cm}^{-1}$) μm
GaLaS	$70\text{Ga}_2\text{S}_3:30\text{La}_2\text{S}_3$	0.57 – 9.5
GaLaSCsSI	$65\text{Ga}_2\text{S}_3:10\text{La}_2\text{S}_3:25\text{CsCl}$	0.48 - 8.8
AsS	As_2S_3	0.6 - 11
AsGeSe	$\text{As}_{38}\text{Ge}_5\text{Se}_{57}$	0.84 - 16
GeSeTe	$\text{Ge}_{22}\text{Se}_{20}\text{Te}_{58}$	~1.7 - 17

Furthermore, Chalcogenide glasses have high nonlinear refractive index, rendering the potential of using fibers tens of centimeters long, greatly reducing the impact of dispersion fluctuation and polarization decoupling effect. Also, short fiber length relaxes the fiber loss requirement. The reason of high nonlinearity for chalcogenide glasses is not clear yet. “Adair and co-workers pointed out that the large polarisability and hyperpolarisability of the S^{2-} ion implies large linear and nonlinear refractive indices for sulphide glasses¹⁶¹. In addition, the high densities possible with sulphide glasses contribute to achieving large linear indices, which in turn imply large

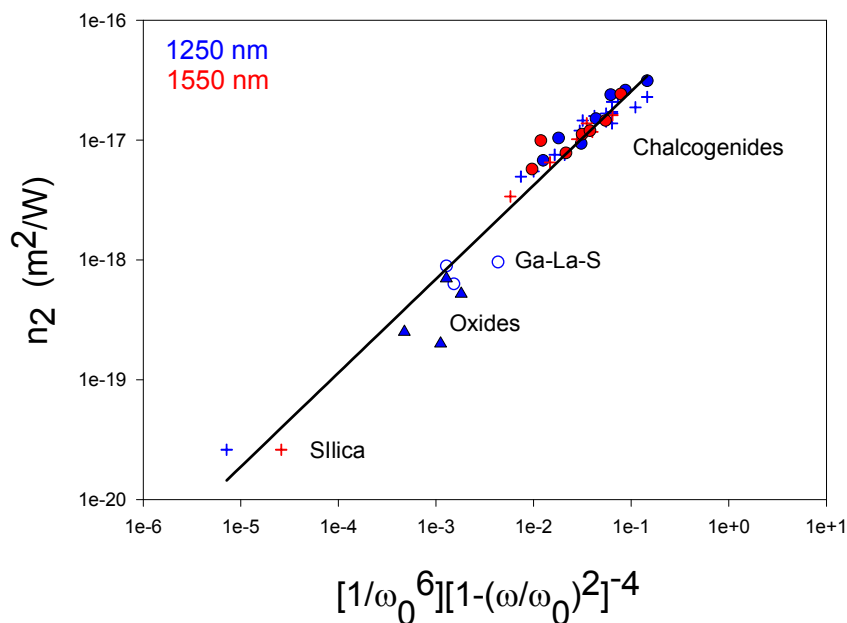


Figure 124 nonlinear refractive index of chalcogenide and silica glass. Chalcogenide glass shows an n_2 that is 1000 times higher than that of silica glass.

non-linear indices through BGO formula...With regard to the non-linear optical properties, much less work has been done on sulphide glasses than on oxide glasses¹⁶². In Figure 124, chalcogenide glass nonlinear refractive index n_2 are plotted, and compared with that of the silica glass in the same figure, indicating that chalcogenide glass has a

nonlinear refractive index 1000 times higher than that of silica glass. Material dispersion of Chalcogenide glasses is another property that draws special attention, which is in turn defined by the linear refractive index of Chalcogenide glasses. For different Chalcogenide glasses, the linear refractive index is different, so is the dispersion profile, which renders general equations modeling the refractive index of Chalcogenide glasses impossible, unlike in the silica fiber case. For example, Rodney et al¹⁶³ fitted the data of Arsenic Trisulfide glasses (As_2S_3) using a five term Sellmeier equation

$$n^2 - 1 = \sum_{i=1}^5 \frac{K_i \lambda^2}{\lambda^2 - \lambda_i^2} \quad (96)$$

Where λ is the wavelength, K_i and λ_i are the fitting coefficients, shown in Table 6

Table 6 Fitting terms of the Sellmeier equation for As_2S_3 glass

i	λ_i^2	K_i
1	0.0225	1.8983678
2	0.0625	1.9222979
3	0.1225	0.8765134
4	0.2025	0.1188704
5	750	0.9569903

In another case, Klocek and Colombo¹⁶⁴ presented the fitting result for $\text{Ge}_7\text{Sb}_3\text{Se}_{15}$ glass by using a five-term Herzberger polynomial

$$n = A_1 + \frac{A_2}{\lambda^2 - 0.028} + \frac{A_3}{(\lambda^2 - 0.028)^2} + A_4 \lambda^2 + A_5 \lambda^4 \quad (97)$$

Where A_i are the fitting coefficients are the following (see Table 7)

Table 7 Fitting coefficients the Herzberger polynomial equation for Ge₇Sb₃Se₁₅ glass

	0.9 – 2.5 μm	2.5 – 6.0 μm	6.0 – 14.0 μm
A ₁	2.609048	2.616916	2.612545
A ₂	0.1113049	0.1265583	0.3536862
A ₃	- 0.725286×10 ⁻³	-0.129672	-3.561954
A ₄	- 0.196917×10 ⁻²	- 0.1171826×10 ⁻³	-0.8917×10 ⁻⁶
A ₅	- 0.1546277×10 ⁻³	- 0.1154375×10 ⁻⁶	- 0.3215095×10 ⁻⁶

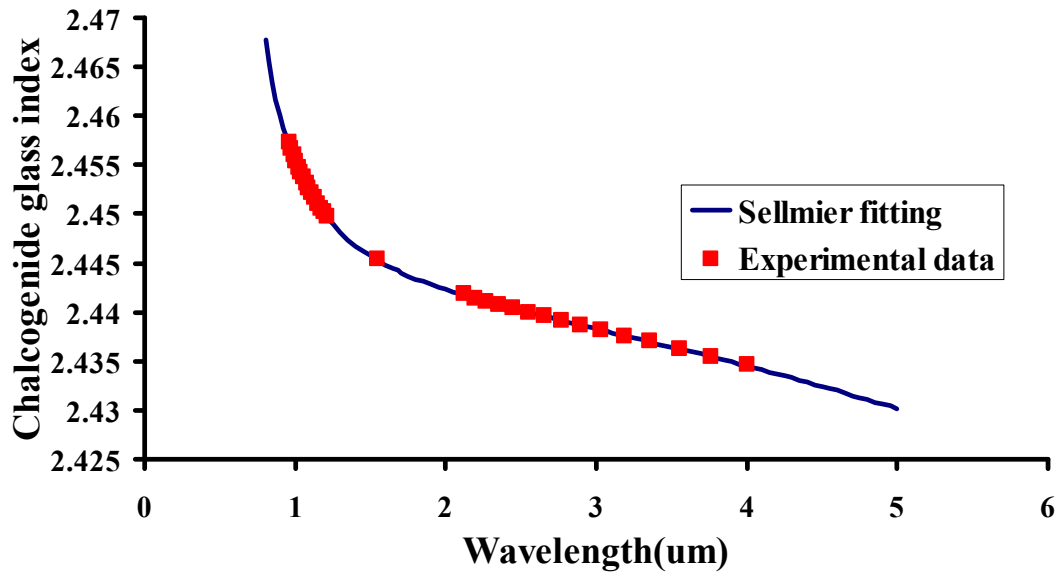


Figure 125 Measured chalcogenide PCF material refractive index overlapped with the fitted curve using Sellmier equation.

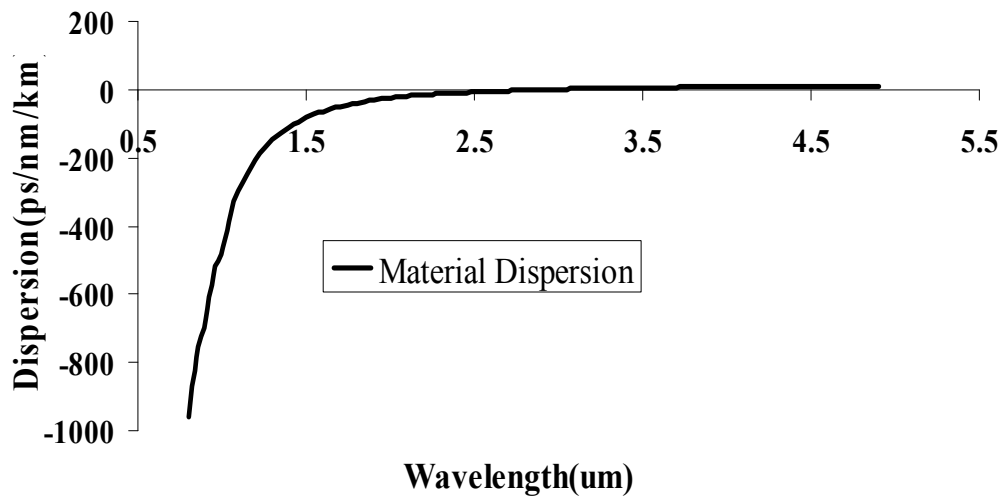
Generally speaking, for a specific Chalcogenide glass, the refractive indices have to be measured and then fitted with proper equations. In Figure 125, material index of the chalcogenide PCF used in this work are shown. The measured data points are overlapped with the fitted curve, using the Sellmier equation, shown in equation (98).

$$n_{chalcogenide} = \sqrt{A_1 + \frac{A_2}{\lambda^2 + \lambda_1^2} + \frac{A_3}{\lambda^2 + \lambda_2^2} + \frac{A_4}{\lambda^2 - \lambda_3^2}} \quad (98)$$

A_i and B_i are the fitting coefficients, the values of which are shown in Table 8.

Table 8 Fitting coefficients the Sellmier equation for the experimental chalcogenide PCF

i	A	B
1	4.091	798.7233
2	1493.0136	0.7665
3	-0.1296	-0.1898
4	0.6307	

**Figure 126 Material dispersion profile of the chalcogenide PCF used in the experiment.**

Strictly speaking, equation (98) is rational polynomial equation instead of Sellmier equation. However, it can be easily transformed into the Sellmier equation form. The material dispersion profile calculated based on the fitted Sellmier equation is shown in Figure 126, closely resembling the chalcogenide glass material dispersion profile in literatures^{165, 166}.

6.3 Chalcogenide PCF

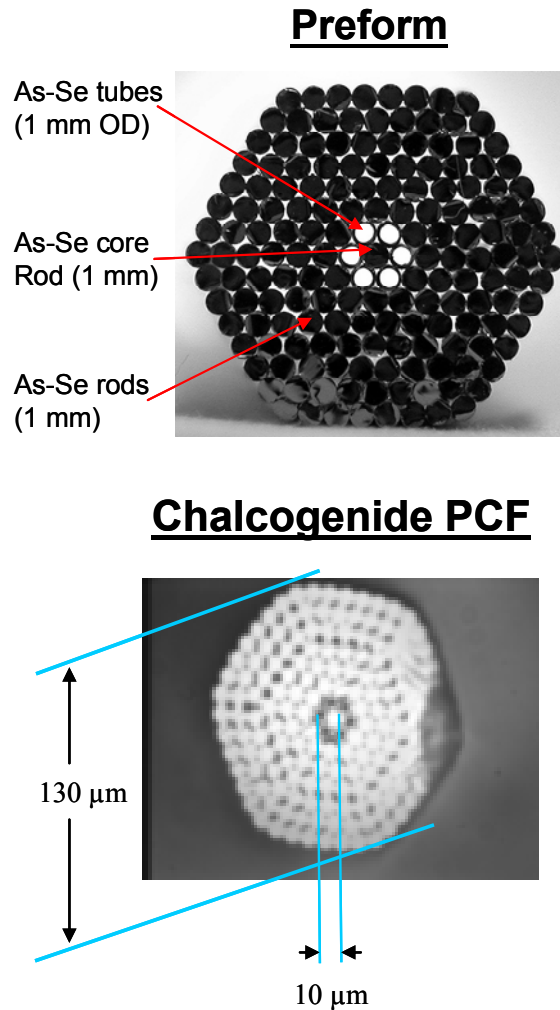


Figure 127 a) preform and cross section of a typical chalcogenide PCF

The large frequency shift involved in the telecom-to-MWIR translation eliminated the using of step-index chalcogenide fibers. Chalcogenide PCF was chosen for targeting the telecom-to-MWIR translation application. Fabrication of chalcogenide PCF was performed at Navy Research Laboratories (NRL). In Figure 127 preform and cross section of a typical Chalcogenide PCF are shown. In order to make the chalcogenide PCF single-mode guiding across broad optical spectrum, the air-filling factor d/Λ needs to be

small (see chapter 3). A first guess is to have $d/\Lambda = 0.5$ and $\Lambda = 2.2\mu\text{m}$. The waveguide dispersion and total dispersion profile are then calculated using BPM method, illustrated in Figure 128. The waveguide dispersion creates two ZDWL, with the first ZDWL located at $\sim 1.6\mu\text{m}$ range, shifted $2\mu\text{m}$ from the material ZDWL, and the second ZDWL at $4.8\mu\text{m}$, which renders the potential of phase matching $1.55\mu\text{m}$ telecom-band pump, 980 nm signal and MWIR idler.

We then fix the period value and vary the air hole size from $0.9\mu\text{m}$ to $1.3\mu\text{m}$, which corresponds to vary the air-filling factor from 41% to 59.1%. Guiding properties of the various structures was calculated using EIM mode, the results of which are shown in Figure 129. Since pump ($1.5\mu\text{m}$), signal ($0.98\mu\text{m}$) and idler ($\sim 3.4\mu\text{m}$) resembles normalized frequency at 1.47, 2.24 and 0.65, respectively, it is then clear from Figure 129 that all the structures with air-hole size $d \leq 1.1\mu\text{m}$ are single-mode guiding for each three interacting wave.

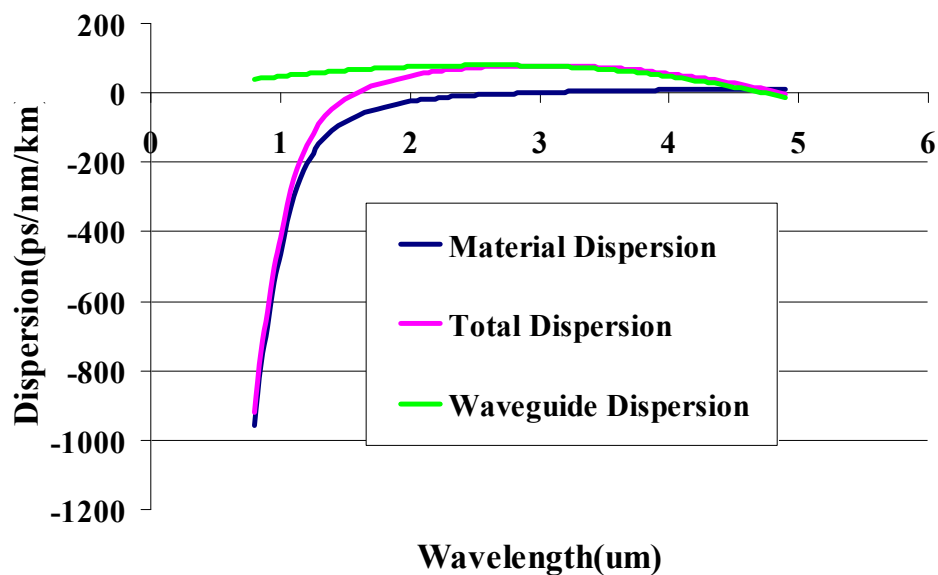


Figure 128 Material dispersion, waveguide dispersion and total dispersion overlapped in one plot for the Chalcogenide PCF with $\Lambda = 2.2 \mu\text{m}$ and $d/\Lambda = 0.5$

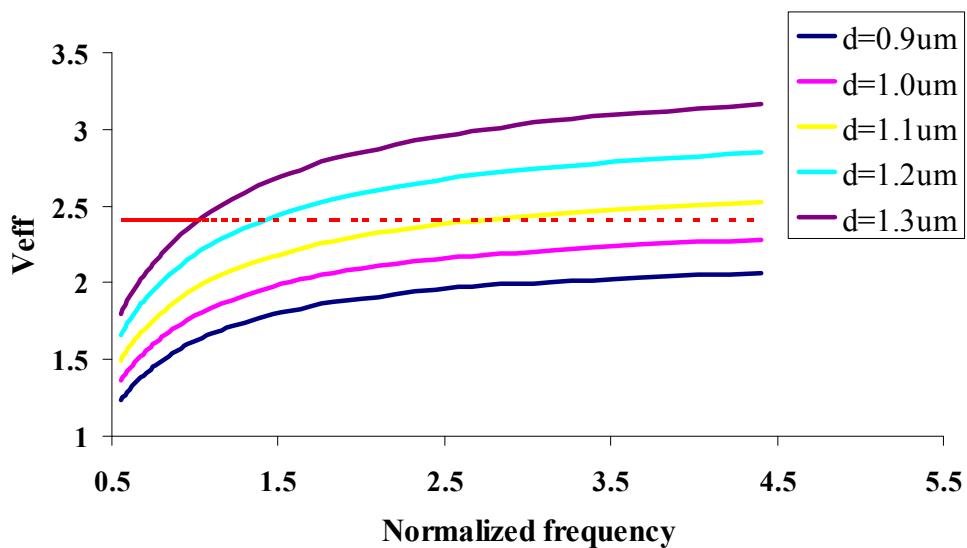


Figure 129 V_{eff} vs. Normalized frequency curve for various air-filling factors. The period is fixed at $2.2\mu\text{m}$. When $d < 1.1\mu\text{m}$, the Chalcogenide PCF becomes single-mode guiding at all three interacting waves. Normalized frequency = Λ/λ .

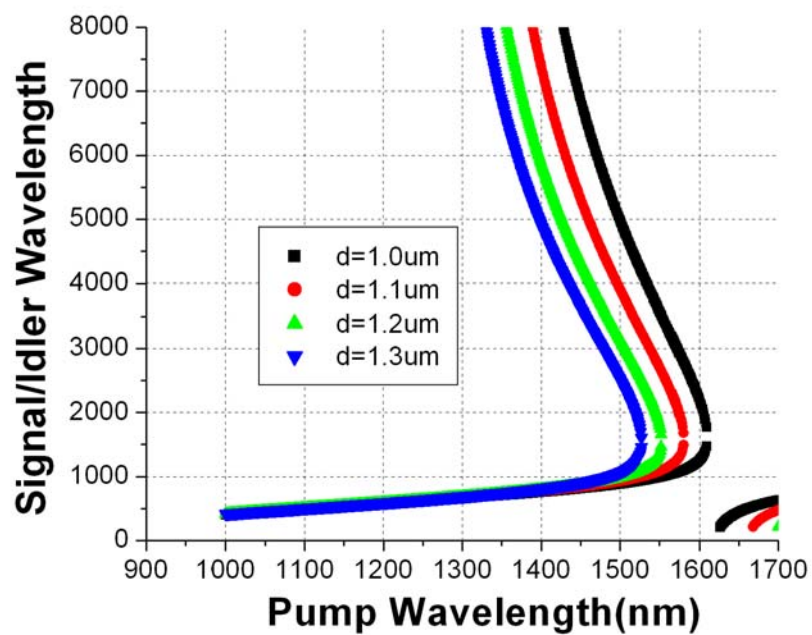
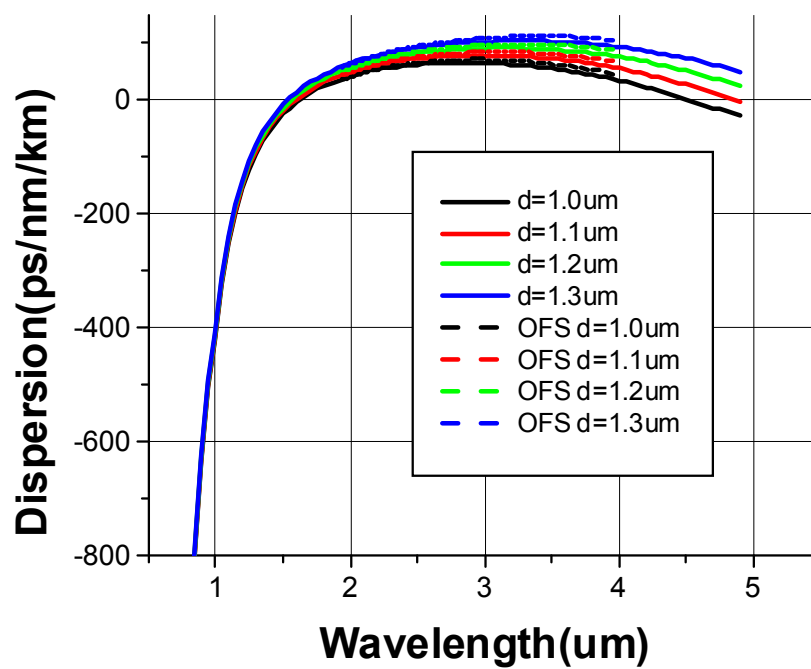


Figure 130 a) dispersion profiles of various Chalcogenide PCF structure and b) their corresponding phase matching contour.

Dispersion profiles of the above-mentioned structures are calculated accordingly, the results of which are shown in Figure 130a. Corresponding phase matching contours are calculated and displayed in Figure 130b. We compared our dispersion results with those from OFS Lab's calculation and found good match. The $d = 1.1\mu\text{m}$ structure can phase-match $1.55\mu\text{m}$ pump, 980nm signal and $3\mu\text{m}$ idler; while $d=1.0$ structure is able to phase-match $1.58\mu\text{m}$ pump, 980nm signal and $3.4\mu\text{m}$ idler. As the air-hole size sweeps within this range, it is therefore able to cover the MWIR from $3\mu\text{m}$ to $3.4\mu\text{m}$.

Some trial chalcogenide PCF fibers from NRL have been tested. Unfortunately, imaging the fiber cross-section clearly shows the collapse of the cladding structure and the incident light at telecom-band was not confined in the core.

6.4 Theoretical results on telecom-to-MWIR translation

Theoretical calculations were performed on the telecom-to-MWIR translation. One uncertain parameter during the calculations is the value of nonlinearity γ of the chalcogenide PCF, which depends on the PCF structure (particularly the core size) and the chalcogenide components. Also γ is wavelength dependent. In literature, γ was projected to be several hundred to several thousand per Watt per kilometer for chalcogenide glasses. In this calculation we choose a value from $500\text{W}^{-1}\text{km}^{-1}$ to $5000\text{W}^{-1}\text{km}^{-1}$. Since γ is uncertain by all means, we neglect the wavelength dependency temporarily. The idea of the calculation is to get an estimation on the conversion efficiency of the parametric process in chalcogenide PCF, instead of understanding the behavior of a particular fiber. Parametric power evolution for the two γ values ($\gamma=500\text{W}^{-1}\text{km}^{-1}$ and $\gamma=5000\text{W}^{-1}\text{km}^{-1}$) is shown in Figure 130c.

1km^{-1} and $\gamma=5000\text{W}^{-1}\text{km}^{-1}$) is shown in Figure 131. We assume typical experimental condition as pump power 1W and signal power 0.5 W. The calculations show high conversion efficiency in both cases. For a lower value of γ , the optimized fiber length is

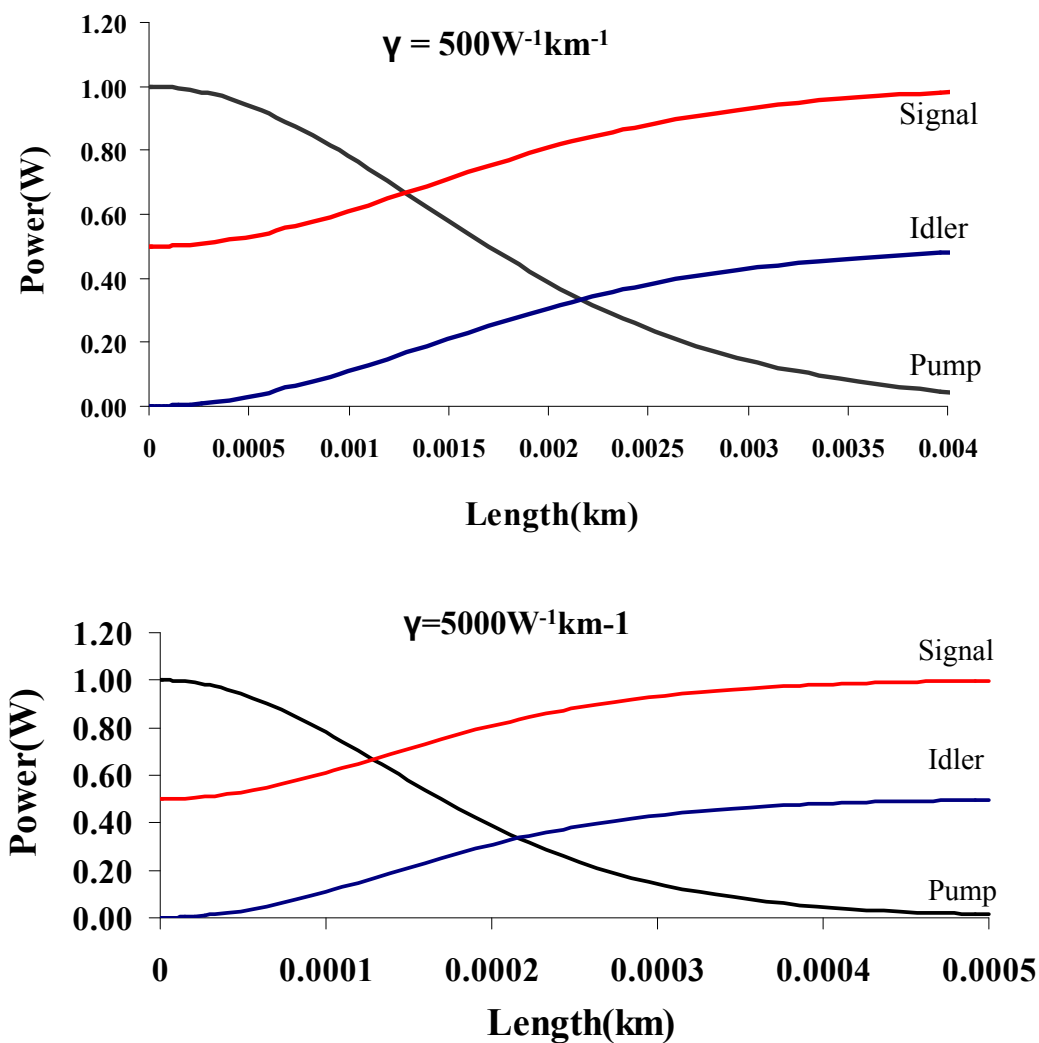


Figure 131 Power evolution in Chalcogenide PCF for a) $\gamma=500\text{W}^{-1}\text{km}^{-1}$ b) $\gamma=5000\text{W}^{-1}\text{km}^{-1}$.

High conversion efficiency was achieved in both cases. Calculations show that fibers from tens of centimeters to several meters could be used.

less 4 meters; while for the larger value of γ , the optimized fiber length is less 40 centimeters. In both cases, relatively short length of fiber could be used, which results in a lot of advantages such as alleviated dispersion fluctuation and polarization decoupling effect.

6.5 Conclusion

In this chapter, we investigated the telecom-to-MWIR band translation using chalcogenide PCF. We first discussed the chalcogenide glass properties. Refractive index of the experimental chalcogenide glass was fitted and material dispersion profile of the chalcogenide PCF was calculated. We further established the BPM method for calculating chalcogenide PCF structures, and proper PCF structure was designed for the purpose of telecom-band to MWIR translation. Due to the high nonlinearity of chalcogenide glass, very short fiber (several millimeters to centimeter) could be used to avoid dispersion fluctuation while maintain the high conversion efficiency.

Chapter 7 Conclusion

7.1 Review of the work

In this thesis, we have proposed and demonstrated the idea of optical mixer operation based on parametric processes in high-confinement fibers. The project originated from the effort of addressing the challenge of building high-speed optical communication and sensing link. Traditional underwater communication uses ultrasound technology which transmits information at several kb/s. Optical technology could potentially leverage the communication speed more than one million times. However, conventional optical communication works in the NIR range which renders great absorption in the sea water. On the other hand, sea water has the optical transmission window in the 460-560 nm band, the blue-green range. The problem narrows down to “Is it possible to build an optical communication link within this blue-green window?” Although there are currently optical sources within this window, their performance characteristics generally fall short of those required for reasonable optical communication. Moreover, there are no robust modulation or amplification technique at the blue-green window and fast receiver are not available either, which truly present a huge obstacle to underwater communications since it is very impractical to develop a complete set of technologies from transmission, modulation, amplification and reception at the blue-green range for the reasons that has been discussed in previous context. One solution is seen by building an optical band translator that aims to convert power from the telecom to visible band, so that all the complicated optical modulation and processing are done in the telecom band to take advantage of the existing optical communication

technologies. This idea of band translation is quite general and actually points out one common issue in optics: current optical technology is very band specific. The optical spectrum is divided into discrete bands such as the visible, NIR, SWIR and MWIR bands and technologies within different bands are very different. The idea of band translation could be extended to other optical spectral windows as well, which breeds the concept of an optical mixer. Again, an optical mixer is desirable to realize the availability of complicated modulation techniques, high performance optical sources and high-speed, high-sensitivity detection techniques across the optical spectrum. An optical mixer not only performs optical frequency mixing, but translates the amplitude and phase modulation with high fidelity. In this thesis, we investigated in detail band translation from telecom to different spectral bands, namely, to telecom, to visible, to SWIR and to MWIR bands, with HCF based parametric process. We have experimentally demonstrated optical mixer operation within the telecom band and telecom-to-SWIR band with silica HNLF and telecom-to-visible band translation with silica PCF through parametric interaction. We also analyzed theoretically the telecom-to-MWIR band translation with Chalcogenide PCF and designed a proper PCF structure for such purpose. Mathematical tools base on coupled-mode models have been established to predict the parametric performance, accounting for different pumping schemes (one pump vs. two pumps) and fiber parameters.

In the telecom-to-telecom band translation work, record gain-bandwidth product operation has been achieved. Fast all-optical switching and multi-casting up to 40Gb/s have been demonstrated experimentally. We have also established both numerical and analytical models analyzing the impact of dispersion fluctuation in a two-pump

parametric structure. The models are quite general and can be adapted to one-pump structure or to account for two-pump MI, BS or PC processes individually. It is also worth noting that with HNLF telecom-to-SWIR (up to $2\mu\text{m}$) band translation has been demonstrated with high efficiency⁴⁷.

In telecom-to-visible band translation work, we demonstrated record translation with 400THz frequency shift (signal to idler). 1Gb/s amplitude and phase modulation translation has been demonstrated from telecom to visible with error free performance. At the same time, a widely tunable visible idler has been obtained and the WDM channel translation was verified with each channel being demultiplexed and detected individually.

The ultimate goal is to design fibers that are optimized for the telecom-to-visible band translation. To achieve this goal, we first identified and experimentally measured four impairment mechanisms that severely degrade the wavelength conversion efficiency, namely: polarization dependent SBS, multi-mode guiding at short-wavelength range, polarization decoupling and dispersion fluctuation. Solutions to these problems were studied respectively. At the same time, we developed three numerical models (EIM, Fourier analysis and BPM method) that calculate the transverse structures of PCF. PCF properties including wave-guiding, dispersion profile and birefringence were studied using these models. We then designed fiber structures that are suitable for the telecom-to-visible translation purpose, with the above-mentioned impairment mechanisms partially addressed.

In the telecom-to-MWIR work, Chalcogenide PCF was chosen for the purpose due to its high transmission at MWIR range and high nonlinearity. We successfully fitted

the refractive index curve with the Sellmier equation. We also designed proper structure that aims to phase-match $1.55\mu\text{m}$ telecom pump, $0.98\mu\text{m}$ signal and $3.4\mu\text{m}$ idler.

7.2 Future direction

The works related to distant-band translation (telecom-to-visible and telecom-to-MWIR) using PCF are quite new and there are still many problems yet to be solved. For example, PCF structure design could be further improved to better address the impairment mechanisms. Most importantly, the success of this work heavily depends on the improvement of the PCF manufacturing technology. It is clear that, due to the large frequency shift for distant-band parametric translation, the multi-mode guiding at short wavelengths, the polarization decoupling among interacting waves and dispersion fluctuation cause severe problems. The larger the frequency shift, the more stringent requirement on controlling the accuracy of PCF structure dimensions: not only the real dimension has to closely resemble the original design (error $< 0.1\%$), but also the longitudinal structural variation has to be smaller than 0.1% , which puts very high requirements on the manufacturing technology, thus making the high-efficiency telecom-to-visible translation (frequency shift $\sim 200\text{THz}$ from pump to signal/idler) very difficult. On the other hand, the telecom-to-MWIR translation has a frequency shift of only $\sim 100\text{THz}$ (pump to signal/idler). Furthermore, due to the high nonlinearity of Chalcogenide glasses, very short PCF (several millimeters to centimeters) could be used for the translation purpose according to the calculation in chapter 6. These two attributes greatly reduce the requirement on the PCF structural variation and renders highly efficient translation possible. However, manufacturing of Chalcogenide fiber remains a

challenge due to the fact that Chalcogenide glasses are mechanically brittle and require great care and superior mechanical control when drawn into fibers. NRL has developed a system to manufacture Chalcogenide PCF, which are subject to further improvement for enhanced mechanical and optical property and reliability.

Appendix: Free-space-to-PCF Coupling Protocol

The coupling procedures are used in the experiments have been used throughout this work and are described as follows:

1. Find out the height H you prepare to work with, which is usually determined either by the stage that holds the PCF, or by the source height in some cases. Prepare two irises with height H .
2. Align the pump arm first. The pump source should be mounted on a kinematic mount whose angle can be adjusted 3-dimensionally. Measure the initial beam size d_0 and divergence angle θ with a beam profiler.
3. Collimate the pump beam. Place the two irises along the same line of holes on the optical table, one at the near field of the source and the other at the far field of the source. Adjust the source angle so that the laser beam can pass the two irises freely. This is to guarantee the laser beam is well leveled (shooting straight and parallel to the optical table).
4. If the output of the source is not well linear polarized, a polarizer is needed after the source. Make sure the laser beam incident normally onto the polarizer and overlap with its optical axis. This can be achieved by minimizing the back-reflection and using the two irises to make the beam coming out of the polarizer well leveled. This step should be followed whenever a new optical element is added into the setup.
5. Add the $\lambda/2$ wave-plate as described in step 4. Add the beam sampler to monitor the back-scattering from PCF.

6. The telescope system functions in two ways:

- 1) Adjust the beam size;
- 2) Collimate the beam if needed.

Function 1) is accomplished by choosing the right magnification power M of T , which is closely related to how the objective MO is chosen. In the experiment, the coupling-in MO is either 40× or 60×. The chosen telescope system parameters are described in section 4.1.2

Function 2) is accomplished by offsetting the distance L from its default value f_1+f_2 by an amount $\Delta L = \frac{-f_1\theta}{d_0 + f_1\theta}$, where f_1 is the focal length of lens L1; divergence angle θ is defined as positive if the beam is focusing and negative if the beam is diverging when it hits lens L1. In practice, beam coming out of T is guaranteed to be collimated by moving one lens (L2 usually) and observing the output beam on a white screen (or IR card) and with irises, until the beam keep the same size in both near field and far field and well leveled as well.

7. Start aligning signal arm. Repeat step 2-6 for signal arm. The first lens of signal telescope now is mounted on a translation stage.

8. Insert a dichroic mirror that reflects 780nm wave but transmits the 1550nm wave. The optical path of the two waves shall overlap after this dichroic mirror.

9. Insert the MO.

10. Insert the 5-axis (3 translation and 2 angle axis) stage. The fiber V-clamps are mounted on this stage. At the output of the fiber, a 40× or 60× is used to collimate the output into freespace again.

11. Insert a visible bandpass filter to select the idler band (parametric down conversion)

Following these steps should be able to achieve reasonable coupling. Typical coupling efficiency for 780nm wave is 40%-45% while for 1550nm at most 30%-40%. The coupling efficiency here refers to the ratio of the power coupled into the PCF (which is measured by coupling light into a short PCF piece) and the power immediate after MO. The low coupling efficiency for the pump is due to the bad laser beam quality, which has a M^2 factor of ~ 2 for the long axis and ~ 1.5 for the short axis, thus hindering the simultaneous focus the two axes of the beam within the small core and the NA range of the PCF: optimizing for the long axis makes the short axis has an NA higher than $(NA)_{PCF}$ and thus penetrate into cladding; while optimizing for the short axis results in a focal spot that is larger than the core size for the long axis. The coupling efficiency of 1550nm wave was firstly limited by the bad resolution of MO at this wavelength, measured to be around $3.2\mu\text{m}$. The overall coupling efficiency is further lowered down due the relatively MO (80-85% transmission for 780nm and $\sim 60\%$ transmission for 1550nm). By all means, the lack of a MO that has both good transmission and resolution at both 1550nm and 780nm limited our experimental performance, which is very particularly important for a CW operation.

Reference:

-
- ¹ W.R. Garmer, "An Improved Acoustic Communication System for Autonomous Underwater Vehicles", Proceeding of the 1992 Symposium on Autonomous Underwater Vehicle Technology, Jun. 2-3, 1992, Washington, DC, USA.
 - ² R. Coates, "Underwater Acoustic Communications", IEEE, Feb. 1993, pp. III-420-424.
 - ³ I. Kaminow and Tingye Li, 'Optical Fiber Telecommunications IVB: Systems and Impairments', Academic Press, San Diego, 2002
 - ⁴ G. P. Agrawal, "Fiber-optic Communication Systems", 3rd edition, Wiley-Interscience, (John Wiley & Sons), New York, 2002
 - ⁵ Ed Friedman and J. L. Miller, "Photonics Rules of Thumb", SPIE Press, McGraw-Hill, 2003
 - ⁶ J. E. Tyler, "Light in the Sea", Dowden, (Hithinsons and Ross), Strounburg, Pennsylvania, 1977.
 - ⁷ I. Kaminow and Tingye Li, 'Optical Fiber Telecommunications IVB: components', Academic Press, San Diego, 2002
 - ⁸ R. Jiang, R. E. Saperstein, N. Alic, M. Nezhad, C. J. McKinstrie, J. E. Ford, Y. Fainman and S. Radic, "Continuous-Wave Band Translation between the Near-Infrared and Visible Spectral Ranges", IEEE Journal of Ligh. Wav. Tech., 2007
 - ⁹ C.N. Banwell and E.M. McCash, "Fundamentals of Molecular Spectroscopy", 4th edition, McGraw-Hill (London), 1994.
 - ¹⁰ Personal communication with a Lockheed Martin scientist
 - ¹¹ A. V. Kudryashov and H. Weber, "Laser Resonator: Novel Design and Development", SPIE Optical Engineering Press, Bellingham, Washington, 1999
 - ¹² G. M. Gibson, M. H. Dunn, and M. J. Padgett, "Application of a continuously tunable, cw optical parametric oscillator for high-resolution spectroscopy," Opt. Lett. 23, 40–42 1998
 - ¹³ D. M. Pazar, "Microwave Engineering", 3rd Ed., John Wiley & Sons, New York, 2005
 - ¹⁴ <http://www.electronics-manufacturers.com/products/rf-microwave-components/rf-mixer/>

-
- ¹⁵ W. F. Egan, "Practical RF System Design", John Wiley & Sons, Hoboken, New Jersey, 2003
- ¹⁶ P. Vizmuller, "RF Design Guide: Systems, Circuits, and Equations", 2nd edition, Artech House Publishers, Norwood, Massachusetts, 1995
- ¹⁷ http://en.wikipedia.org/wiki/Sound_reinforcement_system
- ¹⁸ T. S. Rappaport, "Wireless Communication: Principles and Practice", Prentice Hall PTR, Upper Saddle River, New Jersey, 2002.
- ¹⁹ United States Frequency Allocation Chart:
<http://www.ntia.doc.gov/osmhome/allochrt.pdf>
- ²⁰ O. Svelto, "Principles of Lasers", 4th Ed., Plenum Press, London, 1998
- ²¹ R. Jiang, R. Saperstein, N. Alic, M. Nezhad, C. J. McKinstrie, J. E. Ford, Y. Fainman and S. Radic, "Parametric Wavelength Conversion From Conventional Near-Infrared to Visible Band", IEEE Photon. Technol. Lett., Vol. 13, pp.194-196, 2001.
- ²² G. Einarsson and M. Leeson, "Principle of Lightwave Communications", John Wiley & Sons, New York, 1997
- ²³ http://www.polymtl.ca/phys/journal/num1/art_1_3.pdf
- ²⁴ K. Inoue, E. Waks and Y. Yamamoto, "Quantum key distribution system and method using regulated single-photon source", US patent 7346166, March 2008
- ²⁵ P. Horowitz and W. Hill, "The Art of Electronics", 2nd Ed., Cambridge University Press, Cambridge, 1999.
- ²⁶ G.P. Agrawal, "Nonlinear fiber optics", 3rd Ed., Academic Press, San Diego, 2001
- ²⁷ R. W. Boyd, "Nonlinear Optics", 2nd Ed., Academic Press, San Diego, 2003
- ²⁸ Y. R Shen, "The Principles of Nonlinear Optics", Wiley-Interscience, New York, 1984
- ²⁹ Z. Sun, R. Li, Y. Bi, X. Yang, Y. Bo, W. Hou, X. Lin, H. Zhang, D. Cui and Z. Xu, "Generation of 4.3-W coherent blue light by frequency-tripling of a side-pumped Nd:YAG laser in LBO crystals", Opt. Express, Vol. 12, pp. 6428-6433, 2004
- ³⁰ V. Petrov, F. Rotermund, F. Noack, J. Ringling, O. Kittelmann and R. Komatsu, "Frequency Conversion of Ti:sapphire-Based Femtosecond Laser System to the 200-nm

Spectral Region Using Nonlinear Optical Crystals," IEEE J. Select. Topics in Quantum Electron. 5, pp.1532-1542, 1999

³¹ H. Zhao, P. Wang, J. Zhu, Z. Wei, and Q. Du, "Generation of 460nm femtosecond laser by sum frequency synchronized picosecond Nd:YVO₄ laser and femtosecond Ti:sapphire laser", Proceedings of the 15th International Conference, Pacific Grove, USA, 2006

³² D. N. Nikogosyan, "Nonlinear optical crystals: a complete survey", Springer, New York, 2005

³³ M. Ebrahimzadeh, G. A. Turnbull, T. J. Edwards, D. J. Stothard, I. D. Lindsay and M. H. Dunn, "Intracavity CW singly resonant optical parametric oscillators," J. Opt. Soc. Am. B Vol. 16., p1499-1511, 1999

³⁴ L. B. Jeunhomme, "Single-mode fiber optics : principles and applications", Marcel Dekker, New York, 1990

³⁵ M. Takahashi, J. Hiroishi, R. Suqizaki and Y. Taniquchi, "Highly nonlinear optical fiber and highly nonlinear optical fiber module", US patent 700742

³⁶ T. Nakanishi, M. Hirano, T. Okuno, and M. Onishi "Silica-based highly nonlinear fiber with $\gamma = 30/W/km$ and its FWM-based conversion efficiency", Optical Fiber Communication Conference, OtuH7 paper, Anaheim, 2006

³⁷ A. R. Chraplyvy, "Limitations imposed on lightwave communications by optical-fiber nonlinearities", IEEE Journal of Ligh. Wav. Tech., Vol. 8, pp1548-1557, 1990.

³⁸ Forgheri, R. W. Tackh, A. R. Chraplyvy, and D. Marcuse, 'Reduction of four-wave mixing crosstalk in WDM systems using unequally spaced channels,' IEEE Photon. Technol. Lett. Vol. 6, pp754-756, 1994.

³⁹ S. Radic, C. J. McKinstrie, R. M. Jopson, A. H. Gnauck, J. C. Centanni, and A. R. Chraplyvy, "Multiple-band bit-level switching in two-pump fiber parametric devices," IEEE Photon. Technol. Lett., vol. 16, pp. 852-854, 2004.

⁴⁰ R. H. Stolen and J. E. Bjorkholm, "Parametric amplification and frequency conversion in optical fibers," IEEE J. Quantum Electron., Vol. QE-18, pp.1062-1072, 1982

⁴¹ M. Yu, C.J. McKinstrie and G.P. Agrawal, "Instability due to CPM in normal-dispersion regime". Phys. Rev. E, Vol.48, pp2178-2186, 1993.

-
- ⁴² J. Hansryd, P. A. Andrekson, M. Westlund, J. Li, and P. O. Hedekvist, "Fiber-based optical parametric amplifiers and their applications," *IEEE J. Sel. Topics Quantum Electron.*, vol. 8, pp. 506-520, 2002.
- ⁴³ S. Radic and C. J. McKinstrie, "Optical Amplification and Signal Processing in Highly Nonlinear Optical Fiber," *IEICE Trans. Electron.*, v. E88-C, No5, p.859-869, 2005
- ⁴⁴ S. Radic, C.J. McKinstrie, R.M. Jopson, J.C. Centanni, Q. Lin, G.P. Agrawal, "Record performance of parametric amplifier constructed with highly nonlinear fibre", *Electronics Letters*, vol 39, No. 11, pp838-839, 2003
- ⁴⁵ M. Marhic, "Fiber Optical Parametric Amplifiers, Oscillators and Related Devices", Cambridge University Press, Cambridge, 2007
- ⁴⁶ S. Radic and C. J. McKinstrie, "Two pump fiber parametric amplifier", *Optical Fiber Technology*, Vol. 9, pp7-23, 2003
- ⁴⁷ J.M. Chavez Boggio, S. Tenenbaum, H.L. Fragnito, Amplification of broadband noise pumped by two lasers in optical fibers, *J. Opt. Soc. Am. B*, Vol.18, pp1428-1435, 2001
- ⁴⁸ C. J. McKinstrie, S. Radic and A. R. Chraplyvy, "Parametric amplifiers driven by two pump waves", *IEEE Sel. Top. Quantum Electron.* 8, p.538, V8, No.3, 538-547, 2002
- ⁴⁹ S. Radic, R. M. Jopson, A. Gnauck, C. J. McKinstrie, J. C. Centanni, and A. R. Chraplyvy, "Stimulated-Brillouin-scattering suppression using a single modulator in two-pump parametric architectures", *Optical Fiber Communication Conference, OBN5 paper*, Anaheim, 2005
- ⁵⁰ S. Radic, C. J. McKinstrie, R. M. Jopson, A. H. Gnauck, J. C. Centanni and A. R. Chraplyvy, "Performance of fiber parametric-processing devices using binary-phase-shift-keyed pump modulation," *IEEE Photon. Technol. Lett.*, vol. 16, pp. 548-550, 2004.
- ⁵¹ S. Radic, J. McKinstrie, R. M. Jopson, J. C. Centanni, A. R. Chraplyvy, C. G. Jorgensen, K. Brar, and C. Headley, "Selective suppression of idler spectral broadening in two-pump parametric amplifiers," *IEEE Photon. Technol. Lett.* Vol.15, pp673-675, 2003.
- ⁵² T. Tanemura and K. Kikuchi, "Polarization-independent broad-band wavelength conversion using two-pump fiber optical parametric amplification without idler spectral broadening," *IEEE Photon. Technol. Lett.* Vol. 15, pp1573-1575, 2003.
- ⁵³ J. M. Jopson, "Polarization insensitive optical four photon mixer with orthogonally polarized pumps," *US Patent 5386314* (January 31, 1995).

-
- ⁵⁴ G. W. Lu, K. S. Abedin, T. Miyazaki, "Wavelength Multicasting of DPSK Signals Using Dual-Pump FWM in a Bismuth-Oxide Highly Nonlinear Fiber", Optical Fiber Communication Conference, OMP4 Paper, San Diego, 2008.
- ⁵⁵ Q. Lin, R. Jiang, C. F. Marki, C. J. McKinstrie, R. Jopson, J. Ford, G. P. Agrawal, and S. Radic, "40-Gb/s optical switching and wavelength multicasting in a two-pump parametric device," IEEE Photon. Technol. Lett. Vol. 17, pp2376-2378, 2005
- ⁵⁶ Sumitomo Electric, internal material
- ⁵⁷ P. Russell, "Photonic crystal fibers," Science, Vol. 299, pp. 358-362, 2003.
- ⁵⁸ A. Bjarklev and J. Broeng and A. S. Bjarklev, "Photonic Crystal Fibers", Springer, New York, 2003
- ⁵⁹ M. Yan, P. Shum and X. Yu, "Heterostructured Photonic Crystal Fiber", IEEE Photon. Technol. Lett. Vol. 17, pp1438-1440, 2005
- ⁶⁰ M. Onishi, T. Okuno, T. Kashiwada, S. Ishikawa, N. Akaska, and M. Nishimura, "Highly nonlinear dispersion shifted fiber and its application to broadband wavelength converter," in Proc. 23rd Eur. Conf. Optical Communications, vol. 2, , pp. 115–116, 1997
- ⁶¹ M. Westlund, P. A. Andrekson, H. Sunnerud, J. Hansryd and J. Li, "High performance optical-fiber-nonlinearity-based optical waveform monitoring", IEEE Journal of Ligh. Wav. Tech., Vol. 23, pp2012-2022, 2005
- ⁶² J. H. Lee, T. Nagashima, T. Hasegawa, S. Ohara, N. Sugimoto and K. Kikuchi, "Bismuth-oxide-based nonlinear fiber with a high SBS threshold and its application to four-wave-mixing wavelength conversion using a pure continuous-wave pump", IEEE Journal of Ligh. Wav. Tech., Vol. 24, pp22-28, 2006
- ⁶³ N. Sugimoto, T. Nagashima, T. Hasegawa, S. Ohara, K. Taira, and K. Kikuchi, "Bismuth-based optical fiber with nonlinear coefficient of $1360 \text{ W}^{-1} \cdot \text{km}^{-1}$," Optical Fiber Communications Conference, Paper PDP26, Anaheim, 2004.
- ⁶⁴ I. D. Aggarwal and J. S. Sanghera, "Development and applications of chalcogenide glass optical fibers at NRL", Journal of Optoelectronics and advanced materials, vol. 4, pp665-678, 2002
- ⁶⁵ L. B. Fu, M. Rochette, V. G. Ta'eed, D. J. Moss and B. J. Eggleton, "Investigation of self-phase modulation based optical regeneration in single mode As₂Se₃ chalcogenide glass fiber", Opt. Express, Vol. 13, pp. 7637-7644, 2005

-
- ⁶⁷ B. J. Eggleton, V. G. Ta'eed and B. Luther-Davies, "Chalcogenide Glass, advanced for all-optical processing", *Photonics Spectra*, Laurin Publishing, September, 2007
- ⁶⁸ T. Torounidis, P. A. Andrekson, and B. Olsson, "Fiber-optical parametric amplifier with 70-dB gain", *IEEE Photon. Technol. Lett.* Vol. 18, pp1194-1196, 2006
- ⁶⁹ J. Hansryd and P. Andreksen, "Broad-band continuous-wave-pumped fiber optical parametric amplifier with 49-dB gain and wavelength conversion efficiency," *IEEE Photon. Technol. Lett.* Vol. 13, pp.194-196, 2001.
- ⁷⁰ M. Tang, Y. Gong, and P. Shum, "Broad-band tunable wavelength conversion using Raman-assisted parametric four-wave mixing in highly nonlinear fibers with double-pass geometry", *IEEE Photon. Technol. Lett.* Vol. 17, pp.148-150, 2005
- ⁷¹ K. K. Y. Wong, G. W. Lu, K. C. Lau and L. K. Chen, "All-optical wavelength conversion and multicating by cross-gain modulation in a single-stage fiber optical parametric amplifiers", *Optical Fiber Communication Conference*, paper OTuI4, Anaheim, 2007.
- ⁷² R. Jiang, N. Alic, C. McKinstrie, S. Radic, "Two pump parametric amplifier with 40 db of equalized continuous gain over 50 nm," *Optical Fiber Communication Conference*, paper OWB2, Anaheim, 2007.
- ⁷³ T. V. Andersen, K. M. Hilligsøe, C. K. Nielsen, J. Thøgersen, K. P. Hansen, S. R. Keiding and J. J. Larsen, "Continuous-wave wavelength conversion in a photonic crystal fiber with two zero-dispersion wavelengths," *Opt. Express*, Vol. 12, pp. 4113-4122, 2004
- ⁷⁴ G. Cappellini and S. Trillo, "Third-order three-wave mixing in single-mode fibers: exact solutions and spatial instability effects", *J. Opt. Soc. Am. B*, Vol. 8, pp824-838, 1991
- ⁷⁵ C.G. Joergensen, T. Veng, L. Gruner-Nielsen and M. Yan, "Dispersion flattened highly nonlinear fiber", *European Conference on optical Communication*, Rimini, Italy, 2003
- ⁷⁶ M. Hirano, T. Nakanishi, T. Okuno and M. Onishi, "Selective FWM-based Wavelength Conversion Realized by Highly Nonlinear Fiber", *Optical Fiber Communication Conference*, Anaheim, 2007
- ⁷⁷ C. J. McKinstrie, "Phase-sensitive amplification in a fiber", US Patent 20060285197
- ⁷⁸ A. H. Gnauck, R. M. Jopson, C. J. McKinstrie, J. C. Centanni and S. Radic, "Demonstration of low-noise frequency conversion by Bragg scattering in a fiber", *Opt. Express*, Vol. 14, pp. 8989-8994, 2006

-
- ⁷⁹ P. Parolari, L. Marazzi, E. Rognoni and M. Martinelli, "Influence of pump parameters on two-pump optical parametric amplification", *IEEE Journal of Ligh. Wav. Tech.*, Vol. 23, pp 2524-2530, 2005
- ⁸⁰ M. Gao, C. Jiang, W. Hu and J. Wang, "Optimized design of two-pump fiber Optical parametric amplifier with two-section nonlinear fibers using genetic algorithm ", *Opt. Express*, Vol. 12, pp. 5603-5613, 2004
- ⁸¹ J. Ren, N. Alic, E. Myslivets, R. E. Saperstein, C. J. McKinstrie, R. M. Jopson, A. H. Gnauck, P. A. Andrekson³ and S. Radic, "12.47ns Continuously-Tunable Two-Pump Parametric Delay", *European Conference on optical Communication*, paper PD-2, Cannes, France, 2006.
- ⁸² R.M. Jopson and R.E Tench, *Electron. Lett.*, "Polarisation-independent phase conjugation of lightwave signals", Vol. 29, pp.2216-2217, 1993
- ⁸³ K.K. Y. Wong and M. Marhic, "Polarization-independent two-pump fiber optical parametric amplifier", *IEEE Photon. Technol. Lett.*, V14, p. 911, 2002.
- ⁸⁴ F. Yaman, Q. Lin, S. Radic, G. P. Agrawal, 'Impact of dispersion fluctuation on dual-pump fiber-optic parametric amplifiers', *IEEE Photonics Technology Letters*, Vol. 16, pp1292-1294, 2004
- ⁸⁵ M. Karlsson, "Four-wave Mixing in fibers with randomly varying zero-dispersion wavelength", *J. Opt. Soc. Amer. B*, vol. 15, pp2269-2275, 1998
- ⁸⁶ R. Jiang, N. Alic, C. J. McKinstrie and S. Radic, "Four-sideband analysis of dispersion fluctuations in two pump fiber parametric devices", *Conference on Lasers and Electro-Optics*, paper CMW1, Long Beach, 2006
- ⁸⁷ R. M. Jopson and R. E. Tench, "Polarization-independent phase conjugation of lightwave signals," *Electron. Lett.*, vol. 29, pp2216–2217, 1993
- ⁸⁸ O. Aso, Y. Tashiro, M. Tadakuma, and S. Namiki, "Effect of modulation instability on broadband wavelength conversion using four-wave mixing in optical fiber," in *Optical Fiber Communication Conference*, paper ThL6, Baltimore, 2000.
- ⁸⁹ L. F. Mollenauer, P. V. Mamyshev, and M. J. Neubelt, 'Method for facile and accurate measurement of optical fiber dispersion maps', *Opt. Lett.*, Vol. 21, pp1724-1726, 1996
- ⁹⁰ T. Torounidis, M. Westlund, H. Sunnerud, B. E. Olsson, and P. A. Andrekson, "Signal generation and transmission at 40, 80, and 160 Gb/s using a fiber-optical parametric pulse source," *IEEE Photon. Technol. Lett.*, vol. 17, pp.312–314, 2005.

-
- ⁹¹ S. Radic, C. J. McKinstrie, R. M. Jopson, J. C. Centanni, and A. R. Chraplyvy, "All-optical regeneration in one- and two-pump parametric amplifiers using highly nonlinear optical fiber," *IEEE Photon. Technol. Lett.*, vol. 15, no. 7, pp. 957–959, Jul. 2003.
- ⁹² K. Onohara, Y. Awaji, N. Wada, F. Kubota, and K. Kitayama, "Agile and highly efficient wavelength conversion using highly nonlinear fiber for optical code-labeled packets," *IEEE Photon. Technol. Lett.*, vol. 17, pp. 627–629, 2005
- ⁹³ F. Poli, A. Cucinotta and S. Selleri, "Photonic Crystal Fibers", Springer, New York, 2007
- ⁹⁴ J. C. Knight, "Photonic crystal fibers and fiber lasers", *J. Opt. Soc. Amer. B*, Vol. 24, pp. 1661-1668, 2007
- ⁹⁵ <http://www.crystal-fibre.com/>
- ⁹⁶ R. M. Wynne, "A fabrication process for microstructured optical fibers", *IEEE Journal of Ligh. Wav. Tech.*, Vol. 24, pp. 4304-4313, 2006
- ⁹⁷ P. St. J. Russell, "Photonic-crystal fibers", *IEEE Journal of Ligh. Wav. Tech.*, Vol. 24, pp. 4729-4749, 2006
- ⁹⁸ J. C. Knight, T. A. Birks, P. St. J. Russell, and D. M. Atkin, "Pure silica single-mode fiber with hexagonal photonic crystal cladding," *Optical Fiber Communication Conference*, Paper PD3, San Jose, 1996.
- ⁹⁹ T. Ritari, H. Ludvigsen, M. Wegmuller, M. Legre, N. Gisin, J. R. Folkenberg and M. D. Nielsen, "Experimental study of polarization properties of highly birefringent photonic crystal fibers", *Opt. Express*, Vol. 12, pp. 5931-5939, 2004
- ¹⁰⁰ J. R. Folkenberg, M. D. Nielsen, N. A. Mortensen, C. Jakobsen and H. R. Simonsen, "Polarization maintaining large mode area photonic crystal fiber", *Opt. Express*, Vol. 12, pp. 956-960, 2004
- ¹⁰¹ A. Kudlinski, A. K. George, J. C. Knight, J. C. Travers, A. B. Rulkov, S. V. Popov, and J. R. Taylor, "Zero-dispersion wavelength decreasing photonic crystal fibers for ultraviolet-extended supercontinuum generation", *Opt. Express*, Vol. 14, pp. 5715-5722, 2006
- ¹⁰² K.P. Hansen, J.R. Folkenberg, C. Peucheret, and A. Bjarklev, "Fully Dispersion Controlled Triangular-Core Nonlinear Photonic Crystal Fiber", *Optical Fiber Communication Conference*, paper PD2, Atlanta, 2003.

-
- ¹⁰³ N. I. Nikolov, O. Bang, and A. Bjarklev. "Designing the dispersion for optimum supercontinuum bandwidth using picosecond pulses", Technical Digest Optical Fiber Communication Conference, Atlanta, vol. 1, pp. 17-18, 2003
- ¹⁰⁴ K. Hansen, J. Folkenberg, A. Petersson, and A. Bjarklev. "Properties of nonlinear photonic crystal fibers for telecommunication applications", Optical Fiber Communication Conference, paper FI2, Atlanta, 2003.
- ¹⁰⁵ K. P. Hansen, J. R. Jensen, C. Jacobsen, H. R. Simonsen, J. Broeng, P. M. W. Skovgaard, A. Petersson, and A. Bjarklev. "Highly nonlinear photonic crystal fiber with zero-dispersion at 1.55 μ m". Optical Fiber Communication Conference, paper FA9, Anaheim, 2002
- ¹⁰⁶ S. Coen, A. H. L. C. Chau, R. Leonhardt, J. D. Harvey, J. C. Knight, W. J. Wadsworth, P. St. J. Russell, "Supercontinuum generation by stimulated Raman scattering and parametric four-wave mixing in photonic crystal fibers," J. Opt. Soc. Am. B, Vol. 19, pp. 753-764, 2002.
- ¹⁰⁷ K Cook, C Xiong and W J Wadsworth, "Enhanced four-wave mixing and parametric oscillation in photonic crystal fibre", J. Opt. A: Pure Appl. Opt. vol. 9 pp. 1095–1099, 2007
- ¹⁰⁸ J. S. Y. Chen, G. K. L. Wong, S. G. Murdoch, R. J. Kruhlak, R. Leonhardt and J. D. Harvey, "Cross-phase modulation instability in photonic crystal fibers," Opt. Lett., Vol. 31, pp. 873-875, 2006
- ¹⁰⁹ W. J. Wadsworth, A. Ortigosa-Blanch, J. C. Knight, T. A. Birks, T.-P. Martin Man, P. St. J. Russell, "Supercontinuum generation in photonic crystal fibers and optical fiber tapers: a novel light source," J. Opt. Soc. Am. B, Vol. 19, pp. 2148-2155, 2002
- ¹¹⁰ E. M. Dianov and V. M. Mashinsky, "Germania-based core optical fibers," Journal of Ligh. Wav. Tech.,, vol. 23, pp. 3500–3508, 2005
- ¹¹¹ J. C. Knight, T. A. Birks, P. St.J. Russell, and D. M. Atkin, "All-silica single-mode fiber with photonic crystal cladding," Opt. Lett., vol. 21, pp. 1547–1549, 1996.
- ¹¹² ———, "All-silica single-mode fiber with photonic crystal cladding: Errata," Opt. Lett., vol. 22, pp. 484–485, Apr. 1997.
- ¹¹³ T. A. Birks, J. C. Knight, and P. St.J. Russell, "Endlessly singlemode photonic crystal fiber," Opt. Lett., vol. 22, pp. 961–963, 1997.

-
- ¹¹⁴ B. Zsigri, J. Laegsgaard, and A. Bjarklev. "A novel photonic crystal fibre design for dispersion compensation". *Journal of Optics A: Pure and Applied Optics*, Vol. 6, pp.717-720, 2004
- ¹¹⁵ Y. Li, C. Wang, Y. Chen, M. Hu, B. Liu and L. Chai, "Solution of the fundamental space-filling mode of photonic crystal fibers: numerical method versus analytical approaches", *Applied Physics B: Lasers and Optics*, Vol. 85, pp 597-601, 2006
- ¹¹⁶ Michele Midrio, Mukesh P. Singh, and Carlo G. Someda, "The Space Filling Mode of Holey Fibers: An Analytical Vectorial Solution", *Journal of Ligh. Wav. Tech.*, vol. 18, pp. 1031-1037, 2000
- ¹¹⁷ J. C. Knight, T. A. Birks, P. St. J. Russell, and J. P. de Sandro, "Properties of photonic crystal fiber and the effective index model", *J. Opt. Soc. Am. A*, Vol. 15, pp748-752, 1998
- ¹¹⁸ Y. Li, C. Wang and M. Hu, "A fully vectorial effective index method for photonic crystal fibers: application to dispersion calculation", *Optics Communications*, Vol. 238, pp. 29-33, 2004
- ¹¹⁹ A. Yariv, "Photonics: Optical Electronics in Modern communication", th Ed., Oxford University Press, ,USA 2006
- ¹²⁰ C. H. Henry and B. H. Verbeek., "Solution of the scalar wave equation for arbitrary shaped dielectric waveguides by two dimensional Fourier analysis", *Journal of Ligh. Wav. Tech.*, vol. 7, pp. 308-313, 1989
- ¹²¹ C. H. Henry and Y. Shani, "Analysis of mode propagation in optical waveguide devices by Fourier expansion", *IEEE J. Quantum Electron.*, vol. 27, pp. 523-530, 1991
- ¹²² K. Saitoh and M. Koshiba, "Full-Vectorial Imaginary-Distance Beam Propagation Method Based on a Finite Element Scheme: Application to Photonic Crystal Fibers", *IEEE J. Quantum Electron.*, vol. 98, pp. 927-933, 2002
- ¹²³ K. Kawano and T. Kitoh, "Introduction to Optical Waveguide Analysis: Solving Maxwell's Equation and the Schrödinger Equation", Wiley-Interscience, New York, 2001
- ¹²⁴ User Guide, BeamProp 8.0, Rsoft design group, Ossining, New York
- ¹²⁵ <http://www.rsoftdesign.com/products.php?sub=Component+Design&itm=BeamPROP>
- ¹²⁶ http://ab-initio.mit.edu/wiki/index.php/MIT_Photonic_Bands

-
- ¹²⁷ R. Jiang, C.S. Bres, N. Alic, E. Myslivets and S. Radic, "Translation of Gbps Phase Modulated Optical Signal from Near-Infrared to Visible Band, *IEEE Journal of Ligh. Wav. Tech.*, Vol. 26, pp.131-137, 2008
- ¹²⁸ J. W. Goodman, "Introduction to Fourier Optics", 3rd Ed., Roberts & Company Publishers, Greenwood Village, Colorado, 2004
- ¹²⁹ S. Diddams and J.C. Diels, "Dispersion measurements with white-light interferometry," *J. Opt. Soc. Am. B*, vol. 13, pp. 1120-1128, 1995.
- ¹³⁰ P. Hlubina, "White-light spectral interferometry with the uncompensated Michelson interferometer and the group refractive index dispersion in fused silica," *Opt. Commun.* Vol. 193, pp. 1-7, 2001.
- ¹³¹ P. Hlubina, M. Szpulak, D. Ciprian, T. Martynkien, and W. Urbanczyk, "Measurement of the group dispersion of the fundamental mode of holey fiber by white-light spectral interferometry", *Opt. Express*, Vol. 15, pp. 11073-11081, 2007
- ¹³² R. Jiang, N. Alic, C.B Sophie, S. Moro, and S. Radic. "Continuous-Wave Parametric Generation at Visible band in Photonic Crystal Fibers." 20th Annual meeting of the IEEE Lasers and Electro-optics Society, paper WQ5, Orlando, 2007.
- ¹³³ G. K. L. Wong, A. Y. H. Chen, S. G. Murdoch, R. Leonhardt, J. D. Harvey, N. Y. Joly, J. C. Knight, W. J. Wadsworth and P. St. J. Russell, "Continuous-wave tunable optical parametric generation in a photonic-crystal fiber," *J. Opt. Soc. Am. B*, Vol. 22, pp. 2505-2511, 2005.
- ¹³⁴ A. Y. H. Chen, G. K. L. Wong, S. G. Murdoch, R. Leonhardt, J. D. Harvey, J. C. Knight, W. J. Wadsworth and P. St. J. Russell, "Widely tunable optical parametric generation in a photonic crystal fiber," *Opt Lett.*, Vol. 30, pp. 762-764, 2005
- ¹³⁵ Y. Deng, Q. Lin, F. Lu, G. P. Agrawal, W. H. Knox, "Broadly tunable femtosecond parametric oscillator using a photonic crystal fiber", *Opt. Lett.*, Vol. 30, pp. 1234-1236, 2005.
- ¹³⁶ R. Jiang, N.Alic, J. E. Ford, C. J. McKinstrie and S. Radic, " Gbps-rate channel translation from near-infrared to visible band", Optical Fiber Communication conference, Anaheim, paper OWQ4, 2007
- ¹³⁷ R. Jiang, R. Saperstein, N. Alic, M. Nezhad, C. McKinstrie, J. Ford, Y. Fainman and S. Radic, "375 THz Parametric Translation of Modulated Signal from 1550nm to Visible Band", Optical Fiber Communication Conference, paper PDP16, Anaheim, 2006

-
- ¹³⁸ L. E. Myers and W. Bosenberg, "Periodically Poled Lithium Niobate and Quasi-Phase-Matched Optical Parametric Oscillators," *IEEE J. Quantum Electron.* V33, p1663, 1997
- ¹³⁹ S. E. Bisson, K. M. Armstrong, T. J. Kulp and M. Hartings, "Broadly tunable, mode-hop-tuned CW optical parametric oscillator based on periodically poled lithium niobate," *Appl. Opt.*, v. 40, p6049, 2001
- ¹⁴⁰ G. Jacobsen, "Noise in Digital Optical Transmission Systems", Artech House, Norwood, MA, 1994.
- ¹⁴¹ G. L. Eesley, M.D. Levenson, and W. M. Colles, "Optically heterodyned coherent Raman spectroscopy", *IEEE J. Quantum Electron.*, Vol. 14, pp45-49, 1978
- ¹⁴² E.O. Potma, C. L. Evans, and X. Sunney Xie, "Heterodyne coherent anti-Stokes Raman scattering (CARS) imaging", *Opt. Lett.*, Vol 31, pp241-243, 2006
- ¹⁴³ R. Jiang, N. Alic, R.E. Saperstein, E. Myslivets, C. J. McKinstrie and S. Radic, "Parametric Translation of a Phase-Coded Signal Over a Record Spectral Range", *Optical Fiber Communication conference*, Anaheim, paper PDP37, 2007,
- ¹⁴⁴ P. Dainese, P. St. J. Russell, N. Joly, J.C. Knight, G.S. Wiederhecker, H. L. Fragnito, V. Laude and A. Khelif, "Stimulated Brillouin scattering from multi-GHz-guided acoustic phonons in nanostructured photonic crystal fibres", *Nature Physics*, Vol 2, pp388-392, 2006
- ¹⁴⁵ M. Oskar van Deventer and Andre J. Boot, "Polarization properties of stimulated Brillouin scattering in single-mode fibers", *Journal of Ligh. Wav. Tech.*, Vol. 12, pp585-590, 1994
- ¹⁴⁶ J. Hansryd, F. Dross, M. Westlund, P. A. Andrekson, and S. N. Knudsen, "Increase of the SBS Threshold in a Short Highly Nonlinear Fiber by Applying a Temperature Distribution", *Journal of Ligh. Wav. Tech.*, Vol. 19, pp1691-1697, 2001
- ¹⁴⁷ D. Derickson, "Fiber Optic Test and Measurement", Prentice Hall PTR, Upper Saddle Village, New Jersey, 1998
- ¹⁴⁸ K. Saitoh and M. Koshiba, "Numerical modeling of photonic crystal fibers", *Journal of Ligh. Wav. Tech.*, Vol. 23, pp3580-3590, 2005
- ¹⁴⁹ K. Saitoh, Y. Tsuchida and M. Koshiba, "Endlessly single-mode holey fibers: the influence of core design", *Opt. Express*, Vol. 13, pp. 10833-10839, 2005

-
- ¹⁵⁰ J. S. Y. Chen, S. G. Murdoch, R. Leonhardt, and J. D. Harvey, "Effect of dispersion fluctuations on widely tunable optical parametric amplification in photonic crystal fibers", *Opt. Express*, Vol. 14, pp. 9491-9501, 2006
- ¹⁵¹ R. H. Stolen, "Phase-matched-stimulated four-photon mixing in silica-fiber waveguides", *IEEE J. Quantum Electron.*, Vol. 11, pp.100-103, 1975
- ¹⁵² M. J. Weber, "Handbook of Optical Materials", CRC Press, New York, 2003
- ¹⁵³ T. Toyoda and M. Yabe, "The temperature dependence of the refractive indices of fused silica and crystal quartz", *J. Phys. D: Appl. Phys.*, vol. 16, pp. L97-L100, 1983
- ¹⁵⁴ V.Ya. Aleshkina, A.A. Afonenkob, A. Biryukovc, V.I. Gavrilenkoa, A.A. Dubinova, Vl.V. Kocharovskyd, S.V. Morozova, K.V. Maremynina, S.M. Nekorkinc, B.N. Zvonkovc and N.B. Zvonkovc, "Parametric Generation of Middle and Far Infrared Radiation in GaAs-Based Semiconductor Lasers and Waveguides", *Proceedings of the 12th International Symposium UFPS, Vilnius, Lithuania, 2004*
- ¹⁵⁵ V. Ya. Aleshkin, V. I. Gavrilenko, S. V. Morozov, K. V. Marem'yanin, B. N. Zvonkov, and S. M. Nekorkin, "Observation of the Middle-Infrared Emission from Semiconductor Lasers Generating Two Frequency Lines in the Near-Infrared Region of the Spectrum", *Semiconductors*, Vol. 39, pp. 139-141, 2005
- ¹⁵⁶ <http://www.jtingram.com/sitebuildercontent/sitebuilderfiles/cir.pdf>
- ¹⁵⁷ S. Somkuarnpanit, D. Su, F. Villarreal, A.D. Colley, H. J. Baker, J. D. C. Jones and D. R. Hall, "Beam Delivery Characteristics of Optical Fibres for Carbon Monoxide Lasers", *Opt. and Lasers in Engineering*, vol. 23, pp.221-231, 1995
- ¹⁵⁸ S. Sato, K. Igarashi, and M. Taniwaki, "Multihundred-watt CO laser power delivery through chalcogenide glass fibers", *Appl. Phys. Lett.* Vol. 62, pp. 669-671, 1993
- ¹⁵⁹ Navy Research Lab, internal material
- ¹⁶⁰ D. Hewak, "Properties, Processing and Applications of Glass and Rare Earth-Doped Glass for Optical Fibres", INSPEC, IEEE Michael Faraday House, Stevenage, UK, 1998
- ¹⁶¹ R. Adair, L. L. Chase and S. A. Payne, "Nonlinear refractive-index measurements of glasses using three-wave frequency mixing", *J. Opt. Soc. Am. B*, Vol. 4, pp. 875-881, 2005.
- ¹⁶² M. E. Lines, "Scattering losses in optic fiber materials. I. A new parametrization", *J. Appl. Phys.*, vol. 55, pp. 4052-4057, 1984

-
- ¹⁶³ W. S. Rodney, I. H. Malitson and T. A. King, "Refractive index of arsenic trisulfide", *J. Opt. Soc. Am.*, Vol. 48, pp. 633-636, 1958.
- ¹⁶⁴ P. Klocek and L. Colombo, "Index of refraction, dispersion, bandgap and light scattering in GeSe and GeSbSe glasses", *J. Non-Cryst. Solids (Netherlands)*, vol. 93, pp. 1-16, 1987.
- ¹⁶⁵ P. Klocek, ed. "Handbook of Infrared Optical Materials", Marcel Dekker, New York, 1991.
- ¹⁶⁶ V. Ta'eed, N. J. Baker, L. Fu, K. Finsterbusch, M. R. E. Lamont, D. J. Moss, H. C. Nguyen, B. J. Eggleton, D. Choi, S. Madden, and B. Luther-Davies, "Ultrafast all-optical chalcogenide glass photonic circuits", *Opt. Express*, Vol. 15, pp. 9205-9221, 2007